

1225-0767(ISSN Print)
2287-6715(ISSN Online)
한국연구재단 우수등재학술지

Journal of Ocean Engineering and Technology

Vol. 34, No. 5 (Serial Number 156)

October 2020

한국해양공학회지



www.joet.org



The Korean Society of Ocean Engineers

Editorial Board

■ Editor-in-Chief

Joonmo Choung Inha University, Korea

■ Manuscript Editors

Hyeongsik Choi Korea Maritime and Ocean University, Korea

Joon-Young Kim Korea Maritime and Ocean University, Korea

Seokhwan Ahn Jungwon University, Korea

Sungwon Shin Hanyang University, Korea

Woo Dong Lee Gyeongsang National University, Korea

■ Editorial Board Members

Ahmet Ergin Istanbul Technical University, Turkey

Atila Incecik University of Strathclyde, UK

Beom-Seon Jang Seoul National University, Korea

Bo Woo Nam Seoul National University, Korea

Chang Yong Song Mokpo National University, Korea

Chong Hyun Lee Jeju National University, Korea

Do Kyun Kim Newcastle University, UK

Dongho Jung Korea Research Institute of Ships & Ocean Engineering, Korea

Erkan Oterkus University of Strathclyde, UK

Geoffrey Lyons BPP-TECH, UK

Gökhan Tansel Tayyar Istanbul Technical University, Turkey

Gyungsoo Cho Tongmyong University, Korea

Hee Jin Kang Korea Research Institute of Ships & Ocean Engineering, Korea

Hooi-Siang Kang Universiti Teknologi Malaysia, Malaysia

Hyeon Kyu Yoon Changwon National University, Korea

Hyun-Sik Kim Tongmyong University, Korea

Jinwhan Kim Korea Advanced Institute of Science and Technology, Korea

Jong Chun Park Pusan National University, Korea

Kangsu Lee Korea Research Institute of Ships & Ocean Engineering, Korea

Kookhyun Kim Tongmyong University, Korea

Kwang-Jun Paik Inha University, Korea

Masashi Kashiwagi Osaka University, Japan

Moo Hyun Kim Texas A&M University, USA

Narakorn Srinin Newcastle University, UK

Norimi Mizutani Nagoya University, Japan

Se-Min Jeong Chosun University, Korea

Seongim Choi Virginia Tech, USA

Seung Min Park Hyein Engineering & Construction, Co., Ltd., Korea

Soonchul Kwon Pusan National University, Korea

Sungnam Hong Gyeongsang National University, Korea

Sung-Woong Choi Gyeongsang National University, Korea

Taemin Ha Kangwon National University, Korea

TaeSeong Kim Loughborough University, UK

TaeSoon Kang GeoSystem Research Corp., Korea

Tak Kee Lee Gyeongsang National University, Korea

Weoncheol Koo Inha University, Korea

Yeon-Joong Kim Inje University, Korea

Yong Uk Ryu Chonnam National University, Korea

Younghun Kim Kyungnam University, Korea

Youngsub Lim Seoul National University, Korea

Research Ethics Board

■ Chief

Sung-Bu Suh Dongeui University, Korea

■ Research Ethics Board Members

Han Koo Jeong Kunsan National University, Korea

Jinwhan Kim Korea Advanced Institute of Science and Technology, Korea

Yong Uk Ryu Chonnam National University, Korea

Published on October 31, 2020

Published by The Korean Society of Ocean Engineers (KSOE)

Room1302, 13, Jungang-daero 180beon-gil, Dong-gu, Busan, 48821, Korea

TEL: +82-51-759-0656 FAX: +82-51-759-0657 E-mail: ksoehj@ksoe.or.kr URL: http://www.ksoe.or.kr

Printed by Hanrimwon Co., Ltd., Seoul, Korea E-mail: hanrim@hanrimwon.co.kr

ISSN(print) 1225-0767 **ISSN(online)** 2287-6715

This journal was supported by the Korean Federation of Science and Technology Societies (KOFST) grant funded by the Korean government.

© 2020 by The Korean Society of Ocean Engineers (KSOE)

This is an open access article distributed under the terms of the creative commons attribution non-commercial license (<http://creativecommons.org/licenses/by-nc/4.0>) which permits unrestricted non-commercial use, distribution, and reproduction in any medium, provided the original work is properly cited.

Journal of Ocean Engineering and Technology

한국해양공학회지

CONTENTS

Volume 34, Number 5

October, 2020

<Original Research Articles>

- A Study on the Dynamic Analysis of Mooring System During Hook-up Installation
Min Jun Lee, Hyo Jae Jo, Sung Wook Lee, Jea Hyuk Hwang, Jea Heui Kim,
Young Kyu Kim and Dong Il Baek 285
- Speed-Power Performance Analysis of an Existing 8,600 TEU Container Ship using SPA(Ship Performance Analysis)
Program and Discussion on Wind-Resistance Coefficients
Myung-Soo Shin, Min Suk Ki, Beom Jin Park, Gyeong Joong Lee, Yeong Yeon Lee,
Yeongseon Kim and Sang Bong Lee 294
- Effect of the Turret's Rotational Damping on the Heading Stability of a Turret-Moored FPSO
Soo Young Min, Sung Boo Park, Seong Yun Shin, Da Gyun Shin, Kwang Hyo Jung, Jaeyong Lee,
Seung Jae Lee, Solyoung Han and Yun Suk Chung 304
- Reliability Analysis for Structure Design of Automatic Ocean Salt Collector Using Sampling Method of
Monte Carlo Simulation
Chang Yong Song 316
- Study on Vortex-Induced Vibration Predictions for Ship Rudders
Won-Seok Jang, Suk-Yoon Hong, Jee-Hun Song, Hyun-Wung Kwon and Woen-Sug Choi 325
- Feasible Positions of Towing Point and Center of Gravity for Towfish Attitude Control
Min-Kyu Kim, Dong-Jin Park, Jong-Hwa Kim and Jin-Kyu Choi 334
- Investigation of Hydrate Inhibition System for Shallow Water Gas Field: Experimental Evaluation of KHI and
Simulation of MEG Regeneration Process
Suk Lee, Hyunho Kim, Ki-Heum Park and Yutaek Seo 342
- ### <Technical Articles>
- Preliminary Investigation for Feasibility of Wave Energy Converters and the Surrounding Sea as Test-site for
Marine Equipment
Jin-Yeong Park, Hyuk Baek, Hyungwon Shim and Jong-Su Choi 351
- Study for Operation Method of Underwater Cable and Pipeline Burying ROV Trencher using Barge and Its
Application in Real Construction
Min-Gyu Kim, Hyungjoo Kang, Mun-Jik Lee, Gun Rae Cho, Ji-Hong Li, Tae-Sam Yoon,
Jaeheung Ju and Han-Wan Kwak 361
- ### <Review Article>
- Underwater Acoustic Research Trends with Machine Learning: Ocean Parameter Inversion Applications
Haesang Yang, Keunhwa Lee, Youngmin Choo and Kookhyun Kim 371

GENERAL INFORMATION

“Journal of Ocean Engineering and Technology” is the official journal published by “The Korean Society of Ocean Engineers (KSOE)”. The ISO abbreviation is “J. Ocean Eng. Technol.” and acronym is “**JOET**”. It was launched in 1987. It is published bimonthly in February, April, June, August, October, and December each year. Supplement numbers are published at times.

Journal of Ocean Engineering and Technology (JOET) is a medium for the publication of original research and development work in the field of ocean engineering. JOET covers the entire range of issues and technologies related to the following topics:

Ships and offshore platforms: Design of marine structures; Resistance and propulsion; Seakeeping and maneuvering; Experimental and computational fluid dynamics; Ocean wave mechanics; Fatigue strength; Plasticity; Optimization and reliability; Arctic technology and extreme mechanics; Noise, vibration, and acoustics; Concrete engineering; Thermodynamics and heat transfer; Hydraulics and pneumatics;
Coastal civil engineering: Coastal structures; Port and harbor structures; Soil mechanics; Drilling and exploration; Hydraulics of estuary; Seismic engineering; Coastal disaster prevention engineering;
Ocean renewable energy platforms: Offshore wind turbines; Wave energy platforms; Tidal current energy platforms; Floating photovoltaic energy platforms;
Marine robots: Robot sensor system; Autonomous navigation; Robot equipments; Spatial information and communications; Underwater network; Design of underwater vehicles;
Multidisciplinary areas: Design for safety; IT-based design; IT-based production engineering; Welding mechanics; Control engineering; GPS and GIS; Inspection and sensor; Port and logistics; Leisure boat and deep sea water; Offshore process systems engineering; Marine metallic materials; Marine organic materials; Marine Composite materials; Materials properties; Corrosion and Anti-corrosion; Tribology;

It contains original research articles, case reports, brief communications and reviews on technical issues. Conference papers, research papers, diploma papers and academic articles can be submitted.

All of the manuscripts are peer-reviewed. **JOET** has a system where two or more peer reviewers must review each submitted paper and it is operated very strictly.

JOET is an open access journal distributed under the terms of the creative commons attribution non-commercial license (<http://creativecommons.org/licenses/by-nc/4.0>). Therefore, all ocean engineers and researchers around the world can easily access all journal articles via the journal homepage (<http://www.joet.org>) and download the PDF-based original texts or view the web-based XML texts for free.

JOET is being indexed in some prominent database such as Korean Citation Index (KCI), Google Scholar, Science Central, Korea Science and Directory of Open Access Journals (DOAJ).

For correspondences concerning business matters, author needs to contact KSOE Secretariat by email or phone (e-mail: ksoehj@ksoe.or.kr or Tel: +82 51 759 0656). Correspondences for publication matters can be asked via email to the Editor-in-Chief (email: heroeswise2@gmail.com).

A Study on the Dynamic Analysis of Mooring System During Hook-up Installation

Min Jun Lee¹, Hyo Jae Jo², Sung Wook Lee², Jea Hyuk Hwang²,
Jea Heui Kim¹, Young Kyu Kim¹ and Dong Il Baek³

¹Graduate Student, Division of Naval Architecture and Ocean Systems Engineering, Korea Maritime and Ocean University, Busan, Korea

²Professor, Division of Naval Architecture and Ocean Systems Engineering, Korea Maritime and Ocean University, Busan, Korea

³Professor, Department of Civil Engineering, Korea Maritime and Ocean University, Busan, Korea

KEY WORDS: Hook-up, Mooring line, Tugboat, Dynamic analysis, Station keeping

ABSTRACT: This study evaluated the Hook-up installation of an offshore site construction process, which is the final step in an offshore site installation process. During Hook-up installation, the offshore structure can have a detrimental effect on the work stability due to low-frequency motion. Moreover, economic costs can be incurred by the increase in available days of a tugboat. Therefore, this study developed a numerical analysis program to assess the dynamic behavior of mooring systems during hook-up installation to analyze the generally performed installation process and determine when the tugboat should be released. In this program, the behavior of an offshore structure was calculated using Cummin's time-domain motion equation, and the mooring system was calculated by Lumped mass method (LMM). In addition, a tugboat algorithm for hook-up installation was developed to apply the Hook-up procedure. The model used in the calculations was the barge type assuming FPSO (Floating production storage and off-loading) and has a taut mooring system connected to 16 mooring lines. The results of the simulation were verified by comparing with both MOSES, which is a commercial program, and a calculation method for restoring coefficient matrix, which was introduced by Patel and Lynch (1982). Finally, the offset of the structure according to the number of tugboats was calculated using the hook-up simulation, and the significant value was used to represent the calculation result.

Nomenclature

M_{kj}	Ship mass (kg, kg·m ²)	F_{moor}	Mooring tension (N, N·m)
$m_{kj}(\infty)$	Infinite frequency added mass (kg, kg·m ²)	H_s	Significant wave height (m)
$K_{kj}(t)$	Memory effect function	T_s	Significant wave period (s)
C_{kj}	Restoring coefficient (N/m, N·m)	γ	Peak parameter
$F_k(t)$	Exciting force (N, N·m)	α	Heading angle (deg)
F_w, F_c	Wind force, Current force (N, N·m)		
ρ_{air}, ρ_{water}	Air density, Water density (kg/m ³)		
V_w, V_c	Wind velocity, Current velocity (m/s)		
$C_x(\beta), C_y(\beta), C_\theta(\beta)$	Drag coefficient		
$A_x, A_y, A_\theta(\beta)$	Projected Area (m ²)		
$m_{kj}(\omega)$	Added mass coefficient (kg, kg·m ²)		
$b_{kj}(\omega)$	Wave-making damping coefficient		
$H(\omega)$	Wave exciting force transfer function		
F_{wave}	Wave exciting force (N, N·m)		

1. Introduction

According to the environment of the operating site, offshore structures that are used to develop submarine resources generally use a range of mooring systems, such as mooring lines, a dynamic positioning system. The offshore structure should be operated on a specific site for a long time, so mooring lines are generally used for safety. The conventional installation procedure of a mooring system is divided largely into four steps, as shown in Fig. 1. First, anchor piles should be installed at the seabed (Anchor installation). Second,

Received 13 April 2020, revised 27 August 2020, accepted 1 September 2020

Corresponding author Hyo-Jae Jo: +82-51-410-4302, hjjo@kmou.ac.kr

It is a recommended paper from the proceedings of 2019 autumn conference of the Korean Society of Ocean Engineering (KSOE).

© 2020, The Korean Society of Ocean Engineers

This is an open access article distributed under the terms of the creative commons attribution non-commercial license (<http://creativecommons.org/licenses/by-nc/4.0>) which permits unrestricted non-commercial use, distribution, and reproduction in any medium, provided the original work is properly cited.

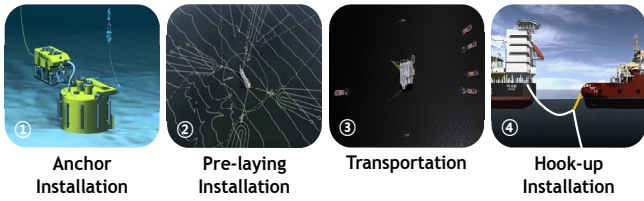


Fig. 1 Offshore site installation process

mooring lines are connected to the installed anchor pile on the seabed (Pre-laying installation). Third, the constructed offshore structures are transported to the site (Transportation). Finally, the installation process of the mooring system is completed after attaching mooring lines, which are pre-layed on the seabed, with the offshore structure (Hook-up installation). In particular, the likelihood of low-frequency motion during the hook-up installation process is high. Therefore, a work safety assessment is needed to prevent negligent accidents due to the marine environment.

Regarding the general installation of a mooring system in the ocean, Lee (2011) examined the transportation of a truss spar using a barge. Song and Kim (2018) assessed the installation of a suction anchor pile in the deep sea to determine if it is possible to install, dividing three steps: lifting the anchor pile from the barge (Pick-up), passing the water level (Lowering through the splash zone) and putting down the anchor pile on the seabed (Landing). In addition, Yoon and Kim (2018) analyzed pre-laying installation in the deep sea to review work safety.

Before analyzing the motion response of the moored offshore structure, the motion calculation module of the structure is first required. Jo (1991) developed an analysis program that applied frequency domain analysis results using the Green function to the time domain motion equation and studied the dynamic response characteristics of a semi-submersible offshore structure. The reliability was verified by comparing the results of Pinkster's theory and model experiments. The Lumped mass method (LMM) and Finite element method (FEM) are generally used to analyze the mooring system. The LMM has the advantage of a relatively simple calculation process and fast calculation time (Hwang, 1988).

This study developed the numerical analysis program to calculate the motion response of the offshore structure during the hook-up procedure based on Jo (1991)'s program. The structure has the taut mooring system composed of fiber ropes considering the excessive weight due to an increase in the mooring line length (Park et al., 2017) in the deep sea. The results derived from the developed program were then verified using the commercial program, MOSES (Multi operational structural engineering simulator), and a determination method for restoring coefficient matrix. Finally, the hook-up installation, which is generally known, was analyzed, and dynamic analysis of the mooring system related to the work stability was performed. This paper also suggests the withdrawal timing of a tugboat during the hook-up installation using the results of the simulation.

2. Theoretical Background

2.1 Motion Equation

In this study, the motion response of the floating body was calculated using the time domain motion equation reported by Cummins (1962) as Eq. (1). Time-domain analysis takes relatively more time to yield results than frequency domain analysis, but it can be calculated with high accuracy, including non-linear properties.

$$\sum_{j=1}^6 [\{M_{kj} + m_{kj}(\infty)\}] \ddot{x}(t) + \int_0^t K_{kj}(t-\tau) \dot{x}_j(\tau) d\tau + C_{kj} \dot{x}_j(t) = F_k(t) \quad (1)$$

($k = 1, 2, \dots, 6$)

2.2 Analysis of Mooring System

An analysis of the mooring system is classified largely into two steps: static analysis and dynamic analysis. According to Berteaux (1976), it can be possible to calculate the initial coordinate and the tension of mooring lines using the suggested equation, which is about static analysis. The fluctuating tension can be estimated by dynamic mooring analysis. Moreover, dynamic analysis of a mooring system can be performed by applying the displacement information of a floating body derived from the motion equation after conducting static analysis of a mooring system (as shown in Fig. 2). This study estimated the fluctuating tension for dynamic analysis of a mooring system using LMM. The results were verified by comparing it with the determination method of restoring coefficient matrix.

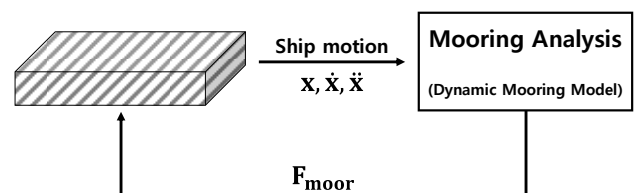


Fig. 2 Mooring analysis process

2.2.1 Lumped Mass Method (LMM)

LMM is based on the FEM, which means analyzing the mooring line by dividing the segment according to the number of nodes and imposing mass on each node. At this time, each segment of the mooring line comprised the mass-spring system. Van den Boom (1985) introduced the LMM, which is relatively fast and simplifies the problem of complex mooring systems (Hwang, 1998). In particular, because the calculation, including the mass, is performed, it can analyze the catenary mooring system in the shallow water afterward

2.2.2 Determination Method of Restoring Coefficient Matrix

Patel and Lynch (1982) proposed a 6×6 restoring coefficient matrix, which can estimate restoring forces due to the taut mooring system. The fluctuating tension can be calculated by multiplying the matrix suggested by Patel and the displacement matrix of the structure. While Patel's theory yielded high-accuracy results for the taut mooring system, it did not consider the effects of inertia and damping

of mooring lines.

2.3 Wind and Current Force

Wind and current forces that affect a floating body are determined by their respective velocities and the incident angle of the force (Kim et al., 2018). They are defined as Eqs. (2)-(3), respectively. Eq. (4) defines the variation of the projected area by the incident angle.

$$F_w = \frac{1}{2} \rho_{air} V_w^2 \begin{bmatrix} C_X(\beta) A_X \\ C_Y(\beta) A_Y \\ C_\theta(\beta) A_\theta(\beta) \end{bmatrix} \quad (2)$$

$$F_c = \frac{1}{2} \rho_{water} V_c^2 \begin{bmatrix} C_X(\beta) A_X \\ C_Y(\beta) A_Y \\ C_\theta(\beta) A_\theta(\beta) \end{bmatrix} \quad (3)$$

$$A_\theta(\beta) = [(Breadth) \times \cos\beta + (Length) \times \sin\beta] \times (Depth) \quad (4)$$

2.4 Tugboat

The hook-up algorithm of a tugboat, which is applied in this study, is a method for calculating the fairlead coordinate (x_n, y_n) , which varies at every time step and returns to the initial coordinate (x_0, y_0) , as shown in Figs. 3-4. Each thrust induced by the tugboat is calculated by the relationship between the calculated coordinate (x_n, y_n) and the initial coordinate (x_0, y_0) , but the thrust does not exceed their maximum capacity. Finally, the position of the tugboat and the relative angle with the structure are calculated and used as the initial condition for the next time step. On the other hand, the motion of the structure by the thrust only considers surge, sway, and yaw (x, y, θ_z) , and the behavior of the tugboat by the external force can be ignored.

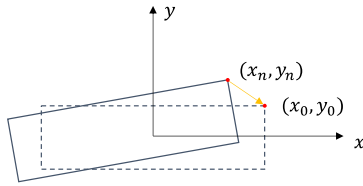


Fig. 3 Initial position of a tugboat

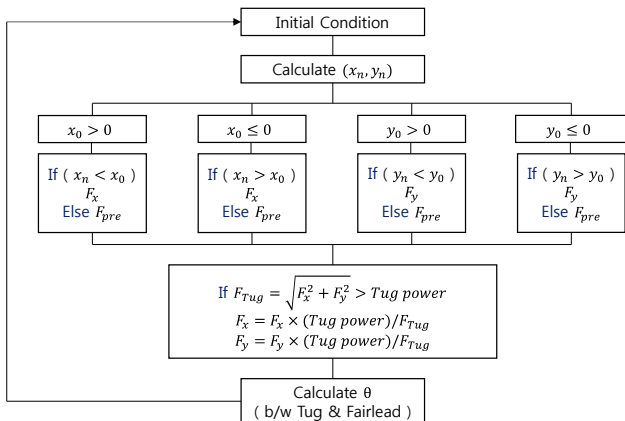


Fig. 4 Flowchart of tug boat calculation

2.5 Analysis Process

Fig. 5 shows the analysis process of the program developed in this study. First, the infinite frequency-added mass $m_{kj}(\omega)$, memory effect function $K_{kj}(t)$, and wave exciting force $F_{wave}(t)$ are calculated using the input data: added mass coefficient $m_{kj}(\omega)$, wave-making damping coefficient $b_{kj}(\omega)$, and the transfer function of wave-exciting force $F_{wave}(t)$ from the analysis result of the frequency domain. And then, each external force ($F_{wind}(t)$, $F_{current}(t)$, $F_{tug}(t)$) is calculated by applying their information, and numerical simulation is performed, including the external force term of the motion equation. Finally, the fluctuating tension of the mooring line F_{moor} is calculated using the displacement information of the structure and mooring information. The iterative calculation is then performed by including this force (F_{moor}) in the external force term of the motion equation at the next step.

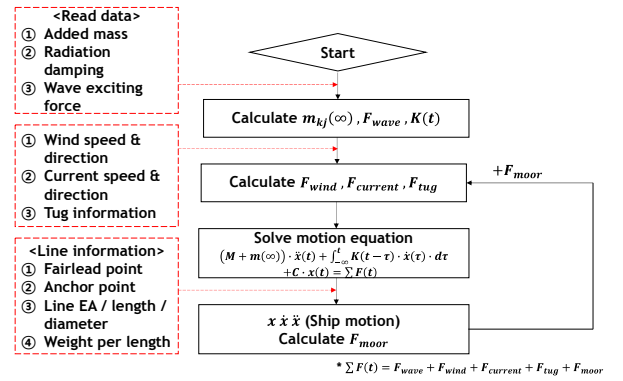


Fig. 5 Offshore site installation process

3. Validation of the Program

3.1 Definition of the Model and Mooring System

The structure used in this study is a barge model that assumes Floating production storage and off-loading (FPSO). Table 1 and Fig. 6 present the main dimension and shape of the model, respectively.

The mooring type is a taut mooring comprised of fiber ropes. In addition, 16 mooring lines consist of four bundles of four each and are spread structure (as shown in Fig. 7). Table 1 lists the main dimensions of the mooring line.

Table 1 Main dimension of the barge

Description	Magnitude
Length between perpendicular (m)	120
Breadth (m)	40
Draft (m)	8
Weight (t)	38,400
Center of gravity (m)	8
Water depth (m)	1,000
Radius of gyration around X-axis (m)	12.32
Radius of gyration around Y-axis (m)	35.29
Radius of gyration around Z-axis (m)	36.94

Table 2 Main dimension of a Mooring line

Description	Magnitude
Elasticity (MN)	300
Initial length (m)	1211.64
Weight/Length (kg/m)	7
Diameter (m)	0.178
Number of lines	16
Pretension (kN)	2200

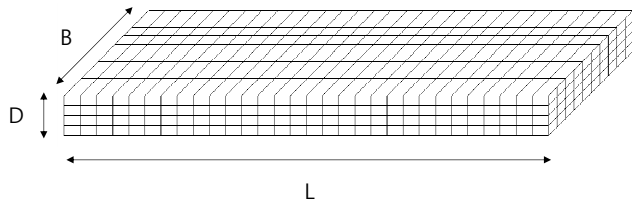


Fig. 6 Barge model

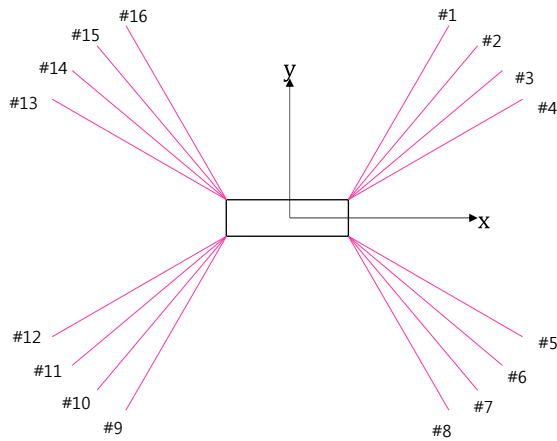


Fig. 7 Mooring layout

3.2 Motion Response

To verify the analysis results of the program (LMM) developed in this study, the motion response results of the moored structures are compared using MOSES and Patel’s theory (as shown in Figs. 8-10).

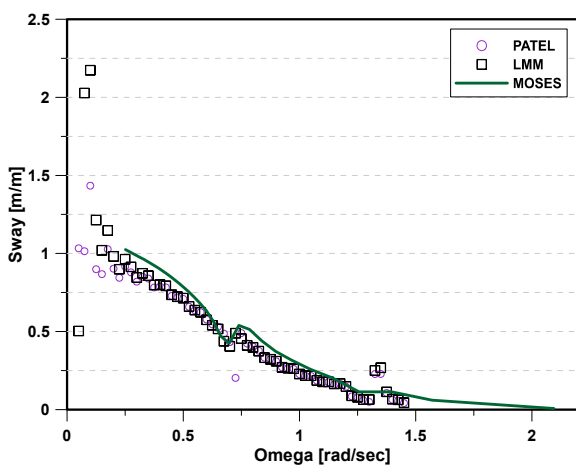


Fig. 8 Sway motion response

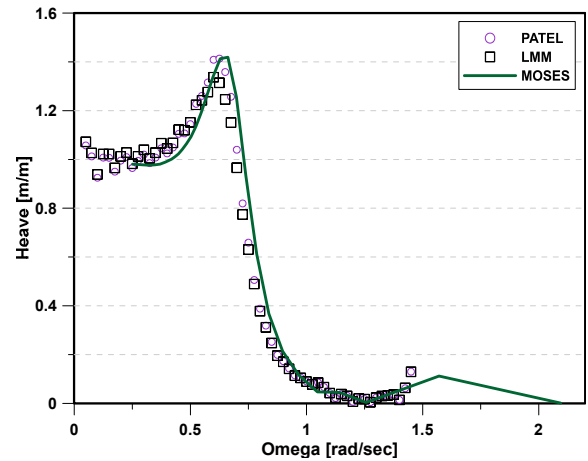


Fig. 9 Heave motion response

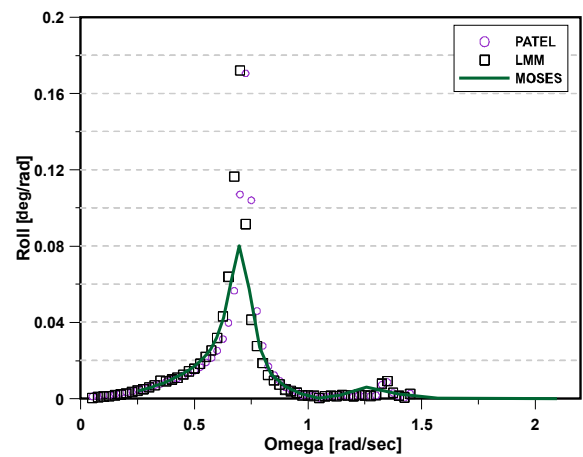


Fig. 10 Roll motion response

Each graph represents the motion response to sway, heave, and roll, and they are in good agreement.

3.3 Hook-up Algorithm of a Tugboat

Tugboats are used for station keeping of the structure in the hook-up procedure. The analysis results of MOSES are compared to determine if the algorithm of the tugboat applied in this study is suitable for an analysis of the hook-up procedure. First, the structure and two tugboats are positioned, as shown in ① of Fig. 11, and when a thrust is generated by tugboats in both horizontal directions, an examination is performed to determine if the structure rotates to the target position, as shown in ③ of Fig. 11. Fig. 12 shows the analysis results of LMM and MOSES. In the case of LMM, the structure converges to the target position (0°), as shown in ③ of Fig. 9, but in the case of MOSES, it converges to -18.39°. According to Bentley systems (2016), the tugboat can be analyzed by receiving the initial towing direction and the maximum capacity of the tugboat. Once the towing direction is applied, it is towed at a certain angle without change until the end time of the calculation. Therefore, the calculated result in MOSES does not converge to 0°, as shown in ③ of Fig. 11, but converges to -18.39°, where the two tugboats and the structure are in equilibrium.

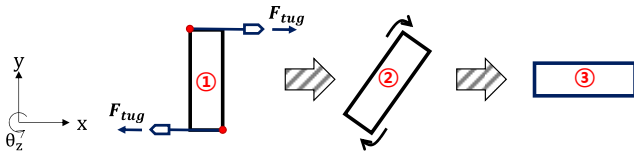


Fig. 11 Tugboat validation

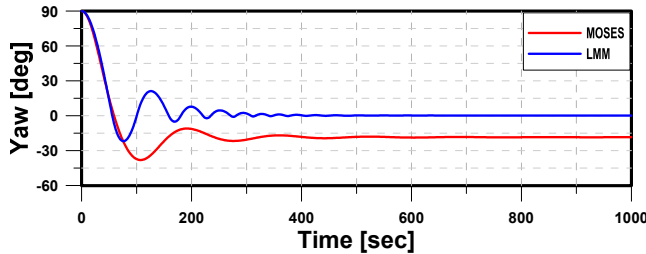


Fig. 12 Yaw motion of the barge

4. Hook-up Simulation

The hook-up installation refers to lifting the mooring line previously arranged on the sea bed and connecting it with the structure that has arrived at the installation site. The dynamic behavior of the structure can be controlled using several tugboats and, at the same time, proceeds with a hook-up installation using AHTS (Anchor handling tug supply vessels) and ROV (Remotely operated vehicle). The procedure can be planned in various ways depending on the environmental conditions, shape of the structure, number of mooring lines, and mooring method. In this study, an analysis was conducted on the hook-up procedure, which is generally performed during offshore installation work.

4.1 General Hook-up Procedure

The hook-up installation procedure is generally performed as shown in Table 3. ‘Step’ is the order of installation, ‘Line number’ is the number assigned to each mooring line, and ‘Pre-tension’ is the ratio of the designed initial tension. After the structure arrives at the site, Step 1 represents the waiting situation before the hook-up installation, and Steps 2-5 mean that each mooring line is connected to the structure and maintains 50% of the designed pre-tension. When the four lines and the structure are in equilibrium, the designed pre-tension is set in Step

6 (Pre-tension: 100%). The pre-tension can be adjusted using winches inside the structure, and Steps 7-21 are repeated in the same way as the work of Steps 2-6. The mooring line arrangement, at this time, is shown in Fig. 13.

4.2 Environmental Condition

According to DNV (2011), an appropriate environmental condition should be selected considering the working period when conducting an offshore construction. In this case, the work period was expected to take approximately one month. The environmental conditions at this time were selected, as shown in Table 4, by referring to Yoon and Kim (2018) and DNVGL (2018).

Table 3 Hook-up installation procedure (Mermaid Consultant’s Naval Architects & Marine Consultants, n.d.)

Step	Line Number	Pre-tension	Step	Line Number	Pre-tension
1	-	-	12	#2	50%
2	#4	50%	13	#7	50%
3	#5	50%	14	#10	50%
4	#12	50%	15	#15	50%
5	#13	50%	16	#2, #7, #10, #15	100%
6	#4, #5, #12, #13	100%	17	#1	50%
7	#3	50%	18	#8	50%
8	#6	50%	19	#9	50%
9	#11	50%	20	#16	50%
10	#14	50%	21	#1, #8, #9, #16	100%
11	#3, #6, #11, #14	100%			

Table 4 Environmental conditions

Wave				Wind		Current	
H_s (m)	T_s (s)	γ	α (°)	V (m/s)	α (°)	V (m/s)	α (°)
4.22	9.15	3.3	0	10	30	1.37	45
JONSWAP ¹							

¹JONSWAP: Joint North Sea wave project spectrum

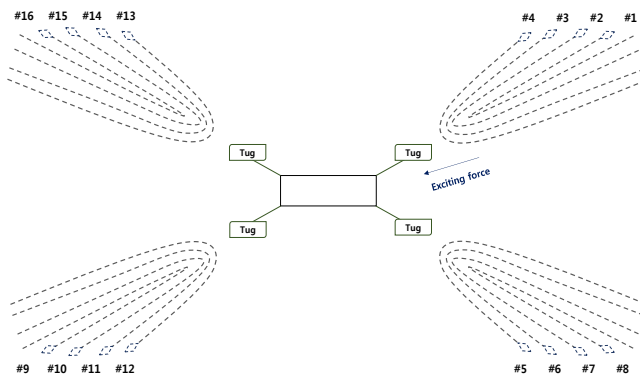


Fig. 13 Pre-laid installation before the hook-up operation

4.3 Hook-up Simulation

In this study, a simulation was performed to evaluate the stability of the structure during hook-up installation. Table 5 lists the main dimensions of the tugboat for station keeping of the structure, and Fig. 14 shows the arrangement of the tugboat. In the simulation, the analysis was performed for all hook-up procedures (Steps 1–21) for the case where four tugboats were arranged (Tug 4). For two tugboats (Tug 2) and no tugboat (Tug 0), the analysis was performed from Step 6, where four mooring lines were connected and adjusted to designed pre-tension, to Step 21.

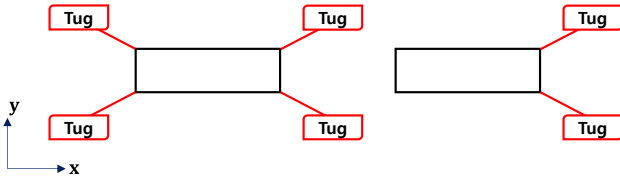


Fig. 14 Layout of the tugboats

Table 5 Main dimensions of the tugboat

Description	Magnitude
Tug maximum power (t)	100
Tug line length (m)	100
Line elasticity (MN)	200

Figs. 15-17 show the x , y offset of the structure and the rotational direction θ_z on the x - y plane in Step 1, which is the step of maintaining the position only with the thrust of four tugboats without connecting mooring lines. First, the structure shows large movement in the x -direction after 2,250 s have passed (as shown in Fig. 15). To determine the cause, Fig. 18 shows the time history of the second-order wave force, which confirmed that more than 300 t of wave force was acting before the large behavior of the structure occurred. As shown in Table 5, the maximum thrust of one tugboat is 100 t, and the upper limit of the total thrust of a tugboat that can be

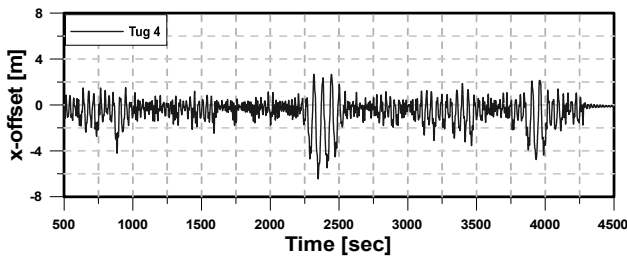


Fig. 15 Time history of the x -offset with tug 4 (Step 1)

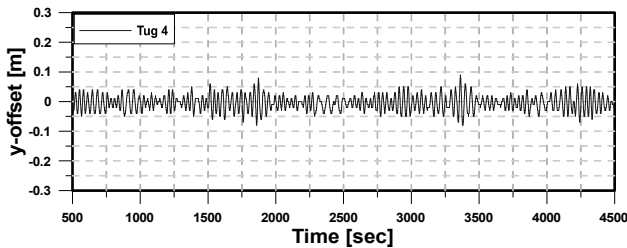


Fig. 16 Time history of the y -offset with tug 4 (Step 1)

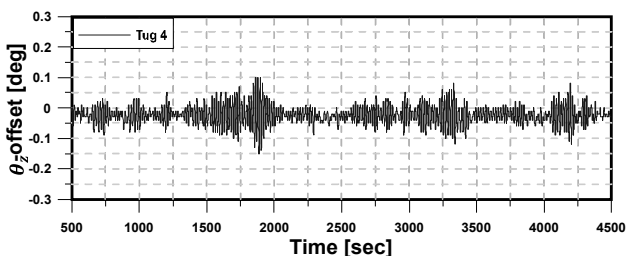


Fig. 17 Time history of the θ_z -offset with tug 4 (Step 1)

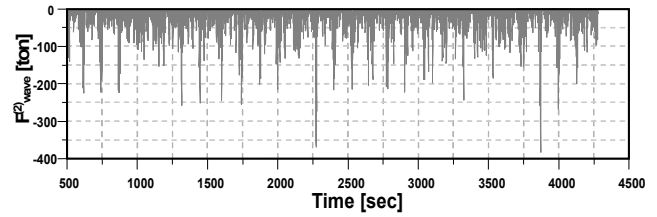


Fig. 18 Time history of the second-order wave force

produced in one direction is 200 t. In other words, due to the limit of the total thrust of the tugboat, the large motion of the structure occurred by the second-order wave force. The behavior in the y -direction and θ_z -direction is a result of the current and wind forces acting on the structure in different directions, suggesting that the offset of the structure is well maintained with only the thrust of the four tugboats.

Figs. 19-21 present the x , y , and θ_z offset of the structure in Step 6, which is connected with four mooring lines by designed pre-tension. Each graph compares the behavior of the structure according to the number of tugboats. Tug 4 has four tugboats with mooring lines; Tug 2 has two tugboats with mooring lines; Tug 0 has no tugboat with connecting mooring lines only. First, the analysis of the time history of the x -direction offset resulted in stronger behavior when there were two tugs than when there were four tugs. When there was no tugboat, large motion of the structure occurred at a distance away from the origin due to the steady drift force.

Among the external forces acting on the structure, the wave force is dominant. To control it, the tugboat generates an excessive force in the x -direction. The thrust in the x -direction of the tugboat causes a rotational moment in the structure. To control the y -direction offset of the structure due to the rotational moment, the tugboat produces a moment in the opposite direction by generating thrust. Therefore, when maintaining the position of the structure using two tugboats, the offset of the structure is larger in the case of the y -direction and θ_z -direction than the other cases. Therefore, the offset of the structure without connecting the tugboat converges to the point away from the origin and returns to the origin when using four tugboats. In other words, if two tugboats are used in Step 6, the x offset of the structure can be controlled, but y and θ_z offset appears unstable. In addition, when the tugboat is not connected, the offset of the structure deviates from the origin due to the steady drift force, causing instability. Therefore, it is important to maintain the position of the structure using four tugboats in this step.

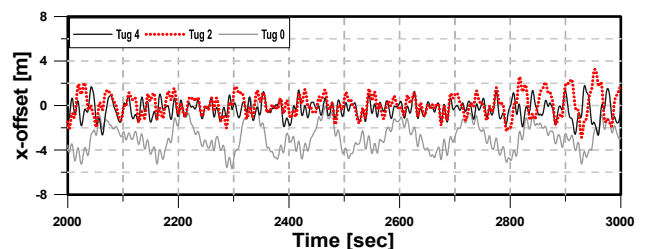


Fig. 19 Time history of the x -offset (Step 6)

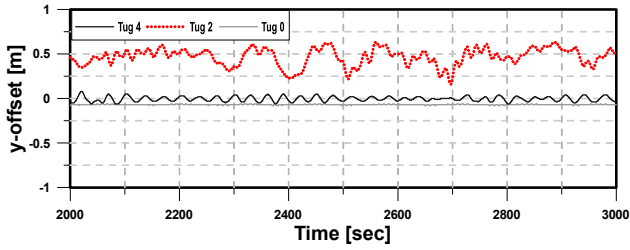


Fig. 20 Time history of the y -offset (Step 6)

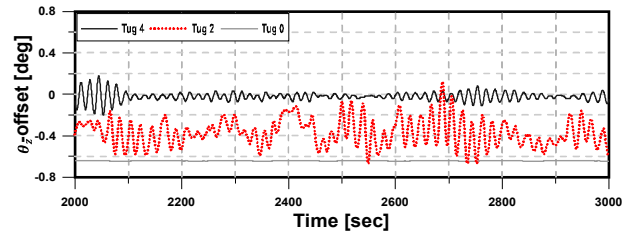


Fig. 21 Time history of the θ_z -offset (Step 6)

And in the situation where two tug boats were arranged, the structure shows larger amplitudes in the y and θ_z directions than other cases, but was relatively stable compared to Step 6.

Figs. 22-24 show the x , y , and θ_z offset of the structure in Step 11, which is connected to eight mooring lines by designed pre-tension. In this step, the x -offset of the structure was largely reduced by four tugboats, and there was no difference in the behavior of the structure between Tugs 2 and 4. In the absence of a tugboat, the effect of the steady drift force was reduced significantly compared to Step 6, as shown in Fig. 19, but the amplitude of the offset was increased. Fig. 25 presents the results of frequency analysis, i.e., FFT (Fast Fourier transform), of the time history of surge motion and second-order wave force when the tension of eight mooring lines was set to the designed pre-tension. In this graph, the two peak frequencies almost coincided. As a result, a large amplitude of x -offset occurred.

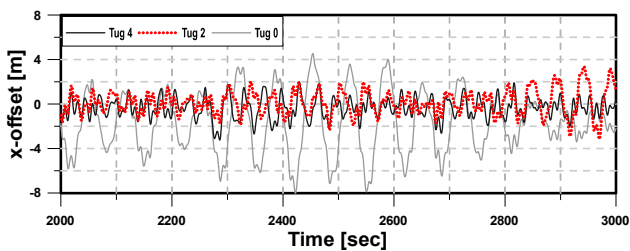


Fig. 22 Time history of x -offset (Step 11)

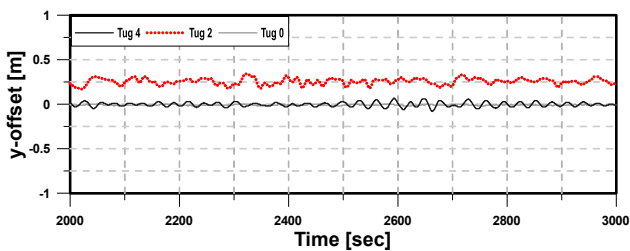


Fig. 23 Time history of the y -offset (Step 11)

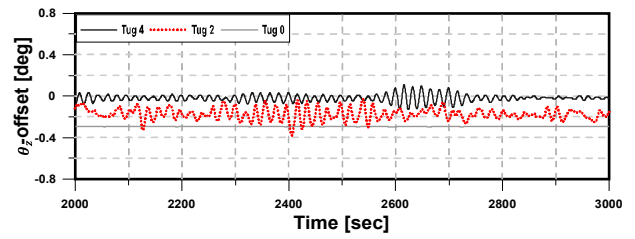


Fig. 24 Time history of the θ_z -offset (Step 11)

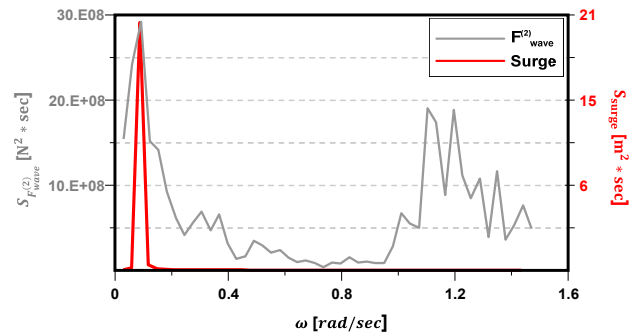


Fig. 25 Second-order wave force spectrum with a surge

In the situation where two tugboats were arranged, the structure showed larger amplitudes in the y and θ_z directions than the other cases, but it was relatively stable compared to Step 6.

Figs. 26-28 show the x , y , and θ_z offset of the structure in Step 16,

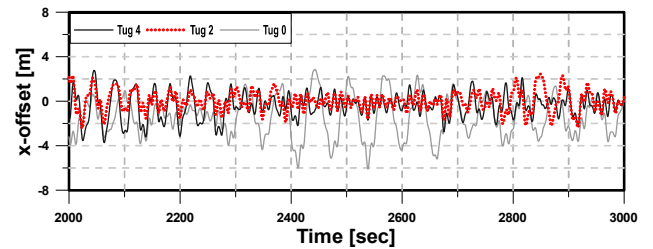


Fig. 26 Time history of the x -offset (Step 16)

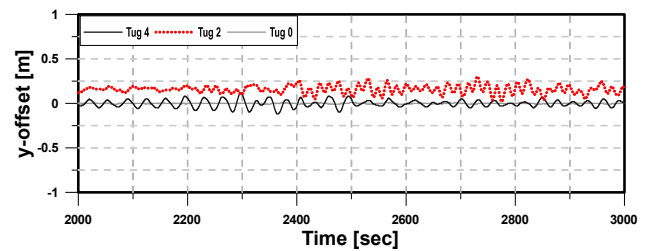


Fig. 27 Time history of the y -offset (Step 16)

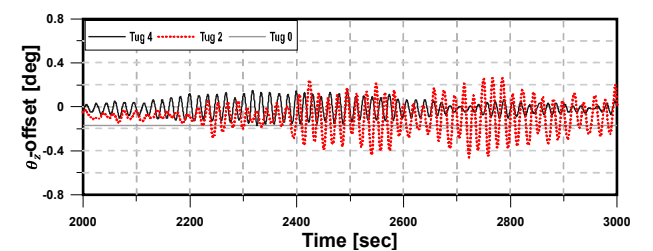


Fig. 28 Time history of the θ_z -offset (Step 16)

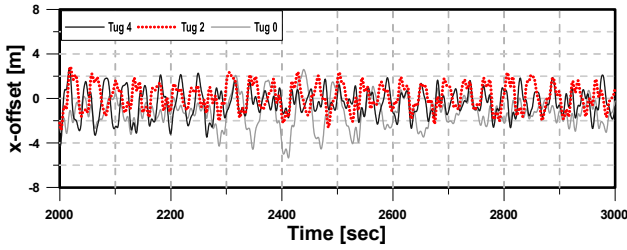


Fig. 29 Time history of the x -offset (Step 21)

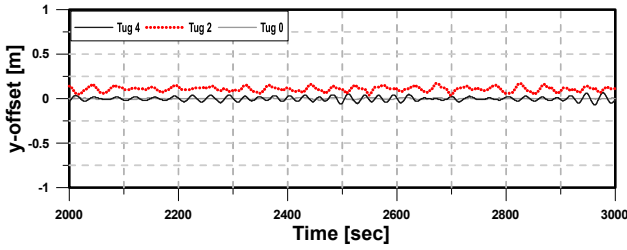


Fig. 30 Time history of the y -offset (Step 21)

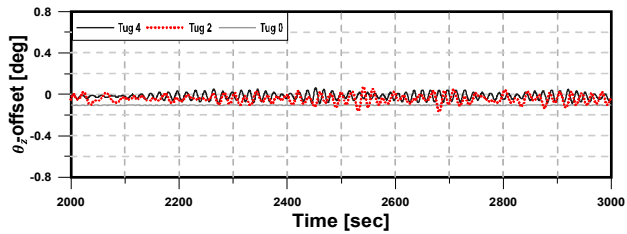


Fig. 31 Time history of the θ_z -offset (Step 21)

which is connected to 12 mooring lines by designed pre-tension. No significant differences in the offset of the structure were observed between Tugs 4 and 2. When the position is maintained only by the tension of the mooring line without a tugboat, the y and θ_z offset is extremely small. In the case of the x -offset, the movement was reduced significantly compared to Step 11.

Figs. 29-31 show the x , y , and θ_z offset of the structure in Step 21, which is the final step in the hook-up procedure. When the entire mooring line was connected to the structure, the x -offset behaves stably without connecting a tugboat (as shown in Fig. 29). In addition, even in the y and θ_z offsets, the motion of the structure maintained a minute value without connecting a tugboat.

4.4 Results

The simulation results for the behavior of the structure during the hook-up installation derived in this study are represented using significant values (as shown in Figs. 32-34). The thick solid line indicates the final hook-up procedure. The structure, which arrived at the installation site by transportation, starts the hook-up installation by connecting the first mooring line while maintaining its position using four tugboats. When the step of connecting the 6th mooring line (Step 8) was over, the two tugboats were withdrawn, and the position of the structure was maintained until 12 mooring lines were connected with the remaining two tugboats (Step 16). In this way, by arranging only

two tugboats, the structure can control large movements in the x -direction, which occurred due to the second-order wave force in Step 11 (eight mooring lines are connected with designed pre-tension). All tugboats were withdrawn at Step 17, and installation was carried out until Step 21, which is a final step, while the structure maintains its position by only mooring lines.

Therefore, the significant value of the structure offset was set not to exceed 6 m when organizing the installation procedure by summarizing the simulation results according to the arrangement of the tugboat. Each classification society and certification body present only the external environmental conditions according to the installation period for mooring system installation. Moreover, there were no regulations during the installation process, such as stability and installation plans. Normally, during hook-up installation, all tugboats are withdrawn when half of the entire mooring line is connected. In the case of this study, however, at the stage of Step 11, when half of the mooring lines

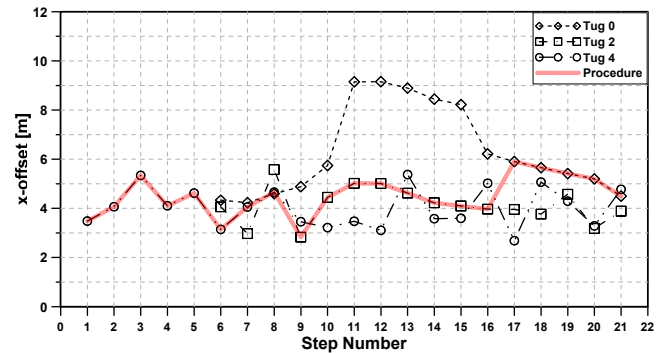


Fig. 32 Result of the x -offset during hook-up installation

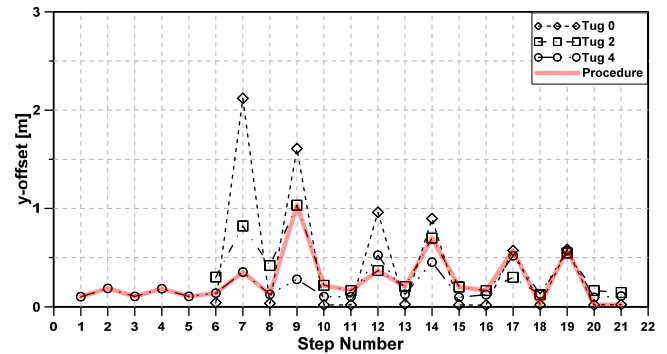


Fig. 33 Result of the y -offset during hook-up installation

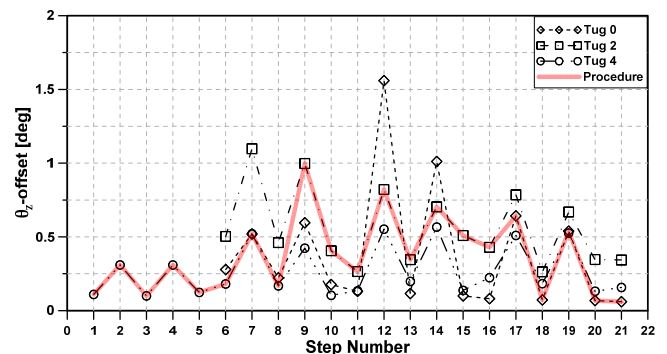


Fig. 34 Result of the θ_z -offset during hook-up installation

are connected, the structure exhibited large behavior due to the low-frequency motion. Therefore, the significant x -offset of the structure in Step 16, which is considered relatively stable, was adopted and used as a reference. In addition, after the four mooring lines were connected (Step 6), the structure did not exceed the reference value with only two tugs, but considering the steady drifting force and unstable motion of the structure in the y and θ_z direction, two tugboats were configured to withdraw after Step 8.

5. Conclusion

In this study, a dynamic analysis program of a mooring system during the hook-up installation was developed, and the simulation results were analyzed for the generally performed procedure. The reliability was verified by comparing the analysis results of the developed program with the simulation results of the commercial program MOSES, and the behavior of the structure during the hook-up installation was analyzed according to the number of tugboats under the complex environmental conditions. The installation procedure was configured so that the significant value of the structure offset did not exceed 6m by comparing the simulation results according to the arrangement of the tugboat.

The conclusions of this study are as follows:

(1) The reliability was verified by comparing the developed program with the simulation result of MOSES. The appropriateness of the hook-up algorithm used in this study was confirmed during the hook-up installation procedure.

(2) During the hook-up installation, the motion response of the structure at the stage where eight mooring lines were connected with designed pre-tension was the greatest due to the second-order wave force, but it could be controlled by arranging only two tugboats.

(3) There are various methods and steps in the hook-up procedure considering the offshore structure, tugboat, mooring type, and installation site. Hence, it will be necessary to review and analyze the installation procedures other than the simulation performed in this study.

(4) Overall, the timing of the withdrawal of the tugboat with secure work stability can be determined, and the thrust of the tugboat required for hook-up installation can be predicted.

Acknowledgments

Following are the results of a study on the ‘Leaders in Industry-university Cooperation +’ Project, supported by the Ministry of Education and National Research Foundation of Korea

References

Cummins, W.E. (1962). The Impulse Response Function and Ship Motions (No. DTMB-1661). David Taylor Model Basin Washington DC.

- Bentley Systems. (2016). MOSES Reference Manual.
- Berteaux, H.O. (1976). Buoy Engineering. New York, USA: A Wiley-Interscience.
- DNV. (2011). Marine Operations (DNV-OS-H101)
- DNVGL. (2018). Position Mooring (DNVGL-OS-E301).
- Hwang, Y.L. (1998). Numerical Model Test for Mooring Damping. Proceedings of the 17th International Conference on Offshore Mechanics and Arctic Engineering, OMAE98.
- Jo, H.J. (1991). A Study on the Effect of Multi-directional Waves Affecting on the Response Characteristics of Floating Structures with Mooring (Ph.D. Thesis). University of Tokyo, Japan.
- Kim, Y.S., Kim, J.H., Kang, K.J., Han, S., Kim, J. (2018). Ice Load Generation in Time Domain Based on Ice Load Spectrum for Arctic Offshore Structures. Journal of Ocean Engineering and Technology, 32(6), 411-418. <https://doi.org/10.26748/KSOE.2018.32.6.411>
- Lee, J.H. (2011). Dynamic Analysis of Spar Hull Transportation. Journal of the Korean Society of Marine Engineering, 35(6), 867-873. <https://doi.org/10.5916/jkosme.2011.35.6.867>
- Mermaid Consultant’s Naval Architects & Marine Consultants. (n.d.). Transportation & Installation. Retrieved May 2019 from <https://www.mermaid-consultants.com/>
- Park, S.M., Lee, S.J., & Kang, S.W. (2017). A Study on Creep Effect of Synthetic Fiber Rope Mooring System on Motion Response of Vessel and Tension of Mooring Line. Journal of Ocean Engineering and Technology, 54(2), 151-160. <https://doi.org/10.3744/SNAK.2017.54.2.151>
- Patel, M.H., & Lynch, E.J. (1982). Coupled Dynamics of Tensioned Buoyant Platforms and Mooring Tethers. London Centre for Marine Technology, 5(4), 299-308. [https://doi.org/10.1016/0141-0296\(83\)90009-3](https://doi.org/10.1016/0141-0296(83)90009-3)
- Song, C.W., & Kim, B.J. (2018). Deep Sea Installation Analysis of Suction Pile with Passive Heave Compensator. Proceedings of Fall Conference of the Korean Society of Ocean Engineers, 53-56.
- Van den Boom, H. (1985). Dynamic Behaviour of Mooring Lines. Proceedings of the BOSS Conference, Delft, Netherlands.
- Yoon, S.J., & Kim, B.J. (2018). A Numerical Study for the Tension Characteristics of Fiber Rope Mooring System During Pre-laying Installation. Proceedings of Fall Conference of the Korean Society of Ocean Engineers, 57-61.

Author ORCIDs

Author name	ORCID
Lee, Min-Jun	0000-0003-3175-7746
Jo, Hyo-Jae	0000-0002-7847-0462
Lee, Sung-Wook	0000-0001-6089-303X
Hwang, Jea-Hyuk	0000-0002-1888-3214
Kim, Jea-Heui	0000-0003-0806-2524
Kim, Young-Kyu	0000-0002-0708-9322
Baek, Dong-Il	0000-0002-8680-7467

Speed-Power Performance Analysis of an Existing 8,600 TEU Container Ship using SPA(Ship Performance Analysis) Program and Discussion on Wind-Resistance Coefficients

Myung-Soo Shin¹, Min Suk Ki², Beom Jin Park², Gyeong Joong Lee¹,
Yeong Yeon Lee¹, Yeongseon Kim³ and Sang Bong Lee⁴

¹Principal Researcher, Korea Research Institute of Ships & Ocean Engineering, Daejeon, Korea

²Senior Researcher, Korea Research Institute of Ships & Ocean Engineering, Daejeon, Korea

³Head of R&D Team, HMM Co., LTD, Pusan, Korea

⁴CEO of LAB021, Pusan, Korea

KEY WORDS: Speed-power analysis, Resistance increase at real sea, Wind resistance, Wave resistance, Water temperature deviation, 8,600 TEU Container

ABSTRACT: This study discusses data collection, calculation of wind and wave-induced resistance, and speed-power analysis of an 8,600 TEU container ship. Data acquisition system of the ship operator was improved to obtain the data necessary for the analysis, which was accomplished using SPA (Ship Performance Analysis, Park et al., 2019) in conformation with ISO15016:2015. From a previous operation profile of the container, the standard operating conditions of mean draft were 12.5 m and 13.6 m, which were defined with the mean stowage configuration of each condition. Model tests, including the load-variation test, were conducted to validate new ship performance and for the speed-power analysis. The major part of the added resistance of container ship is due to the wind. To check the reliability of wind-resistance calculation results, the resistance coefficients, added resistance, and speed-power analysis results using the Fujiwara regression formula (ISO15016:2015) and Computational fluid dynamics (Ryu et al., 2016; Jeon et al., 2017) analysis were compared. Wind speed and direction measured using an anemometer were used for wind-resistance calculation and the wave resistance was calculated using the wave-height and direction-data from weather information. Also, measured water temperature was used to calculate the increase in resistance owing to the deviation in water density. As a result, the SPA analysis using measured data and weather information was proved to be valid and able to identify the ship's resistance propulsion performance. Even with little difference in the air-resistance coefficient value, both methods provide sufficient accuracy for speed-power analysis. The differences were unnoticeable when the speed-power analysis results using each method were compared. Also, speed-power analysis results of the 8,600 TEU container ship in two draft conditions show acceptable trends when compared with the model test results and are also able to show power increase owing to hull fouling and aging. Thus, results of speed-power analysis of the existing 8,600 TEU container ship using the SPA program appropriately exhibit the characteristics of speed-power performance in deal conditions.

Nomenclature

A_{XV}	Transverse projected area above the waterline	R_{AW}	Resistance increase in short crested irregular waves
C_{AA}	Wind resistance coef. ($C_{AA}(0)$ means head wind)	R_F	Frictional resistance for the actual water
$C_F(C_{F0})$	Frictional resistance coef. (C_{F0} ; at reference temp.)	R_{T0}	Total resistance for the reference water temp.
E	Directional spectrum in square meter seconds	R_{WAVE}	Resistance increase in regular waves
P_{Did}	Delivered power in ideal condition	TM	Draught at midships (m)
P_{Dms}	Measured delivered power	UTC	Coordinated Universal Time
R_{AA}	Resistance increase due to relative wind in newtons	V_G	Ship's speed over ground
R_{AS}	Resistance increase due to deviation of water	V_S	Ship's speed through the water
		V_{WRef}	Relative wind velocity at the reference height
		α	Angle between ship's heading and component waves

Received 9 August 2020, revised 16 September 2020, accepted 18 September 2020

Corresponding author Beom Jin Park: +82-42-866-3416, bjpark@kriso.re.kr

© 2020, The Korean Society of Ocean Engineers

This is an open access article distributed under the terms of the creative commons attribution non-commercial license (<http://creativecommons.org/licenses/by-nc/4.0>) which permits unrestricted non-commercial use, distribution, and reproduction in any medium, provided the original work is properly cited.

ΔR	Total resistance increase
ζ_A	Wave amplitude
ξ_{P_s}	Load variation coefficient
ρ_A	Mass density of air (kg/m ³)
$\rho_S (\rho_{S0})$	Sea water density (ρ_{S0} ; at reference temperature)
ψ_{WRef}	Relative wind direction at reference height
ω	Circular frequency of regular waves

1. Introduction

To prevent global warming, the reduction of greenhouse gases (GHG) that originated from ship operation is a crucial issue, and relevant regulations are under discussion in International Maritime Organization (IMO) continuously. Among these, Energy Efficiency Design Index (EEDI) that is applicable to new ships has already been implemented, and the Energy Efficiency Existing Ship Index (EEXI) for the existing ships is currently under discussion (IMO, 2014; IMO, 2019).

For the improvement of EEDI of new ships, many technologies have been developed with shipyards at its core, and in particular, considerable progress had been made with the development of design technology. However, for the existing ships built prior to the EEDI regulation, as the regulations will come into effect in near future, retrofitting for energy saving devices and an eco-friendly operation for the increase of operational efficiency are the technologies that need to be secured by ship companies with their efforts.

In order to secure ship operators' competitiveness through reducing GHG emitted during ship operation and saving fuel, it is necessary to identify the accurate estimations of the ship operational performance in real sea. Newly constructed ships exhibit the best resistance propulsion performances with their clean bodies and propellers. The reference speed in a calm sea environment is obtained from speed trials in such conditions and attained EEDI is calculated.

For the assessment of speed and power, ISO15016:2015 standard was developed, which is used to estimate the reference speed in a calm sea environment. The authors developed i-STAP (ISO15016:2015 Speed Trial Analysis Program), and are currently using it for estimating the reference speed of various types of ships, including container ships, with widely acknowledged high accuracy. (Shin et al., 2016; Lee et al., 2016; Yu et al., 2016; Kim and Kim, 2016). After delivery of a new ship, hull and propeller performance are expected to degrade with aging. When the ship undergoes periodic dry docking, sanding, cleaning and painting of the ship hull and its propeller are performed, these result restoring the resistance propulsion performance. Therefore, the resistance propulsion performance of a ship is periodically increased and degraded within the ship's life cycle. However, there has been no precise qualitative or quantitative evaluation method for this.

In addition, it is extremely difficult to estimate the resistance propulsion performance of the existing ships that have been already

degraded in performance under operation. There is a case wherein shipyard experts boarded an operating ship to conduct a performance trial to verify speed-power performance of the existing ship in real sea. In this case, speed through water was used instead of the Global positioning system (GPS) speed to obtain acceptable results, since performing double run during ship operation was difficult. (Lee et al., 2016). This shows why an automated implementation of a speed-power performance analysis system is required.

Lim et al. (2019) introduced the results of performance monitoring in real sea for the hull and propeller performance verification of the operating ship. They measured shaft power against the ship's speed using data gathered over one month. The results showed no noticeable trends due to a large variance. Furthermore, Freitas et al. (2019) performed a full-scale measurement to verify the effect of an air-lubrication system and illustrated the measured shaft power against the ship's speed. Only filtering was applied and it also failed to verify the effects of the air-lubrication system due to a large variance. Therefore, it is necessary to convert resistance propulsion performance to a calm sea environment by analysing the added resistance to draw any meaningful comparison results.

Murrant et al. (2019) performed a speed trial before and after hull and propeller cleaning in order to identify the operation performance of an offshore patrol vessel. This speed trial was performed using the same procedure as that used for the new ships. However, it was stated that it was difficult to verify the effect of the hull and propeller cleaning owing to the 8% difference in displacement across all three speed trials.

To interpret the speed-power performance of the existing ship, target displacement and speed range should be defined. In addition, as it is difficult to perform a double run during operation, an automatic data collection and transmission system for measured data including an accurate speed log. Data that are difficult to measure such as wave data, should be extracted from weather information. And the speed-power performance should be identified and compared with delivered horse power (DHP) in calm sea environment derived by analysing added resistance in real sea environment.

This study aimed to perform a highly accurate analysis of speed-power performance of a currently operating 8,600 TEU container ship using the SPA (Ship Performance Analysis) program (Park et al., 2019; Lee et al., 2019), which is developed in conformance with the speed trial analysis method for new ships. To begin with, container stowage shapes of frequently operated conditions were determined by reviewing the operation data. Data required for the analysis were secured by improving the ship operator's own data collection system. A model test including the load-variation test presented in ISO15016:2015 standard was performed to identify the performance at the design stage. Air-resistance coefficients were derived from previously determined container stowage shapes. And the added resistance due to wind in operation is calculated using wind speed and direction measured by anemometer onboard. Added resistance due to waves is calculated using the weather-information data. It was

confirmed that the speed-power characteristics at calm sea environment estimated from the analysis show similar trends as model test results. Furthermore, discussions on the analysis results with air-resistance coefficients derived using the Fujiwara regression formula (ISO15016:2015) and CFD (Computational fluid dynamics) simulation (Ryu et al., 2016; Jeon et al., 2017) are included as well.

It is expected that the results of this study will be utilized for the analysis of cleaning effects of the ship hull and propellers, painting, GHG reduction from retrofitted ESD (Energy Saving Device) and environment friendly shipping.

2. Ship Data and Standard Operating Conditions

2.1 Data of Target Ship

The target ship is an 8,600 TEU container ship, and principal dimensions and images of the ship are shown in Table 1 and Fig.1, respectively. As shown in Fig. 2, the main route travels through Korea,

Table 1 Principal dimensions of the 8,600 TEU container ship

Length	339.60 m		
Breadth	45.60 m	Maximum continuous rating	108,920 kW × 102 r/min
Depth	24.60 m	Normal continuous rating	98,030 kW × 98.5 r/min
Designed draft	13.00 m	Service speed	27.5 knot (14.1 m/s)
Scantling draft	14.50 m		



Fig. 1 Photograph of the 8,600 TEU container ship

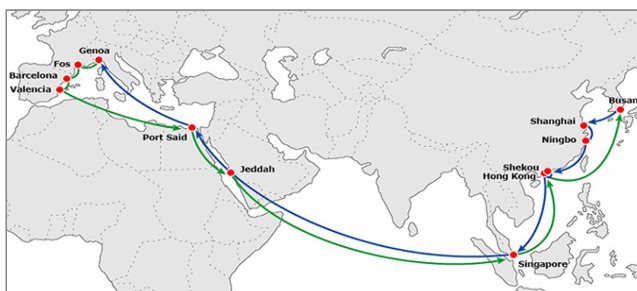


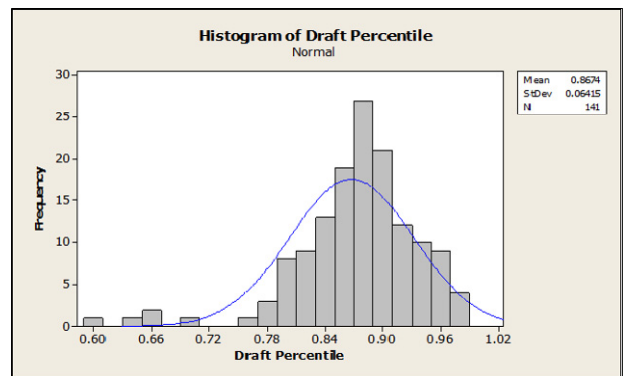
Fig. 2 Main route of the 8,600 TEU container ship

China, Singapore, the Middle East, and Europe. The target ship was built prior to the enforcement of EEDI regulation, and the ship operator required high speed at the time. Therefore, this ship is equipped with an engine that provides a large output that exceeds the 100,000 kW and has an extremely high design speed of 27.5 knot (14.1 m/s).

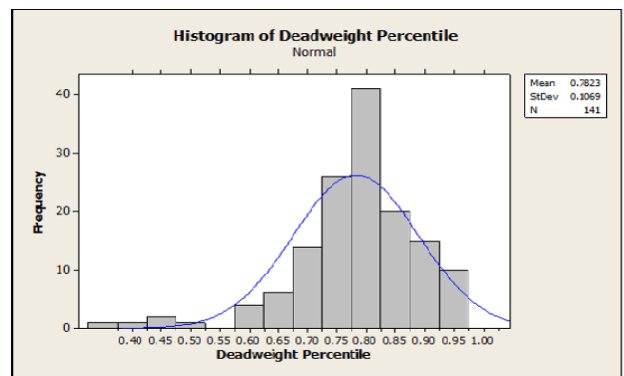
2.2 Standard Operating Condition

After the EEDI regulation came into effect, the ship operator put an effort into the energy-efficiency improvement and GHG reduction in their own ships. The method which is most easily and widely used is slow steaming. This is attributed to the benefits of fuel saving and GHG reduction being more than the loss from prolonged transporting time. Although the target ship had a design speed of 27.5 knot (14.1 m/s), it is operating now within the actual range of 15–18 knot (7.7–9.3 m/s).

The ship operating profiles show that more than 70% of operation was within 80–95% of full load displacement and more than 80% of operation was within 70–95% of full load displacement as shown in Fig. 3. Moreover, as a result of analyzing operation data gathered over a year, the condition that shows the highest frequency among the head hauls that depart from Korea is TM 12.5 m, which implies a displacement of 109,961 t; and the same among back hauls is TM 13.6 m, which corresponds to a displacement of 122,954 t. Furthermore, the most frequent speeds in these conditions are 18.5 knots (9.5 m/s) and 15.4 knots (7.9 m/s), respectively. A ship that corresponds to these conditions was determined as the standard operating condition and are summarized in Table 2.



(a) Draft percentile



(b) Deadweight percentile

Fig. 3 Histogram of the draft and deadweight percentile

Table 2 Standard operating conditions for the speed-power analysis

	<i>TM</i> 12.5 (Head haul)	<i>TM</i> 13.6 (Back haul)
Length between Perpendiculars, Breadth (m)	322.6, 45.6	
Displacement (t)	109,961.5	122,954.4
Volume (m ³)	107118.5	119784.0
Wetted surface area (m ²)	16125.4	17178.3
Draught aft, Draught forward (m)	12.5, 12.5	13.7, 13.5
<i>TM</i> (m)	12.5	13.6
Reference speed (knots)	18.5 (9.5 m/s)	15.3 (7.9 m/s)
Speed range (knots)	12.5–22 (6.4–13 m/s)	
Transverse projected area (m ²)	1754.6	1704.5
Anemometer height from base line (m)	46.5	45.4
Measurement range of draught	<i>TM</i> : 11–13 m	<i>TM</i> : 13–15 m

According to ISO15016:2015, the recommended displacement correction is within 2%, and this correction amount is equivalent to *TM* 0.2 m. However, to practically obtain and analyse the speed-power performance data, the displacement was corrected within the range of ±0.5 m with the same formula as proposed in ISO15016:2015. A tank test was performed on displacement and speed conditions that correspond to this standard operating condition, and the actual ship’s measured data were obtained and analysed.

3. The Actual Ship’s Performance Estimation and Data Measurement

This chapter discusses the result of the tank test and data measurements for the actual ship’s performance estimation. Target speeds under standard operating conditions are 18.5 knots (9.5 m/s) and 15.3 knots (7.9 m/s). The actual ship’s performance at a given displacement and speed under standard operating conditions was estimated using the result of the tank test performed when the ship was built. However, as there were no results for speed less than 20 knots (10.3 m/s), the tank test was re-performed.

3.1 Tank Test

As mentioned previously, to analyse the target ship’s speed-power performance under standard operating conditions, tank tests were performed. The test was performed in a towing tank (200-m length, 16-m width, and 7-m depth) at the Korea Research Institute of Ships & Ocean Engineering (KRISO), Korea Institute of Ocean Science & Technology (KIOST), and the model’s scale ratio was 1/36. Fig. 4 shows the models for tank test and photographs of self-propulsion test. This ship is a high-speed ship with the design speed of 27.5 knots (14.1 m/s) when it was built, and it is equipped with hexapropeller for this purpose.



(a) Photographs of model the ship and propeller



(b) Photographs of the self-propulsion test

Fig. 4 Photographs of models and propulsion test of the 8,600 TEU container ship (*TM* 12.5 m)

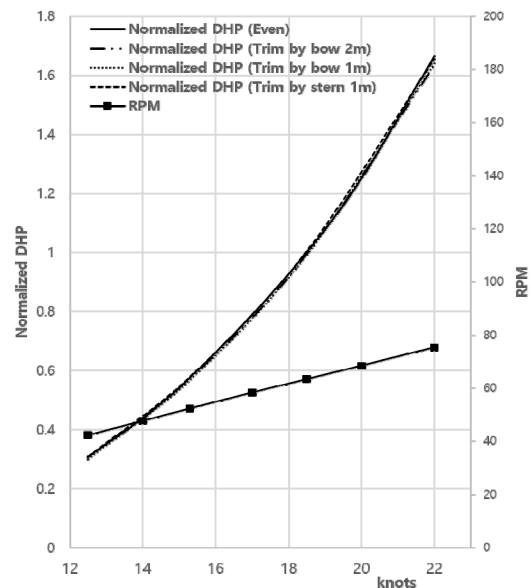


Fig. 5 Self-propulsion model test results of the 8,600 TEU container ship (*TM* 12.5 m)

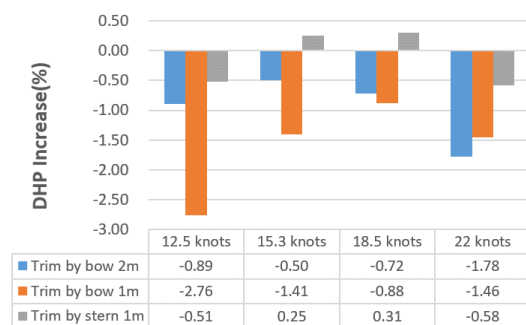


Fig. 6 Trim variation test results of the 8,600 TEU container ship (*TM* 12.5 m)

Table 3 Load variation parameter as per ISO15016:2015 (*TM* 12.5 m)

V_S (knots)	ξ_P
15.3 (7.9 m/s)	-0.1146
17 (8.7 m/s)	-0.1149
18.5 (9.5 m/s)	-0.1126
22 (11.3 m/s)	-0.1099

The tank model test was performed under the standard conditions listed in Table 2. The speed range was within the actual operating speed range of 12.5–22 knots (6.4–11.3 m/s). The predicted DHPs of the ship were all normalized to DHP values of 18.5 knots (9.5 m/s) and 15.3 knots (7.9 m/s), which are the reference speeds described in the standard conditions in Table 2. Results of resistance test of *TM* 12.5 m and trim resistance test were shown in Fig. 5 and Fig. 6, respectively. According to Fig. 6, the trim by bow shows a relatively lower DHP. DHP is reduced by 2.76% at trim by bow (1 m), and this corresponds to 0.8% of DHP at 18.5 knots (9.5 m/s). The predicted results of DHP and RPM (revolution per minute) across the entire speed range are shown in Fig. 5.

According to ISO15016:2015, to predict DHP at a certain speed through water in clam sea environment, DHP from additional resistance are deducted from the measured DHP (P_{Dms}). If the added resistance is applied, the speed of the ship is reduced and to consider propulsion efficiency at this speed, load-variation test is to be performed in model basin. This requires derivation of the load-variation parameter, ξ_P performing self propulsion test while changing propeller RPM at fixed towing speed. The measured load-variation test parameter is presented in Table 3. This value is used in Eq. (5) to solve P_{Did} in a calm water environment. Although ISO15016:2015 also requires the correction of RPM by considering shallow water and load-variation effects, these are not considered as they are not in the scope of this study.

3.2 The Actual Ship's Data Measurement and Collection

The target ship is operated with an EEMS (energy efficiency monitoring system) installed, which is shown in Fig. 7. This system is for real-time collection and land transmission of various types of operation data. Its major features include identifying normal state of operation, fuel-efficiency analysis, early warnings of abnormal state of operation, and sharing best practices between ships through a correlation analysis among operating data. Forty items of data, including course, heading, and ballast water, and eighty items of data, including measured DHP, fuel consumption, water temperature, and wind speed, are collected. To improve the accuracy of wind speed data, an ultrasonic anemometer was newly installed. The anemometer was installed by selecting a location that is less affected by the air flow from the ship, the photographs of which are shown in Fig. 8.

The measurements had been performed for four years since 2015. To obtain the measured data with high accuracy, the monitoring system of the ship operator was improved as well as increasing the

**Fig. 7** Photographs of energy efficiency monitoring system (EEMS)**Fig. 8** Photographs of anemometer

accuracy of some measurement equipment such as anemometer and mass flow meter. In addition, wind speed, wave, and water temperature data at the location and time of the ship were extracted from the National Oceanic and Atmospheric Administration data and weather-information data.

4. Speed-power Analysis

4.1 Speed-power Analysis Procedure

The SPA program was developed for analyzing the powering performance and speed-power performance of the existing ship (Park et al., 2019).

The program analysis procedure is illustrated in Fig. 9. The overall procedure are in conformance with ISO15016:2015, the standard for speed trial data analysis. Although current effect are corrected with more than 3 double runs using GPS speed, since it is not applicable for operating ships, speed through water from speed log is used for the analysis. Furthermore, although ISO15016:2015 requires considering shallow water effect, data only at sufficient depths, outside the shallow water range, was used for the analysis.

The data acquisition interval of the target ship was 2 min, and the standard filtering criteria that determines a normal variation state is shown in Table 4. If measured data variation for 2 min was less than the criteria shown in Table 4, it was determined as a steady state and then analyzed, and all others were filtered out after determining it as unsteady. This steady state criterion is determined by the ship's size, speed, and marine conditions, and there are no fixed rules. The condition in Table 4 is the criteria valid only for the target ship's draft, operating speed, and measurement interval. After filtering,

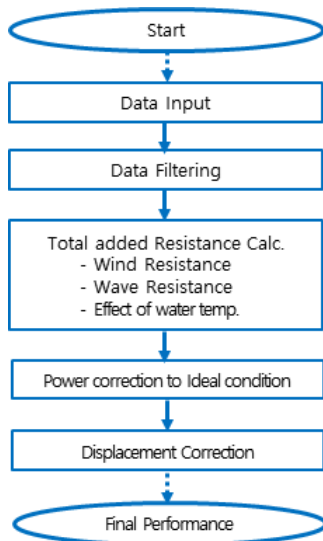


Fig. 9 SPA (Speed power analysis) procedure for existing ship based on ISO15016:2015 (Park et al., 2019; Lee et al., 2019)

Table 4 Steady state criteria for speed-power analysis (8,600 TEU container ship, 2-min interval between the measured data)

Sea depth	Deeper than shallow water criteria by ISO15016:2015
Rudder angle change	Less Than 5°
DHP change	Less Than 100 kW
Speed change	Less Than 0.1 knots (0.051 m/s)
Wave direction	Less Than 45°
Difference between GPS and gyro head	Less Than 5°

approximately 15% of the data remains, from which speed-power curve, the purpose of this study, can be derived well.

The measured data list and the analysis procedure for the speed-power analysis are equivalent to those of Park et al. (2019) and Lee et al. (2019). For the engine power, the measured power (P_{Dms}) was obtained using a torque sensor installed on the propeller shaft and rotation speed. Moreover, added resistance due to wind, wave and water temperature difference calculated with data measured or obtained from weather information was used to calculate required power. Lastly, the difference in displacement was corrected to obtain the DHP (P_{Did}) in a calm sea environment in ideal conditions.

As shown in Eq. (1), the added resistance of the operating ship in real sea is the sum of the added resistance due to wind, wave, and the changes in water temperature and density.

$$\Delta R = R_{AA} + R_{AW} + R_{AS} \quad (1)$$

The added resistance due to wind is calculated using equation (2). In older version of the standard, ISO15016:2002, air resistance from ship moving forward in the absence of wind was considered as the added resistance, however it is not regarded as the added resistance in

ISO15016:2015. There are various methods to obtain the air-resistance factor (C_{AA}); however, the Fujiwara regression formula of the reference ISO (2015), which is known to have the highest accuracy, was mainly used. The comparison with the air-resistance coefficients obtained using CFD simulation (Ryu et al., 2016; Jeon et al., 2017) will be discussed in chapter 4.2, Analysis Result, of this study.

$$R_{AA} = \frac{1}{2} \rho_A \cdot C_{AA}(\psi_{WRef}) \cdot A_{XV} \cdot V_{WRef}^2 - \frac{1}{2} \rho_A \cdot C_{AA}(0) \cdot A_{XV} \cdot V_G^2 \quad (2)$$

The added resistance due to waves is calculated using Eq. (3). After calculating the added resistances from regular waves, these are combined using the JONSWAP (Joint North Sea Wave Atmosphere Program) frequency spectrum to obtain the added resistance in irregular waves. STWAVE-II method was used in this study. (ISO15016:2015).

$$R_{AW} = 2 \int_0^{2\pi} \int_0^\infty \frac{R_{WAVE}(\omega, \alpha)}{\zeta^4} E(\omega, \alpha) d\omega d\alpha \quad (3)$$

$$R_{AS} = R_{T0} \left(\frac{\rho_S}{\rho_{S0}} - 1 \right) - R_F \left(\frac{C_{F0}}{C_F} - 1 \right) \quad (4)$$

Added resistance due to changes in water temperature (R_{AS}) is calculated with Eq. (4) with the measured water temperature data, and the total added resistance (ΔR) of Eq. (1) is calculated. After using Eq. (5) is used obtain DHP (P_{Did}) of the ideal condition, Admiral-formula (ISO15016:2015) is used to obtain DHP at displacements in the standard operating condition.

$$P_{Did} = \frac{1}{2} \left\{ P_{Dms} - \frac{\Delta R \cdot V_S}{\eta_{Did}} + \sqrt{\left(P_{Dms} - \frac{\Delta R \cdot V_S}{\eta_{Did}} \right)^2 + 4 D_{ms} \frac{\Delta R \cdot V_S}{\eta_{Did}} \cdot \xi_P} \right\} \quad (5)$$

4.2 Speed-power Analysis

4.2.1 Comparison of the air resistance based on air resistance factor

For speed-power analysis of the existing ship, it is important to perform an accurate estimation of the added resistance in the actual sea environment. To perform an accurate estimation of the air resistance of the container ship, it is crucial to determine the container stowage shape in the previously mentioned TM 12.5 m (Head haul) and TM 13.6 m (Back haul). Mean stowage diagram, which is determined by analyzing the records of the ship operator, is shown in Fig. 10. It was assumed that the height of container stowage in the lateral direction is consistent, and air resistance was calculated using this diagram. Although the container stowage shape of TM 12.5m is somewhat unnatural in the aspect of air resistance, nevertheless it is used for the analysis as it is the actual operation data.

The comparison of the air-resistance coefficients of the Fujiwara

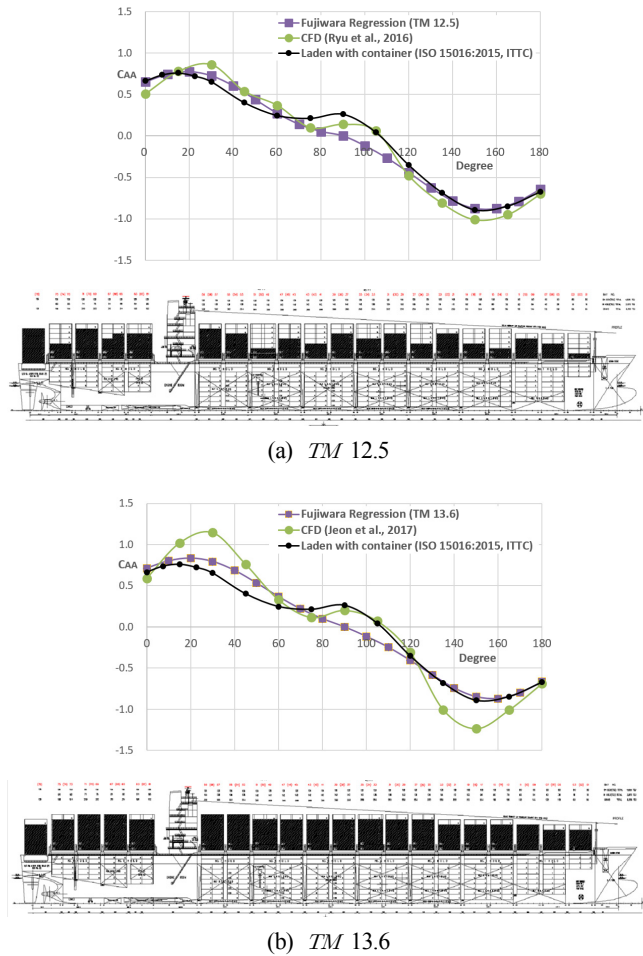


Fig. 10 Mean stowage diagram of the container ship and comparison of air drag coefficients between the Fujiwara regression formula by ISO 15016:2015 and CFD simulation (Ryu et al., 2016; Jeon et al., 2017) results

regression formula, ITTC (International towing tank conference) from ISO15016:2015 and calculated using CFD (Ryu et al., 2016; Jeon et al., 2017) is shown in a diagram in Fig. 10. Here, the x-axis is the angle from the bow, and the y-axis is the air-resistance coefficient (C_{AA}) from this angle. Overall, the air-resistance factors (C_{AA}) of Fujiwara and ITTC (ISO15016:2015) are similar. Compared with the result of CFD (Ryu et al., 2016; Jeon et al., 2017), the result of *TM* 12.5 m is observed to be similar but that of *TM* 13.6 m shows difference near 30° and 150° from the bow. This could be attributed to the effects of container stowage shape and the shape of wheel house.

The 8,600 TEU Container ship, which is the target ship herein, had been operating on the Dubai route from Port Kelang of Malaysia for nine days since September 20, 2016. The *TM* during the operation was 12.1 m, which corresponds to standard operating conditions of *TM* 12.5 m listed in Table 2. The wind speed and wind direction measured during the operation are shown in Fig. 11. The absolute wind velocity, which is the actual speed of wind, was less than 10 m/s; however, it can be seen that the measured relative wind velocity was high as it combined the ship’s speed. GPS heading of the ship was in the

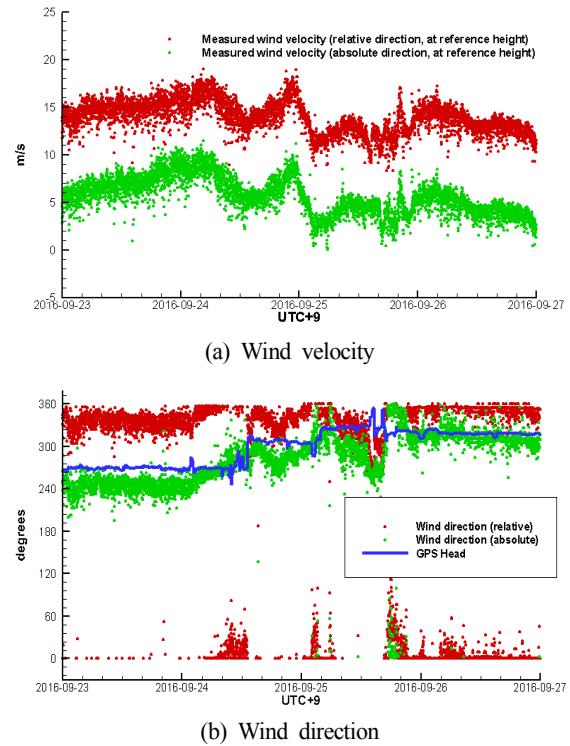


Fig. 11 Time history of the wind velocity and direction at the reference height

north-west direction at angle between 250°–320°, and the wind direction was also similar to that of the GPS head. Therefore, it can be seen that the relative wind direction is mostly head wind within an incidence angle of 30°.

The added resistance due to the measured wind is shown in a diagram in Fig. 12. The thin solid lines represent the resistance due to relative winds, and dots represent the air resistance due to the ship moving forward. As shown in Eq. (2), the resistance due to the ship moving forward is to be deducted when calculating the added resistance, this is indicated as negative values. The additional resistance due to wind is shown in thick solid lines and are within the range of approximately 100–200 kN. In predicting the added resistance

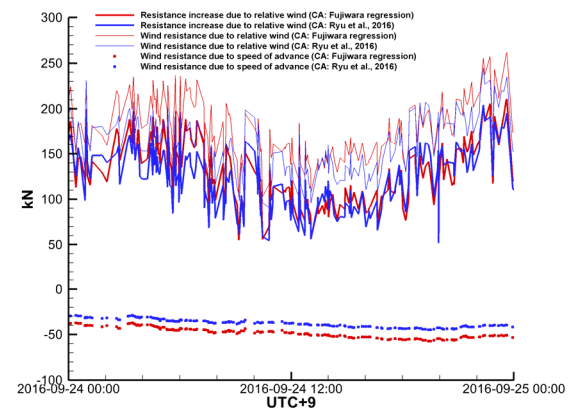


Fig. 12 Comparison of wind resistances owing to air drag coefficients using the Fujiwara regression formula (ISO15016:2015) and CFD (Ryu et al., 2016) result

due to wind, it can be seen that the added resistances calculated with coefficients obtained by the Fujiwara regression in ISO (2015) and CFD in Ryu et al. (2016) show similar trends and no significant difference in values.

4.2.2 Total added resistance calculation

The wave and added resistances measured in the same period are shown in a diagram in Fig. 13. The weather data was used as the wave-height and wave-direction data. The added resistance due to sea waves and swell are calculated separately. STAWAVE-II was used for the analysis, and this method only considers the waves within 45° from the bow. The swell in this period is less than 1 m of the wave height, and as the direction is greater than 45° from the bow, the added resistance is 0. As shown in Fig. 13, the sea-wave height is within the range of 1.5–2 m. The added resistance due to waves are the sum of added resistance from motion and from reflection waves, and most of the added resistance in Fig. 13 is from reflection waves.

The measured water temperature is shown in Fig. 14. It is in the range of 25°–28°, which is higher than the standard temperature of 15°C, and the correction amount is approximately -40 kN.

Total added resistance and the added resistance due to wind, waves and changes in water temperature are shown in Fig. 15. Wind speed and wind direction were measured by the anemometer, and the Fujiwara regression formula (ISO15016:2015) was used for air resistance coefficients. In addition, waves were analyzed using STAWAVE-II of the reference ISO (2015) with the weather forecast data, and water temperatures are measured values.

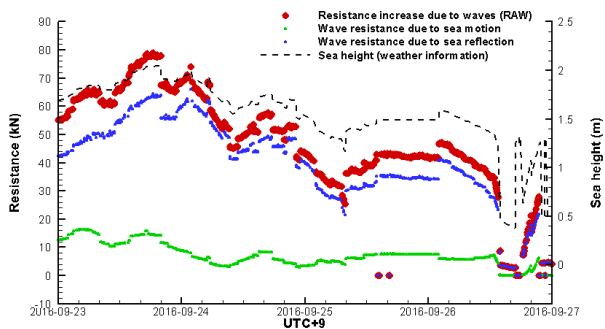


Fig. 13 Resistance increase owing to sea waves by ISO15016:2015 (STAWAVE-II)

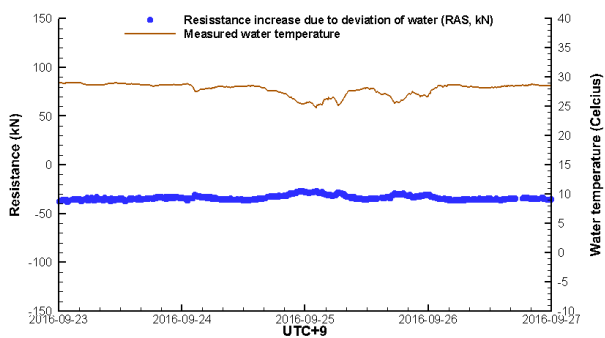


Fig. 14 Resistance increase owing to deviation of water and measured water temperature

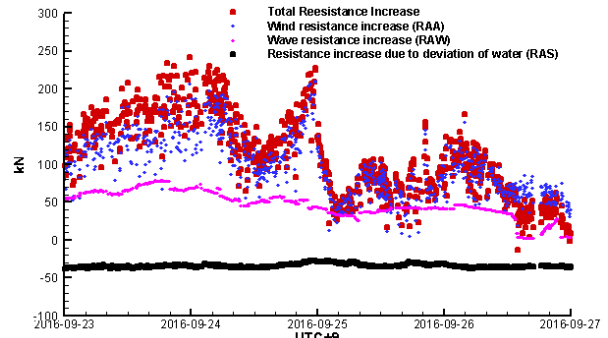


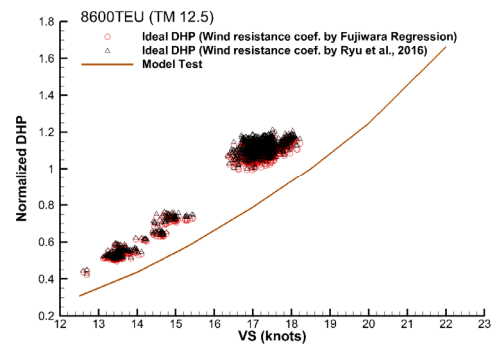
Fig. 15 Total resistance increase

It can be seen that the most of added resistance is due to wind. This could be attributed to it being relatively fast compared with other types of ships and because the area above the waterline is relatively wide due to container loading.

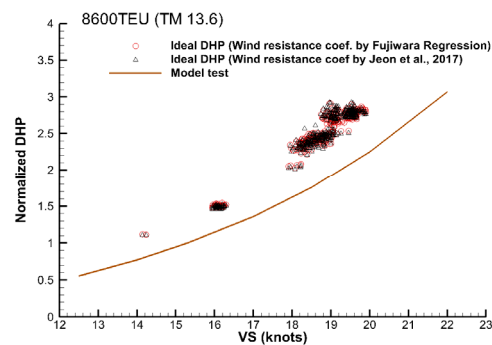
4.2.3 Speed-power analysis using SPA

Speed-power(Ideal DHP) analysis result considering the total added resistance calculated by Eq. (5) is shown in Fig. 16. The analysis procedure of waves and water temperature is the same, and wind resistance coefficients from Fujiwara regression (ISO15016:2015) and CFD simulation (Ryu et al., 2016; Jeon et al., 2017) are both used.

As previously mentioned, the analysis results in Fig. 16(a) are using operating data in the standard operating condition of *TM* 12.5 m of



(a) *TM* 12.5 m



(b) *TM* 13.6 m

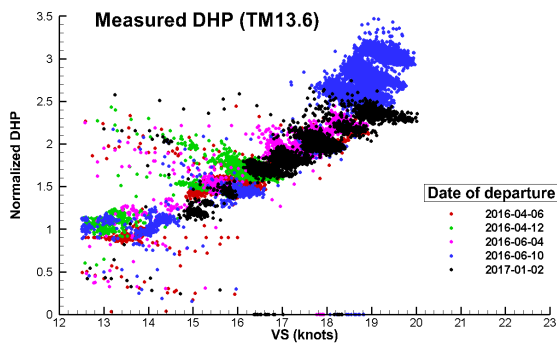
Fig. 16 Comparison of the speed-power analysis results in a calm sea environment between the Fujiwara regression formula (ISO15016:2015) and CFD results (Ryu et al., 2016; Jeon et al., 2017) for wind resistance

Dubai route from Port Kelang of Malaysia for nine days since September 20, 2016 and Fig. 16(b) is that of *TM* 13.6 m of the same route for nine days since June 11. It can be seen that difference in speed-power analysis results from the difference in air resistance coefficients method in Fig. 10 and from the difference in the added resistance due to wind in Fig. 12, is very small. The results are highly accurate enough not to show difference in the wind resistance coefficients.

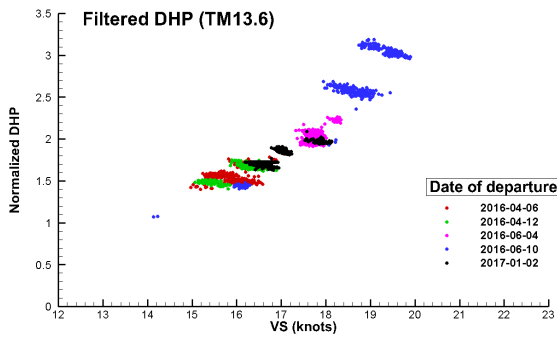
For an overall speed-power analysis of the target ship, operation data from 2016 to early 2017 was obtained and analyzed.

The analysis results, which correspond to the standard operating conditions of *TM* 12.5 m and 13.6 m, are shown in Figs. 17–18. The operation routes include China, Taiwan, Hong Kong, Singapore, Malaysia, and the United Arab Emirates.

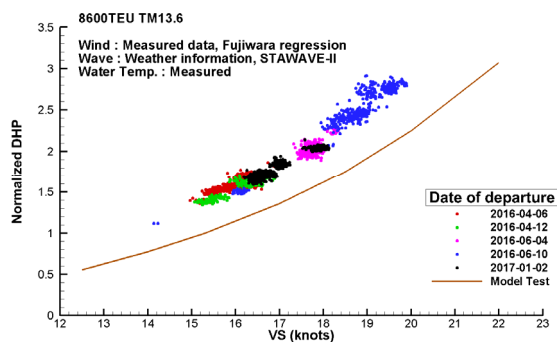
DHP measured at *TM* 12.5 m is indicated in Fig. 17(a). It can be seen that measured DHPs are scattered to the extent that it is difficult



(a) Measured DHP



(b) Filtered DHP



(c) DHP at calm sea by SPA (Speed-power analysis)

Fig. 17 Measured DHP and speed-power analysis results (*TM* 13.6 m)

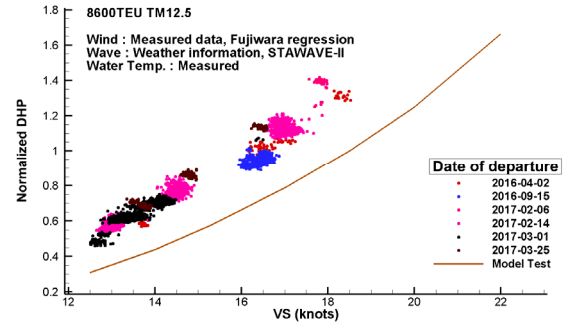


Fig. 18 Speed-power analysis results in a calm sea environment (*TM* 12.5 m)

to identify speed-power characteristics of the existing ship. Fig. 17(b) shows data that are filtered with criteria in Table 4. The operating pattern of using only a few RPM setting is noticeable. In the same RPM setting, when the added resistance increases, speed decreases and DHP increases with torque. A Speed-power analysis results with corrected the DHP is shown in Fig. 17(c) and Fig. 18. It can be seen that there is a difference between the analyzed result and the result of the model test, and this is due to the deterioration of the ship hull. Analysis of wind was performed using the Fujiwara regression formula (ISO15016:2015) with the measured data, the wave was analyzed using STAWAVE-II with weather information data, and with measured water temperature (ISO, 2015).

5. Conclusion

To secure a competitiveness of ship operators for GHG reduction and fuel savings in the ship, accurate analysis of powering performance in the real sea condition and speed-power analysis of the operating ships are important. The effectiveness of measures for improving the efficiency of the currently existing ships pursued by ship operators can be verified only if an accurate resistance propulsion performance is identified.

This study aimed to perform an accurate speed power analysis with SPA program in conformance with the speed trial data analysis method for newly built ships. The results obtained from this study are as follows:

(1) This study attempted to perform speed-power analysis of the currently existing ship by supplementing the operation data monitoring system of ship operators and analyzing the weather forecasting data. Applying the ISO15016:2015 standard, which is used in analyzing the speed trial data of new ships, algorithm and the analysis program SPA were developed. The measured data and analysis result were valid, and the resistance propulsion performance of the currently existing ship were identified.

(2) The added resistance due to wind using air-resistance coefficients based on the Fujiwara regression formula (ISO15016: 2015) and CFD simulation (Ryu et al., 2016; Jeon et al., 2017) were compared. Although there was a small difference in the air-resistance coefficients, both methods provided a sufficient level of accuracy in

speed-power analysis. It can be said that both methods estimated the added resistance due to wind with a high accuracy to the extent that differences were hardly noticeable in the result of speed-power analysis.

(3) The speed-power analysis results in two draft conditions of the target ship, i.e., 8,600 TEU Container ship, show a satisfactory trend line compared with the result of model test. And they present appropriately the increase in power due to the deterioration of the ship hull in a qualitative manner.

Verification of the effects of hull sanding, painting, propeller cleaning, and retrofitting ESD is possible by applying the technology developed in this study. Future work includes increasing accuracy of the measured data, continuous verification, and development of the analysis methods

Acknowledgments

Authors would like to express their gratitude to Dr. Tae-II Lee of Hyundai Heavy Industries Co., Ltd. for immensely helping them in procuring and analyzing the data used in this study.

This research was funded by the Ministry of Trade, Industry & Energy (Korea Government), grant number PNS3650, under the project “Optimal hull cleaning and propeller polishing scheduling for minimal ship operating cost using operating performance analysis.”

References

- Freitas, L.D., Silberschmidt, N., Pappas, T., & Connolly, D. (2019). Full-scale Performance Measurement and Analysis of the Silverstream Air Lubrication System. *Proceeding of the 4th Hull Performance & Insight Conference, Gubbio, Italy*, 201-210. http://data.hullpic.info/HullPIC2019_gubbio.pdf
- ISO. (2015). *Ships and Marine Technology – Guidelines for the Assessment of Speed and Power pPrformance by Analysis of Speed Trial Data (ISO15016:2015)*. International Standardization Organization, Geneva, Switzerland.
- IMO. (2014). *2014 Guideline on the Method of Calculation of the Attained Energy Efficiency Design Index (EEDI) for New Ships*. Resolution Marine Environment Protection Committee, 245(66), International Maritime Organization, London.
- IMO. (2019). *Energy Efficiency Improvement Measure for Existing Ships*. Marine Environment Protection Committee, 2/7/2, International Maritime Organization, London.
- Jeon, G.M., Ryu, J.H., Park, J.C., & Shin, M.S. (2017). CFD Simulation of Aerodynamic Effects due to Arrangement of Superstructures of Container Ship. *Proceedings of the International Symposium on Marine Engineering (ISME), Tokyo, Japan*.
- Kim, J.G., & Kim, D.E. (2016). Comparison of the Speed Trial Results using ISO15016:2015 and Optimization (Tanker, Bulk Carrier). *Bulletin of the Naval Architects of Korea*, 53(1), 35-38.
- Lee, G.J., Shin, M.S., Park, B.J., Ki, M.S. & Jeon, K.H. (2019). Validity Analysis of Speed, Wave Height and Wind Speed for the Operational Performance of Bulk Carrier. *Journal of the Korean Society of Marine Engineering*, 43(3), 183-196. <https://doi.org/10.5916/jkosme.2019.43.3.183>
- Lee, T.I, An, G.S., Ok, Y.B., & Kim, M.U. (2016). Analysis of the Speed Trial and Application of ISO15016:2015 (Container). *Bulletin of the Naval Architects of Korea*, 53(1), 22-27.
- Lim, S., Teo, R., & Sia, T.C. (2019). A Digital Business Model for Vessel Performance Monitoring. *Proceedings of the 4th Hull Performance & Insight Conference, Gubbio, Italy*, 103-113. http://data.hullpic.info/HullPIC2019_gubbio.pdf
- Murrant A., Kennedy, A., Pallare, R., & Montrose, M. (2019). Effect of Hull and Propeller Cleaning on Propulsion Efficiency of an Offshore Patrol Vessel. *Proceedings of the 4th Hull Performance & Insight Conference, Gubbio, Italy*, 272-291. http://data.hullpic.info/HullPIC2019_gubbio.pdf
- Park, B.J., Shin, M.S., Lee, G.J., & Ki, M.S. (2019). A New Method to Analyse the Speed Power Performance of Operating Ships and Its Implementation. *Journal of Advanced Marine Engineering and Technology*, 43(10), 822-829. <https://doi.org/10.5916/jkosme.2019.43.10.822>
- Ryu, J.H., Jeon, G.M., Ock, D.K., Park, J.C., & Shin, M.S. (2016). CFD Simulation of Aerodynamic Drag on Superstructures of Container Ship. *Proceedings of Korean Society for Computational Fluids Engineering*, 186-187. <http://www.dbpia.co.kr/journal/articleDetail?nodeIdNODE07066013>
- Shin, M.S., Park, B.J., Lee, G.J., & Ki, M.S. (2016). Revision of the ISO15016 and Analysis Program (i-STAP) for the Analysis of the EEDI Reference Speed. *Bulletin of the Naval Architects of Korea*, 53(1), 17-21.
- Yu, G.B., Han, Y.S., & Gang, D.Y. (2016). Analysis of the Speed Trial and the Accuracy Validation of ISO15016:2015 (COT, LNGC). *Bulletin of the Naval Architects of Korea*, 53(1), 28-34.

Author ORCIDs

Author name	ORCID
Shin, Myung-Soo	0000-0002-6017-5369
Ki, Min Suk	0000-0001-6253-0531
Park, Beom Jin	0000-0001-9729-4313
Lee, Gyeong Joong	0000-0001-7555-9034
Lee, Yeong Yeon	0000-0002-0408-6222
Kim, Yeongseon	0000-0002-0089-138X
Lee, Sang Bong	0000-0002-3300-2411

Effect of the Turret's Rotational Damping on the Heading Stability of a Turret-Moored FPSO

Soo Young Min¹, Sung Boo Park¹, Seong Yun Shin¹, Da Gyun Shin¹, Kwang Hyo Jung², Jaeyong Lee³, Seung Jae Lee⁴, Solyoung Han⁵ and Yun Suk Chung⁶

¹Graduate student, Department of Naval Architecture and Ocean Engineering, Pusan National University, Busan, Korea

²Professor, Department of Naval Architecture and Ocean Engineering, Pusan National University, Busan, Korea

³Professor, Department of Naval Architecture and Ocean Engineering, Dong-Eui University, Busan, Korea

⁴Professor, Division of Naval Architecture and Ocean Systems Engineering, Korea Maritime and Ocean University, Busan, Korea

⁵Senior engineer researcher, Samsung Heavy Industries Co., LTD (SHI), Daejeon, Korea

⁶Head of advanced Technology Team/R&D, Bureau Veritas Korea, Busan, Korea

KEY WORDS: Turret-moored FPSO, Heading stability, Turret rotational damping, Yaw motion, Hydrodynamic characteristics

ABSTRACT: The main features of offshore turret platforms are station-keeping and weathervaning functions. Due to the complexity of the yaw motion, abundant research is being done to verify the factors that affect the heading stability. Simulations are used for studies that are not possible with experiments, but the conditions must be verified using experimental results. This study presents methods to estimate turret-related parameters such as the rotational stiffness and rotational damping. A time series analysis was performed, and the results showed that the calculation using the obtained parameters agreed well with experimental results.

1. Introduction

Certain types of facilities operating offshore need to maintain their position, for which diverse mooring systems are employed, such as single point mooring (SPM), spread mooring, and turret mooring systems (TMSs). TMSs are widely used in relatively harsh environments. The use of a turret allows a vessel to rotate towards a predominant external load to reduce its effective load. However, floaters equipped with a turret might experience a fish-tailing phenomenon in specific conditions, and in severe cases, the motion will worsen.

Since turrets are widely utilized, abundant research has been accomplished, which has mainly been about the yaw behavior or factors related to heading stability. Various causes have been suggested as factors in yaw motion of turret-moored floaters, but the underlying causes still need to be verified. Munipalli et al. (2007) examined the response of the heading under conditions with multiple regular waves and fixed steepness from head sea. They found that large yaw motion occurred for a shorter wave period. Cho et al. (2013)

experimented with the yaw motion of a turret-moored floating body in regular waves with fixed wave steepness.

Studies have examined the effect of the distance between the turret and the center of gravity (C_G) of a system and the distance between C_G and the center of the turret (C_T). The maximum yaw angle in regular waves was analyzed, and it was found that when the turret is closer to C_G , the yaw motion is larger (Yadav et al., 2007). Sanchez-Mondragon et al. (2018) compared the results of a similar study with different configurations and wave steepness. The configuration and the environmental conditions were varied, and the turret position and the mooring stiffness influenced the specific wave period between 15.0 and 19.0 s.

Kaasen et al. (2017) concluded that the interaction between yaw and sway is most important in their research on the heading control of turret-moored floating production storage and offloading (FPSO), which they performed with a simplified model. Garza-Rios and Bernitsas (1999) presented a mathematical model for the nonlinear dynamics of slow motions in the horizontal plane of a TMS in terms of the equation of motion. They proved that if the friction moment

Received 25 July 2020, revised 22 August 2020, accepted 25 August 2020

Corresponding author Kwang Hyo Jung; +82-51-510-2343, kjung@pusan.ac.kr

© 2020, The Korean Society of Ocean Engineers

This is an open access article distributed under the terms of the creative commons attribution non-commercial license (<http://creativecommons.org/licenses/by-nc/4.0>) which permits unrestricted non-commercial use, distribution, and reproduction in any medium, provided the original work is properly cited.

between the turret and the vessel is ignored, the dynamics in the parametric design space for both SPM and TMSs are qualitatively the same.

Mathematical approaches have been used to investigate yaw instability. Pinkster (1979) computed the second-order mean drift force through direct integration of the pressure on the wetted surface. The yaw motion depends on the wave drift force exerted by the first-order body motion and 2nd order low-frequency wave excitation force, which various studies have investigated. Morandini and Wong (2007) outlined a method to estimate the heading of a turret-moored vessel in terms of the relation between the equilibrium heading and stability. Milne et al. (2016) presented a reliable method to estimate the heading of an operating FPSO by combining numerical-based prediction of MetOcean conditions. They indicated that the mean drift force and wind load are dominant in the turret moment. However, these studies considered regular waves from the head sea or used information provided by a particular agency.

In this study, experiments were conducted on an FPSO that will be installed in the Arctic Ocean, where it will experience various wave conditions and incoming wave directions. The parameters related to the turret were used to reproduce the yaw motion. Simulations were done with consideration of the rotational stiffness and rotational damping on the turret, and the results were compared with experimental results.

2. Model Description

A model test of a turret-moored FPSO in deep water conditions was conducted in the wave basin at Changwon National University, Korea. The dimensions of the basin are 19 m (L) \times 14 m (B) with an available depth of 1.5 m. With a scale ratio of 133.33, the total volume of the model achieves a 1.00% difference between the measured and target displaced volume (measured: 163,554 m³) for full load conditions. The main parameters of the original FPSO designed by Samsung Heavy Industries and the scale model are summarized in Table 1.

Table 1 Main parameters of the FPSO model

Description	Prototype	Model	Unit
LOA	250.3	1.880	m
LPP	244.0	1.830	m
Breadth	50.0	0.375	m
Depth	44.0	0.330	m
Draft	18.6	0.140	m
Volume	163,215.0	0.069	m ³
XCG	117.7	0.883	m
YCG	0.0	0.000	m
VCG	19.5	0.146	m

2.1 Coordinate System

The origin of the global-fixed reference frame (K_G) is regarded as C_T , and that of the locally fixed reference frame (K_L) is regarded as the center of the midship section. When the FPSO rotates with respect to C_T , the surge and sway forces and yaw moment are applied to C_G . Thus, the movement of C_G (\vec{X}) is described with respect to K_G and the turret position (\vec{X}_T), as shown in Fig. 1. \vec{X}_T can be described using Eqs. (1)-(3) (Ragazzo and Tannuri, 2003; Sanchez-Mondragon et al., 2018).

$$\vec{X}_T \in K_G, \quad (T: K_L \rightarrow K_G) \quad (1)$$

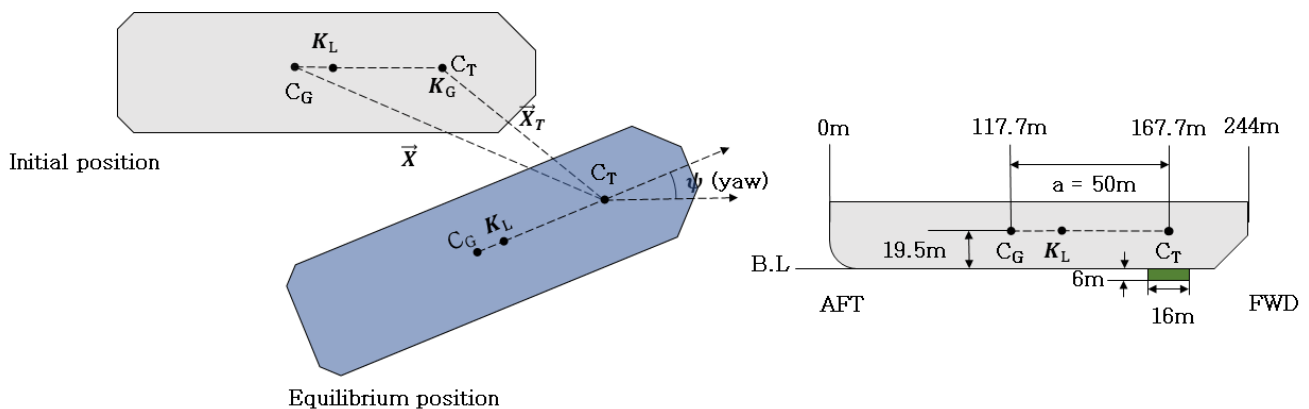
$$\vec{X}_T = \vec{X} + aT(\psi)\vec{e}_1 \quad (2)$$

where a is the distance between C_G and C_T , ψ is the yaw angle, and ($T(\psi)$) is the attitude matrix of the vessel.

$$T(\psi) = \begin{pmatrix} \cos\psi & -\sin\psi \\ \sin\psi & \cos\psi \end{pmatrix} \quad (3)$$

2.2 Turret Mooring Arrangement

To provide a weathervaning function, the model is equipped with an internal turret as a structural component, which allows the



(a) Global-fixed reference frame (K_G) and local-fixed reference frame (K_L)

(b) Reference origin

Fig. 1 Coordinate system and reference origin

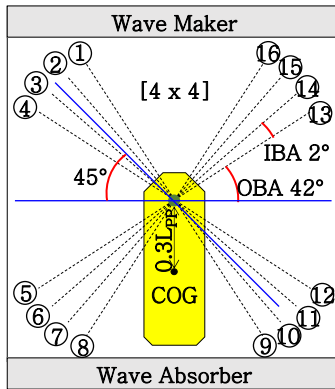


Fig. 2 Diagram of mooring arrangement

Table 2 Properties of mooring line elements

	TOP	MID	BTM	unit
Segment	Chain	Wire	Chain	-
Length	60	200	780	m
Diameter	171	153	171	mm
Grade	Studless, R4S	Spiral strand	Studless, R4S	-
Weight in water	508.63	107.22	508.63	kg/m
Weight in air	581.89	122.18	581.89	kg/m
Pretension		2,703		kN
Pretension angle		125		deg
Inner/outer bundle angle		2 / 42		deg
Footprint radius		1,000		m
Single line stiffness	2.497E6 (Chain) / 1.237E6 (Rope)			kN/m

vessel to rotate to the equilibrium angle to counteract to the varying environment. The turret is located at 50 m in front of. It has a diameter of 16 m and a projection area of 6 m underneath the baseline. The turret is fixed to the seabed through 16 identical mooring lines, which are composed upper and lower chain segments and middle wire segments. A catenary mooring system was adopted.

The mooring lines are symmetrically arranged in four groups of four lines, and the lines are 2° away from each other. Each group is separated by an angle of 42°, as shown in Fig. 2. The properties of each mooring element are shown in Table 2. The designated pretension for all lines is 2,703 kN in loaded conditions.

2.3 Test Conditions

Regular wave sets were tested, and their parameters are summarized in Table 3. The incoming waves were considered as coming from three directions at counterclockwise intervals of 45° from 180°. Head sea, oblique sea, and beam sea were examined, and the incident wave angles were 180°, 225°, and 270°, respectively. The ITTC (2002) recommends analyzing 5 to 20 signals to obtain steady-state results from model tests in regular waves. Therefore, signals were measured

Table 3 Test matrix for regular waves and scale prototype

Case	Wave period	Wave frequency	Wave length	Wave height
	T (s)	ω (rad/s)	λ (m)	H (m)
RW01	8.08	0.78	102.7	5.33
RW02	9.24	0.68	133.3	5.33
RW03	10.39	0.60	169.3	5.33
RW04	10.97	0.57	188.0	5.33
RW05	11.55	0.54	208.0	5.33
RW06	12.70	0.49	252.0	5.33
RW07	13.86	0.45	300.0	5.33
RW08	15.01	0.42	350.7	5.33
RW09	16.17	0.39	406.7	5.33

for 2,000 seconds using a scale prototype. Various wave directions were not available in the model test, so the model was tested in multiple directions by rotating it.

3. Experiment of Heading Stability

3.1 Experimental Setup

Several instruments were used to measure the motion of the FPSO and the tension of the mooring lines, as illustrated in Fig. 3. To achieve the target wave conditions in Table 3, the wave height at the position where the model would be installed was measured by a wave gauge with 1% tolerance. An optical measuring instrument (RODYM-6D) was used to measure the 6-degree-of-freedom (DOF) motion of the vessel at . Its tolerance is 0.1 mm in this arrangement, which is considered adequate to collect data. The mooring tension on the turret was measured by water-proof load cells, which each have a maximum capacity of 30 N with 1% tolerance. All channels were calibrated.

3.2 Experimental Results

Static analysis was conducted to verify the horizontal restoring-force characteristics of the full-scale prototype. Since the mooring lines were arranged symmetrically, the mooring restoring forces in the surge and sway directions were considered to be the same. A static pull-out test was performed in the surge direction by applying different weights to move the model slowly, and the mooring tension was recorded. The test results were compared to those obtained from Orcaflex 10.3 and are plotted in Fig. 4. Both results match well, so the mooring system was deemed suitable.

Model tests were performed under several regular wave conditions. Various wave heights were applied in the model test, but in this study, a wave height (H) of 5.33 m was considered. The results of the yaw angle for each period in Table 3 are shown in Fig. 5. The heading angles converged depending on the varying wave periods, and the vessel heading rotated closer to the incoming direction of regular waves, which have relatively short periods in both sea states.

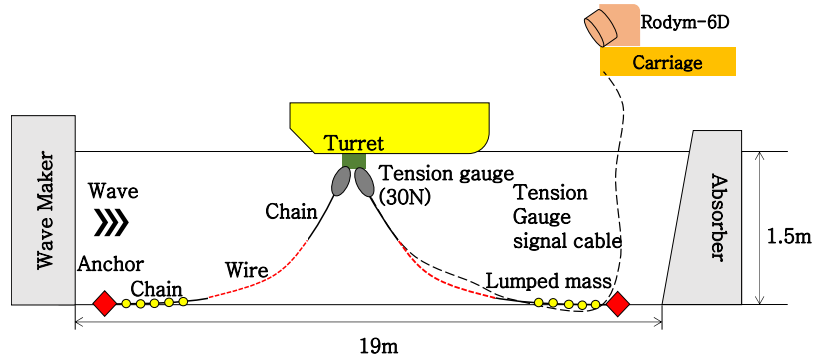


Fig. 3 Diagram of experimental set up

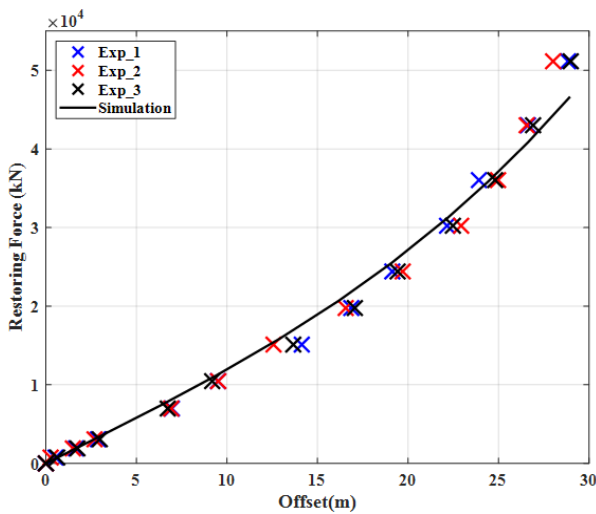


Fig. 4 Results of static pull-out test

Moreover, the equilibrium headings are identical for both oblique sea and the beam sea conditions at the same wave period except for the three longest wave periods.

4. Numerical Analysis

4.1 Hydrodynamic Computation

To obtain the hydrodynamic properties of the model, a numerical

analysis was performed using Hydrostar v7.3, which was developed by Bureau Veritas. This software is capable of calculating the first-order and the second-order wave-induced forces and motions on a floating structure. Diffraction and radiation problems are solved based on potential flow theory (Chen, 2009), and the velocity potential is solved by the panel method. The examined FPSO has a box shape (Fig. 6), so there is negligible influence of the hull shape due to the limited analysis range of potential theory, which is limited to below the free surface. For computational efficiency, 3,250 mesh elements were applied, and 40 wave frequencies of .05 to 2.00 rad/s were used with 36 headings at 10-degree intervals from 0 to 360°. To validate the results, the displaced volume was compared, and it had a 0.11% difference from the prototype results, so it is regarded as suitable for further analysis.

The wave drift force is a second-order load acting on the vessel subject to the waves. It is important for the horizontal motion of the vessel as the force occurs in a region of relatively low frequency. The second-order wave drift force can be estimated from the first-order QTF matrix using a middle-field formulation presented by Chen (2007). In the new middle-field formulation, the second-order wave loads are obtained by applying two variants of Stokes's theorem and Gauss's theorem to the near-field formulation. The shape of the bow and stern near the free surface is not quite wall-sided, the middle-field formulation was selected to calculate the second-order wave load.

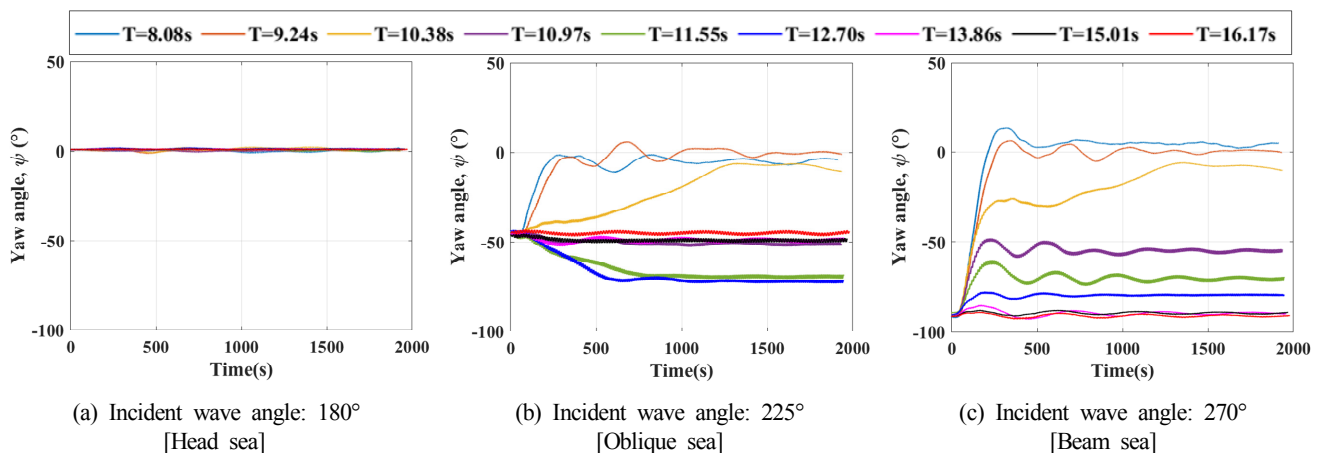


Fig. 5 Yaw angle of FPSO over time with waves (model test)

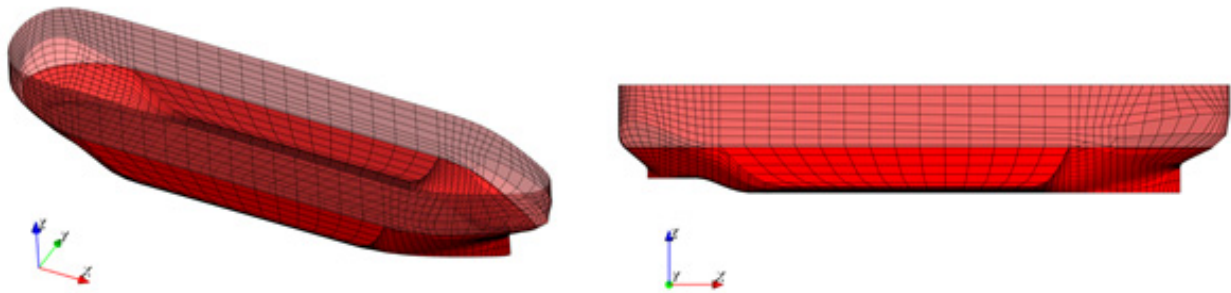


Fig. 6 Mesh generation

4.2 Heading Stability Analysis with the Vessel's Hydrodynamic Characteristics

Orcaflex 10.3 was used to analyze the heading stability of the turret-moored FPSO. The reference system in Orcaflex consists of a global-fixed frame of reference, in which the centers of the turret and local fixed frame of reference are located at the center of gravity (Fig. 1) (Orcina, 2018). The FPSO motion was modeled with 6 DOF, and the wave frequency (WF) excitation forces were obtained from the results of Hydrostar v7.3. Newman's approximation was chosen for wave drift QTFs at the draft. The equilibrium position of mooring lines was computed based on the catenary method.

The vessel can rotate independently of the turret, so the turret was modeled with limited rotation in only the z-direction, and a mooring line was attached to the turret edge. The build-up period was set to twice the wave period, and the dynamic calculation period was set to 2,000 s. Static analysis was not performed so that the vessel response to the changing incident wave directions could be monitored.

Only the hydrodynamic properties of the FPSO acquired from

Hydrostar v7.3 were considered, which means that none the parameters were applied to the turret. Figs. 7-9 show the yaw angles in the head sea, oblique sea, and beam sea conditions with the regular wave conditions specified in Table 3. The results show that Orcaflex might require an additional parameter, such as the turret's rotational stiffness or damping, which is related to the rotational velocity.

4.3 Relative Motion of the Turret and Vessel

A parametric study was conducted to examine the dependency of the parameters on the heading stability in regular waves (RW02). The parameter settings are shown in Table 4. The linear damping coefficient in the surge (B_{11}), sway (B_{22}), and yaw (B_{66}) directions was calculated based on the recommendations of BV NR-493 (Bureau Veritas, 2015). To minimize the effect of roll on the yaw motion (Lugni et al., 2015), the linear roll damping coefficient (B_{44}) was considered based on the result of a free decay test, which was obtained using the relative decrement method. The rotational stiffness (k) and rotational damping (τ) were alternately applied in the range of 0 to

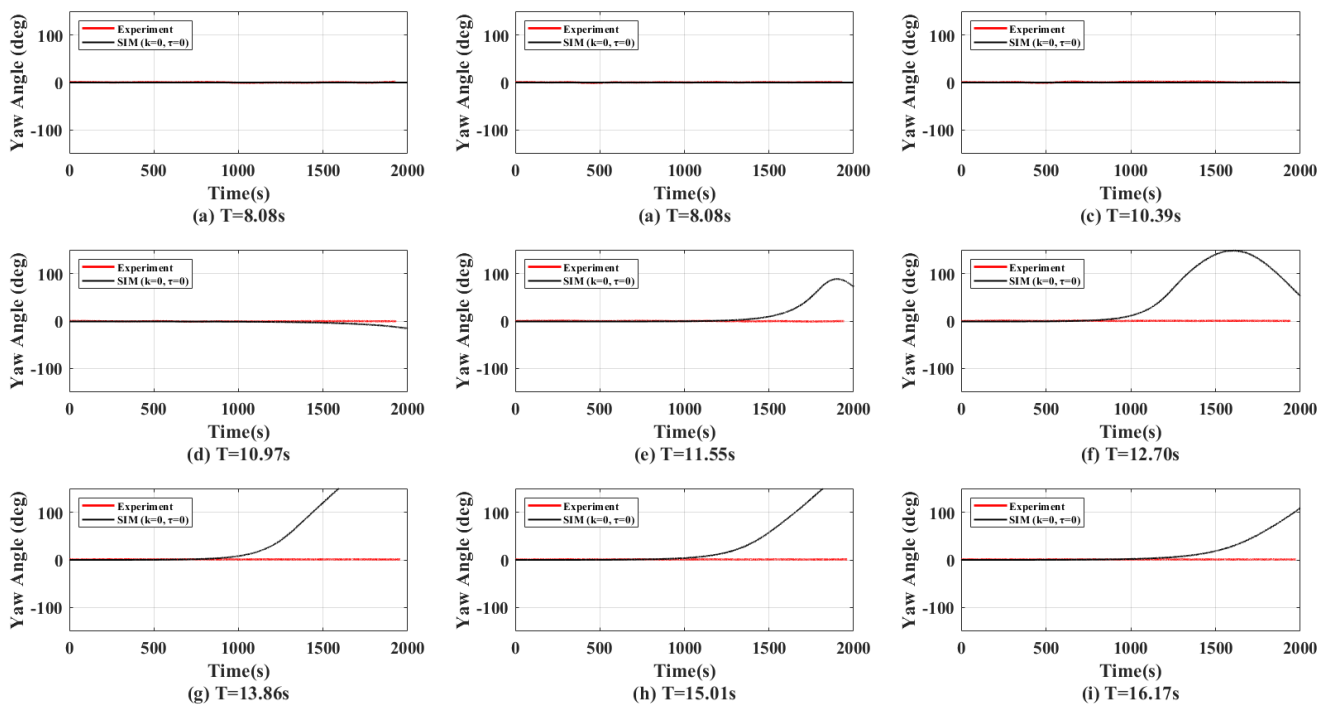


Fig. 7 Yaw angle of turret-moored FPSO in time history (Head sea. Wave incident angle: 180°)

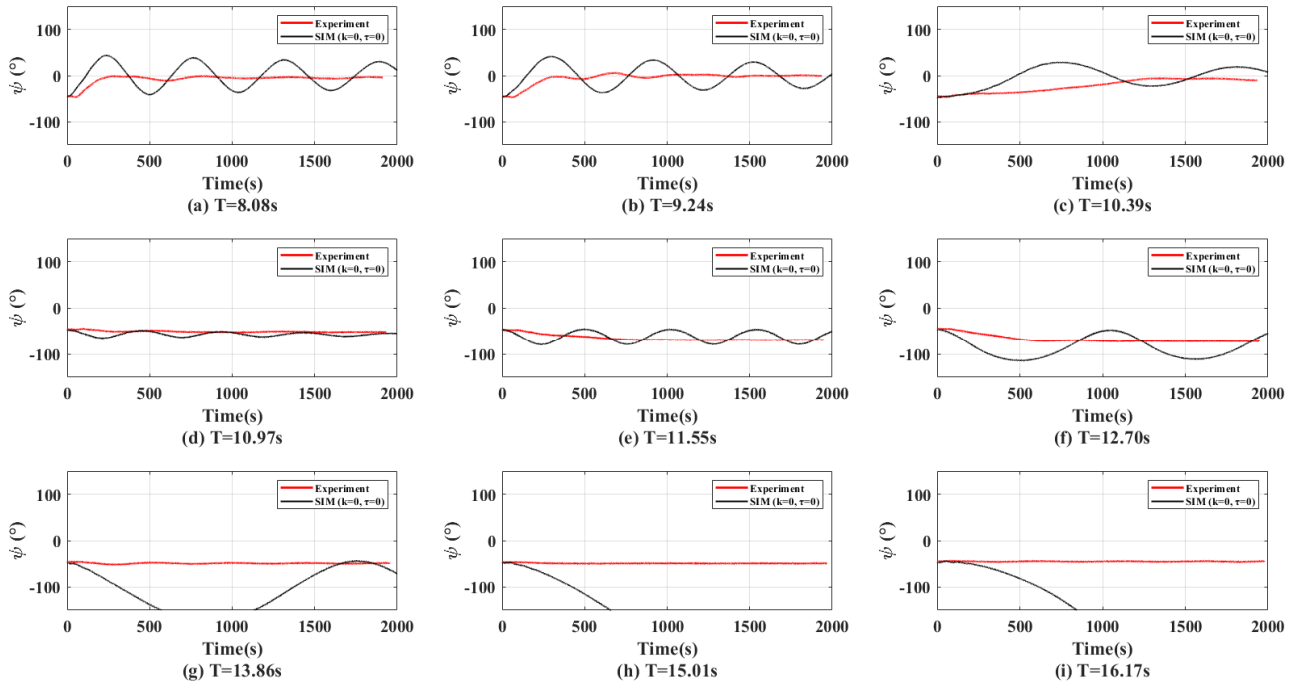


Fig. 8 Yaw angle of turret-moored FPSO over time (Oblique sea. Incident wave angle: 225°)

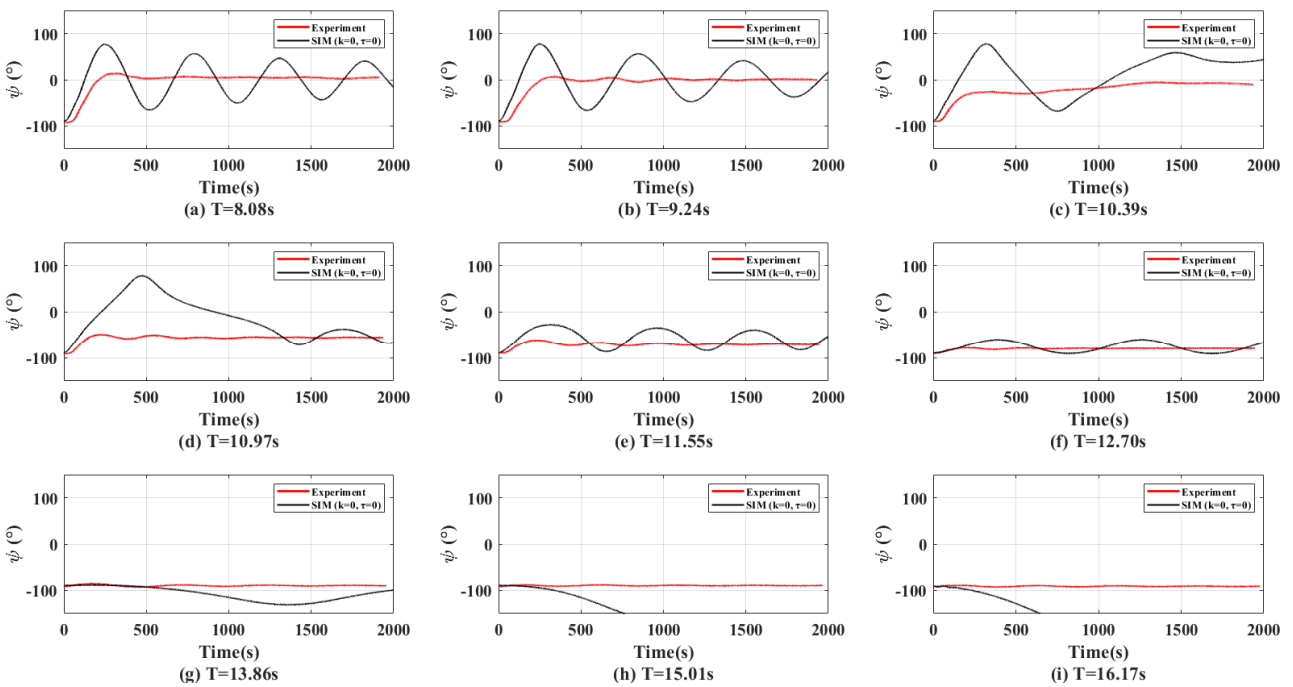


Fig. 9 Yaw angle of turret-moored FPSO over time (Beam sea. Incident wave angle: 270°)

1.00E07.

The maximum turret angle in beam sea conditions varied with the rotational stiffness (see Fig. 10). When the turret's rotational stiffness was high ($1E06$ kN·m/deg), the turret rotated up to 58° with the vessel. On the other hand, the turret's maximum rotation was 3° when the turret rotational stiffness was 10 kN·m/deg. Caille et al. (2014) estimated the turret release angle as 3.7° . Since the turret's rotational stiffness is relatively small, the result can be considered reliable. For Fig. 10(b), a smaller turret rotational damping of 10 kN·m·s/deg was

applied. The results fluctuate evenly, and the converged heading does not face the incident wave direction. However, in the case in Fig. 10(c), the damping was $1E06$ kN·m·s/deg, and the heading converges with a skewed fish-tailing phenomenon toward the incident wave direction.

Based on the results of the parametric study, Fig. 11 illustrates the relationship between the turret and vessel when the vessel rotates under the influence of external forces. When the environmental load increases, the vessel rotates with the turret until the moment on vessel

Table 4 Matrix characteristics for parametric study of turret parameters

B_{11} (kN/(m/s))	B_{22} (kN/(m/s))	B_{44} (kN.m/(rad/s))	B_{66} (kN.m/(rad/s))	Rotational Stiffness (k) (kN.m/deg)	Rotational Damping (τ) (kN.m.s/deg)
				0.00E00	0.00E00
				1.00E01	1.00E01
341	1,361	7.04E05	6.73E06	1.00E02	1.00E02
				1.00E04	1.00E04
				1.00E06	1.00E06
				1.00E07	1.00E07

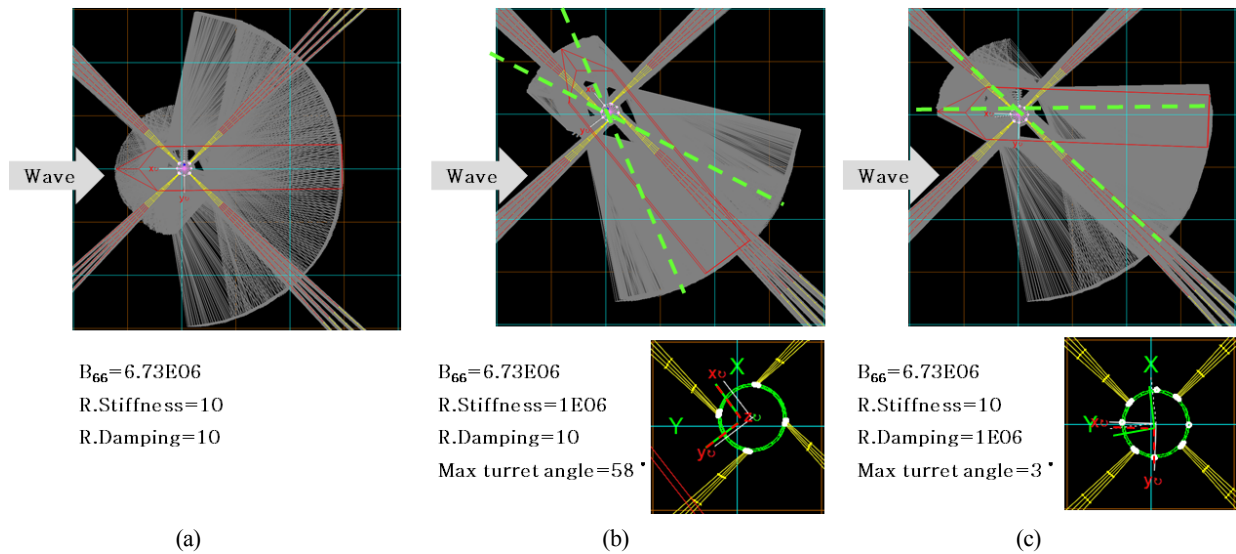


Fig. 10 Trajectory from the parametric study with respect to the turret's rotational stiffness and damping

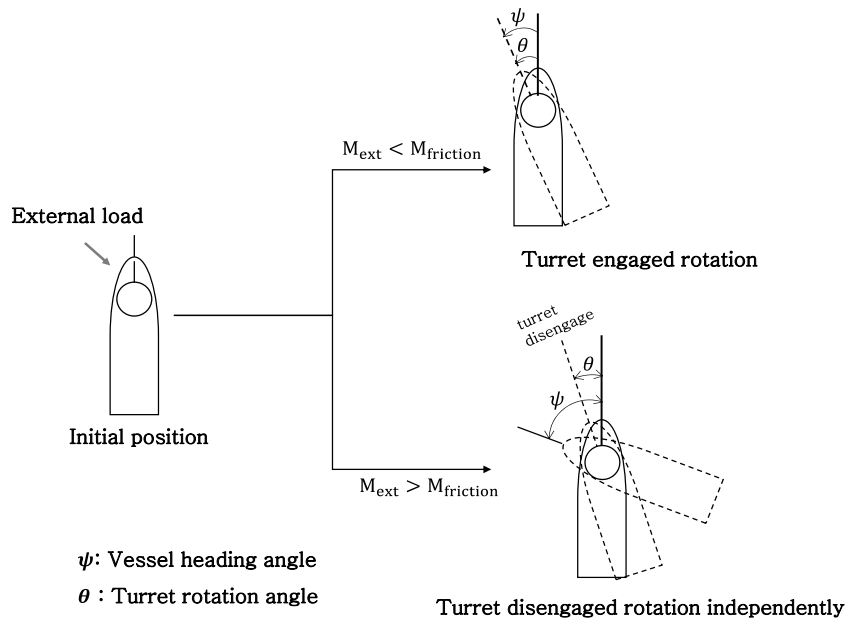


Fig. 11 Relative rotation of turret against the vessel

due to the external load (M_{ext}) becomes greater than the moment due to friction ($M_{friction}$) on the contact surface between the vessel and turret. As the external load increases, the turret is released from the vessel and then both rotate independently. The vessel rotates toward

the predominant environmental load, while the turret rotates until the difference between moments caused by the external force and the moment generated by the distortion of mooring line (Caille et al., 2014).

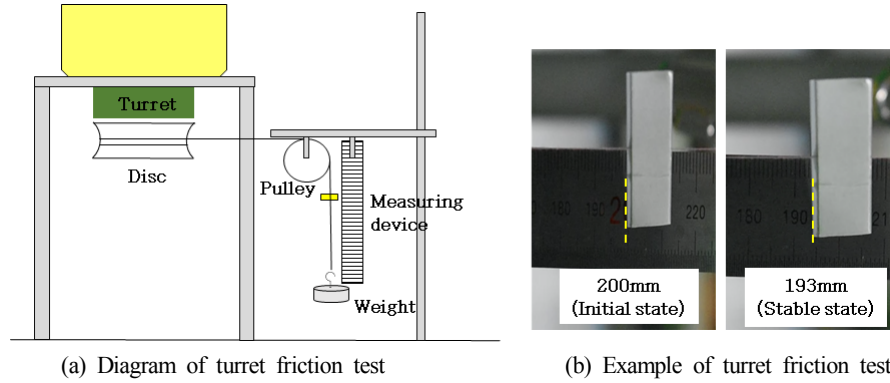


Fig. 12 Turret friction test

5. Estimation of Turret Parameters

5.1 Rotational Stiffness

The friction of the turret was tested in the air to obtain the rotational stiffness (k) caused by the turret. The model ship was placed on a cradle and a disc to wrap it with a wire that is attached to the bottom of the turret. One end of the wire was secured to the disc, and the other was connected to the weight through a pulley, as shown in Fig. 12(a). The traveling time and distance were measured when the turret rotates with differing weights (Fig. 12(b)). Constant velocity sections were considered to obtain the rotational velocity of the turret.

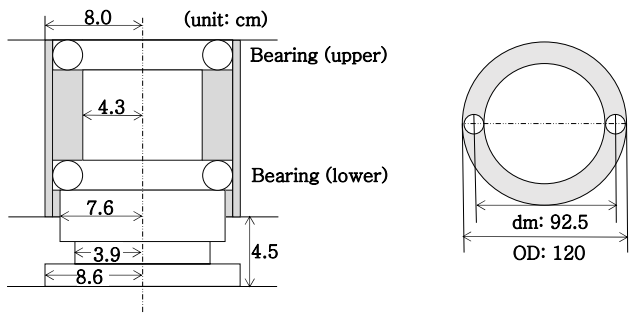
The rotational stiffness was calculated using Eq. (4) with the result of the turret friction test and the properties. The rotational stiffness (k) was approximately 1.93 kN for the scale prototype.

$$\text{Rotational stiffness } (k) = \frac{\text{Frictional Moment}}{\text{Rotational Velocity}} \quad (4)$$

where the frictional moment of the roll bearing is obtained by Eq. (5) (Koyo, 2007)

$$\text{Frictional Moment} = \frac{P \times \mu \times dm}{2} \quad (5)$$

where P is an equivalent weight load on the bearing, μ is the friction coefficient and equal to 0.0015 (Koyo, 2007), and dm is the diameter between the ball centers (Fig. 13(b)).



(a) Detail of turret (section) (b) Detail of the bearing (plan)

Fig. 13 Information to estimate the turret's rotational friction moment

5.2 Rotational Damping using Rotational Velocity (RDV Method)

As mentioned in 4.3, additional parameters to suppress the rotational velocity was considered. Generally, acting like a decelerator is known as damping, and this might be related to the rotational velocity as well as the moment in this case. Thus the difference of the velocity between simulation without additional parameter and the experiment was used. As only the wave load had been considered for the experiment, the total moment ($M_{total} = M_{wave}$) on the vessel in the yaw direction due to environmental load is the same as the sum of load RAO and wave drift force. So the difference between the rotational velocity with ($\dot{\psi}_{with} = \dot{\psi}_{exp}$) and without ($\dot{\psi}_{without}$) additional parameter acting on turret deemed as a turret rotational damping which should be considered for the turret-moored FPSO in Orcaflex. As a result, the rotational damping (τ) using the difference between the rotational velocity of the model test, and the simulation without consideration of additional parameters on turret can be defined as Eq. (6).

As mentioned, additional parameters were considered to suppress the rotational velocity. The damping can be related to the rotational velocity and the moment. Thus, the difference of the velocity between the simulation without additional parameters and the experiment was used. Only the wave load was considered for the experiment, so the total moment ($M_{total} = M_{wave}$) on the vessel in the yaw direction due to environmental load is the same as the sum of response amplitude operator (RAO) load and wave drift force. The turret's rotational damping is considered as the difference between the rotational velocity with additional parameters ($\dot{\psi}_{with} = \dot{\psi}_{exp}$) and without them ($\dot{\psi}_{without}$) acting on turret deemed. As a result, Eq. (6) defines the rotational damping (τ) obtained using the difference between the rotational velocity of the model test and the simulation without additional turret parameters.

$$\left| \frac{M_{wave}}{\dot{\psi}_{exp}} - \frac{M_{wave}}{\dot{\psi}_{without}} \right| = \tau \quad (6)$$

5.3 Rotational Damping using Equilibrium State (RDE Method)

To obtain the turret's rotational damping, an equilibrium state in yaw is considered as in Eq. (7) (Sanchez-Mondragon et al., 2018).

$$(F_{m_y} + f_y)(I_{66} + m_{66}) - (aF_{m_y} + M_{ext})(mx_g + m_{26}) = 0 \quad (7)$$

m : mass of the vessel

m_{ij} : added mass or added moment of inertia of the vessel with respect to the K_L ($i=1,2,6, j=1,2,6$)

x_g : the C_G position with respect to the K_L

I_{66} : moment of the inertia of the vessel with respect to the K_L

a : distance between C_G and C_T

F_{m_y} : restoring force from the mooring system on C_G in sway, and can be obtained by Eq. (8)

$$F_{m_y} = -F_x \sin(\psi) + F_y \cos(\psi) \quad (8)$$

where F_x and F_y are the mooring restoring forces on C_T in the surge and sway directions, respectively.

f_y : environmental force on the vessel in sway direction, which is defined in Eq. (9)

$$f_y = \frac{M_{ext}(m + m_{22})}{(mx_g + m_{26})} \quad (9)$$

M_{ext} : moment in yaw direction generated by external force, and is defined in Eq. (10) (Sanchez-Mondragon et al., 2018).

$$M_{ext} = M_{C_G} + M_{C_T} \quad (10)$$

M_{C_G} : yaw moment at C_G due to the environmental forces

M_{C_T} : rotational moment at C_T induced by the interaction between the turret and vessel

Sanchez-Mondragon et al. (2018) described $M_{C_T} = \tau(r_{turret} - r_{vessel})$, where r_{vessel} and r_{turret} are the rotational velocity of the vessel and turret, respectively, and τ is the rotational damping. τ can be obtained by solving Eqs. (7) and (10). It is assumed that the restoring force in the sway direction is equal to the restoring force in the surge direction, so the results of the static pull-out test in the surge direction were used for the sway direction.

Figs. 14–16 show the yaw angles in head sea, oblique sea, and beam sea conditions that were calculated while considering the rotational stiffness (k) and the rotational damping (τ) on turret surface obtained by the RDV method and RDE methods. The red, blue, and magenta lines represent the experimental results, the simulated results with turret parameters obtained in the RDV method, and the simulated results with turret parameters obtained in the RDE method, respectively. The RDV results and RDE results showed a tendency of a large fish-tailing phenomenon appearing before approximately 1,000 s. However, compared with Figs. 7–9, the overall heading angles tend to agree well with the experimental results. As with the results of the model tests, the amount of fish-tailing was decreased, and there was no rotation toward the wave direction at wave periods longer than 10.38 s.

The equilibrium heading angles from the experiment and computation are shown in Table 5. The equilibrium headings were

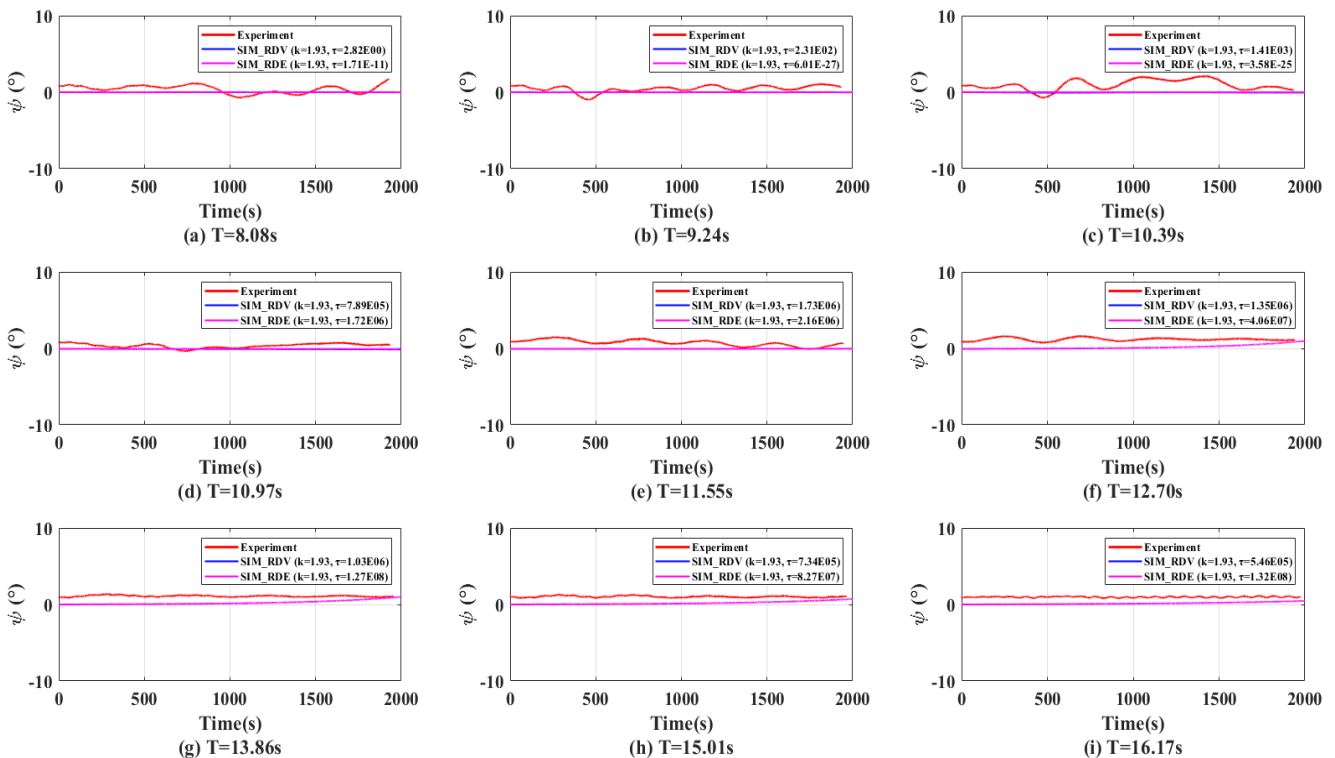


Fig. 14 Yaw angle of turret-moored FPSO over time (Head sea. Incident wave angle: 180°)

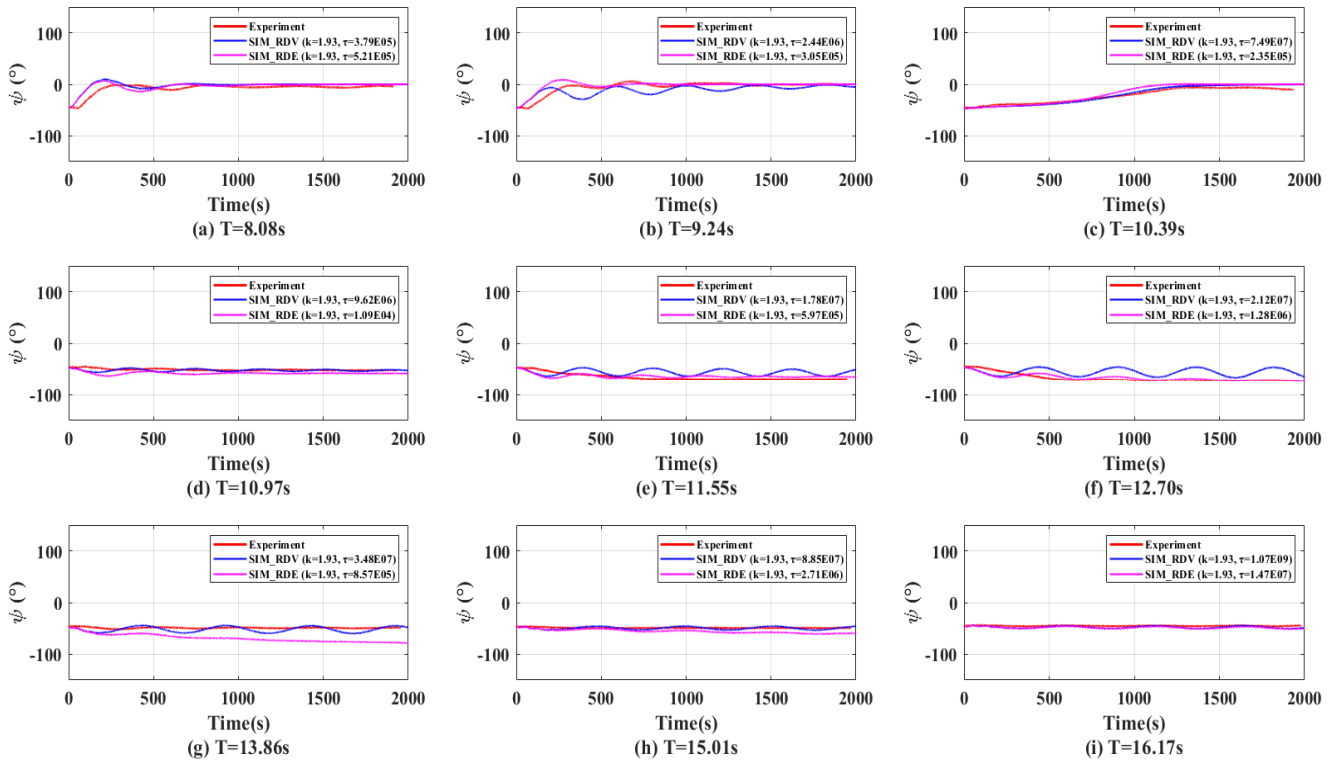


Fig. 15 Yaw angle of turret-moored FPSO over time (Oblique sea. Incident wave angle: 225°)

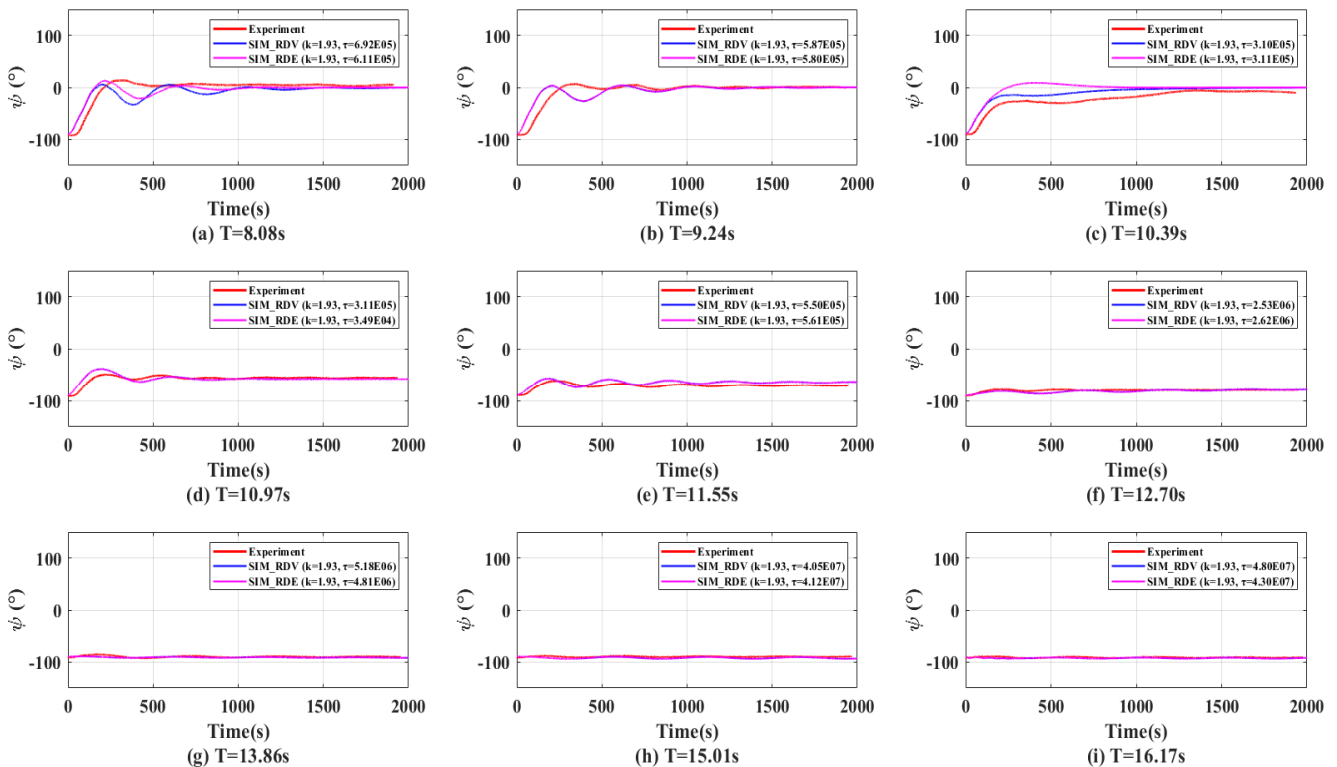


Fig. 16 Yaw angle of turret-moored FPSO over time (Oblique sea. Incident wave angle: 270°)

considered the average of the angles from the first peak to the end in each case. The difference in equilibrium heading was compared between the experiment and simulation with additional parameters.

The error range of the equilibrium heading angles between the experiment and simulation was 2 to 10%, excluding the maximum and minimum errors for each sea state. Thus, the τ results are reasonable.

Table 5 Equilibrium heading angles differences between experiment and simulation (Orcaflex)

Case	Head sea (incident wave angle: 180°)				
	Exp	RDV	Error	RDE	Error
RW01	0.31	0.00	0.32	-0.01	0.33
RW02	0.76	-0.01	0.77	-0.01	0.44
RW03	0.52	-0.04	0.56	-0.01	1.02
RW04	0.60	-0.06	0.65	-0.01	0.38
RW05	0.24	0.01	0.23	0.01	0.73
RW06	1.20	0.56	0.64	0.23	1.01
RW07	1.05	0.57	0.48	0.25	0.85
RW08	0.96	0.44	0.52	0.20	0.82
RW09	1.00	0.31	0.69	0.15	0.82

Case	Oblique sea (incident wave angle: 225°)				
	Exp	RDV	Error	RDE	Error
RW01	-4.67	-1.12	3.55	-2.43	2.24
RW02	-0.91	-9.72	8.81	-0.13	0.78
RW03	-19.06	-16.32	2.74	-13.26	5.80
RW04	-50.60	-51.18	0.58	-56.97	6.37
RW05	-66.97	-55.21	11.76	-63.40	3.57
RW06	-69.67	-54.14	15.53	-67.52	2.15
RW07	-49.03	-51.73	2.69	-70.48	21.45
RW08	-49.10	-49.38	0.28	-56.04	6.94
RW09	-45.05	-47.63	2.58	-48.42	3.37

Case	Beam sea (incident wave angle: 270°)				
	Exp	RDV	Error	RDE	Error
RW01	5.20	-5.54	10.74	-2.85	8.05
RW02	0.38	-3.66	4.05	-3.58	3.97
RW03	-16.44	-5.35	11.08	1.61	18.05
RW04	-54.70	-57.19	2.50	-57.19	2.50
RW05	-70.03	-64.45	5.58	-64.47	5.56
RW06	-79.65	-81.13	1.48	-81.27	1.62
RW07	-89.88	-91.10	1.23	-91.14	1.26
RW08	-89.54	-91.93	2.39	-91.92	2.39
RW09	-91.12	-92.41	1.28	-92.43	1.31

6. Conclusions

A turret-moored FPSO has been analyzed under different regular wave conditions with various wave periods and directions. It was found that the heading change was greater with relatively short waves. A numerical analysis was performed for verification, and factors that affect the yaw behavior were investigated to reproduce the heading results from model tests.

The turret's rotational stiffness was obtained using the physical properties of the bearings and a friction test. It acts as the maximum static frictional force against the contact surface between the turret and

the vessel. The turret's rotational damping mainly affects the rotational velocity, which plays an important role in the fish-tailing phenomenon, so the rotational velocity and equilibrium state were considered. The simulation results were compared to the experimental results, and both methods showed good agreement. However, the RDV method is more appropriate if the turret friction has not been tested. Even if practical data are unavailable, as long as an experimental study is performed, the presented methods can be applied.

Acknowledgments

This work was supported by the following technology innovation programs: of "Development of Arctic Ocean-Based Floating Offshore Structure Geometry Capable of Year-Round Operation Under ARC7 Condition by Applying Position Maintenance and Mooring Systems (Project No.: 10063405)", "Construction of Equipment for Assessing the Performance of Hydrogen Fuel Cell ESS Systems for MW-Class Vessels and Test Method Development (Project No.: 20006636)", and "the Korea-U.K. Offshore Plant Global Professional Training Program (Project No.: 0001288)," which were funded by the Ministry of Trade, Industry, and Energy of the Republic of Korea.

References

- Bureau Veritas. (2015). Classification of Mooring Systems for Permanent and Mobile Offshore Units (BV-NR-493).
- Caille, F., Prieur, J., & Mamoun, N. (2014). New Insights in Turret Mooring Systems Yaw Dynamics. ASME 2014 33rd International Conference on Ocean, Offshore and Arctic Engineering, American Society of Mechanical Engineers. <https://doi.org/10.1115/OMAE2014-24490>
- Chen, X.B. (2007). Middle-field Formulation for the Computation of Wave-Drift Loads. *Journal of Engineering Mathematics*, 59(1), 61-82. <https://doi.org/10.1007/s10665-006-9074-x>
- Chen, X.B. (2009). Hydrostar User Manual. BV, France.
- Cho, S.K., Sung, H.G., Hong, J.P., & Choi, H.S. (2013). Experimental Study of Excessive Yaw Motion of Turret Moored Floating Body. *Journal of the Society of Naval Architects of Korea*, 50(1), 8-13. <https://doi.org/10.3744/SNAK.2013.50.1.8>
- Garza-Rios, L., & Bernitsas, M. (1999). Slow Motion Dynamics of Turret Mooring and Its Approximation as Single Point Mooring. *Applied Ocean Research*, 21(1), 27-39. [https://doi.org/10.1016/S0141-1187\(98\)00035-2](https://doi.org/10.1016/S0141-1187(98)00035-2)
- ITTC. (2002). ITTC-Recommended Procedures and Guidelines (7.5-02 07-03.2). Retrieved from <https://itc.info/media/1323/75-02-07-032.pdf>
- Kaasen, K.E., Ludvigsen, H., Nygaard, I., & Aas, K. (2017). Theoretical and Experimental Study of Heading Stability and Heading Control of a Turret-Moored FPSO. ASME 2017 36th International Conference on Ocean, Offshore and Arctic Engineering, American Society of Mechanical Engineers. <https://doi.org/>

10.1115/OMAE2017-61390

- Koyo. (2007). Frictional Coefficient. Retrieved 12 August 2020 from <https://koyo.jtekt.co.jp/en/support/bearing-knowledge/8-4000.html>
- Lugni, C., Greco, M., & Faltinsen, O.M. (2015). Influence of Yaw-roll Coupling on the Behavior of a FPSO: An Experimental and Numerical Investigation. *Applied Ocean Research*, 51, 25-37. <https://doi.org/10.1016/j.apor.2015.02.005>
- Milne, I.A., Delaux, S., & McComb, P. (2016). Validation of a Predictive Tool for the Heading of Turret-moored Vessels. *Ocean Engineering*, 128, 22-40. <https://doi.org/10.1016/j.oceaneng.2016.10.007>
- Morandini, C., & Wong, J. (2007). Heading Analysis of Weathervaning Floating Structures: Why, How and Where to Make the Best of Them. The 17th International Offshore and Polar Engineering Conference, International Society of Offshore and Polar Engineers.
- Munipalli, J., Pistani, F., Thiagarajan, K. P., Winsor, F., & Colbourne, B. (2007). Weathervaning Instabilities of a FPSO in Regular Waves and Consequence on Response Amplitude Operators. ASME 2007 26th International Conference on Offshore Mechanics and Arctic Engineering, American Society of Mechanical Engineers, 405-412. <https://doi.org/10.1115/OMAE2007-29359>
- Norwegian Petroleum Directorate (NPD). (2019). NPD Resource Report 2019 - Discovery and Fields. Retrieved from <https://www.npd.no/en/facts/publications/reports2/resource-report/resource-report-2019/>
- Orcina, L.T.C. (2018). OrcaFlex User Manual: OrcaFlex 10.2 c. Daltongate Ulverston Cumbria, UK.
- Pinkster, J.A. (1979). Mean and Low Frequency Wave Drifting Forces on Floating Structures. *Ocean Engineering*, 6(6), 593-615. [https://doi.org/10.1016/0029-8018\(79\)90010-6](https://doi.org/10.1016/0029-8018(79)90010-6)
- Ragazzo, C.G., & Tannuri, E.A. (2003). On the Dynamics of Turret Systems in Deep Water. *Applied Ocean Research*, 25(1), 37-51. [https://doi.org/10.1016/S0141-1187\(03\)00030-0](https://doi.org/10.1016/S0141-1187(03)00030-0)
- Sanchez-Mondragon, J., Vázquez-Hernández, A.O., Cho, S.K., & Sung, H.G. (2018). Yaw Motion Analysis of a FPSO Turret Mooring System under Wave Drift Forces. *Applied Ocean Research*, 74, 170-187. <https://doi.org/10.1016/j.apor.2018.02.013>
- Yadav, A., Varghese, S., & Thiagarajan, K.P. (2007). Parametric Study of Yaw Instability of a Weathervaning Platform. Proceedings of 16th Australasian Fluid Mechanics Conference, Gold Coast, Australia, 1012-1015.

Author ORCIDs

Author name	ORCID
Min, Soo Young	0000-0002-3431-5655
Park, Sung Boo	0000-0001-9587-2183
Shin, Seong Yun	0000-0001-6665-9092
Shin, Da Gyun	0000-0002-3976-1961
Jung, Kwang Hyo	0000-0002-8229-6655
Lee, Jaeyong	0000-0002-4469-7765
Lee, Seung Jae	0000-0001-8992-6915
Han, Solyoung	0000-0002-9463-1780
Chung, Yun Suk	0000-0001-7621-0352

Reliability Analysis for Structure Design of Automatic Ocean Salt Collector Using Sampling Method of Monte Carlo Simulation

Chang Yong Song¹

¹Professor, Department of Naval Architecture and Ocean Engineering, Mokpo National University, Jeonnam, Korea

KEY WORDS: Monte Carlo simulation, Sampling method, Reliability analysis, Meta-model, Automatic ocean salt collector

ABSTRACT: This paper presents comparative studies of reliability analysis and meta-modeling using the sampling method of Monte Carlo simulation for the structure design of an automatic ocean salt collector (AOSC). The thickness sizing variables of structure members are considered as random variables. Probabilistic performance functions are selected from strength performances evaluated via the finite element analysis of an AOSC. The sampling methods used in the comparative studies are simple random sampling and Sobol sequences with varied numbers of sampling. Approximation methods such as the Kriging model is applied to the meta-model generation. Reliability performances such as the probability failure and distribution are compared based on the variation of the sampling method of Monte Carlo simulation. The meta-modeling accuracy is evaluated for the Kriging model generated from the Monte Carlo simulation and Sobol sequence results. It is discovered that the Sobol sequence method is applicable to not only to the reliability analysis for the structural design of marine equipment such as the AOSC, but also to Kriging meta-modeling owing to its high numerical efficiency.

1. Introduction

Whereas the marine fishery equipment industry is expected to increase in market size worldwide as a major industry for securing food resources, the level of fishery equipment expertise in South Korea is extremely low and the ratio of localization relative to the market size is only approximately 50% (KMI, 2019). A salt collector is marine fishery equipment used to collect salt from marine salt ponds; it is an equipment that must be automated to facilitate the labor-intensive operation of salt pans. The domestic development of electrically driven automatic ocean salt collectors (AOSCs) has begun to improve the safety level during traditional marine salt collection and transfer processes as well as increase the production output per unit area of crystallization ponds. Owing to the lack of domestic and international regulations in the design of marine fishery equipment, the structural safety of new types of fishery equipment, such as AOSCs, is evaluated during the design stage by determining design load conditions that satisfy the operational requirements and applying them in the structural analysis of the equipment. However, the reliability of AOSCs' structural performances must be evaluated while considering unavoidable uncertainties in the operation of salt ponds, such as corrosion issues, to appropriately determine the safety of the structural

design.

Several studies have been conducted to verify the design safety of marine fishery equipment by applying reliability analysis. Lee and Kim (2006) applied the first and second reliability analysis techniques for the reliability evaluation of pipelines and verified the reliability analysis results by comparing them to Monte Carlo simulation (MCS) results. To optimize the reliability-based design of floating production storage & offloading riser add-ons, Song et al. (2011) investigated an optimal design plan to minimize design risks by applying the constraint-feasible moving least-squares method, which is a conservative approximation model. Bai et al. (2015) performed a finite element analysis and used surface response methods for MCS-based reliability analysis on lightweight subsea pipelines. Lee and Kim (2017) calculated the probability of failure in a limit state function using first and second reliability analysis techniques to perform probabilistic defect assessments of defects inherent in mooring chains; subsequently, the probabilities of failure obtained from the limit state function and MCS were compared to verify the adequacy of the approximated probability of failure. Yin et al. (2018) developed a non-probabilistic reliability convex model for the reliability analysis and sensitivity evaluation of valve port plates of deep-sea hydraulic pumps.

Received 15 September 2020, revised 24 September 2020, accepted 25 September 2020

Corresponding author Chang Yong Song: +82-61-450-2732, cysong@mokpo.ac.kr

© 2020, The Korean Society of Ocean Engineers

This is an open access article distributed under the terms of the creative commons attribution non-commercial license (<http://creativecommons.org/licenses/by-nc/4.0>) which permits unrestricted non-commercial use, distribution, and reproduction in any medium, provided the original work is properly cited.

In this study, reliability analysis was performed by applying the general MCS and the Sobol sequence method (SSM), which is one of the quasi-MCS methods, to derive an efficient reliability evaluation method to ensure the structural design safety of AOSCs. Furthermore, the probability of reliability based on the sampling method and the accuracy of the Kriging metamodeling were compared. In the reliability analysis, the thickness of the major structural components of the AOSC were set as a random variable, while considering possible corrosions caused by the nature of the work environment; meanwhile, the strength performance was assumed as a probabilistic performance function. The strength performance of the AOSC was evaluated by calculating the design load conditions considering the actual operating conditions and applying them to the structural analysis model based on the finite element method (FEM) to calculate the maximum stress for each design load condition. To review the reliability probability, probability performance function distribution, and efficiency of numerical calculations, the SSM was used by varying the sampling frequency at a constant ratio, and the results were compared with those of the general MCS, which uses the simple random sampling method. The SSM is effective for reliability analysis owing to its excellent numerical efficiency; however, a review of reasonable sampling methods is required based on the characteristics of the analysis subject because the sampling frequency for the target confidence level is not fixed. In this study, to establish an SSM that is applicable to the analysis of fishery equipment structures, sampling methods for the SSM were investigated to achieve the results of MCS for estimating the reliability of AOSC structural design with a confidence level of 95% and an error rate of 5%. Additionally, to analyze the correlation between the design space approximation characteristics and sampling methods, the approximation accuracy was compared using Kriging metamodels suitable for approximation with random sampling data. This paper is organized as follows. The theoretical backgrounds of the MCS, SSM, and Kriging metamodeling are briefly outlined in Section 2. The FEM-based strength performance evaluation, reliability analysis result comparison, and Kriging metamodeling result comparison are presented in Section 3. Finally, the overall research findings are summarized in the Conclusions section.

2. Theoretical Background

2.1 MCS

MCS is a practical reliability analysis method to determine the uncertainties associated with random variables in a probability performance function for a suitable sampling frequency that satisfies the target confidence level in the evaluation of the probabilities of reliability or failure. However, because the MCS involves a simple random sampling method in which the sampling frequency increases with the target confidence level and accuracy, the efficiency of reliability analysis may be lower. Therefore, numerical calculation experiments, rather than physical experiments, are applied in MCS-based reliability analysis (Siddall, 1983). As shown in Fig. 1, an

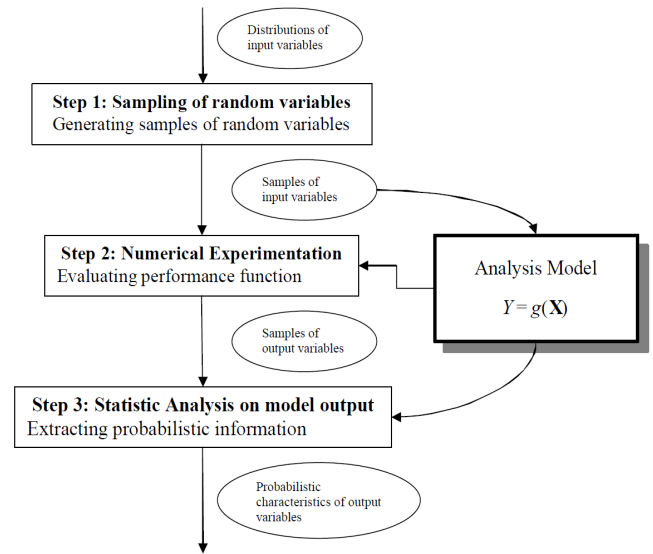


Fig. 1 Procedure of MCS

MCS is performed in three stages, i.e., sampling of random variables, numerical experimentation, and statistical analysis, for random variables $X = (X_1, X_2, \dots, X_n)$ and a probability performance function $Y = g(X)$.

In the statistical analysis stage, the probability performance function, Y , is calculated as many times as the sampling frequency, N , to perform reliability analysis by calculating the mean \bar{Y} , variance σ_Y^2 , and probability of failure p_f , as follows:

$$\bar{Y} = \frac{1}{N} \sum_{i=1}^N y_i \quad (1)$$

$$\sigma_Y^2 = \frac{1}{N-1} \sum_{i=1}^N (y_i - \bar{Y})^2$$

$$p_f = P(g \leq 0) = \int \dots \int_{g(x) \leq 0} f_{X_1, X_2, \dots, X_n}(x_1, x_2, \dots, x_n) dx_1 dx_2 \dots dx_n \\ = \int_{g(x) \leq 0} f_X(x) dx$$

where $X = (X_1, X_2, \dots, X_n)$ and $x = (x_1, x_2, \dots, x_n)$

The probability of failure, p_f , in Eq. (1) can be expressed using an indicator function, $I(x)$, as follows:

$$p_f = \int_{-\infty}^{+\infty} I(x) f_X(x) dx \quad (2)$$

where $I(x) = \begin{cases} 1 & \text{if } g(x) \leq 0 \\ 0 & \text{otherwise} \end{cases}$

The probability of failure is arranged as follows using the mean value of the indicator function:

$$p_f = \bar{I}(x) = \frac{1}{N} \sum_{i=1}^N I(x_i) = \frac{N_f}{N} \quad (3)$$

Here, N_f is the sampling frequency when $g \leq 0$. The probability of reliability, R , is defined as follows:

$$R = P\{g > 0\} = 1 - p_f = \frac{N - N_f}{N} \quad (4)$$

The probability of failure is obtained in terms of a cumulative distribution function (CDF), $F_Y(y)$, and a probability density function (PDF), $f_Y(y)$, as shown below:

$$F_Y(y) = P(g \leq y) = \frac{1}{N} \sum_{i=1}^N I(y_i) \quad (5)$$

$$\text{where } I(x) = \begin{cases} 1 & \text{if } g(x) \leq y \\ 0 & \text{otherwise} \end{cases}$$

$$f_Y(y) = [F_Y(y)]'$$

As shown in Eq. (5), the PDF is a differential of the CDF. The accuracy of the MCS can be assessed as a function of error rate, e , based on the 95% confidence level as follows:

$$e [\%] \approx 200 \sqrt{\frac{(1 - p_f)}{N p_f}} \quad (6)$$

As shown in Eq. (6), once the target probability of failure and error rate are defined, the sampling frequency required for the reliability analysis can be determined. The accuracy of the probability of failure evaluated in the MCS may be improved if the sampling frequency requirement is satisfied; however, the sampling frequency should be determined based on the characteristics of the analysis subject and the efficiency of numerical calculations in engineering design.

2.2 SSM

SSM is a quasi-MCS method designed to allow a consistent sampling with a low sampling frequency of multidimensional variables in a design space (Sobol & Levitan, 1999; Saltelli et al., 2010). In the SSM, a sampling position is selected based on the previous sampling point, thereby minimizing the gap with a cluster. A Sobol sequence is generated from a combination of binary fractions with a length of w beats and the direction numbers of v_i^j , [$i = 1, 2, \dots, w$; $j = 1, 2, \dots, d$]. To generate directional numbers in the j dimension, the following primitive and recursive polynomials of directional numbers are defined:

$$p_j(x) = x^q + a_1 x^{q-1} + \dots + a_{q-1} x + 1 \quad (7)$$

$$v_i^j = a_1 v_{i-1}^j \oplus a_2 v_{i-2}^j \oplus \dots \oplus a_{q-1} v_{i-q+1}^j \oplus v_{i-q}^j \oplus (v_{i-q}^j / 2^q)$$

where $i > q$

In Eq. 7, \oplus refers to the XOR bitwise operation. The Sobol sequence of the j dimension, $x_q^j = \sum_{i=0}^w b_i 2^i$, $b_i \in \{0, 1\}$, is generated

using primitive polynomials at each dimension, as follows:

$$x_n^i = b_1 v_1^i \oplus b_2 v_2^i \oplus \dots \oplus b_w v_w^i \quad (8)$$

The sampling frequency, N_T , required in the SSM is defined as follows:

$$N_T = N_S(m+1) \quad (9)$$

where $N_S = 2^k$, $k = 1, 2, 3, \dots$

m in Eq. (9) refers to the number of random variables. The sampling frequency in the SSM is not fixed and should be determined based on the complexity of the analysis subject and the number of random variables.

2.3 Kriging Metamodel

Because metamodels are generated from the sampled data in the experimental planning or design space, the accuracy of the generated metamodels can be quantitatively reviewed to verify the approximation of the design space based on the sampling method (Lee & Song, 2013). Creating a highly accurate metamodel is one of the most important tasks in the exploratory research of the design space as it can significantly reduce the numerical inefficiencies by utilizing it for multipurpose or reliability-based design optimizations that involve a high number of calculation iterations.

A Kriging model is expressed as the sum of the global model of the actual design space function to be approximated and the local model that corresponds to the difference between the actual function and the global model (Cho et al., 2009).

$$\tilde{g}(x)_K = Z(x)^T A_K + E(x) \quad (10)$$

Here, $A_K = \{a_1, a_2, \dots, a_p\}^T$ is an unknown coefficient vector, and $Z(x) = \{z_1(x), z_2(x), \dots, z_p(x)\}^T$ is a global model vector defined with a design variable, $x \in E^{n_d}$. The global model can be defined as $p=1$ in a constant case, $p=n_d+1$ in a linear case, and $p=(n_d+1)(n_d+2)/2$ in a second-order polynomial case. $E(x)$ represents an independent normal distribution, and the response vector obtained from n experimental positions is defined as follows:

$$g = [g(x^1), g(x^2), \dots, g(x^n)]^T \quad (11)$$

$E(x)$ is a spatial correlation of the design data and is generally defined as a Gaussian correlation function, expressed as follows:

$$E(\theta, x^i, x^j) = \exp\left[-\sum_{k=1}^{n_d} \theta_k (x^i - x^j)^2\right] \quad (12)$$

Here, $\theta, x \in E^{n_d}$ and the correlation matrix is a positive definite matrix

with diagonal elements of 1. The correlation coefficient, θ_k , is a parameter that expresses the correlation of the response values in the x_k -direction and determines the curvature of the Kriging model in the x_k -direction. The correlation decreases with increasing θ_k , as shown in Eq. (12), and the approximation of the Kriging metamodel in the direction of the input variables shows nonlinear characteristics. The correlation becomes more evident with decreasing θ_k , as shown in Eq. (12), and the approximation of the Kriging metamodel in the direction of the input variables shows linear characteristics. The correlation coefficient, θ , with the highest probability can be calculated through the maximum likelihood estimation, which maximizes the likelihood function.

3. Review of Reliability Analysis

3.1 Evaluation of AOSC Strength Performance

The system configuration of the entire AOSC and the thickness of the major structural components for FEM modeling are shown in Fig. 2. As shown in Fig. 2(a), the AOSC has a salt collector and a towing unit system for automatic salt collection; a drive and power system for delivering electric drive power; a rail frame for transferring collected

salt; and a collector frame, rail frame, and a main frame for the system installation and load support. As shown in the FEM analysis model in Fig. 2(b), the main frame structure was created as a shell element, the weight of each system was realized as a lumped mass, and the rigid link element was used to connect each structural component and apply the lumped mass and design load. The thicknesses of the main frame, rail frame, collector frame, and bracket were designed to be 6.0, 1.0–3.0, 1.0, and 4.0 mm, respectively. The FEM model contained 112,896 elements and 114,431 nodes with the following material properties applied: a density of 8,000 kg/m³, elastic modulus of 193 GPa, the Poisson's ratio of 0.29, and a yield strength of 216 MPa, as in austenitic stainless steel (SUS316).

During the initial design phase, the design load conditions for the AOSC strength performance evaluation were determined by combining the system weight and operating load to reflect the worst-case scenario and by selecting the maximum loading conditions as well as the operating and braking conditions under the maximum load, as listed in Table 1. The inertial load in the direction of gravity, the acceleration of operating conditions in the transfer direction, and the acceleration of the braking conditions in the opposite direction of transfer were applied. The design load conditions listed in Table 1 were applied in the FEM analysis, and all degrees of freedom were

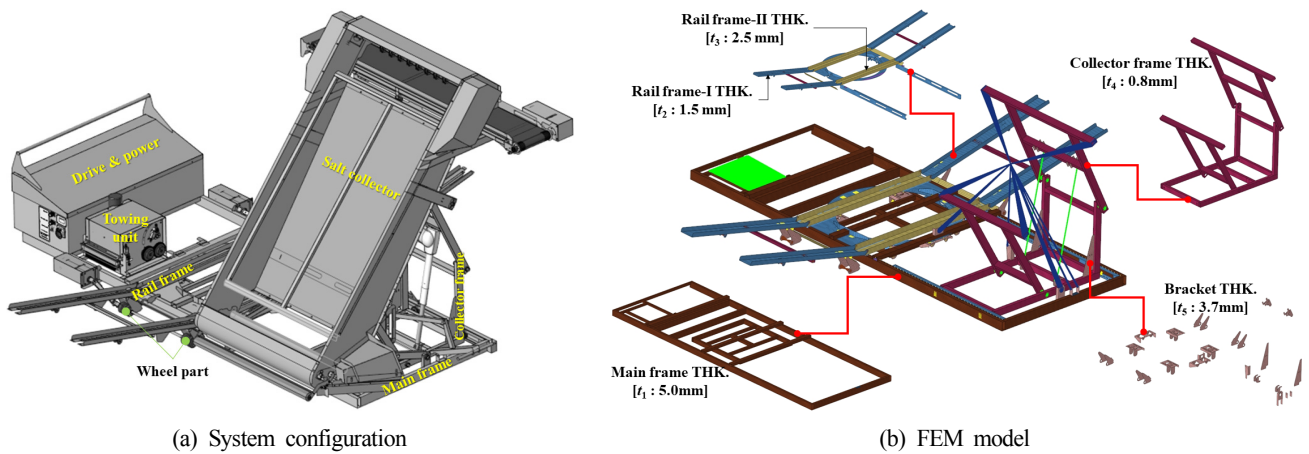


Fig. 2 System configuration and structure analysis model

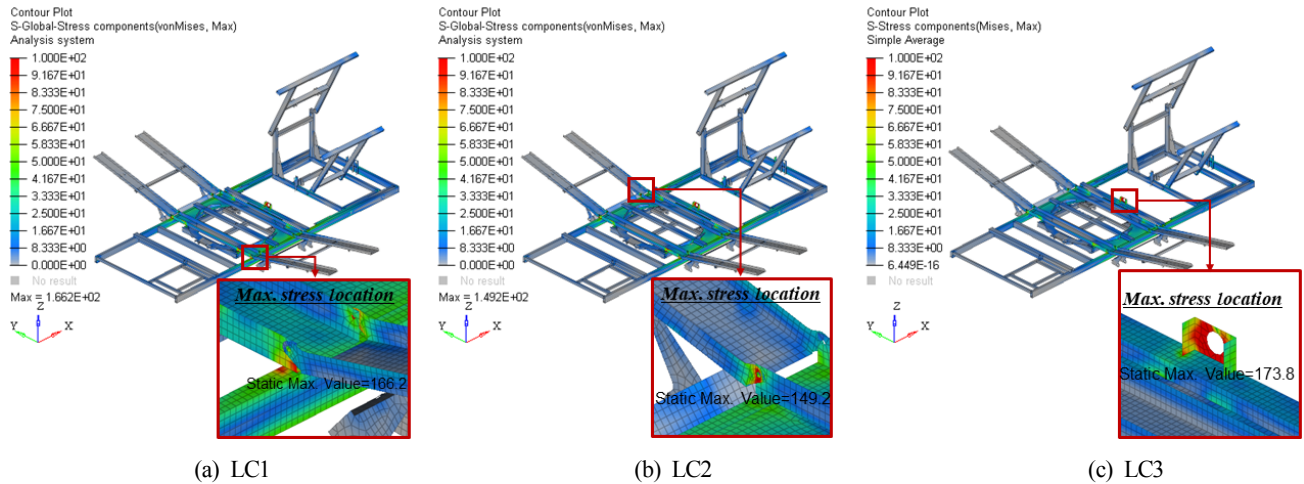
Table 1 Design load cases

Design loads	Load cases		
	Loading [LC1]	Operating [LC2]	Braking [LC3]
Salt collector weight (0.2 t)	✓	✓	✓
Drive & power part weight (0.23 t)	✓	✓	✓
Towing part weight (0.07 t)	✓	✓	✓
Wheel part weight (0.03 t)	✓	✓	✓
Inertial load (1.0 G ¹)	✓	✓	✓
Max. salt collecting capacity (0.7 t)	✓	✓	✓
Max. towing capacity (490 N)	-	✓	-
Acceleration at operating (1.25 G)	-	✓	-
Acceleration at braking (-1.25 G)	-	-	✓

¹G (gravitaional acceleration): 9.8 m/s²

Table 2 Structure analysis results

Structure part	Max. von-Mises stress (MPa)			Safety check
	LC1	LC2	LC3	
Overall structure	166.2	149.2	173.8	OK
Main frame	166.2	142.0	164.2	OK
Rail frame	151.7	149.2	155.5	OK
Collector frame	51.0	55.4	54.1	OK
Bracket	159.9	139.7	173.8	OK

**Fig. 3** Stress contour results (unit: MPa)

restricted for the boundary conditions, except for the degree of freedom associated with the rotation of each wheel mounted at the bottom of the rail. As shown in Table 2, the general-purpose finite element analysis program, Abaqus/Implicit (Simulia, 2018), was used in the FEM analysis to calculate the maximum von Mises stress for each design load condition and evaluate the structural safety based on the yield stress of the material. The structure was considered to be safe if the maximum stress under each design load condition was less than 85% of the yield stress, or 183 MPa (DNV-GL, 2015). As outlined in Table 2, the structural safety was adequate in all of the design load conditions, with the highest stress of 173.8 MPa occurring at the bracket part in LC3. The structural components with the highest stress were the main frame part in LC1, rail frame part in LC2, and bracket part in LC3, whereas the collector frame part in all of the load conditions indicated the lowest stress level.

The stress distribution result for each design load condition is shown in Fig. 3. The maximum stress in LC1 occurred at the main frame part connected to the rail frame, the maximum stress in LC2 was at the rail

frame connection, and the maximum stress in LC3 was at the center of the bracket. The maximum stress occurred at the center of the bracket part in LC3 because the weight of the salt collector part and the weight of the collected salt concentrated at the center, resulting in a high level of load under the braking conditions. Whereas the strength performance of the AOSC structural design satisfied the structural safety standard, a safety margin of less than 5% before reaching the performance limit was indicated in LC3; therefore, a quantitative reliability review is necessary to address uncertainties in the design factors.

3.2 Reliability Analysis of AOSC Structural Design

Unlike marine structures that have design regulations regarding corrosion allowance, an AOSC is a fishery equipment with insufficient design regulations. Because AOSCs are used in marine salt ponds and their material thickness is the design factor, corrosion can be considered as a key uncertainty. Therefore, in the reliability evaluation of AOSCs, the thickness of the major structural components was set as

Table 3 Random variables

Random variable	RSD	Distribution type	Design variable	Mean
X_1	10 %	Normal	Main frame (t_1)	5.0 mm
X_2	10 %	Normal	Rail frame-I (t_2)	1.5 mm
X_3	10 %	Normal	Main frame-II (t_3)	2.5 mm
X_4	10 %	Normal	Collector frame (t_4)	0.8 mm
X_5	10 %	Normal	Bracket (t_5)	3.7 mm

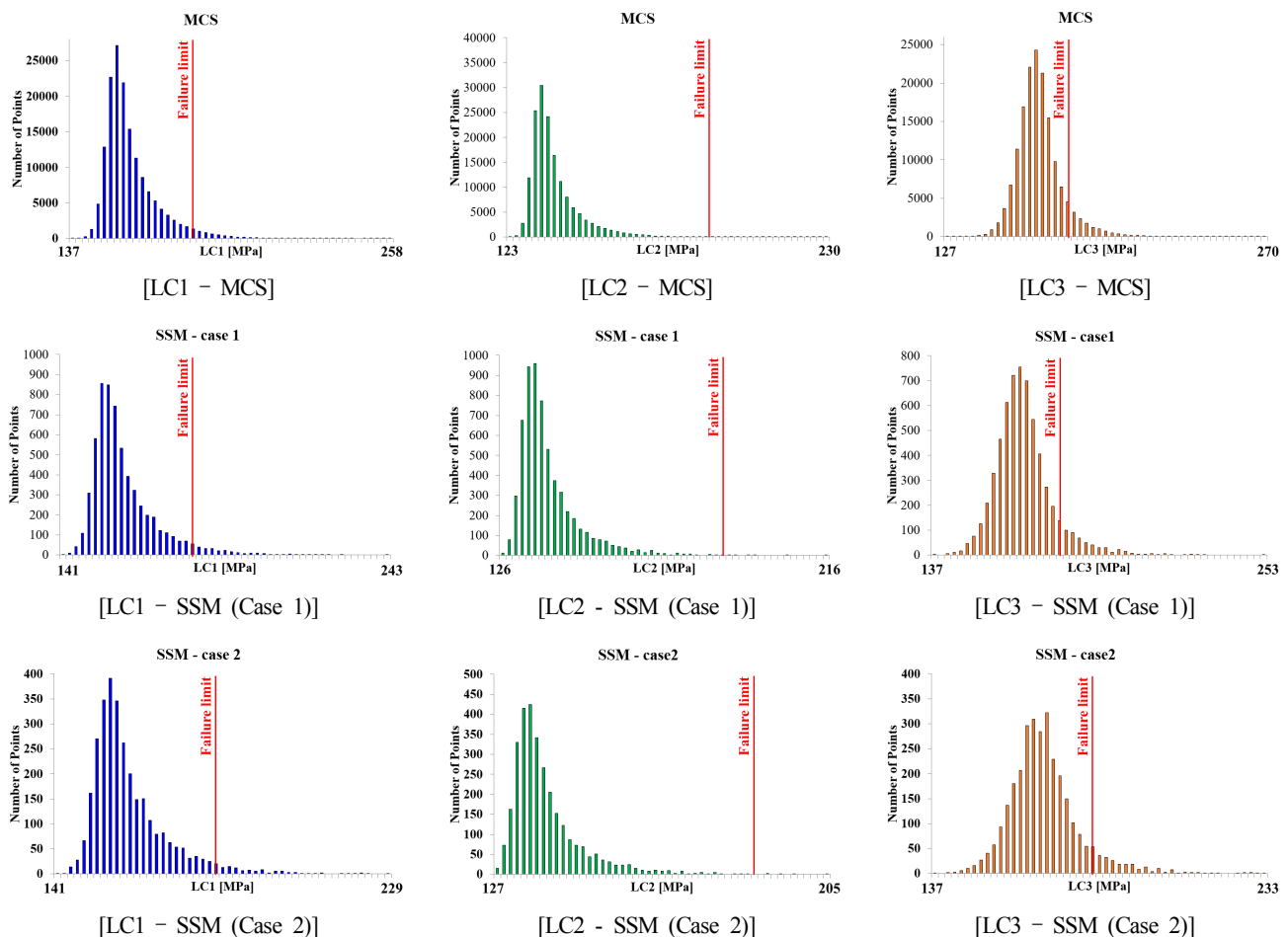
Table 4 Comparison of reliability analysis results

Sampling method	# of sampling	Probability of reliability (≤ 183 MPa)			
		LC1	LC2	LC3	
MCS	158,400	96.1 %	99.7 %	91.9 %	
Case 1	6,144	96.1 %	99.7 %	91.9 %	
Case 2	3,072	96.1 %	99.7 %	92.0 %	
Case 3	1,536	96.1 %	99.7 %	91.9 %	
SSM	Case 4	768	96.3 %	99.9 %	92.3 %
Case 5	384	96.5 %	99.9 %	92.4 %	
Case 6	192	96.9 %	100 %	92.5 %	
Case 7	96	97.9 %	100 %	92.9 %	

a random variable to account for corrosions that may be caused by the nature of the work environment, whereas the strength performance was considered as a probability performance function. To address the uncertainty around the thickness of the structural components as a random variable, the mean was set to the initial design thickness, and the relative standard deviation (RSD) was set as 10% based on the experimental study results pertaining to the corrosion properties of austenitic stainless steel (Han and Park, 2012); furthermore, they were defined to follow a normal distribution because the variability in the strength performance with corrosion was reviewed for a normal

operation of the AOSC in this study. The settings of the random variables used in the reliability analysis are listed in Table 3.

In this study, the limit of the strength performance as a probability performance function was set to be 183 MPa, which is the standard for structural safety, whereas the reliability of the structural design was evaluated based on a probability of failure, p_f , of 0.01. Reliability analysis was performed based on the MCS and SSM. The sampling frequency in the MCS was set to 158,400 based on Eq. (6) with a 95% confidence level and an error rate of 5%. The frequency of sampling in the SSM was varied sequentially by changing the constant k in Eq. (9)


Fig. 4 Comparison of PDF results (continuation)

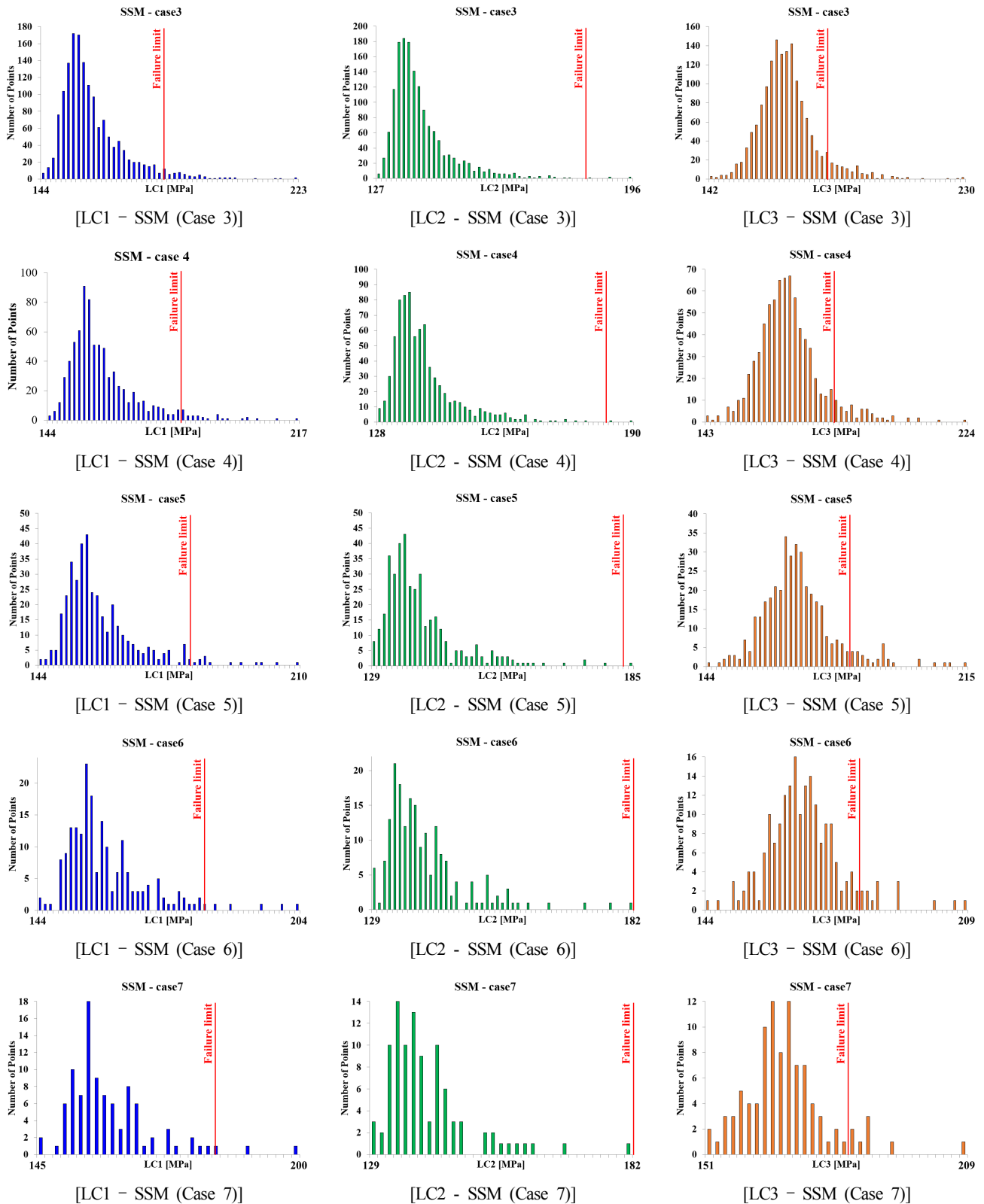


Fig. 4 Comparison of PDF results

from 10 to 4, for the following seven cases: 6,144 (Case 1), 3,072 (Case 2), 1,536 (Case 3), 768 (Case 4), 384 (Case 5), 192 (Case 6), and 96 (Case 7). The results of reliability analysis based on the MCS and SSM with varying sampling frequency are presented in Table 4, and the PDF results from the reliability evaluation of the strength

performance in each case are illustrated in Fig. 4.

As shown in Table 4, similar probabilities of reliability were calculated from Cases 1 to 3 when using the SSM and MCS. Furthermore, the PDF results from Cases 1 to 3 based on the SSM and MCS were similar, as shown in Fig. 4. However, the probability of

Table 5 Comparison of Kriging meta-modeling results

Sampling method	# of sampling	R^2 value		
		LC1	LC2	LC3
MCS	158,400	0.995	0.994	0.995
Case 1	6,144	0.947	0.942	0.941
Case 2	3,072	0.940	0.939	0.947
Case 3	1,536	0.930	0.933	0.934
SSM	768	0.921	0.913	0.924
Case 4	768	0.921	0.913	0.924
Case 5	384	0.907	0.902	0.911
Case 6	192	0.852	0.871	0.863
Case 7	96	0.826	0.835	0.817

reliability of Cases 4 through 7 when using the SSM reduced in proportion to the decrease in the sampling frequency, whereas the probability of reliability tended to be higher than based on the MCS, which can be considered as an indicator of reduced design safety. Additionally, the differences in the PDF results of Cases 4 through 7 obtained using the SSM compared with those obtained using the MCS increased significantly with decreasing sampling frequency. To apply the SSM in the reliability estimation of the AOSC's structural design addressed in this study, it was discovered that at least 1% of the sampling frequency used in the MCS would be required. Therefore, the efficiency of numerical calculations in the SSM-based reliability analysis was high, and the analysis method would be effective for evaluating the structural design safety of fishery equipment, such as AOSCs.

3.3 Comparison of Kriging Metamodeling Characteristics

In this study, a Kriging metamodel was created for each sampling method used for the reliability analysis of the AOSC, and the correlation between the sampling method characteristics and metamodels was reviewed by analyzing the accuracy of the result in each metamodel. Because a Kriging metamodel can approximate multiple design variables and highly nonlinear problems in the design space by incorporating random sampling, Kriging metamodeling was applied to the data used in the random sampling methods, i.e., MCS and SSM (Cho et al., 2009). The accuracy in the design space exploration of the Kriging metal model created for each strength performance response in the design load conditions, i.e., LC1 through LC3, was reviewed based on each of the sampling methods used in the MCS and SSM for reliability analysis. The accuracy of the metamodel approximation was determined in terms of R^2 , as shown in the following equation:

$$R^2 = 1 - \frac{\sum (t_i - y_i)^2}{\sum (t_i - \bar{t}_i)^2} \quad (13)$$

Here, t_i is an actual value, y_i is a predicted value in the approximation model, and \bar{t}_i is the mean of the actual values. An R^2

value of 1.0 indicates that the predicted values from the metamodel correspond exactly to the actual values in the entire design space. The accuracy of the Kriging metamodel result for each sampling method is summarized in Table 5. As shown in Table 5, the design space can be approximated with a 0.5% error rate in the MCS with a sampling frequency of 158,400 times, whereas the approximation accuracies from Cases 1 to 3 in the SSM were similar with 5% to 6% higher error rates than those in the MCS. The approximation accuracies of Cases 4 and 5 in the SSM with sampling frequencies of 768 and 384, respectively, tended to exhibit higher error rates of 7 to 9% than in the MCS, respectively. In Cases 6 and 7 with a sampling frequency of 192 or less, the approximation accuracy reduced significantly and was considered to be unsuitable for a metamodel. Although the correlation between the sampling frequency and the accuracy of the Kriging metamodel appeared to be proportional in general, a certain level of sampling frequency would be required to ensure an equivalent level of accuracy in Kriging metamodels, as demonstrated in Cases 1 through 3 in the SSM. Furthermore, as shown in the reliability analysis results in Table 4 and Fig. 4, the SSM incorporating more than 1% of the sampling frequency of the MCS is applicable not only to the reliability analysis, but also to the Kriging metamodeling of the structural design of fishery equipment, such as AOSCs.

4. Conclusions

In this study, reliability analysis was performed by applying a general MCS and the SSM, i.e., a type of quasi-MCS, to derive efficient reliability evaluation methods to ensure the structural design safety of AOSCs. Furthermore, the probability of failure and the accuracy of metamodeling were compared for various sampling frequencies. The key findings of this study are summarized as follows:

(1) The strength performance of the AOSC was evaluated by determining the design load conditions reflecting the actual operating conditions and applying them in a finite element model to calculate the maximum stress under each design load condition. Although the result from the strength performance evaluation satisfied the structural safety standard, a quantitative review of reliability was necessary to address the uncertainties in the design factors because the safety margin of the

strength performance was small.

(2) The thickness of the major structural components of the AOSC was selected as a random variable for reliability analysis, and the strength performance for each design load condition was considered as a probability performance function. Through this reliability analysis, the probability of failure, probability performance function distribution, and efficiency of numerical calculations based on the sampling method were verified by varying the sampling frequency in the SSM and comparing the results to the MCS with a sampling frequency that estimated the reliability with a confidence level of 95% and an error rate of 5%.

(3) To apply the SSM in the structural design of AOSCs, a sampling frequency equivalent to at least 1% of the MCS sampling frequency would be required to achieve the same probability of reliability and PDF results as those of the general MCS method.

(4) Kriging metamodels suitable for the approximation of random sampling data were applied to review the correlation between the characteristics of the design space approximation and the sampling methods as well as to compare the approximation accuracy. Although the correlation between the accuracy of the Kriging metamodels and the sampling frequency was discovered to be proportional in general, the sampling frequency in the SSM should be at least 1% of the MCS sampling frequency to achieve the same level of accuracy as the Kriging metamodels.

(5) Because the SSM is highly efficient for numerical calculations, it is applicable to the reliability analysis of the structural design of fishery equipment, such as AOSCs, as well as to Kriging metamodeling. The results from this study regarding the sampling method requirements for an effective reliability analysis based on the SSM and Kriging metamodeling will be useful for the reliability analysis of other similar fishery equipment using the SSM.

Acknowledgments

This study was conducted with the support of the National Research Foundation of the Korea Onsite Customized Science and Engineering Talent Cultivation Support Program (No.2019H1D8A1105567) and was supported by the Research Funds of MNU Innovative Programs for University in 2020.

References

- Bai, Y., Tang, J., Xu, W. & Ruan, W. (2015). Reliability-based Design of Subsea Light Weight Pipeline Against Lateral Stability. *Marine Structures*, 43(1), 107-124. <https://doi.org/10.1016/j.marstruc.2015.06.002>
- Cho, S.K., Byun, H. & Lee, T.H. (2009). Selection Method of Global Model And Correlation Coefficients for Kriging Metamodel, *Transactions of the Korean Society of Mechanical Engineers-A*,

- 33(8), 813-818. <https://doi.org/10.3795/KSME-A.2009.33.8.813>
- DNV-GL. (2015). *Structural Design of Offshore Units - WSD Method (DNVGL-OS-C201)*. Det Norske Veritas AS.
- Han, J.W., & Park, Y.S. (2012). Evaluation of Corrosion Characteristics of Pipeline Material (SUS316) for the Geothermal Power Plant. *Korean Journal of Air-Conditioning and Refrigeration Engineering*, 24(2), 142-146. <https://doi.org/10.6110/KJACR.2012.24.2.142>
- Korea Maritime Institute (KMI). (2019). *KMI Trend Analysis*. 161, Seoul.
- Lee, O.S. & Kim, D.H. (2006). The Reliability Estimation of Pipeline Using FORM, SORM and Monte Carlo Simulation with FAD. *Journal of Mechanical Science and Technology*, 20(12), 2124-2135. <https://doi.org/10.1007/BF02916329>
- Lee, C.H. & Kim, Y. (2017). Reliability-based Flaw Assessment of a Mooring Chain Using FORM and SORM. *Journal of the Society of Naval Architects of Korea*, 54(5), 430-438. <https://doi.org/10.3744/SNAK.2017.54.5.430>
- Lee, J., & Song, C.Y. (2013). Estimation of Submerged-arc Welding Design Parameters Using Taguchi Method and Fuzzy Logic. *Proceedings of the Institution of Mechanical Engineers, Part B: Journal of Engineering Manufacture*, 227(4), 532-542. <https://doi.org/10.1177/0954405413476487>
- Saltelli, A., Annoni, P., Azzini, I., Campolongo, F., Ratto, M. & Tarantola, S. (2010). Variance Based Sensitivity Analysis of Model Output. Design and Estimator for the Total Sensitivity Index. *Computer Physics Communications*, 181(2), 259-270. <https://doi.org/10.1016/j.cpc.2009.09.018>
- Siddall, J.N. (1983). *Probabilistic Engineering Design*. Marcel Dekker Inc., New York. <https://doi.org/10.1115/1.3269441>
- Simulia. (2018). *Abaqus User Manual*. Simulia.
- Sobol, I.M. & Levitan, Y.L. (1999). A Pseudorandom Number Generator for Personal Computers. *Computers & Mathematics with Applications*, 37(4-5), 33-40. [https://doi.org/10.1016/S0898-1221\(99\)00057-7](https://doi.org/10.1016/S0898-1221(99)00057-7)
- Song, C.Y., Lee, J., & Choung, J. (2011). Reliability-based Design Optimization of an FPSO Riser Support Using Moving Least Squares Response Surface Meta-models. *Ocean Engineering*, 38(1), 304-318. <https://doi.org/10.1016/j.oceaneng.2010.11.001>
- Yin, F., Nie, S., Ji, H., & Huang, Y. (2018). Non-probabilistic Reliability Analysis and Design Pptimization for Valve-port Plate Pair of Seawater Hydraulic Pump for Underwater Apparatus. *Ocean Engineering*, 163(1), 337-347. <https://doi.org/10.1016/j.oceaneng.2018.06.007>

Author ORCIDs

Author name	ORCID
Song, Chang Yong	0000-0002-1098-4205

Study on Vortex-Induced Vibration Predictions for Ship Rudders

Won-Seok Jang¹, Suk-Yoon Hong², Jee-Hun Song³, Hyun-Wung Kwon⁴ and Woen-Sug Choi⁵

¹Graduate Student, Department of Naval Architecture and Ocean Engineering, Seoul National University, Seoul, Korea

²Professor, Department of Naval Architecture and Ocean Engineering, Seoul National University, Seoul, Korea

³Professor, Department of Naval Architecture and Ocean Engineering, Chonnam National University, Yeosu, Korea

⁴Professor, Department of Shipbuilding and Marine Engineering, Koje College, Koje, Korea

⁵Postdoctoral Researcher, Department of Naval Architecture and Ocean Engineering, Seoul National University, Seoul, Korea

KEY WORDS: Fluid-structure interaction, Vortex-induced vibration, Hydroelasticity, Hydrofoil, Lock-in, Resonance

ABSTRACT: As regulations concerning ship vibration and noise are becoming stricter, considerable attention is being drawn to prediction technologies for ship vibration and noise. In particular, the resonance and lock-in phenomena caused by vortex-induced vibration (VIV) have become considerably important with increases in the speed and the size of ships and ocean structures, which are known to cause structural problems. This study extends the fluid-structure interaction (FSI) analysis method to predict resonances and lock-in phenomena of high modes and VIV of ship rudders. Numerical stability is secured in underwater conditions by implementing added mass, added damping, and added stiffness by applying the potential theory to structural analysis. An expanded governing equation is developed by implementing displacements and twist angles of high modes. The lock-in velocity range and resonant frequencies of ship rudders obtained using the developed FSI method agree well with the experimental results and the analytic solution. A comparison with local vibration guidelines published by Lloyd's Register shows that predictions of resonances and lock-in phenomena of high modes are necessary in the shipbuilding industry due to the possible risks like fatigue failure.

1. Introduction

As the regulations related to ship vibration and noise have recently become stricter, prediction technology for ship vibration and noise has become important. In particular, with an increase in the risk of vortex-induced vibration (VIV) arising from the growing trend of building large and high-speed ships, various studies are actively being conducted to address this issue. VIV refers to the structural vibration caused by the periodic vortex shedding in the wake of the bluff body. It mainly occurs in ship rudders and propellers, as well as in submarine sails. Structural problems caused by VIV also occur in offshore risers (Jung et al., 2019; Son et al., 2019).

When the vortex shedding frequency approaches the structure's natural frequency, resonance occurs in which the structure vibrates severely into the natural frequency component. At the same time, lock-in occurs in which the vortex shedding frequency shifts to the natural frequency due to the structure's resonance. As the amplitude of VIV is highest when resonance and lock-in occurs, the prediction and control of VIV is essential in cases of resonance and lock-in phenomena in terms of the ship's structural stability.

To predict VIV, there are methods for conducting experiments by building a model ship and performing analytical fluid-structure interaction (FSI) analysis. FSI analysis is an analysis methodology that obtains the response of a structure (fluid) by a fluid (structure). Research on FSI analysis has been actively carried out since 1970 (Felippa et al, 2001). FSI analysis can largely be classified into the monolithic method and the partitioned method. In the monolithic method, fluid and structure calculations are performed using a single matrix equation. This method has the advantage of being mathematically rigorous; however, it has a disadvantage in that the complexity of the analysis becomes high because of the large-scale system. In the partitioned method, fluid and structure calculations are performed using separate governing equations, and then the two results are integrated through boundary conditions at every time step. It is an analysis method that is easy to develop because it utilizes currently available computational fluid dynamics (CFD) and structural analysis programs, although it is less mathematically rigorous than the monolithic method. The partitioned method is classified into a tight (or strong) coupling method and a loose (or weak) coupling method. The tight-coupling method determines the degree of convergence of the

Received 19 July 2020, revised 22 August 2020, accepted 25 August 2020

Corresponding author Jee-Hun Song: +82-61-659-7156, jhs@jnu.ac.kr

© 2020, The Korean Society of Ocean Engineers

This is an open access article distributed under the terms of the creative commons attribution non-commercial license (<http://creativecommons.org/licenses/by-nc/4.0>) which permits unrestricted non-commercial use, distribution, and reproduction in any medium, provided the original work is properly cited.

results within one time step and performs subiterations. It has the advantage of high accuracy, but has the disadvantage of high computational cost. The loose-coupling method performs only one CFD analysis and one structural analysis within one time step without the subiteration process. It has the advantage of low computational cost but has the disadvantage of relatively low accuracy. In particular, FSI analysis based on the loose-coupling method has limitations in an underwater environment where the added mass effect is strong.

Campbell (2010) and Lee (2014) performed a 3D FSI analysis using the tight-coupling method for a hydrofoil and derived analysis results that favorably matched the experimental results. However, to predict the VIV of various ship rudders at design stage, there is a need for an FSI analysis method that can sufficiently reflect the added mass effect of an underwater environment while lowering the computational cost. By applying the empirical equation for the fluid force developed by Munch et al. (2010) to the aeroelastic analysis model used to predict the flutter of aircraft wings, Young et al. (2012) developed a hybrid algorithm, which is an FSI analysis algorithm that considers the fluid added mass. They predicted vortex-induced twisting vibration of the hydrofoil using this algorithm. In particular, by performing analysis of the hydrofoil model, which the fluid added mass has a significant impact on, they verified the effectiveness of the hybrid algorithm compared with the tight-coupling and loose-coupling methods in terms of convergence and accuracy. Chae (2015) established the bend-twist (BT) FSI analysis procedure by integrating the hybrid algorithm with CFD and verified the analysis results of the NACA0015 hydrofoil using the experimental results. The BT FSI analysis has a considerable advantage in terms of the computational cost because it uses a 2D CFD analysis without subiterations to obtain the VIV of the hydrofoil with the same wing cross-section in the span direction. However, there is a disadvantage in that it reflects only the effects of the first bending and twisting mode.

In this study, we develop a high-mode BT FSI analysis method by extending the BT FSI analysis method of Chae (2015) to analytically implement the high-mode resonance and lock-in phenomena of ship rudders with low computational cost. We perform a high-mode BT FSI analysis on a hydrofoil, which is similar to the shape of a ship rudder, and predict the VIV for the flow velocity. We verify and analyze vibration by comparing the experimental results, analytic solutions, and analysis results.

2. Background Theory

2.1 Motion Equation for Continuum Structure

A ship rudder is regarded as a continuum with infinite degrees of freedom. Unlike the equation of motion of an object with a finite number of degrees of freedom, the Lagrange equation based on the variational approach is required to derive the equation of motion of a continuum structure. The vibration of a continuum structure for an external force can be obtained using the Lagrange equation as follows:

$$\frac{d}{dt} \left(\frac{\partial T}{\partial \dot{q}_j} \right) - \frac{\partial T}{\partial q_j} + \frac{\partial \Gamma}{\partial \dot{q}_j} + \frac{\partial U}{\partial q_j} = \frac{\partial(\delta W)}{\partial(\delta q_j)} \quad (1)$$

where T , Γ , U , W , and q_j refer to kinetic energy, energy dissipation term, potential energy, work, and the j th degree of freedom displacement function, respectively.

The ship rudder can be assumed as a one-dimensional continuum structure. In addition, as the bending and twisting modes predominantly influence the ship rudder, the deformation z of the structure can be assumed as a function of time t and space x , as follows:

$$z(x, t) = \sum_{j=1}^N S_{fj}(x) d_j(t) + S_{gj} \theta_j(t) \quad (2)$$

where S_{fj} and S_{gj} are the j th mode bending and twisting shape functions, respectively; and d_j and θ_j are the j th mode bending- and twisting-mode coefficients, respectively. When the deformation of the structure is defined in this way, T and U are expressed as follows:

$$T = 0.5 \int_0^s \mu \dot{z}^2 dx \quad (3)$$

$$U = 0.5 \int_0^s EI \left(\frac{\partial^2 z}{\partial x^2} \right)^2 dx \quad (4)$$

where μ , EI and s refer to structural linear density, flexural rigidity, and span length, respectively. When Eqs. (3) and (4) are applied to Eq. (1), the motion equation in the form of a matrix is obtained, as follows:

$$M\ddot{z} + C\dot{z} + Kz = F \quad (5)$$

where M , C , K and F refer to structural mass matrix, structural damping matrix, structural elastic matrix, and external force vector, respectively.

2.2 Fluid Force Induced by Structural Response in Flow Velocity Based on the Potential Method

The fluid force and moment exerted on the vibrating wing cross-section should consider the static fluid force and moment variation according to the angle of attack and the amplitude reduction and phase shift due to unsteadiness. The amplitude reduction and phase shift due to unsteadiness depend on the dimensionless frequency k of the wing cross-section, which is expressed by the Theodorsen function $C(k)$ as

$$C(k) = \frac{H_1^2(k)}{H_1^2(k) + iH_0^2(k)} \quad (6)$$

where $H_1^2(k)$ and $H_0^2(k)$ are the Hankel functions of the second kind.

Theodorsen (1949) derived the fluid force and moment L_T , T_T

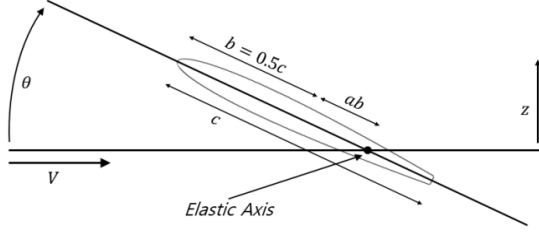


Fig. 1 Two-dimensional hydrofoil

exerted on the thin wing cross-section in flow velocities based on the potential method as follows:

$$L_T = \pi \rho_f b^2 [-\ddot{d} - V\dot{\theta} + ba\ddot{\theta}] - 2\pi \rho V b C(k) [\dot{d} + V\theta + b(0.5 - a)\dot{\theta}] \quad (7)$$

$$T_T = \pi \rho_f b^2 [ba\ddot{d} - Vb(0.5 - a)\dot{\theta} - b^2(0.125 + a^2)\ddot{\theta}] + 2\pi \rho V b^2 (a + 0.5) C(k) [\dot{d} + V\theta + b(0.5 - a)\dot{\theta}] \quad (8)$$

where ρ_f refers to the fluid density; a is the dimensionless distance from the midpoint of the chord to the elastic axis of the wing cross-section; b is half the chord length; and V , d and θ refer to the flow velocity, bending displacement, and twisting angle, respectively. The upward direction of d and L_T is positive, and the counterclockwise direction of θ and T_T is positive. A schematic diagram of a , b , c and V , and the directions of d and θ in the wing cross-section is shown in Fig. 1.

2.3 Governing Equation of BT FSI Analysis

The potential method is based on the assumption of incompressible, inviscid and irrotational condition. In this study, we focused on predicting VIV when vortex shedding occurs in the wake of ship rudders. As vortex shedding occurs due to the viscosity and boundary layer of the fluid, it is theoretically impossible to predict the vortex strength and vortex shedding frequency based on the potential method. Therefore, CFD considering viscosity is essential for deriving the vortex-induced fluid force and moment. Chae (2015) developed a BT FSI analysis method for deriving the VIV of the hydrofoil using CFD. By considering only the first bending- and twisting-mode vibration of the hydrofoil, the bending displacement and twisting angle of the hydrofoil can be assumed, as in Eq. (9).

$$\begin{aligned} d(x, t) &= S_{f1}(x)d_1(t) \\ \theta(x, t) &= S_{g1}(x)\theta_1(t) \end{aligned} \quad (9)$$

The equation of motion Eq. (10) is obtained applying Eq. (9) to the Lagrange equation Eq. (1) described in Section 2.1, as follows:

$$M_s \ddot{z} + C_s \dot{z} + K_s z = F_{CFD} \quad (10)$$

Here,

$$M_s = \mu \begin{bmatrix} S_{ff11} & x_\theta S_{fg11} \\ x_\theta S_{fg11} & r_\theta S_{gg11} \end{bmatrix}$$

$$C_s = \frac{1}{s} \begin{bmatrix} \omega_{b1} \xi S_{ff11} & 0 \\ 0 & r_\theta^2 \omega_{t1} \xi S_{gg11} \end{bmatrix}$$

$$K_s = \begin{bmatrix} EIS_{ff11} & 0 \\ 0 & I_p \omega_{t1}^2 S_{gg11} \end{bmatrix}$$

$$z = \begin{bmatrix} d_1 \\ \theta_1 \end{bmatrix}$$

$$F_{CFD} = \begin{bmatrix} S_{ff11} L_{CFD} \\ S_{gg11} T_{CFD} \end{bmatrix}$$

where x_θ , r_θ , ω_{b1} , ω_{t1} , ξ and I_p refer to the distance from the elastic axis to the center of gravity, the radius of gyration, the first bending-mode natural frequency, the first twisting-mode natural frequency, the damping coefficient, and the polar moment of inertia, respectively; S_{ff11} is the value obtained by integrating the square of the first bending-mode shape function S_{f1} from 0 to s . In the same way, S_{gg11} , S_{ff11} and S_{fg11} are the values obtained by integrating the square of S_{g1} , S_{f1} and $S_{f1}S_{g1}$ from 0 to s , respectively. The loose-coupling method can perform the FSI analysis using Eq. (10) as the governing equation and applying the boundary conditions in Eq. (11) at the fluid-structure boundary interface.

$$\begin{aligned} v^m &= dz/dt \\ \sigma^s \cdot n &= \sigma^f \cdot n \end{aligned} \quad (11)$$

where v^m , σ^s , σ^f and n refer to the mesh movement velocity, structural stress, fluid stress, and normal vector, respectively

F_{CFD} includes the inviscid force $F_T = [S_{ff11}L_T, S_{gg11}T_T]^T$ based on the potential method. When the fluid density is much smaller than the structural density, the effect of the inviscid force of F_{CFD} is inconsiderable. Therefore, it is appropriate to perform the FSI analysis using the loose-coupling method based on Eq. (10). However, in an underwater environment, since the fluid density is quite high, the effect of the inviscid force by the added mass, added damping, and added stiffness is relatively considerable. Therefore, it is inappropriate to use Eq. (10) as the governing equation. Chae (2015) used Eq. (12), where the inviscid force term is excluded on both sides of Eq. (10), as the governing equation for the BT FSI analysis, to reflect the effect of the inviscid force in an underwater environment without subiterations in the partitioned method.

$$(M_s + M_f) \ddot{z} + (C_s + C_f) \dot{z} + (K_s + K_f) z = F_{CFD} - F_T \quad (12)$$

Here,

$$M_f = \pi \rho_f b^2 \begin{bmatrix} S_{ff11} & -abS_{fg11} \\ -abS_{fg11} & b^2(0.125 + a^2)S_{gg11} \end{bmatrix}$$

$$C_f = \pi \rho_f V \begin{bmatrix} 2bCS_{ff11} & b^2(1-fC)S_{fg11} \\ -b^2eCS_{fg11} & 0.5b^3f(eC-1)S_{gg11} \end{bmatrix}$$

$$K_f = \pi \rho_f V^2 \begin{bmatrix} 0 & 2bCS_{fg11} \\ 0 & -b^2eCS_{gg11} \end{bmatrix}$$

where e and f are $2a + 1$ and $2a - 1$, respectively.

2.4 High-mode BT FSI Analysis Governing Equation

While the FSI described in Eq. (12) in the previous section has the advantage of favorably reflecting the effect of the inviscid force by the added mass, etc., without subiteration in an underwater environment, it also has a disadvantage in that it cannot realize resonance and lock-in phenomena caused by high bending- and twisting-mode vibration by taking into account only the first bending- and twisting-mode vibration. Therefore, in this study, we extend the governing equation for the FSI analysis to take into account high bending- and twisting-mode vibration. First, we extend the equation for the bending displacement and twisting angle, yielding

$$\begin{aligned} d(x,t) &= S_{f1}(x)d_1(t) + S_{f2}(z)d_2(t) + \dots \\ \theta(x,t) &= S_{g1}(x)\theta_1(t) + S_{g2}(z)\theta_2(t) + \dots \end{aligned} \quad (13)$$

If the governing equation for FSI analysis that considers high bending- and twisting-mode vibrations is obtained by applying Eq. (13) to Eq. (1) and Eqs. (7) – (8), the equation can be written in the form of a matrix equation of size $2n \times 2n$ for the n th mode. The derived matrix equation has regularity; thus, it can be generalized to a matrix pattern of size 2×2 . The governing equation for the FSI analysis is expressed for a relatively simple second mode as follows:

$$(M_s + M_f)\ddot{z} + (C_s + C_f)\dot{z} + (K_s + K_f)z = F_{CFD} - F_T \quad (14)$$

Here,

$$M_s = \begin{bmatrix} M_{s11} & M_{s12} \\ M_{s21} & M_{s22} \end{bmatrix} \quad M_f = \begin{bmatrix} M_{f11} & M_{f12} \\ M_{f21} & M_{f22} \end{bmatrix}$$

$$C_s = \begin{bmatrix} C_{s1} & 0 \\ 0 & C_{s2} \end{bmatrix} \quad C_f = \begin{bmatrix} C_{f11} & C_{f12} \\ C_{f21} & C_{f22} \end{bmatrix}$$

$$K_s = \begin{bmatrix} K_{s11} & K_{s12} \\ K_{s21} & K_{s22} \end{bmatrix} \quad K_f = \begin{bmatrix} K_{f11} & K_{f12} \\ K_{f21} & K_{f22} \end{bmatrix}$$

$$M_{sij} = \mu \begin{bmatrix} S_{ffij} & x_\theta S_{fgij} \\ x_\theta S_{fgij} & r_\theta S_{ggij} \end{bmatrix}$$

$$C_{si} = \frac{1}{s} \begin{bmatrix} \omega_{bi} \xi S_{ffii} & 0 \\ 0 & r_\theta^2 \omega_{ti} \xi S_{ggii} \end{bmatrix}$$

$$K_{sij} = \begin{bmatrix} EIS_{ff11} & 0 \\ 0 & I_p \omega_{t1}^2 S_{gg11} \end{bmatrix}$$

$$M_{fij} = \pi \rho_f b^2 \begin{bmatrix} S_{ffij} & -ab S_{fgij} \\ -ab S_{fgij} & b^2(0.125 + \alpha^2) S_{ggij} \end{bmatrix}$$

$$C_{fij} = \pi \rho_f V \begin{bmatrix} 2bCS_{ffij} & b^2(1-fC)S_{fgij} \\ -b^2eCS_{fgij} & 0.5b^3f(eC-1)S_{ggij} \end{bmatrix}$$

$$K_{fij} = \pi \rho_f V^2 \begin{bmatrix} 0 & 2bCS_{fgij} \\ 0 & -b^2eCS_{ggij} \end{bmatrix}$$

$$F_{CFD} = \begin{bmatrix} F_{CFD1} \\ F_{CFD2} \end{bmatrix} \quad z = \begin{bmatrix} z_1 \\ z_2 \end{bmatrix}$$

$$F_{CFDi} = \begin{bmatrix} S_{ffii} L_{CFD} \\ S_{ggii} T_{CFD} \end{bmatrix} \quad z_i = \begin{bmatrix} d_i \\ \theta_i \end{bmatrix}$$

$$i, j = 1, 2$$

3. High-mode BT FSI Analysis for Ship Rudders

3.1 CFD Analysis of Hydrofoil

In the process of FSI analysis, we performed the CFD analysis of the hydrofoil by first identifying the reliability of the CFD analysis. In this analysis, we used OpenFOAM, an open-source CFD program. The CFD solver is based on the Reynolds-averaged Navier-Stokes (RANS) governing equation. The $k-\omega$ shear stress transport ($k-\omega$ SST) model combining the $k-\omega$ model and the $k-\epsilon$ model was used as the turbulence model (Kim et al., 2017). The detailed analysis settings are listed in Table 1. For comparison with the experimental results, the same cross-section shape as that of the test object of Ausoni (2009) and Zobeiri (2012) was used as the hydrofoil shape for analysis. The wing cross-section shape to be analyzed is shown in Fig. 2. It is the same as NACA0009; however, it is cut so that the end thickness is 3.22% of the chord length. The chord length of the hydrofoil for analysis is 0.1 m. For comparison with the experimental results (Ausoni, 2009; Zobeiri, 2012), we performed the CFD analysis for a total of 17 flow velocities ranging from 10 m/s to 26 m/s at an interval of 1 m/s. Considering the underwater environment, we set the medium density to 1000 kg/m³ and the kinematic viscosity to 1e⁻⁶ m²/s. The analysis domain is a circle with a radius of 20 times the chord length, where the elastic axis of the analysis object is set to be at the origin. The analysis domain and boundary conditions are shown in Fig. 3, and the analysis mesh is shown in Fig. 4. The number of meshes is approximately 100,000, and the dimensionless number y^+ value related to the thickness of the mesh closest to the wall is approximately 1. By assuming a far-field condition, we applied freestream velocity and freestream pressure boundary conditions to the outer boundary of the analysis domain and applied a no-slip boundary condition to the wing surface. We used 5e⁻⁷ s as the time step, so that the maximum value of the Courant-Friedrichs-Lewy (CFL) number related to analysis stability did not exceed 1.

Table 1 Detailed CFD solver setting

Solver platform	OpenFOAM 4.x
Solver	pimpleFoam
Solver algorithm	PIMPLE ¹ algorithm
Turbulence model	RANS, $k-\omega$ SST
Time derivative schemes	Backward (transient, second order implicit)
Gradient schemes	Gauss linear
Velocity FV solver	Symmetric Gauss-Seidel
Pressure FV solver	PCCG ²

¹PIMPLE: PISO (Pressure implicit split operator) + SIMPLE (Semi implicit method for pressure linked equation), ²PCG: Preconditioned conjugate gradient

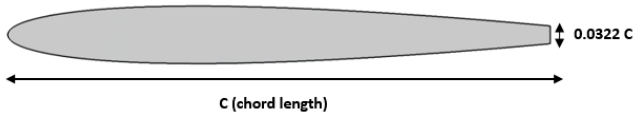


Fig. 2 Hydrofoil section geometry

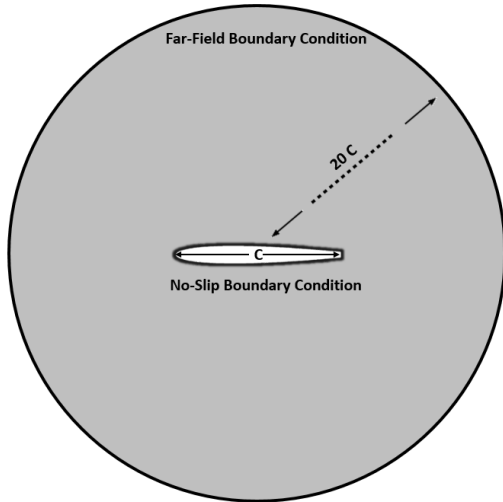


Fig. 3 CFD analysis domain and boundary conditions

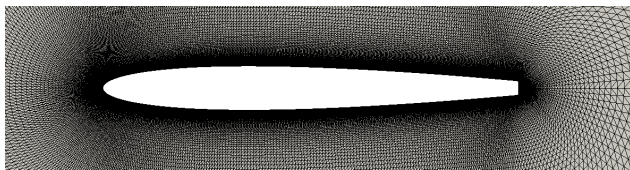


Fig. 4 Mesh domain close to hydrofoil

The CFD analysis result of the flow field around the hydrofoil is shown in Fig. 5, which confirms vortex shedding in the wake. The analysis results of drag and lift coefficients are shown in Fig. 6. Vibration characteristics of one dominant peak component are observed. In particular, the peak frequency of the drag coefficient is twice the peak frequency of the lift coefficient, which is attributed to the characteristics of vortex shedding that occurs alternately on both sides (Blevins, 2001). A comparison of the mean values of the drag and lift coefficients obtained using the experiment and the CFD analysis is shown in Table 2. For the drag coefficient, the analysis results differ from the experimental results by approximately 4% (Zobeiri, 2012); this is attributed to the difference in the 3D effect between the experimental and analysis results (Mittal and Balachandar, 1995). In addition, since this analysis model has a symmetrical shape with an angle of attack of 0° , the lift coefficient was approximately 0 in the experimental and analysis results. The Strouhal number of the hydrofoil for the flow velocity between the experimental and analysis results is shown in Fig. 7. The Strouhal number is a dimensionless number for the vortex shedding frequency f , and is defined as fD/V . Assuming that there is no resonance and lock-in, when D is set as the thickness between separation points, the Strouhal number is approximately 0.2 for a wide range of the Reynolds

number regardless of the cross-section shape (Sarpkaya, 1979). The experimental results (Ausoni, 2009) show that the Strouhal number changes at the flow velocities of 10–14 m/s. This is because the vortex shedding frequency at these flow velocities is close to the structure’s natural frequency, thus causing resonance and lock-in phenomena. At the flow velocity after 14 m/s, the Strouhal number test result shows that it has a constant value of 0.23, and the Strouhal number derived by the CFD analysis (model scale, x) under the same Reynolds number has a constant value of approximately 0.24 in the entire flow velocity range, which is similar to the experimental results. We verified the reliability of this CFD analysis procedure by confirming that the lift coefficient, drag coefficient, and Strouhal number derived by the CFD analysis matches the experimental results.

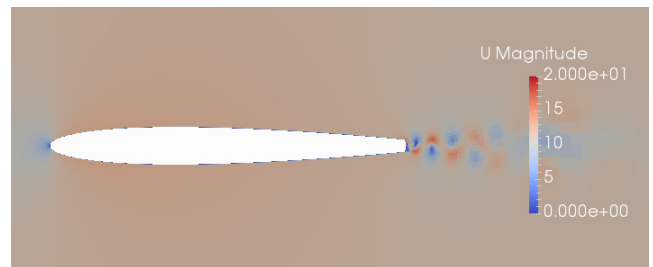
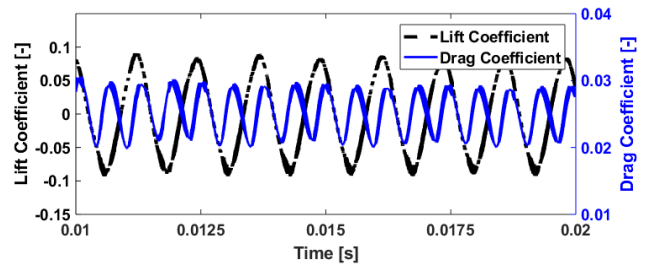
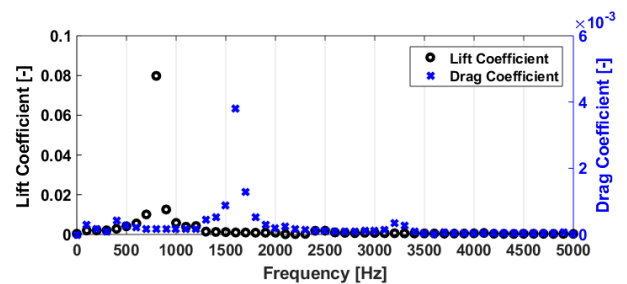


Fig. 5 CFD results of hydrofoil flow field at $Re = 1.1e^6$



(a) Time-domain results



(a) Frequency-domain results

Fig. 6 CFD results of lift and drag coefficient at $Re = 1.1e^6$

Table 2 Comparison of mean value of lift and drag coefficient between CFD and experimental results at $Re = 1.1e^6$

At $Re = 1.1e^6$	Experiment	CFD
Drag Coefficient (C_D)	0.0240	0.0243
Lift Coefficient (C_L)	0	-0.0019

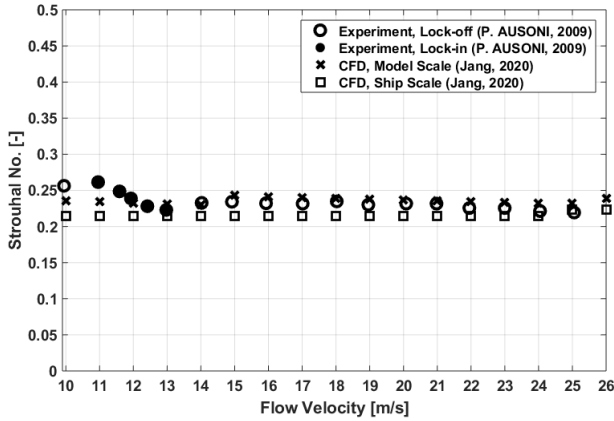


Fig. 7 Comparison of Strouhal number for various flow velocities for CFD results and experimental results

To identify the characteristics of the fluid force frequency of the ship rudder, we performed the CFD analysis for each flow velocity on the model scale shape, enlarged 100 times, and represented the Strouhal number in Fig. 7 (ship scale, square). Despite a 100 times difference in the Reynolds number, the Strouhal number was approximately 0.22 in the entire flow velocity range, which is similar to the experimental and model scale analysis results and also matches Sarpkaya's results (1979).

3.2 High-mode BT FSI Analysis of Hydrofoil

The high-mode BT FSI analysis procedure is shown in Fig. 8. For the CFD analysis, we used OpenFOAM, as in Section 3.1. The pimpleDyMFoam solver suitable for the analysis with mesh movement was used. The detailed analysis settings are listed in Table 3. The equation of motion Eq. (14) was used as the governing equation for the bending-twisting structural analysis.

To simulate the ship rudder, we set the analysis target to the model scale shape, enlarged 100 times, and created the CFD analysis using the same procedure as in Section 3.1. We applied freestream velocity and freestream pressure boundary conditions to the outer boundary of the analysis mesh domain and applied moving wall velocity boundary conditions to the wing surface, which satisfied Eq. (11). We used $2e^{-5}$ s as the time step, so that the maximum value of the CFL number related to analysis stability did not exceed 1.

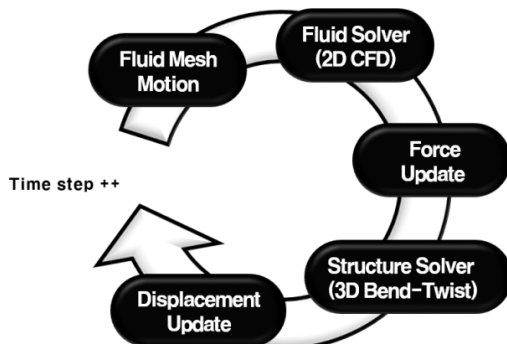


Fig. 8 High-mode BT FSI analysis procedure

Table 3 Detailed CFD solver settings for high-mode BT FSI analysis

Solver platform	OpenFOAM 4.x
Solver	pimpleDyMFoam
Solver algorithm	PIMPLE algorithm
Turbulence model	RANS, $k-\omega$ SST
Time derivative schemes	Euler (transient, first order implicit)
Gradient schemes	Gauss linear
Velocity FV solver	Symmetric Gauss-Seidel
Pressure FV solver	PCG

The structural parameter values required for the FSI analysis are shown in Table 4; ρ_s , EI , ξ , μ , and the center of gravity were derived for the shape, as seen in Fig. 9, and the material properties were derived for the steel structural model. Fixed boundary conditions were applied at the end of the model for the simulation of the ship rudder. The bending-mode natural frequency f_B , and the twisting-mode natural frequency f_T were derived using the 3D finite element method (FEM) to analyze the vibration for the structural model. When the twisting

Table 4 Structural input parameters for second-mode BT FSI analysis

Parameter	Unit	Value
ρ_s	kg/m ³	7800
EI	Nm ²	$988e^8$
ξ	-	0.02
μ	kg/m	64300
Center of gravity	m	4.6642
Elastic axis	m	4.973
f_T	Hz	11.182, 35.00
f_B	Hz	3.1637, 18.94
r_θ	-	2.5718
S_{ff}	m	[3.75, 0.003; 0.003, 3.75]
S_{fg}	m	[5.08, 1.47; -1.45, 4.59]
S_{gg}	m	[7.5, 0; 0, 3.7522]
S_{ff}^{-1}	1/m ³	[$9.16e^{-4}$, $9.36e^{-7}$; $9.36e^{-7}$, 0.036]

S_{ff} , S_{fg} , S_{gg} , S_{ff}^{-1} are 2×2 matrices

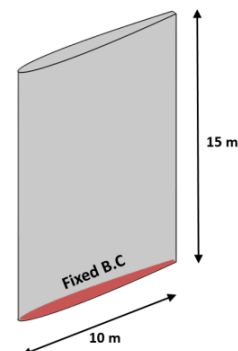


Fig. 9 Rudder model for BT FSI analysis

mode occurs, the position where the deformation was minimal was set as the elastic axis, and r_θ was derived based on this. The values related to the twisting-mode shape function were derived using the Euler-Bernoulli cantilever analytic solution (Abu-Hilal, 2003), and the first and second bending- and twisting-mode shape functions are shown in Fig. 10. It is expected that resonance and lock-in phenomena will occur in the first twisting mode and the second bending mode within the flow velocity range of this analysis; thus, we performed the BT FSI analysis considering the second mode as well.

The vibration displacement and angle derived by the BT FSI analysis at a Reynolds number of 2.3×10^8 are shown in Fig. 11, and periodic vibration is observed in the figure. In particular, peak responses are observed in both the vortex shedding frequency component and the underwater natural frequency component. The VIV frequency for each flow velocity derived by high-mode BT FSI analysis of the hydrofoil is shown in Table 5. Overall, the VIV frequency tends to increase with an increase in the flow velocity. This is because the Strouhal number has a constant value in a wide range of the Reynolds number. We confirmed lock-in phenomena in which the VIV frequency was maintained at a constant value at flow velocities of 13–14 m/s and 23–24 m/s. We obtained the underwater natural frequency for the analysis target using the analytic solution of a cantilever (Ausoni, 2009), and compared this with the lock-in frequencies, as displayed in Table 6. The frequencies favorably matched the first twisting-mode underwater natural frequency and the second bending-mode underwater natural frequency, respectively, which confirm that 13–14 m/s was the first twisting-mode resonance and lock-in region; 23–24 m/s is the second bending-mode resonance and lock-in region. The underwater natural frequency is inversely proportional to the scale and the Strouhal number has a constant value in a wide range of the Reynolds number. Therefore, if the shape is the same, the lock-in velocity at which vortex shedding occurs at the underwater natural frequency, even when the scale is different, is the same as in Eq. 15 (Ausoni, 2009).

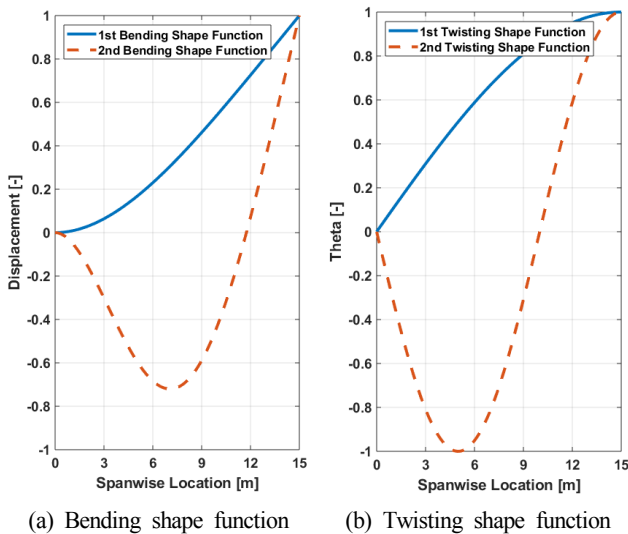
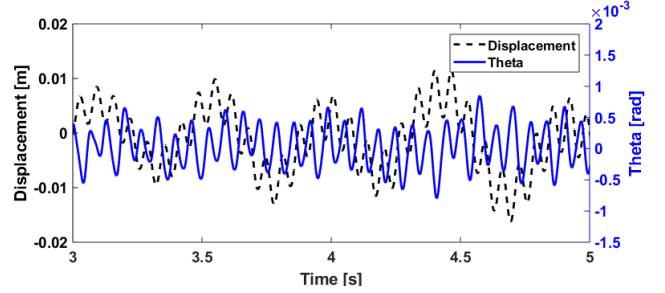


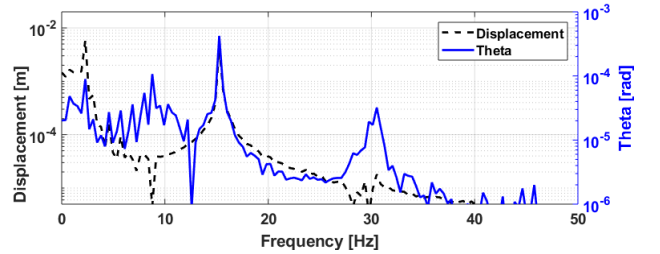
Fig. 10 Bending, twisting mode shape function

$$V_{lock} = St \times f_w \times D = const \times \frac{1}{scale} \times scale = const \quad (15)$$

Here, V_{lock} , St and f_w are the lock-in velocity, Strouhal number, and underwater natural frequency, respectively. Using this, the 1/100 scale model experimental results (Zobeiri, 2012) were compared with the lock-in velocity. The lock-in velocity (11–13 m/s) obtained as a result



(a) Time-domain results



(b) Frequency-domain results

Fig. 11 BT FSI analysis results of displacement and theta at $Re = 2.3 \times 10^8$

Table 5 Vortex-induced vibration frequency for various flow velocities using high-mode BT FSI analysis

Flow velocity (m/s)	Vortex induced vibration frequency (Hz)	Flow velocity (m/s)	Vortex induced vibration frequency (Hz)
10	6.86	19	12.57
11	7.43	20	13.43
12	8.29	21	14
13	8.86	22	14.86
14	8.86	23	15.43
15	9.71	24	15.43
16	10.86	25	16.57
17	11.14	26	17.14
18	11.71		

Table 6 Comparison between FSI analysis lock-in frequency and solution of analytic underwater natural frequency

	Analytic solution	FSI analysis
1 st Twisting/ 1 st Lock-in freq (Hz)	8.46	8.86
2 nd Bending/ 2 nd Lock-in freq (Hz)	15.81	15.43

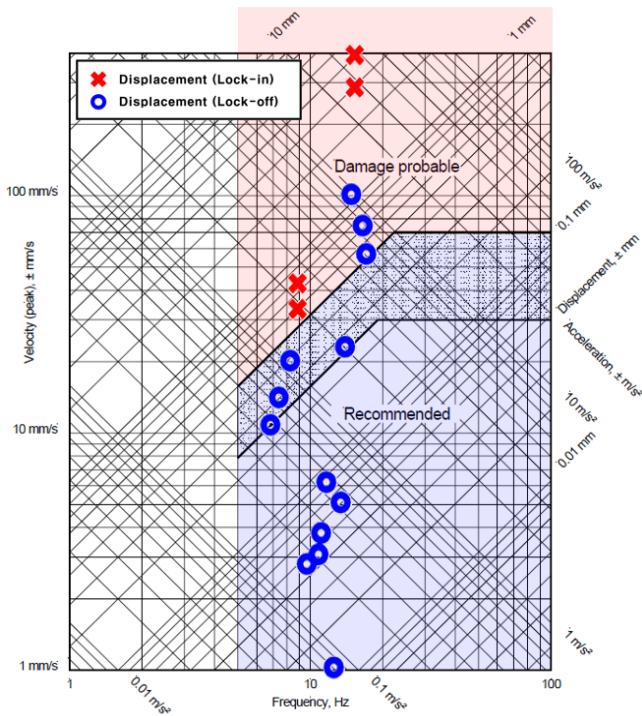


Fig. 12 FSI analysis results of vortex-induced vibration displacements with local vibration guidance published by Lloyd's Register

Table 7 Vortex-induced vibration displacement for various flow velocities using high-mode BT FSI analysis

Flow velocity (m/s)	Vortex induced vibration displacement (m)	Flow velocity (m/s)	Vortex induced vibration displacement (m)
10	2.52×10^{-4}	19	1.29×10^{-5}
11	3.04×10^{-4}	20	6.04×10^{-5}
12	3.90×10^{-4}	21	2.64×10^{-4}
13	7.78×10^{-4}	22	1.10×10^{-3}
14	6.07×10^{-4}	23	3.02×10^{-3}
15	4.58×10^{-5}	24	4.11×10^{-3}
16	4.50×10^{-5}	25	7.28×10^{-4}
17	5.41×10^{-5}	26	5.33×10^{-4}
18	8.44×10^{-5}		

of the experiment and the lock-in velocity (11–13 m/s) obtained as a result of the high-mode BT FSI analysis were similar, which verifies the reliability of this analysis in terms of the frequency.

To examine the structural stability of ship rudders with the VIV responses derived through the analysis performed in this study, we referred to the local vibration guidance suggested by Lloyd's Register (Lloyd's Register, 2006). As seen in Fig. 12, the results of the VIV displacement derived using the high-mode BT FSI analysis are displayed in the ship's local vibration guidance graph. The VIV responses displacement and frequency are shown in Table 5 and Table 7, respectively. An x in red indicates the displacement when lock-in occurs, and a circle in blue indicates the displacement in other

situations. In the frequency range of interest (5–100 Hz), the red shaded area indicates the area where the risk due to vibration is expected to be high, and the other areas are shown as the blue shaded areas. The VIV responses in the lock-off condition was expected to cause a high risk at some flow velocities close to the second bending mode. The VIV responses in the first twisting mode and the second bending mode lock-in condition was expected to cause a high risk in terms of local vibration.

4. Conclusion

In this study, we performed high-mode BT FSI analysis on the hydrofoil to predict the VIV responses in the wake of ship rudders. In particular, the conventional BT FSI analysis method that considers only the first bending- and twisting-mode vibration was extended into the high mode to numerically predict the resonance and lock-in phenomena caused by the high mode. The results of the high-mode BT FSI analysis were verified in terms of the frequency by comparing the analysis results and the experimental results for the analysis target based on the NACA0009 hydrofoil cross-section.

The experimental results and the FSI analysis results confirmed that the vortex shedding frequency generally tends to increase with an increase in the flow velocity, and that the vibration increases and simultaneously the vortex shedding frequency shifts to the structure's natural frequency as the vortex shedding frequency approaches the structure's natural frequency. When the VIV displacement derived from the FSI analysis results was analyzed based on the local vibration guidance published by Lloyd's Register, it was expected that there would be a strong possibility of structural defects occurring due to resonance and lock-in phenomena. Therefore, we confirmed that there was a need for technology to predict the resonant and lock-in phenomena, including the high mode.

We suggest the following two directions for future research. First, to structurally simulate the actual ship's rudder, research on the mode characteristics of the cantilevered structure, including the web structure and rudder stock, must be conducted. Second, research on methods for high-mode BT FSI analysis is necessary when non-uniform flow instead of uniform flow enters as incoming flow. Studies based on these two topics can help further develop technology to predict the VIV of ship rudders in actual ship operation, and this analysis model is expected to facilitate a safety review process when designing an actual ship.

Acknowledgement

This research was conducted with the support of Seoul National University BK21, Education and Research Center for Creative Offshore Plant Engineers. It was also supported by the Research Institute of Marine Systems Engineering (RIMSE) and the Research Foundation (2019R1F1A1062914).

References

- Abu-Hilal, M. (2003). Forced Vibration of Euler-Bernoulli Beams by Means of Dynamic Green Functions. *Journal of Sound and Vibration*, 267(2), 191-207. [https://doi.org/10.1016/S0022-460X\(03\)00178-0](https://doi.org/10.1016/S0022-460X(03)00178-0)
- Ausoni, P. (2009). Turbulent Vortex Shedding from a Blunt Trailing Edge Hydrofoil (Ph.D. Thesis). EPFL, Lausanne, Swiss.
- Blevins, R.D. (2001). *Flow-induced vibration* (2nd ed). Florida, USA: Krieger Publishing.
- Campbell, R.L. (2010). Fluid-structure Interaction and Inverse Design Simulations for Flexible Turbomachinery (Ph.D. Thesis). The Pennsylvania State University, University Park, USA.
- Chae, E.J. (2015). Dynamic Response and Stability of Flexible Hydrofoils in Incompressible and Viscous Flow (Ph.D. Thesis). The University of Michigan, Ann Arbor, USA.
- Felippa, C.A., Park, K.C., & Farhat, C. (2001). Partitioned Analysis of Coupled Mechanical Systems. *Computer Methods in Applied Mechanics and Engineering*, 190(24-25), 3247-3270. [https://doi.org/10.1016/S0045-7825\(00\)00391-1](https://doi.org/10.1016/S0045-7825(00)00391-1)
- Jung, J.H., Jeong, K.L., Gill, J.H., & Jung, D. (2019). Large Eddy Simulation of Free Motion of Marine Riser using OpenFOAM. *Journal of Ocean Engineering and Technology*, 33(5), 387-393. <https://doi.org/10.26748/KSOE.2019.074>
- Kim, J.I., Park, I.R., Kim, K.S., & Ahn, J.W. (2017). Numerical Analysis of Non-Cavitating and Cavitating Performance of a SVA Potsdam Propeller. *Journal of the Society of Naval Architects of Korea*, 54(3), 215-226. <https://doi.org/10.3744/SNAK.2017.54.3.215>
- Lee, A.H. (2014). Fluid-Structure Interaction of Large Amplitude Structure Vibrations and Moderately High Reynolds Number Turbulent Flows (Ph.D. Thesis). The Pennsylvania State University, University Park, USA.
- Lloyd's Register. (2006). *Ship Vibration and Noise Guidance Notes*. London, United Kingdom: Lloyd's Register.
- Mittal, R., & Balachandar, S. (1995). Effect of Three-dimensionality on the Lift and Drag of Nominally Two-dimensional Cylinders. *Physics of Fluids*, 7(8), 1841-1865. <https://doi.org/10.1063/1.868500>
- Münch, C., Ausoni, P., Braun, O., Farhat, M., & Avellan, F. (2010). Fluid-structure Coupling for an Oscillating Hydrofoil. *Journal of Fluids and Structures*, 26(6), 1018-1033. <https://doi.org/10.1016/j.jfluidstructs.2010.07.002>
- Sarpkaya, T. (1979). Vortex-Induced Oscillations: A Selective Review. *Journal of Applied Mechanics*, 46(2), 241-258. <https://doi.org/10.1115/1.3424537>
- Son, H.A., Lee, S.S., & Cho, S.R. (2019). Effects of Flow Acceleration on Drag Force and Wake Field of 2D Circular Cylinder. *Journal of the Society of Naval Architects of Korea*, 56(6), 507-514. <https://doi.org/10.3744/SNAK.2019.56.6.507>
- Theodorsen, T. (1949). *General Theory of Aerodynamic Instability and the Mechanism of Flutter*. Washington, DC, USA: National Advisory Committee for Aeronautics.
- Young, Y. L., Chae, E.J., & Akcabay, D.T. (2012). Hybrid Algorithm for Modeling of Fluid-structure Interaction in Incompressible, Viscous flows. *Acta Mechanica Sinica*, 28(4), 1030-1041. <https://doi.org/10.1007/s10409-012-0118-3>
- Zobeiri, A. (2012). Effect of Hydrofoil Trailing Edge Geometry on the Wake Dynamics (Ph.D. Thesis). EPFL, Lausanne, Swiss.

Author ORCIDs

Author name	ORCID
Jang, Won-Seok	0000-0002-0083-8546
Hong, Suk-Yoon	0000-0002-5520-7047
Song, Jee-Hun	0000-0003-0718-137X
Kwon, Hyun-Wung	0000-0002-9075-2569
Choi, Woen-Sug	0000-0002-1450-1848

Feasible Positions of Towing Point and Center of Gravity for Towfish Attitude Control

Min-Kyu Kim¹, Dong-Jin Park², Jong-Hwa Kim³ and Jin-Kyu Choi⁴

¹Graduate Student, Ocean Science and Technology School, Korea Maritime and Ocean University, Busan, Korea

²Technical Director, Research Institute, Sonartech Co., Ltd., Busan, Korea

³Professor, Ocean Science and Technology School, Korea Maritime and Ocean University, Busan, Korea

⁴Associate Professor, Ocean Science and Technology School, Korea Maritime and Ocean University, Busan, Korea

KEY WORDS: Towfish, Elevator, Cable, Towing Point, Center of Gravity(CG)

ABSTRACT: Most towfish systems do not have propulsive devices and cannot compensate for perturbation motion, which can affect the observation data. This paper discusses attitude control of a towfish with elevators on the left and right tail wings to improve the quality of the observational data. Specifically, we investigate the relationships between the towing point, the center of gravity, and the drag forces produced by the elevators to clarify whether the elevators can control the attitude of the towfish sufficiently for various positions of the towing point and center of gravity. The feasible positions of the towing point and center of gravity are defined by mechanical analyses, and simulations are conducted to verify that the elevators can provide attitude control in these positions. The simulation results show that at some positions, the elevators can control the attitude quickly and sufficiently even if disturbances exist.

Nomenclature

f_c	Towed force
f_e	Elevator force
f_b	Restoring force and moment
r_c	Position vector from CG to towing point
r_e	Position vector from CG to center of elevator
$f_{c(xz)}$	Towed force in xz plane
$f_{e(xz)}$	Elevator force in xz plane
$r_{c(xz)}$	Position vector to towing point in xz plane
$r_{e(xz)}$	Position vector to center of elevator in xz plane
W	Weight
B	Buoyant force
δ_l, δ_r	Left and right elevator angle
δ_s	Synchronous elevator angle
s	Area of a single elevator
C_D	Drag coefficient of elevator
C_L	Lift coefficient of elevator

1. Introduction

A towfish is moved by a cable connected to a mother ship because it does not have a thrust device (Go et al., 2016; Buckham et al., 2003; Isa et al., 2014). Because towfishes are usually convenient to operate and maintain, they have been used recently for underwater target detection and submarine resource detection in civil and military applications and have been operated with various types of sonar (Park and Shin, 2009; Song and Choi, 2016).

The shape of a towfish is designed to enable hydrodynamically stable movement, but towfish cannot always respond optimally to unforeseeable marine or underwater environments and some operating environments. In particular, when a towfish is equipped with a high-resolution sonar system such as interferometric synthetic aperture sonar (InSAS), which uses the phase differences of signals received by array sensors at different positions to obtain three-dimensional images (Lee et al., 2019; Kim et al., 2017), the irregular motion of the towfish causes distortion or defocusing of the InSAS images. To address these problems, the attitude of the towfish must be controlled (Park and Kim, 2015; Lambert et al., 2003; Kim et al., 2016; Choi et al., 2005).

Received 20 April 2020, revised 16 September 2020, accepted 17 September 2020

Corresponding author Jin-Kyu Choi: +82-51-410-4342, jk-choi@kmou.ac.kr

© 2020, The Korean Society of Ocean Engineers

This is an open access article distributed under the terms of the creative commons attribution non-commercial license (<http://creativecommons.org/licenses/by-nc/4.0>) which permits unrestricted non-commercial use, distribution, and reproduction in any medium, provided the original work is properly cited.

Meanwhile, because the motion of the towfish is greatly affected by the cable connected to the mother ship, it is important to identify the optimal towing point. Consequently, the dynamic relationship between the center of gravity and center of buoyancy of the towfish must be analyzed. In particular, when the attitude is controlled using an actuator such as a propeller or an elevator, the analysis must consider the capacity of the actuator, in addition to the center of gravity and center of buoyancy.

In this study, dynamic analyses considering the towing point, center of gravity, center of buoyancy, and elevator capacity are conducted to investigate the attitude control of a towfish with elevators attached to its left and right horizontal tail wings. In addition, the results of these analyses are used to identify a method of selecting appropriate positions of the towing point and center of gravity. Here, the towing force acting on the towfish is assumed to be constant, taking into consideration the state in which the motion of the towfish is stabilized.

The contents of this paper are as follows. The equations of motion of the towfish for use in the dynamic analyses are presented in Section 2. A method of determining appropriate positions of the towing point and center of gravity for eight selected cases considering changes in the towing point and center of gravity is proposed in Section 3. In Section 4, attitude control using the equations of motion of the towfish is simulated to verify the validity of the obtained feasible regions of the towing point and center of gravity.

2. Mathematical Model of the Towfish

Fig. 1 illustrates how the towfish is connected to the mother ship through a cable and shows the forces acting on the towfish. Assuming that elevators are attached to the left and right horizontal tail wings for attitude control, the equation of motion of a towfish with six degrees of freedom can be expressed as follows, considering the elevator force, weight, and buoyant force, including the towing force from the cable:

$$M\dot{\boldsymbol{\nu}} + C(\boldsymbol{\nu})\boldsymbol{\nu} + D(\boldsymbol{\nu})\boldsymbol{\nu} = \begin{pmatrix} \mathbf{f}_c \\ \mathbf{r}_c \times \mathbf{f}_c \end{pmatrix} + \begin{pmatrix} \mathbf{f}_e \\ \mathbf{r}_e \times \mathbf{f}_e \end{pmatrix} + \mathbf{f}_b \quad (1)$$

where $\boldsymbol{\nu}$ is $(u, v, w, p, q, r)^T \in R^6$, and (u, v, w) and (p, q, r) represent the velocity and angular velocity, respectively, along the three axes of

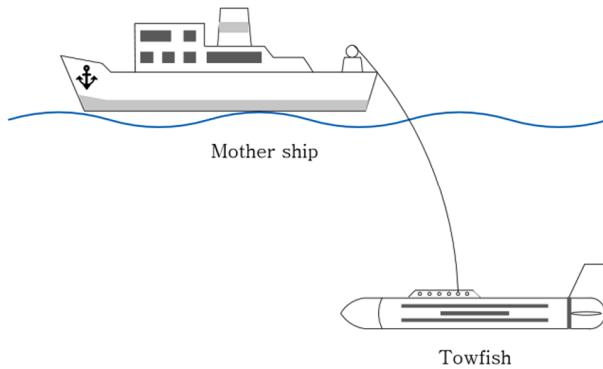


Fig. 1 Towfish system and the forces acting on the towfish

the coordinate system attached to the towfish. $M = M_{RB} + M_A \in R^{6 \times 6}$, where M_{RB} represents the rigid-body inertial matrix, M_A represents the added mass matrix from the hydrodynamic force, and $C(\boldsymbol{\nu}) = C_{RB}(\boldsymbol{\nu}) + C_A(\boldsymbol{\nu})$. Here, $C_{RB}(\boldsymbol{\nu})$ represents the rigid-body Coriolis and centripetal force matrix. $C_A(\boldsymbol{\nu})$ represents the Coriolis and centripetal force matrix of the hydrodynamic force. In addition, $D(\boldsymbol{\nu}) = D_l + D_n(\boldsymbol{\nu}) \in R^{6 \times 6}$, where D_l represents the linear damping matrix of the hydrodynamic force, and $D_n(\boldsymbol{\nu})$ represents a nonlinear damping matrix.

The right-hand terms of Eq. (1) represent the forces and moments acting on the towfish. $\mathbf{f}_c, \mathbf{f}_e \in R^3$, and $\mathbf{f}_b \in R^6$ are the towing force from the cable, the elevator force, and the restoring force generated by the weight and buoyant force, respectively. \mathbf{r}_c and $\mathbf{r}_e \in R^3$ are the position vectors from the center of gravity to the towing point and the elevator center, respectively, and \times represents the vector product. If $S(\mathbf{a})$ is a skew-symmetric matrix, the relational expression $\mathbf{a} \times \mathbf{b} = S(\mathbf{a})\mathbf{b}$, $\mathbf{a}, \mathbf{b} \in R^3$, is satisfied if $\mathbf{a} = (a_x, a_y, a_z)^T$, $S(\mathbf{a})$ is given by

$$S(\mathbf{a}) = \begin{pmatrix} 0 & -a_z & a_y \\ a_z & 0 & -a_x \\ -a_y & a_x & 0 \end{pmatrix} \quad (2)$$

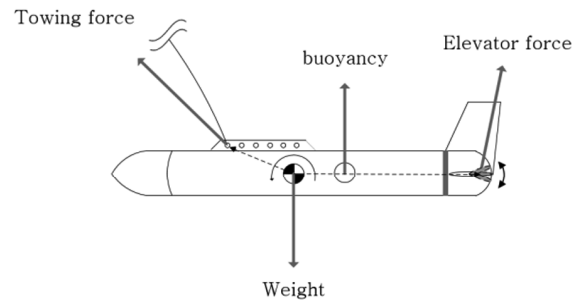
If the right-hand terms of Eq. (1) are defined as $\boldsymbol{\tau}$, $\boldsymbol{\tau}$ is given by

$$\boldsymbol{\tau} = J_C \mathbf{f}_c + J_E \mathbf{f}_e + \mathbf{f}_b \quad (3)$$

$$J_C = \begin{pmatrix} I_{3 \times 3} \\ S(\mathbf{r}_c) \end{pmatrix}, \quad J_E = \begin{pmatrix} I_{3 \times 3} \\ S(\mathbf{r}_e) \end{pmatrix}$$

$$\mathbf{f}_b = \begin{pmatrix} -(W-B)s\theta \\ (W-B)c\theta s\phi \\ (W-B)c\theta c\phi \\ (y_g W - y_b B)c\theta c\phi - (z_g W - z_b B)c\theta s\phi \\ -(z_g W - z_b B)s\theta - (x_g W - x_b B)c\theta c\phi \\ (x_g W - x_b B)c\theta s\phi + (y_g W - y_b B)s\theta \end{pmatrix}$$

where (x_g, y_g, z_g) and (x_b, y_b, z_b) represent the center of gravity and



center of buoyancy, respectively; c and s represent the cosine and sine, respectively. In addition, ϕ and θ represent the roll and pitch angle of the towfish, respectively, which are obtained as follows.

$$\dot{\eta}_2 = J_2(\eta_2)\nu_2 \quad (4)$$

$$J_2(\eta_2)^{-1} = \begin{pmatrix} 1 \\ 0 \\ 0 \end{pmatrix} \vdots R_{x,\phi}^T \begin{pmatrix} 0 \\ 1 \\ 0 \end{pmatrix} \vdots R_{x,\phi}^T R_{y,\theta}^T \begin{pmatrix} 0 \\ 0 \\ 1 \end{pmatrix}$$

where $\eta_2 = (\phi, \theta, \psi)^T \in R^3$, $\nu_2 = (p, q, r)^T \in R^3$, and $R_{i,j}$ is a rotation matrix that represents rotation by an angle j about the i axis.

3. Positions of the Towing Point and Center of Gravity

Fig. 2 shows the forces acting on the towfish in the xz plane. $\mathbf{f}_{c(xz)} = (f_{cx}, f_{cz})^T$ and $\mathbf{f}_{e(xz)} = (f_{ex}, f_{ez})^T$ are the towing forces and elevator forces in the xz plane, respectively. $\mathbf{r}_{c(xz)} = (r_{cx}, r_{cz})^T$ and $\mathbf{r}_{e(xz)} = (r_{ex}, 0)^T$ are the position vectors from the center of gravity to the towing point and to the elevator center, respectively. Using these variables, the pitching moment of the towfish generated by the towing force, restoring force, and elevator force in the xz plane can be calculated as

$$M_y = \mathbf{r}_{c(xz)} \otimes \mathbf{f}_{c(xz)} + \mathbf{r}_{e(xz)} \otimes \mathbf{f}_{e(xz)} + f_{b5} \quad (5)$$

Assuming that the motion of the towfish is stabilized and the forces are in equilibrium, the moment of the hydrodynamic force acting on the body is not included in Eq. (5), where f_{b5} is the fifth component of \mathbf{f}_b in Eq. (3). In addition, \otimes is the vector product in the plane, and satisfies interaction formulas such as $\mathbf{a} \otimes \mathbf{b} = (E\mathbf{a})^T \mathbf{b} = (E^T \mathbf{a}^T) \mathbf{b}$, $\mathbf{a}, \mathbf{b} \in R^2$. Here E is a rotation matrix that represents rotation by 90° in the counterclockwise direction in the plane and is given by

$$E = \begin{pmatrix} 0 & -1 \\ 1 & 0 \end{pmatrix} \quad (6)$$

Multiple cases must be analyzed because the direction and force of the pitching moment vary with the positions of the towing point, center of gravity, and center of buoyancy. In this study, the eight cases shown in Fig. 3 are analyzed.

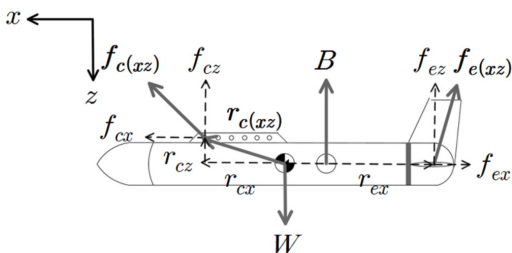


Fig. 2 Forces acting on the towfish in the xz plane

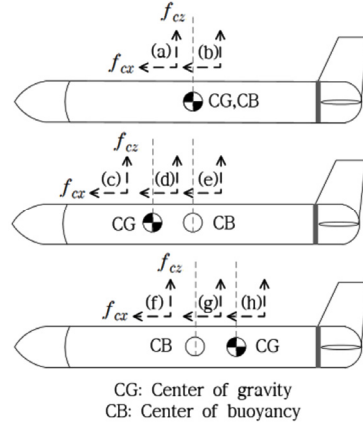


Fig. 3 Eight cases [(a)–(h)] used to examine the effect of the positions of the towing point and center of gravity

3.1 Cases Where Only the Towing Point Changes [Cases (a) and (b)]

In cases (a) and (b), where the towing point is in front of and behind the center of gravity, the center of gravity and center of buoyancy are fixed at the same position. The effect of the restoring force term, f_{b5} , can be ignored because the moments caused by the weight and buoyant force are not generated. r_{cx} , which is in equilibrium with the maximum and minimum elevator forces in Eq. (5), is calculated using the Eq. (7) for cases (a) and (b). The maximum and minimum elevator forces, $f_{ez\max}$ and $f_{ez\min}$ are defined as being generated at the maximum angles in the positive and negative directions. The positions of r_{cx} , which can be controlled by the elevator force, f_{ez} , according to Eq. (7), are shown in Fig. 4.

Case (a): (7)

$$r_{cx\max} = \frac{r_{cz}f_{cx} + r_{ex}f_{ez\min}}{f_{cz}}$$

Case (b):

$$r_{cx\min} = -\left(\frac{-r_{cz}f_{cx} + r_{ex}f_{ez\max}}{f_{cz}}\right)$$

The point at which $r_{cx} = r_{cz}f_{cx}/f_{cz}$ in the area corresponding to case (a) becomes the optimal towing point for maintaining the attitude of

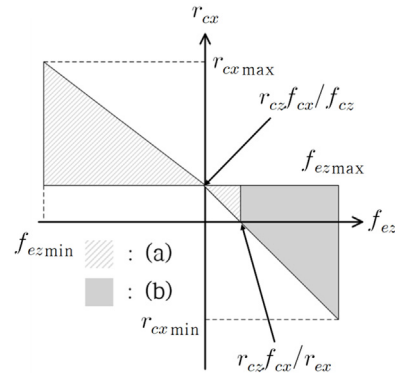


Fig. 4 The feasible positions of r_{cx} at which the elevators are able to control the pitching moment

the towfish without an additional elevator force because $r_{cx}f_{cx}$ is constant, even if r_{cx} changes. The attitude becomes more difficult to control as the towing point, r_{cx} , moves farther away from center of gravity because the elevator force required for attitude control increases.

3.2 Cases in which the Center of Gravity and Towing point Change [Cases (c)–(h)]

In cases (c)–(h), the center of buoyancy is fixed at the origin. The center of gravity is in front of the center of buoyancy in cases (c)–(e) and behind it in cases (f)–(h). Under these conditions, the areas of r_{cx} and x_g that can be controlled by the elevator force, f_{ez} are examined as follows.

(1) The maximum and minimum towing points ($r_{cx\max}$, $r_{cx\min}$) are calculated in the case where the center of gravity and center of buoyancy are at the same position;

(2) The maximum and minimum positions ($x_{g\max}$, $x_{g\min}$) of the center of gravity are calculated when the obtained maximum and minimum towing points and the center of gravity are on the same line of the z -axis;

(3) The maximum and minimum towing points ($r_{cxg\max}$, $r_{cxg\min}$) at the maximum and minimum centers of gravity obtained in procedure (2) are calculated.

The restoring force term in cases (c)–(h) must be considered because, in contrast to cases (a) and (b), the center of gravity and center of buoyancy are at different positions. The restoring force term, f_{ib} , is $-(z_g W - z_b B)s\theta - (x_g W - x_b B)c\theta c\phi$ and can be simplified to $-x_g W$ when the center of buoyancy is fixed at the origin and the towfish is stabilized ($\theta, \phi \approx 0$). The maximum and minimum towing points are obtained equally in Eq. (7) if procedure (1) is performed using Eq. (5) and the maximum and minimum positions $x_{g\max}$, $x_{g\min}$ are calculated as follows if procedure (2) is performed:

$$x_{g\max} = \frac{r_{cz}f_{cx} + r_{ex}f_{ez\max}}{W} \quad (8)$$

$$x_{g\min} = -\left(\frac{-r_{cz}f_{cx} + r_{ex}f_{ez\min}}{W}\right)$$

The maximum and minimum towing points $r_{cxg\max}$, $r_{cxg\min}$ are calculated as follows if procedure (3) is performed:

$$r_{cxg\max} = \frac{r_{cz}f_{cx} + r_{ex}f_{ez\min} - x_{g\max}}{f_{cz}} \quad (9)$$

$$r_{cxg\min} = -\left(\frac{-r_{cz}f_{cx} + r_{ex}f_{ez\max} - x_{g\min}}{f_{cz}}\right)$$

Fig. 5 shows the feasible positions of the center of gravity and towing point at which the elevators can control the pitching moment

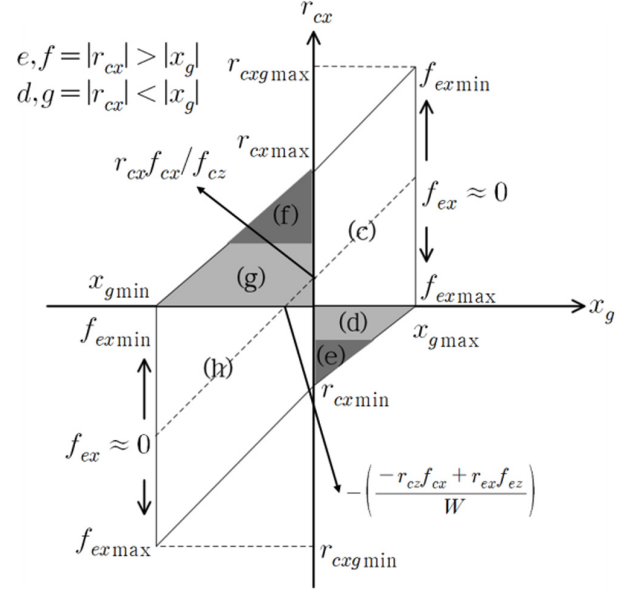


Fig. 5 Feasible positions of r_{cx} and x_g at which the elevators can control the pitching moment

according to the Eqs. (7), (8), and (9). The dotted line represents the points at which the pitching moment of the towfish is not generated, even when the elevator force is not generated. Most of these points appear at positions that correspond to cases (c) and (h); thus, the dotted line indicates advantageous positions for attitude control of the towfish. Conversely, the positions corresponding to cases (e) and (f) do not include the dotted line; thus, attitude control can be considered difficult in these cases.

4. Simulations

Simulations were performed to examine the relationship between the positions obtained in Section 3 and identify the control performance. The attitude of the towfish is controlled by the drag forces generated by the left and right elevators, which are given by the following equations:

$$f_{ez} = C_O C_L + C_O C_L \quad (10)$$

$$f_{ex} = C_O C_D + C_O C_D$$

$$C_L, C_D = \text{function of } \alpha$$

$$C_O = 0.5\rho s u^2$$

Here, ρ , s , u , and α represent the density of water, the area of a single elevator, the velocity of the towfish, and the angle of attack, respectively. C_D and C_L are the drag and lift coefficients, respectively; their values were obtained according to the airfoil model of the National Advisory Committee for Aeronautics (NACA). Because the angle of attack is the same as the elevator angle, f_{ex} and f_{ez} are expressed as functions of the elevator angle (Park et al., 2016).

If δ_l and δ_r are the angles of the left and right elevators, respectively, the pitch angle of the towfish can be controlled by following the value of the synchronous elevator angle, $\delta_s = (\delta_r + \delta_l)/2$. The simulations were performed using the following equations of motion obtained from Eqs. (1) and (10).

$$M\dot{\nu} + C(\nu)\nu + D(\nu)\nu - J_C f_c - f_b = J_E \begin{pmatrix} -0.065 C_O & \vdots & -0.065 C_O \\ 0 & \vdots & 0 \\ 0.11 C_O & \vdots & 0.11 C_O \\ 0 & \vdots & 0 \\ 0.11 C_O r_{cx} & \vdots & 0.11 C_O r_{cx} \\ 0 & \vdots & 0 \end{pmatrix} \begin{pmatrix} \delta_r \\ \delta_l \end{pmatrix} \quad (11)$$

$$\delta_r, \delta_l = K_p(\theta_d - \theta) - K_d\dot{\theta} + K_i \int_0^t (\theta_d - \theta) dt$$

K_p , K_d , and K_i are the control gains in a proportional-integral-derivative [PID] controller and represent the proportional, derivative, and integral gains of the elevator angle, respectively. θ_d and θ represent the target pitch angle (reference input) and current pitch angle, respectively. The values 0.065 and 0.11 used in Eq. (11) are the slopes of the drag and lift coefficients plotted for various elevator angles, respectively, and were linearized by referring to the values for the NACA 0018 model.

Table 1 lists the parameter values of the towfish used in the simulations. The towfish was assumed to be a horizontally symmetric cylinder, with a length and diameter of L and D , respectively. I_y is the moment of inertia of the towfish with respect to the y -axis. The other symbols represent hydrodynamic force derivatives (Fossen, 1994). X_u , Z_w , and M_q were calculated using the towfish data, and X_u , Z_w , M_q , $X_{|u|u}$, $Z_{|w|w}$, and $M_{|q|q}$ were selected on the basis of the simulations.

Table 1 Parameter values used in simulation

Parameter	Value	Parameter	Value
m	300 kg	X_u	-20 kg/s
L	3.5 m	Z_w	-200 kg/s
D	0.4 m	M_q	-200 kg·m ²
I_y	309.25 kg·m ²	$X_{ u u}$	-30 kg/m
X_u	-12.8397 kg	$Z_{ w w}$	-300 kg/m
Z_w	-276.2693 kg	$M_{ q q}$	-300 kg·m ²
M_q	-144.4516 kg·m ²		

4.1 Simulation Conditions

Table 2 shows the simulation conditions. $W' = W - B$ denotes the underwater mass. The control gains of the attitude-maintaining controller, K_p , K_d , and K_i , were set to 3, 5, and 0.01, respectively, and the left and right elevator angles were maintained within $\pm 30^\circ$ to ensure the stability of the towfish.

The simulations were performed by selecting sufficiently controllable positions and positions that are somewhat difficult to control according to the elevator capacity within the areas

Table 2 Simulation conditions

r_{cx}	0.2 m	s	0.025 m ²
f_{cx}	115 N	ρ	1,024 kg/m ³
f_{cz}	2,450 N	u	1.5 m/s
r_{ex} when $CG = (0, 0)$	1.7 m	W'	2,450 N
W	2,940 N	B	490 N

corresponding to cases (a) and (b), cases (e) and (f), and cases (c) and (h). Additionally, cases where disturbances are applied at arbitrary positions within the areas corresponding to case (c) (easy to control) and case (f) (difficult to control) were examined.

4.2 Simulations of Cases (a) and (b)

$r_{cx \max} \approx 0.14$ m and $r_{cx \min} \approx -0.12$ m are obtained from the conditions given in Table 2 and Eq. (5). The simulations were

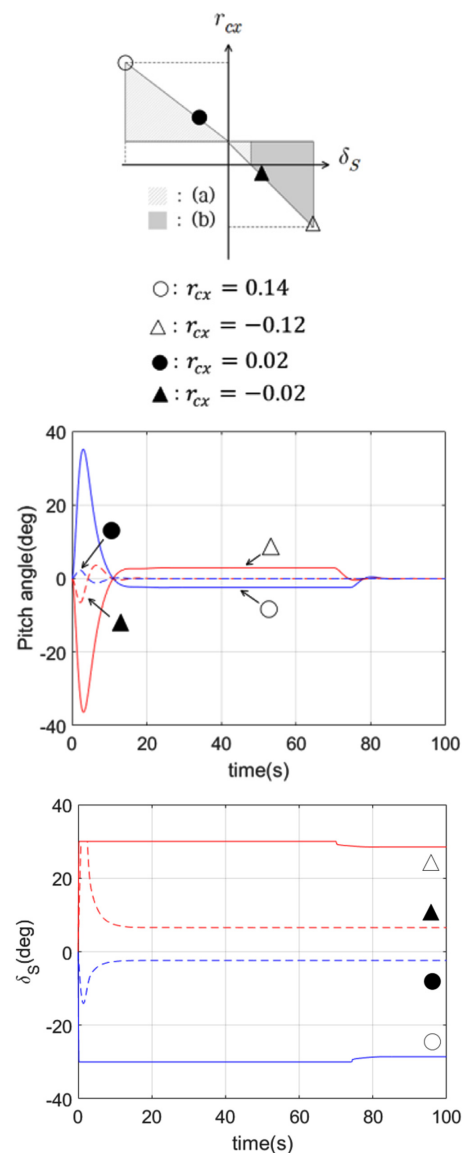


Fig. 6 Pitch angles and δ_s (synchronous elevator angle) for cases (a) and (b)

performed by selecting difficult-to-control cases for $r_{cx \max}$ and $r_{cx \min}$ and easily controlled cases with $r_{cx} = 0.02$ m and $r_{cx} = -0.02$ m, as shown in Fig. 4.

Fig. 6 is a simulation result showing the pitch angle and synchronous elevator angle of the towfish when a pitch angle of 0° is applied as the reference input for the four positions. The blue dotted and solid lines are the results of the simulations at points \bullet and \circ selected from the area for case (a), respectively. The red solid and dotted lines are the results of the simulations at points \blacktriangle and \triangle selected from the area for case (b), respectively. The portions of the solid line indicated by \circ and \triangle represent the cases where the towing point is at $r_{cx \max}$ and $r_{cx \min}$, respectively; they show that the target pitch angle (0°) of the towfish is reached very slowly, even at the maximum elevator angle ($\pm 30^\circ$). In these cases, even if the attitude of the towfish is controlled, it is difficult to address additional disturbances because there is little margin in the elevator angle. By contrast, the portions of the dotted line indicated by \bullet and \blacktriangle are relatively easy to control, and the target pitch angle (0°) can be reached quickly. Moreover, the system can react immediately even when disturbances are applied because there is considerable margin in the elevator angle.

4.3 Simulations of Cases (e) and (f) and Cases (c) and (h)

From the conditions given in Table 2 and Eqs. (8) and (9), the maximum and minimum positions of the center of gravity that the elevator can control are given by $x_{g \max} \approx 0.1$ m and $x_{g \min} \approx -0.12$, respectively. The maximum and minimum towing positions at this time are calculated as $r_{cx \min} \approx 0.27$ m and $r_{cx \max} \approx -0.26$ m. The simulations were performed by selecting cases (e) and (f), in which control is difficult, and cases (c) and (h), in which control is relatively easy. The values of r_{cx} and x_g for each case are listed in Table 3. Fig. 7 is a simulation result showing the pitch angle and synchronous elevator angle of the towfish when a pitch angle of 0° is applied as the reference input for the four positions shown in Table 3. The areas corresponding to cases (e) and (f) (positions \circ and \triangle) have little margin in the elevator angle; therefore, the target pitch angle 0° is reached very slowly. In these cases, it is difficult to immediately address an additional disturbance. However, at the positions (\blacktriangle and \bullet) corresponding to cases (c) and (h), the target pitch angle is obtained quickly because there is considerable margin in the elevator angle. In these cases, it is possible to respond adequately to additional disturbances.

Table 3 Positions of r_{cx} and x_g for cases (e), (f), (c) and (h)

Case	r_{cx}	x_g
(e)	-0.07 m	0.04 m
(f)	0.08 m	-0.04 m
(c)	0.05 m	0.03 m
(h)	-0.04 m	-0.03 m

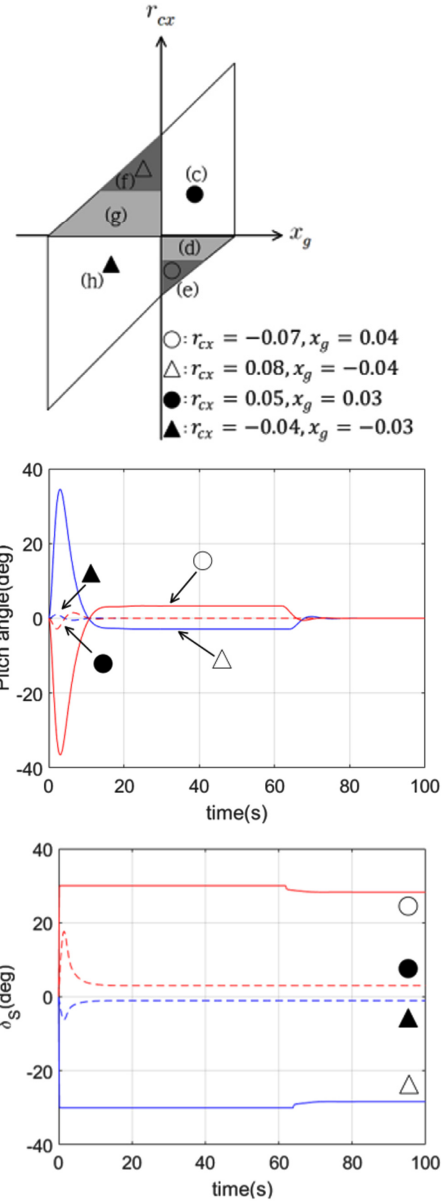


Fig. 7 Pitch angles and δ_s (synchronous elevator angle) for cases (e), (f), (c) and (h)

4.4 If Disturbance is Applied in Cases (c) and (f)

In cases (c) and (f), r_{cx} and x_g were set to the values in Table 3, and disturbances were applied. Fig. 8 is a simulation result showing the pitch angle and synchronous elevator angle of the towfish when a pitching moment of 50 NM is applied as a disturbance at positions \bullet and \triangle among the areas corresponding to cases (c) and (f). The reference input was selected as a pitch angle of 0° , as in the previous simulations. The position indicated by \bullet has considerable margin in the elevator angle; therefore, even if the disturbance is applied, the target pitch angle 0° is reached quickly. However, the position indicated by \triangle has little margin in the elevator angle; thus, the target pitch angle 0° cannot be maintained even if an extreme elevator angle of -30° is continuously applied to both elevators. These results show that it is important to avoid positions at which there is little margin in

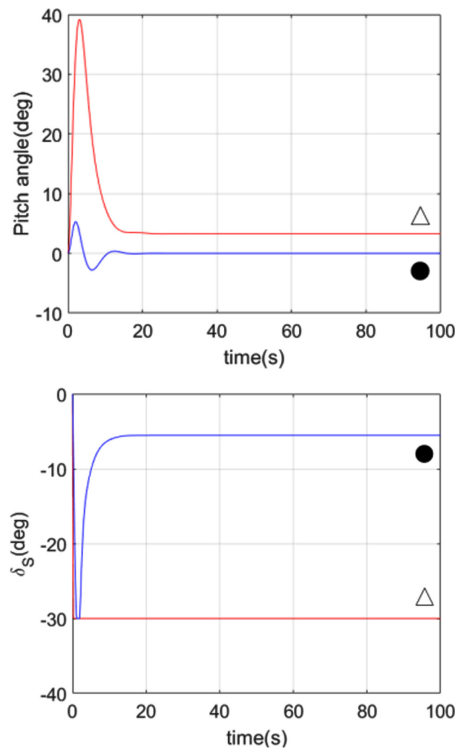


Fig. 8 Pitch angles and δ_s (synchronous elevator angle) under an applied disturbance

the elevator angle. Moreover, if the towing point and center of gravity are located at positions where the elevator angle has considerable margin, the system can respond quickly to additional disturbances.

5. Conclusions

We determined the feasible regions of the center of gravity and towing point at which the attitude of a towfish with elevators attached to its left and right horizontal tail wings can be controlled using dynamic analyses of the towing point, center of gravity, and elevator capacity. In addition, simulations were performed using the equations of motion of the towfish to verify the feasible regions. It was shown that the attitude is easy to control in some regions and difficult to control in others. At the positions at which the attitude is easily controlled, there is a margin in the elevator angle; thus, even if disturbances are applied, the target attitude is reached quickly. However, at the other positions, there was little margin in the elevator angle; thus, the system could not respond quickly to the effects of disturbances. These locations of the towing point and center of gravity are expected to become an index for determining the towing point, center of gravity, and elevator capacity in the design of towfish and their operation in real seas.

Acknowledgment

Support for this research was provided by the Civil-Military Technology Cooperation Project of the Institute of Civil-Military

Technology Cooperation, and the authors would like to express their gratitude for the support (Project Number: 15-CM-SS-01, Project Name: Towing interferometric synthetic aperture sonar (InSAS) development).

References

- Buckham, B., Nahon, M., Seto, M., Zhao, X., & Lambert, C. (2003). Dynamics and Control of a Towed Underwater Vehicle System, Part I: Model Development. *An International Journal of Research and Development. Ocean Engineering*, 30(4), 453-470. [https://doi.org/10.1016/S0029-8018\(02\)00029-X](https://doi.org/10.1016/S0029-8018(02)00029-X)
- Choi, J.K., Sakai, H., & Tanaka, T. (2005). Autonomous Towed Vehicle for Underwater Inspection in Port Area. *Proceedings of the 2005 IEEE International Conference on Robotics and Automation, Barcelona, Spain*, 188-193. <https://doi.org/10.1109/ROBOT.2005.1570117>.
- Fossen, T.I. (1994). *Guidance and Control of Ocean Vehicles*. New York, USA: Willy.
- Go, G.S., Lee, E.T., & Ahn, H.T. (2016). 3D Nonlinear Fully Coupled Simulation of Cable and Tow-fish System. *Journal of Ocean Engineering and Technology*, 30(6), 458-467. <https://doi.org/10.5574/KSOE.2016.30.6.458>
- Isa, K., Arshad, M.R., & Ishak, S. (2014). A Hybrid-driven Underwater Glider Model, Hydrodynamics Estimation, and an Analysis of the Motion Control. *International Journal of Research and Development. Ocean Engineering*, 81, 111-129. <https://doi.org/10.1016/j.oceaneng.2014.02.002>
- Kim, H.S., Ok, S.Y., & Baik, K.M. (2017). Study on 3D Visualization-based Behavior Analysis of Towfish. *Proceedings of Korean Society for Noise and Vibration Engineering, Korea*, 201.
- Kim, M.J., Baek, W.K., Ha, K.N., & Joo, M.G. (2016). Implementation of Hovering AUV and Its Attitude Control Using PID Controller. *Journal of Ocean Engineering and Technology*, 30(3), 221-226. <https://doi.org/10.5574/KSOE.2016.30.3.221>
- Lambert, C., Nahon, M., Buckham, B., & Seto, M. (2003). Dynamics and Control of Towed Underwater Vehicle System, Part II: Model Validation and Turn Maneuver Optimization. *An International Journal of Research and Development, Ocean Engineering*, 30(4), 471-485. [https://doi.org/10.1016/S0029-8018\(02\)00030-6](https://doi.org/10.1016/S0029-8018(02)00030-6)
- Lee, J.E., Oh, Y.S., Park, S.S., & Kim, H.S. (2019). Development of Towed Synthetic Aperture Sonar System. *Journal of the Korea Society for Naval Science & Technology*, 2(1), 28-31. <https://doi.org/10.31818/JKNST.2019.03.2.1.28>
- Park, C.H., Shin, M.S., Choi, J.Y., Hwang, J.H., Shin, Y.H., & Kim, Y.G. (2016). An Experimental Study on Effect of Angle of Attack on Elevator Control Force for Underwater Vehicle with Separate Fixed Fins. *Journal of Ocean Engineering and Technology*, 30(4), 243-252. <https://doi.org/10.5574/KSOE.2016.30.4.243>
- Park, J.M., & Kim, N.W. (2015). Dynamics Modeling of a Semi-submersible Autonomous Underwater Vehicle with a

Towfish Towed by a Cable. *International Journal of Naval Architecture and Ocean Engineering*, 7(2), 409-425.

Park, Y.M., & Shin, S.C. (2009). Simulation System Design and Development for Analysis of the Search Strategy for Underwater Targets. *Journal of the Korean Institute of Maritime Information & Communication Sciences*, 13(12), 2753-2758.

Song, Y.E., & Choi, S.J. (2016). Underwater 3D Reconstruction for Underwater Construction Robot Based on 2D Multibeam Imaging Sonar. *Journal of Ocean Engineering and Technology*, 30(3), 227-233. <https://doi.org/10.5574/KSOE.2016.30.3.227>

Author ORCIDs

Author name	ORCID
Kim, Min-Kyu	0000-0003-2127-5284
Park, Dong-Jin	0000-0003-3950-804X
Kim, Jong-Hwa	0000-0002-9005-0663
Choi, Jin-Kyu	0000-0003-3730-5900

Investigation of Hydrate Inhibition System for Shallow Water Gas Field: Experimental Evaluation of KHI and Simulation of MEG Regeneration Process

Suk Lee¹, Hyunho Kim², Ki-Heum Park² and Yutaek Seo³

¹Assistant Professor, Department of Architecture, Kyung Hee University, Yongin, Korea

²PhD Candidate, Department of Naval Architecture and Ocean Engineering, Seoul National University, Seoul, Korea

³Professor, Department of Naval Architecture and Ocean Engineering, Seoul National University, Seoul, Korea

KEY WORDS: Shallow water gas fields, Hydrates inhibition, MEG regeneration process, KHI performance evaluation, Process simulation, Economic analysis

ABSTRACT: In this study, a hydrate inhibition system is investigated for shallow water gas fields. Mono-ethylene glycol (MEG) injection has been used as a typical method for inhibiting hydrate formation in gas fields; therefore, most offshore platforms are equipped with MEG injection and regeneration processes. A recent application of a kinetic hydrate inhibitor (KHI) has reduced the total volume of MEG injection and hence reduce the operating cost. Experiments are designed and performed to evaluate and verify the KHI performance for inhibiting hydrate formation under shallow water conditions. However, the shut-in and restart operation may require the injection and regeneration of MEG. For this operation, the MEG concentration must be optimized while considering the cost of MEG regeneration. The obtained results suggest that decreasing MEG concentration from 80 wt% to 70 wt% can reduce the life cycle cost (LCC) of MEG regeneration process by approximately 5.98 million USD owing to reduced distillation column cost. These results suggest that the hydrate inhibition system must be evaluated through well-designed experiments and process simulations involving LCC analysis.

1. Introduction

A system for the regeneration, storage, and injection of mono-ethylene glycol (MEG) is installed in gas field production platforms, and the purpose of injecting MEG into subsea pipelines is to inhibit hydrate formation (Kim et al., 2017). Lean MEG (MEG concentration 70–90 wt%) injected into subsea pipelines is mixed with water produced in a reservoir to maintain a certain MEG concentration level. When it reaches the platform, it is separated at the inlet separator to proceed to the regeneration process as rich MEG (MEG regeneration concentration of 20–50 wt%) (Kim et al., 2018a). The MEG regeneration process converts rich MEG into lean MEG through pre-treatment and distillation, constituting a large portion of the upstream of a gas field platform and requiring separate spaces for an MEG injection pump and a storage tank. Therefore, to reduce the production cost of a gas field platform, the design of injection, regeneration, and storage systems for MEG must be optimized during the design process, during which the flow assurance should be sufficiently tested through multiphase flow analysis and hydrate-phase equilibrium simulation (Kim et al., 2020). In particular, There have

been attempts to minimize the MEG regeneration process in production platforms for shallow water gas fields in Southeast Asia, Middle East, and the North Sea, which requires a large volume and a high cost owing to the recent decrease in oil prices. A kinetic hydrate inhibitor (KHI) contains functional groups connected in a polymer chain structure; it can inhibit hydrate nucleation as well as suppress hydrate growth for a certain period of time at 0.5–3 wt%, unlike MEG (Park et al., 2019). When KHI is used, hydrate formation can be suppressed while water produced in a reservoir passes through subsea pipelines in a normal operation, thereby eliminating the need of injecting MEG.

Hydrate formation occurs in low-temperature and high-pressure conditions, and the hydrate formation conditions can be predicted thermodynamically. At a certain pressure, the difference between the minimum temperature of subsea pipelines and the phase equilibrium temperature of hydrates becomes the driving force of hydrate formation. The rate of hydrate formation decreases with the difference in the temperatures. Hence, it is likely that the rate of hydrate formation at production platforms for shallow water gas fields is slow, which is optimal for applying a KHI. A KHI inhibits the cluster

Received 30 June 2020, revised 9 August 2020, accepted 20 August 2020

Corresponding author Yutaek Seo: +82-2-880-7329, yutaek.seo@snu.ac.kr

© 2020, The Korean Society of Ocean Engineers

This is an open access article distributed under the terms of the creative commons attribution non-commercial license (<http://creativecommons.org/licenses/by-nc/4.0>) which permits unrestricted non-commercial use, distribution, and reproduction in any medium, provided the original work is properly cited.

formation process through the ring-structure connected in chains, during which water molecules convert to the hydrate crystal structure, while simultaneously decelerating the growth of hydrates by adhering to growth points after hydrates are formed (Kim et al., 2018b).

Accordingly, a KHI can demonstrate outstanding performances in shallow water gas fields where the driving force of hydrate formation is relatively low.

However, MEG regeneration is inevitable even at production platforms for shallow water gas fields because MEG injection is required for transient operations, such as for halting and resuming the production of subsea pipelines for a long period of time (Brustad et al., 2005). Hence, a flexible strategy in which a KHI is applied in a normal operation while applying MEG in a transient operation can be considered for reducing the operation cost of a production platform. The performance of a KHI must be assessed accurately, and the optimization of MEG injection and regeneration concentrations for transient operations must be investigated. Therefore, the risk of hydrate formation in shallow water gas fields was investigated in this study using a high-pressure stirred-tank reactor, and the hydrate inhibition performance in the presence of KHI was investigated experimentally. The MEG regeneration process was designed to obtain the appropriate lean MEG concentration by evaluating the economic feasibility of such processes for shallow water gas fields. The experimental and simulation results can be utilized as basic information for designing a production platform.

2. Experimental Apparatus and Simulation Model

2.1 Experiment for Evaluating Risk of Hydrate Formation

The formation of hydrates in subsea pipelines must be prevented. In other words, a sufficient amount of MEG must be injected to minimize the possibility of hydrate formation. Therefore, the temperature and pressure conditions for which hydrates can be formed were predicted thermodynamically, and the required MEG concentration was calculated. However, a thermodynamic simulation could not be performed for cases where a KHI was applied; therefore, the risk of

hydrate formation was evaluated experimentally. Experiments regarding formation and dissociation were conducted using a high-pressure stirred-tank reactor since a hydrate is formed in a low-temperature and high-pressure condition. Fig. 1 shows the schematic diagram of the experimental apparatus used for the hydrate formation experiment. The high-pressure stirred-tank reactor was designed to apply a pressure of up to 15 MPa, and the fluid inside the reactor can be mixed at 0–800 rpm using a magnetic stirrer. For simulating subsea pipelines, 80 mL of water was injected to a 360 mL reactor (material: (SUS 316) and then pressurized to 12 MPa using natural gas. The natural gas comprising 90.0% CH₄, 6.0% C₂H₆, 3.0% C₃H₈, and 1.0% n-C₄H₁₀ was supplied by Alpha Gas S.A. The reactor was positioned in a water bath such that it was submerged in a sufficient amount of ethanol solution; furthermore, it was connected to an external heater/refrigerator (Jeiotech RW2025G) to maintain the desired temperature. The temperatures of both the gas and liquid were measured using a platinum resistance thermometer that was accurate to 0.15 °C; the pressure was measured using a pressure transducer that was accurate to 0.01 MPa. The temperature of the solution was maintained at 20 °C at the initial stage of the experiment. Once the pressure inside the reactor stabilized, the temperature decreased to 10 °C, which is the operation condition of subsea pipelines at shallow water gas fields. The reactor was stirred at 600 rpm as the experiment began, during which the torque applied to the impeller was measured using a torque sensor (TRD-10KC) with an accuracy of 0.3%. The temperature, pressure, and torque data obtained through primary sensors were saved in a data storage system every 10 s. Hydrate formation can be observed at a specific point in time when the temperature is below the phase equilibrium of the hydrate. The characteristics of hydrate formation using pure water were analyzed when MEG and KHI were not injected; furthermore, the time hydrate formation was delayed after KHI injection was measured.

2.2 Hysys Simulation Model for MEG Regeneration Process

The shallow water gas fields investigated in this study were assumed to be located at the depth of 60 m underwater. The gas fields in

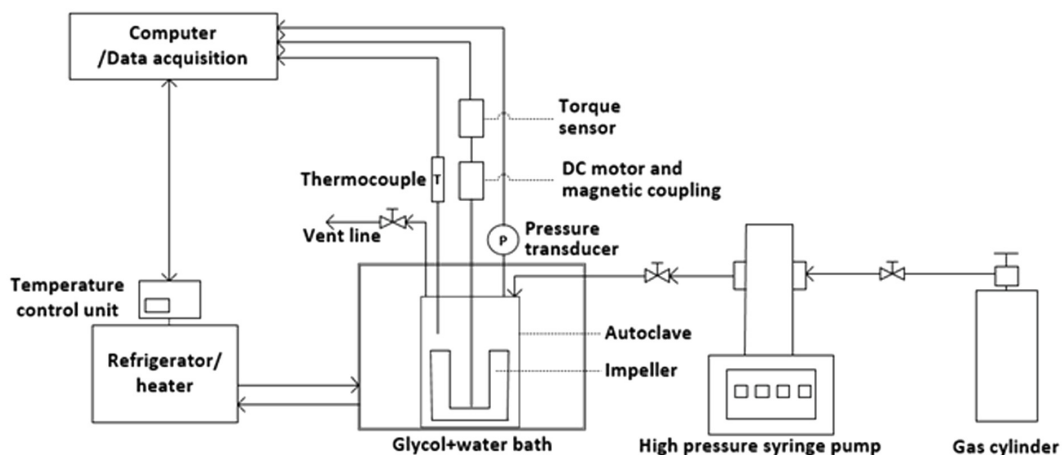
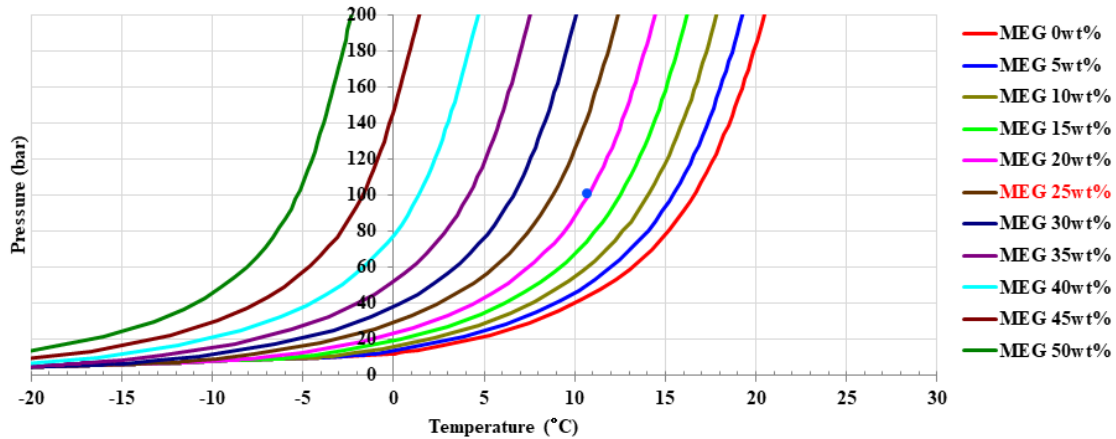
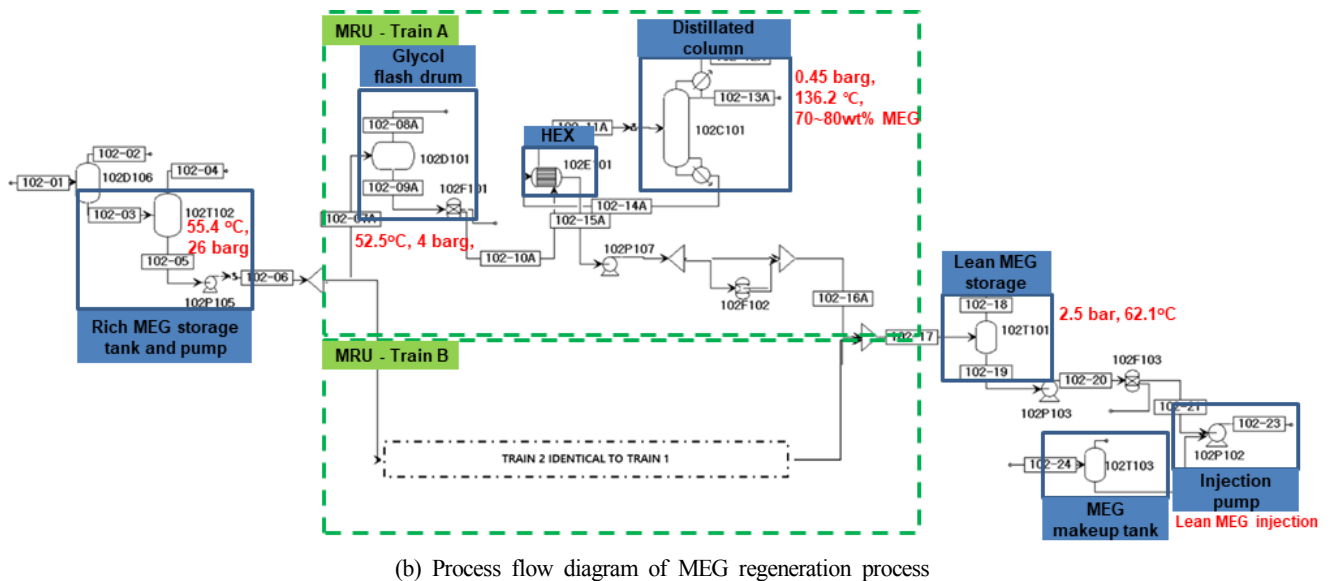


Fig. 1 Schematic diagram of the experimental apparatus



(a) Hydrate equilibrium conditions for gas field



(b) Process flow diagram of MEG regeneration process

Fig. 2 Hydrate equilibrium conditions to determine MEG concentration for subsea flowlines and detailed diagram of MEG regeneration process

Southeast Asia and Middle East are primarily developed at the maximum depth of 100 m, and the water temperature remains at least 30 °C in the summer and 10 °C in the winter. The production pressure of a reservoir is at least 15 MPa, but subsea pipelines are operated at 10 MPa from the subsea tree to the platform. Considering the operation conditions of shallow water gas fields, the conditions for hydrate formation set in the thermodynamic simulation software (Multiflash, version 20) are shown in Fig. 2(a). If the sea water temperature is assumed to be 10 °C, then the hydrate is predicted to form when the pressure of the fluid flowing through the subsea pipelines exceeds 4 MPa. Hydrates may form depending on the season since the subsea pipelines in a typical gas field are operated at a pressure higher than 4 MPa. To prevent hydrate formation, the concentration must be maintained above 25 wt% by adding MEG to the water flowing through subsea pipelines, as shown in the phase equilibrium graph in Fig. 2(a). Therefore, the MEG regeneration process is required, through which MEG is injected into subsea pipelines and the

concentration of the MEG solution is increased from 25 wt% to 70 wt% or greater. Fig. 2(b) shows the simulation model built using Aspen Plus version 9.0 for the MEG regeneration process of shallow water gas fields. It comprises two trains, which account for the production cycle of gas fields. The MEG solution having 25 wt% concentration retrieved from subsea pipelines was stored in the rich MEG storage tank and then increased to 70 wt% concentration or higher in the MEG flash drum and distillation column. The regenerated lean MEG was stored in the lean MEG storage tank and then injected into subsea pipelines using an injection pump. The operation condition of each unit was analyzed using the electrolyte non-random two liquid (ENRTL)-Redlich-Kwong (RK) models. The type, material, and size of the process were determined using the Aspen process economic analyzer. The ENRTL-RK model can be used to predict the major properties of a fluid based on vapor-liquid phase equilibrium. The RK model was used to calculate the fugacity of a vapor. The ENRTL model was used to calculate the activity coefficient

of a liquid and can be applied to various systems containing electrolytes. The binary interaction parameters of the ENRTL model were revised using Aspen Plus version 9.0 and the vapor pressure data of MEG solution reported in the literature.

To express the excess Gibbs energy (G^{ex}), the ENRTL model uses the Pitzer-Debye-Huckel equation ($G^{ex,PDH}$) and Born equation ($G^{ex,Born}$) to calculate long-range ion interactions, as well as $G^{ex,lc}$ to calculate short-range ion, ion-molecule, and molecular interactions. The sum of interactions can be expressed as follows:

$$\frac{G^{ex}}{RT} = \frac{G^{ex,PDH}}{RT} + \frac{G^{ex,Born}}{RT} + \frac{G^{ex,lc}}{RT} \quad (1)$$

Therefore,

$$\ln \gamma_i^{ex} = \ln \gamma_i^{PDH} + \ln \gamma_i^{Born} + \ln \gamma_i^{lc} \quad (2)$$

Here, T is the temperature, R the gas constant, γ the activity coefficient of a liquid, and i the ion type.

The Pitzer-Debye-Huckel equation for expressing long-range ion-ion interactions is as follows:

$$\ln \gamma_i^{PDH} = - \left(\frac{1000}{M} \right)^{\frac{1}{2}} \left[\left(\frac{2Z_i^2}{\rho} \right) \ln \left(1 + \rho I^{\frac{1}{2}} \right) + \frac{Z_i^2 I_x^{1/2} - 2I_x^{1/2}}{1 + \rho I_x^{1/2}} \right] \quad (3)$$

Here, A_ϕ is the Debye-Huckel constant, I_x the ionic strength, Z the charge of an ion, and ρ the density of the mixed solution. The Born equation is shown below.

$$\ln \gamma_i^{Born} = \frac{N_A z_i^2 e^2}{8\pi \epsilon_0 r_i K T} \left(1 - \frac{1}{\epsilon_r} \right) \quad (4)$$

Here, ϵ_0 and ϵ_r are the dielectric constants of the solvent and water, respectively; γ_i is the Born radius of an ion particle i ; N_A is the Avogadro constant; z_i is the charge of an ion; e is the elementary charge.

The short-range ion, ion-molecule, and molecular interactions can be expressed as follows:

$$\frac{X_{ji}}{X_i} = \left(\frac{X_j}{X_i} \right) G_{ji} \quad (5)$$

$$X_i = x_i C_i \quad (6)$$

$$\tau_{ij} = A_{ij} + \frac{B_{ij}}{T} + C_{ij} \left[\frac{T^{ref} - T}{T} + \ln \left(\frac{T}{T^{ref}} \right) \right] \quad (7)$$

Here, x_i is the mole fraction of i ; C_i is the absolute charge of an ion; α_{ij} is the non-randomness factor ($= 0.2$); i and j are the molecule and electrolyte, respectively; τ_{ij} is the binary interaction energy parameter;

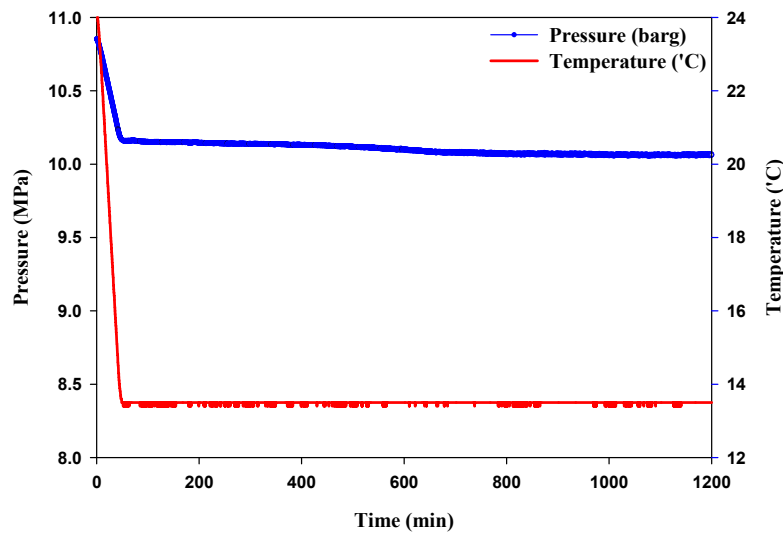
A_{ij} , B_{ij} , and C_{ij} are the temperature coefficients when $T^{ref} = 298.15$ K.

Once the design of the MEG regeneration process has been completed, the capital expenditures (CAPEX) were analyzed based on the equipment cost, whereas the operating expenditures (OPEX) were analyzed considering the fixed CAPEX, utility costs, and operation period. The life cycle cost (LCC) of the MEG regeneration process was calculated by summing the CAPEX and OPEX. In general, a lean MEG concentration of 70–90 wt% is selected to minimize the CAPEX and OPEX of a gas production platform. The platform for deep water gas fields is maintained at 80 wt% or above, but that of shallow water gas fields is maintained at 70 wt%. Hence, the operation adequacy and economic feasibility of the MEG regeneration process must be analyzed simultaneously to determine the optimal lean MEG concentration. In this study, the process design and economic feasibility were analyzed after increasing the MEG solution with 25 wt% concentration retrieved from subsea pipelines to concentrations of 70 wt% and 80 wt%.

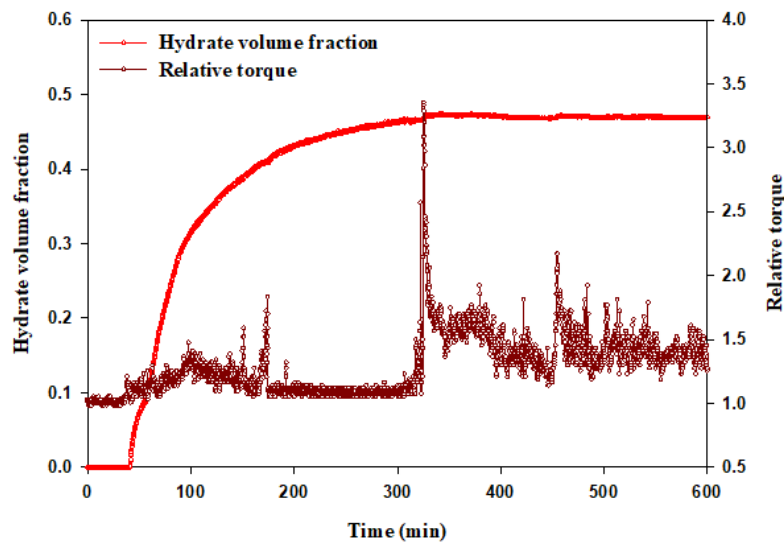
3. Experimental Results of Hydrate Formation Risk Evaluation

3.1 Experimental Results of Hydrate Formation in Pure Water

Hydrate formation in pure water was observed experimentally, in which hydrate inhibitors such as MEG and KHI were not injected. Fig. 3(a) illustrates the pressure-temperature diagram of hydrate formation in the operation conditions of subsea pipelines for shallow water gas fields. The starting temperature of the experiment was 23 °C and then reduced to 10 °C, which is the typical temperature of shallow water region in the winter, for over 1 h. The starting pressure of the experiment was 11 MPa, and hydrate formation occurred at a temperature lower than the hydrate formation temperature despite a decrease in the pressure within the reactor owing to a temperature decrease. Table 1 shows the hydrate formation temperature and pressure, which were measured thrice during the experiment; the delay time of hydrate formation was calculated accordingly. The average delay time of hydrate formation was 21.7 min, and the average water conversion rate was 46%. The experimental results show that water flowing in subsea pipelines can form hydrates after approximately 20 min even in shallow water regions. Fig. 3(b) shows the changes in torque observed during hydrate formation along with the hydrate volume fraction. The hydrate volume began increasing after a 20 min delay in formation time, whereas the torque, or the resistance against the flow, decreased simultaneously. The torque decreased after the volume fraction exceeded 0.3, but the change in torque exhibited several peaks rather than a continuous change after the volume fraction exceeded 0.4. Heterogeneous segregation occurred, in which water and hydrates became separated as the hydrate volume fraction increased beyond 0.4; additionally, a bedding was further developed, where hydrates were deposited on the walls of the stirred-tank reactor. Furthermore, 300 min after the hydrate had started to form, the relative torque reached a peak at 3.5 and showed a continuous fluctuation. The



(a) Pressure-temperature diagram as a function of time in bulk water



(b) Hydrate volume fraction as a function of time during hydrate formation

Fig. 3 Hydrate formation characteristics in bulk water without adding hydrate inhibitors**Table 1** Quantitative analysis of hydrate formation characteristics

Experiment No.	ΔT_{sub}^1 (K)	t_{onset}^2 (min)	Hydrate volume fraction	Water conversion (mol%)	Max relative torque
1	6.0	23.8	0.57	51.73	2.24
2	6.3	25.3	0.47	41.68	3.36
3	3.6	15.8	0.50	45.34	3.51
Average value	5.3	21.7	0.51	46.25	3.04
Standard deviation	1.2	4.2	0.04	4.15	0.69

¹ ΔT_{sub} indicates temperature difference between hydrate formation conditions and equilibrium condition.

² t_{onset} indicates the time when hydrate formation is initiated.

hydrates started to collide and constantly ground with the impeller as the amount of hydrates being deposited on the walls and floor of the reactor increased, thereby resulting in significant fluctuations in the relative torque.

In subsea pipelines, hydrate formation begins as pure water flows through the pipes, and a constant flow can be maintained when the hydrate volume fraction is 0.3 or below. However, plugging occurs, i.e., the increased deposition of hydrate blocks the fluid flow when the

hydrate volume fraction exceeds 0.4. The reactor used in the experiment was constantly applied with mixing energy using an external motor, which caused the hydrates to be ground. However, plugging will occur in subsea pipelines when the amount of energy of gas pushing water through the pipes is insufficient. Furthermore, plugging will occur more easily in subsea pipelines as bended points exist in pipes where the fluid velocity decreases.

3.2 Hydrate Inhibition Performance of KHI

Fig. 4 shows the hydrate experimental results when a KHI was injected. BASF's Luvicap was used as a KHI, and the concentration was maintained at 2.4 wt% for this experiment. As shown in the figure, hydrate formation was not observed for 20 h, during which the concentration of Luvicap was maintained at 2.4 wt%. The experiment was repeated thrice using pure water, but hydrate formation was not observed for 20 h. The temperature and pressure were maintained at 10 °C and 10 MPa, respectively. This result indicates that hydrate formation was inhibited for 20 h when Luvicap was injected to maintain the concentration at 2.4 wt%. When the subsea pipelines in shallow water gas fields were assumed to be 40 km long, the time that water remained in the subsea pipelines was calculated to be 4.4 h at

the maximum when the production output was low. Therefore, water can be prevented from converting to hydrates if a sufficient amount of Luvicap is injected as a hydrate inhibitor to maintain the concentration of water flowing in the subsea pipelines, i.e., 2.4 wt% or higher. Accordingly, it is confirmed that Luvicap suffices as a KHI if the temperature of subsea pipelines in shallow water region can be maintained at 10 °C.

However, as explained earlier, using a KHI alone is insufficient to prevent hydrate formation when an operation is halted for a long time, or for extended shut-ins. Therefore, MEG must be injected, and the injected MEG must be converted to lean MEG through the regeneration process on the offshore platform.

4. MEG Regeneration Process Simulation Results

The simulation results of the MEG regeneration process obtained from Aspen Plus version 9.0 are shown in Fig. 2(b) above. The rich MEG (concentration 25 wt%) injected into the subsea pipelines was stored in the storage tank at 2.6 MPa and then sent to the MEG regeneration process. The flow rate was 27,317.2 kg/h. Natural gas and condensates were removed in the MEG flash drum in advance and then

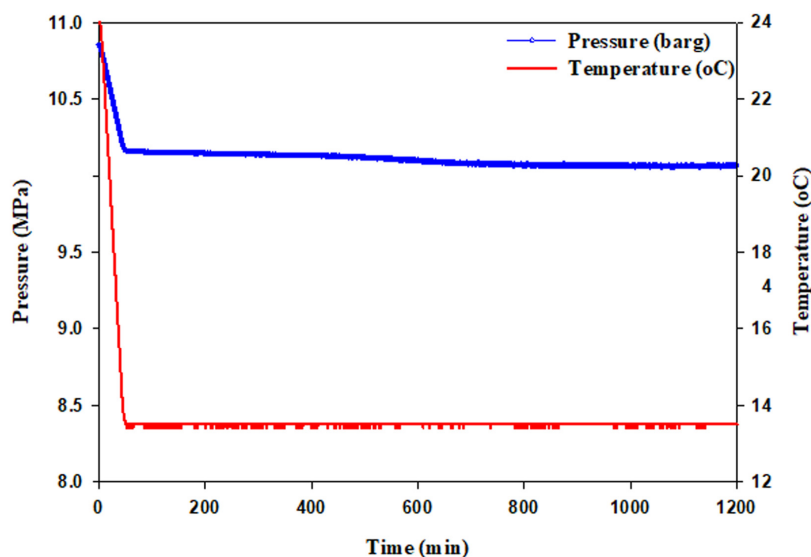


Fig. 4 Pressure-temperature diagram as a function of time in 2.44 wt% Luvicap solution. No hydrate formation was observed.

Table 2 Description of operating conditions of main equipment

Main process equipment		Operating temperature (°C)	Operating pressure (MPa)
Rich MEG flash drum	102D106	55.4	2.6
Glycol flash drum	102D101	52.5	4.0
Column unit	102C101	128.1 (Lean MEG 70 wt%) 137.6 (Lean MEG 80 wt%)	0.15
Heat exchanger between lean MEG and rich MEG (Shell and tube)	102E103	62.5	0.15
Injection pump	102P102	30.0	13.0
Lean MEG tank	102T101	62.1	0.25
Rich MEG tank	102T102	55.4	2.6

supplied to the MEG distillation column through a filter and a heat exchanger. The MEG distillation column was operated at 0.15 MPa. To increase the MEG concentration from 25 wt% to 80 wt% and 70 wt%, the temperature must be maintained at 137.6 °C and 127.5 °C, respectively. Vapor was discharged through the top of the distillation column, and the lean MEG with increased concentration was retrieved through the bottom to be sent to the storage tank. The MEG concentration required for subsea pipelines was 25 wt%; hence, an injection at 13.03 MPa using an injection pump was required. The operating conditions of the main equipment constituting the process are shown in Table 2.

The boiling points of water and MEG are 100 °C and 197 °C, which differ significantly; therefore, rich MEG can be easily converted to lean MEG through the distillation column. However, the water produced from a reservoir flowing into subsea pipelines contains a large amount of salt substances such as NaCl, which can result in the deposition of salt in the reboiler during the distillation process. If the salt concentration of the produced water is assumed to be 30 g/L for the shallow water gas fields being studied, salt deposition will not occur because the allowable NaCl concentration of lean MEG is 76 g/L when the MEG concentration is increased to 80 wt%. A separate study is being conducted to investigate the risk of salt deposition, which will be presented in the near future.

The MEG regeneration process using a distillation column consumes a large amount of energy; therefore, technical implementations are necessitated to reduce the CAPEX and OPEX. More specifically, the

distillation column temperature can be maintained at 137.6 °C while increasing the lean MEG concentration to 80 wt%, or the distillation column temperature can be maintained at 128.1 °C while increasing the lean MEG concentration to only 70 wt%. The lean MEG concentration can be increased up to 90 wt% for deep water gas fields, but the economic feasibility of increasing the lean MEG concentration to 80 wt% by applying a significant amount of heat energy for shallow water gas fields must be investigated. In this study, an LCC analysis was performed for both the CAPEX and OPEX required for the operation and performing the MEG regeneration process. The LCC analysis was conducted to determine the size of major equipment based on the results of simulating the MEG regeneration process, which was performed previously, and to calculate the equipment cost using the Aspen economic analyzer. The CAPEX were calculated based on the cost of each piece of equipment (Peters et al., 1968), whereas the OPEX were predicted based on the CAPEX (Turton et al., 2008). The following were assumed for assessing economic feasibility. First, only the electricity, steam, and coolant costs were considered for the OPEX. The process reliability and annual operation hours were assumed to be 91.3%/y and 8,000 h/y, respectively, for the MEG regeneration process. The pump efficiency was 70%, and the reserved pump and heater were not considered. Low-pressure and high-pressure steams were used for heating, whereas a coolant was used for cooling. The heating and cooling capacities calculated from the process simulation were used. The operation cost including utilities might vary depending on the region and corresponding year; hence, the calculation performed

Table 3 Total capital investment for MEG regeneration package in case of regenerating up to 70 wt% and 80 wt% lean MEG

Equipment	Lean MEG 70 wt%		Lean MEG 80 wt%	
	Size ($D \times L$, m) ¹	Equipment cost (MMUSD) ²	Size ($D \times L$, m)	Equipment cost (MMUSD)
Glycol flash drum	1.37 × 4.27	0.02	1.37 × 4.27	0.02
Rich MEG flash drum	1.67 × 5.03	0.08	1.67 × 5.03	0.08
Lean meg tank	11.52 × 5.76 (600 m ³)	0.34	11.52 × 5.76 (600 m ³)	0.34
Rich meg tank	13.66 × 6.83 (1000 m ³)	1.84	13.66 × 6.83 (1000 m ³)	1.84
Distillation column	3.65 × 7.01	0.64	4.11 × 7.92	0.79
Booster pump after rich MEG storage tank		0.02		0.02
Booster pump after column		0.01		0.01
Lean meg booster pump		0.01		0.01
Injection pump		0.34		0.32
Starting pump (5 m ³ /h)		0.00		0.00
Heat exchanger between lean MEG and rich MEG		0.03		0.03
Rich MEG filter		0.03		0.03
Charcoal filter		0.01		0.01
Lean MEG fileter		0.03		0.03
Purchased equipment cost		3.42		3.54
CAPEX		17.21		17.83

¹ $D \times L$ indicates diameter and length, respectively; ²MMUSD is million US dollars.

in this study was based on the Southeast Asia region in 2018. The LCC was calculated as the sum of the total CAPEX and OPEX that will be input for 20 years, or the total operation time of the MEG regeneration process. The discount rate was assumed to be 8%. The factors affecting the CAPEX included the operation conditions, equipment type, and materials. The CAPEX were mainly affected by the large MEG storage

Table 4 OPEX for MEG regeneration package in case of regenerating up to 70 wt% and 80 wt% Lean MEG

	Lean MEG concentration	
	70 wt% OPEX (MMUSD)	80 wt% OPEX (MMUSD)
Initial raw material cost	2.38	2.38
Raw material costs (C_{RM})	31.11	31.11
Utilities costs (C_{WT})		
Electricity	1.59	1.39
Cooling water	7.33	8.07
LP steam	26.77	29.43
Operating labor (C_{OL})	7.07	7.07
Maintenance and repair (C_{MT})	8.62	8.94
Service, supplies and charges	1.29	1.34
Laboratory charges	1.06	1.06
Patents and royalties	4.17	4.33
Fixed costs		
Depreciation	14.37	14.89
Local tax and Insurance	2.87	2.98
Plant overhead	9.42	9.60
Total manufacturing cost	7.07	7.07
General expenses		
Selling costs	13.89	14.42
General & administrative costs	2.35	2.40
Research and development	6.94	7.21
OPEX	141.25	146.61

tank, distillation column, and injection pump of the MEG regeneration process. The CAPEX increased due to an increase in the height of the distillation column when the lean MEG concentration was set to 80 wt%. By contrast, the MEG injection pump capacity as well as the CAPEX decreased when the flow rate of MEG being injected into the subsea pipelines decreased. Table 3 shows the analysis results of the CAPEX for the MEG regeneration process when the lean MEG concentrations were set to 70 wt% and 80 wt%.

The factors affecting the OPEX included utility and maintenance/repair costs. The MEG injection flow rate and pump capacity both decreased when the lean MEG concentration was 80 wt%, thereby lowering the electricity cost of the injection equipment. However, the energy cost increased with the amount of low-pressure steam usage owing to the temperature increase in the distillation column. The maintenance/repair costs of the major equipment were affected significantly by the initial equipment price and the equipment size. Table 4 shows the OPEX when the lean MEG concentrations were set to 70 wt% and 80 wt%. The initial cost of the raw material included the initial MEG cost and operation cost. The initial MEG injection amount was determined based on the assumption that MEG was injected to the subsea pipelines for 12 h.

The LCC of the MEG regeneration process can be predicted using the CAPEX and OPEX presented in Tables 3–4. Fig. 5 shows the major equipment cost and utility cost of the MEG regeneration process. The LCC, which is the sum of the CAPEX and OPEX, was 158.46 and 164.44 MMUSD when the lean MEG concentrations were set to 70 wt% and 80 wt%, respectively. The major equipment size and operation cost varied based on the lean MEG concentration, and it was confirmed that maintaining the lean MEG concentration at 70 wt% was more advantageous for the MEG regeneration process.

5. Conclusion

This study proposed injecting both KHI and MEG simultaneously to inhibit hydrate formation for shallow water gas fields. For the normal operation state, injecting a KHI prevented the formation of hydrates

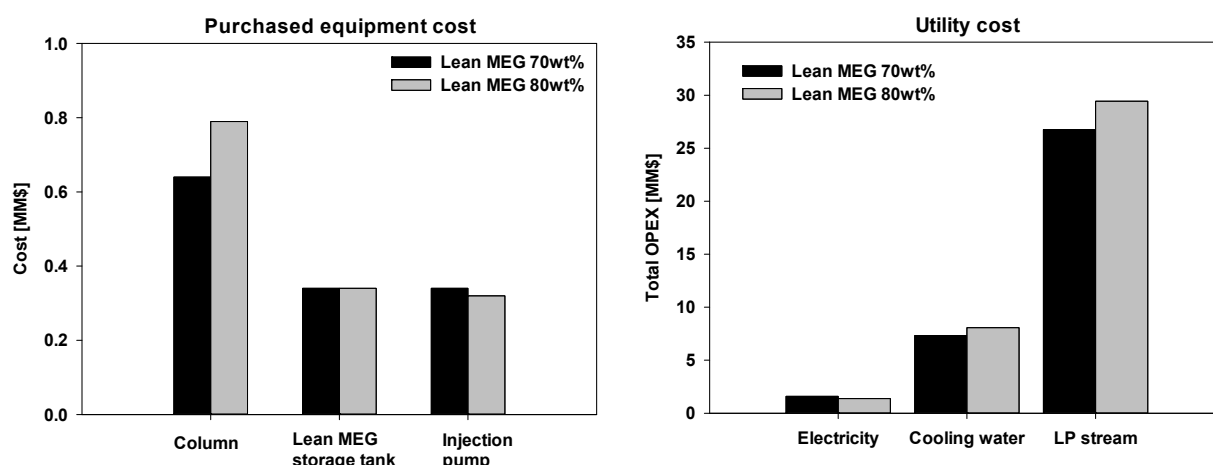


Fig. 5 Major purchased equipment cost and utility costs

while the fluid being produced through subsea pipelines. It was confirmed through experiments that injecting Luvicap at 2.4 wt% suppressed hydrate formation for 20 h. For subsea pipelines measuring 40 km, the fluid remained in the pipes for 4.4 h, thereby enabling the injection of Luvicap to inhibit hydrate formation. As sea water temperature significantly affects hydrate formation, not injecting a KHI in the summer when the sea water temperature is high is an alternative. However, in the winter, a KHI must be injected constantly and MEG should be injected if the platform operation is halted for equipment replacement or maintenance and repair.

The MEG regeneration process is utilized to regenerate the injected rich MEG into lean MEG; therefore, the CAPEX and OPEX must be minimized. In this study, an LCC analysis was conducted by calculating the operation cost, in which the initial cost of the raw material and C_{RM} were the same while the lean MEG concentration in the MEG regeneration process was varied. The calculated LCC was low when the lean MEG concentration was 70 wt%. The initial equipment cost was more economical when the concentration was 70 wt%; hence, it was more favorable to set the concentration to 70 wt% for the operation condition of the MEG regeneration process. Although using hydrate inhibitors such as MEG or KHI can prevent accidents caused by hydrate formation in gas field pipelines and hence reduce the related maintenance/repair costs, an LCC analysis for the economic feasibility through the optimization of lean MEG concentration is crucial in building a sustainable system.

Finally, sustainable and advanced technologies should be applied to actual projects since CAPEX and OPEX can be reduced by selecting flexible strategies for inhibiting hydrate formation.

References

- Brustad, S., Løken, K.-P., & Waalman, J.G. (2005). Hydrate Prevention Using MEG Instead of MeOH: Impact of Experience from Major Norwegian Developments on Technology Selection for Injection and Recovery of MEG. Offshore Technology Conference, Houston, Texas. <https://doi.org/10.4043/17355-MS>
- Kim, H., Lim, Y., Seo, Y., & Ko, M. (2017). Life Cycle Cost Analysis of MEG Regeneration Process Incorporating a Modified Slip Stream Concept. *Chemical Engineering Science*, 166, 181-192. <https://doi.org/10.1016/j.ces.2017.03.045>
- Kim, H., Yoo, W., Lim, Y., & Seo, Y. (2018a). Economic Evaluation of MEG Injection and Regeneration Process for Oil FPSO. *Journal of Petroleum Science and Engineering*, 164, 417-426. <https://doi.org/10.1016/j.petrol.2018.01.071>
- Kim, H., Veluswamy, H. P., Seo, Y., & Linga, P. (2018b). Morphology Study on the Effect of Thermodynamic Inhibitors during Methane Hydrate Formation in the Presence of NaCl. *Crystal Growth & Design*, 18(11), 6984-6994. <https://doi.org/10.1021/acs.cgd.8b01161>
- Kim, H., Kim, J., & Seo, Y. (2020). Economic Benefit of Methane Hydrate Reformation Management in Transport Pipeline by Reducing Thermodynamic Hydrate Inhibitor Injection. *Journal of Petroleum Science and Engineering*, 184, 106498. <https://doi.org/10.1016/j.petrol.2019.106498>
- Peters, M.S., Timmerhaus, K.D., West, R.E., Timmerhaus, K., & West, R. (1968). *Plant Design and Economics for Chemical Engineers*, 4. McGraw-Hill, New York.
- Park, J., Kim, H., da Silveira, K.C., Sheng, Q., Postma, A., Wood, C.D., & Seo, Y. (2019). Experimental Evaluation of RAFT-based Poly (N-isopropylacrylamide)(PNIPAM) Kinetic Hydrate Inhibitors. *Fuel*, 235, 1266-1274. <https://doi.org/10.1016/j.fuel.2018.08.036>
- Turton, R., Bailie, R.C., Whiting, W.B., & Shaeiwitz, J.A. (2008). *Analysis, Synthesis and Design of Chemical Processes*. Pearson Education.

Author ORCIDs

Author name	ORCID
Lee, Suk	0000-0002-9378-0477
Kim, Hyunho	0000-0001-7846-2166
Park, Ki-Heum	0000-0002-4385-2786
Seo, Yutaek	0000-0001-8537-579X

Preliminary Investigation for Feasibility of Wave Energy Converters and the Surrounding Sea as Test-site for Marine Equipment

Jin-Yeong Park¹, Hyuk Baek², Hyungwon Shim³ and Jong-Su Choi⁴

¹Principal researcher, Ocean System Engineering Research Division, KRISO, Daejeon, Republic of Korea

²Senior engineer, Ocean System Engineering Research Division, KRISO, Daejeon, Republic of Korea

³Principal researcher, Alternative Fuels and Power System Research Center, KRISO, Daejeon, Republic of Korea

⁴Principal researcher, Marine Renewable Energy Research Division, KRISO, Daejeon, Republic of Korea

KEY WORDS: Oscillating water column, Multi-beam echo sounder, Single-beam scanning sonar, Test-site, Functional modelling(IDEF0)

ABSTRACT: Of late, demand for test sites for marine equipment such as ASV, AUV, ROV, and various underwater sensors is increasing. The authors have focused on an oscillating water column (OWC), which is being constructed near Chagwido Island Jeju, as one of the test-sites. The main objective of the OWC is to produce wave energy and develop technologies. It has been built in the sea approximately 1 km off the coast. It has berth accommodation and some rooms that can be used as laboratories. To investigate the feasibility of its usage as a test site for marine equipment, we acquired bathymetric data around the OWC by using a multi-beam echo sounder and a single-beam scanning sonar. The accessibility of the OWC from nearby ports and the use of support vessels or ships were also investigated. 3D point cloud data from the multi-beam echo sounder and 2D acoustic images from the scanning sonar are expected to be used as references for identifying changes over time. In addition, through these experiments, we derived a procedure to use this facility as a test site by using the IDEF0 functional modelling method. Based on this preliminary investigation and previously reported examples, we determined the general conditions and preferences for evaluating the performance of various marine equipment heuristically. Finally, we developed five applications that were derived from this investigation.

1. Introduction

Of late, demand for sites and platforms to test the performance of marine equipment and underwater and surface robots during the development process has been increasing in South Korea. The Korea Research Institute of Ships and Ocean Engineering(KRISO) has performed unit performance and overall performance tests at the Jangmok wharf in Geoje-si, where the South Sea Research Institute (SSRI) of the Korea Institute of Ocean Science and Technology (KIOST) is located, and engaged in the development of a deep-sea remotely operated vehicle (ROV), Hemire, and an autonomous underwater vehicle (AUV), ISiMI 100 (Baek et al., 2008; Jun et al., 2009). Tests for the location estimation performance of underwater vehicles were also performed in the inland environment of Jangseongho in Jeollanam-do (Choi et al., 2019a). Defense industry companies carried out experiments for motion characteristic modeling

of AUVs for underwater reconnaissance and hydrodynamic coefficient adjustment and experiments for performance verification in the real sea at the South Sea Research Institute wharf (Park et al., 2015; Lee et al., 2015). Other experiments, mostly for the development performance verification of individual maritime unmanned vehicles, are being carried out in the coastal sea of the Jinhae Naval Academy in Gyeongsangnam-do, the Korea Maritime and Ocean University wharf in Busan, the coastal sea of Pohang, Gyeongcheonho in Mungyeong, and Bangdongho in Daejeon (Jeollabuk-do, 2019). The sites mentioned above need to separately provide facilities required for test preparation, including space for maintenance and repair of test equipment on land including wharf facilities. The need and demand for performance verification in real sea environments is also increasing with the increasing levels of technology and equipment being developed.

The Ministry of Maritime Affairs and Fisheries is building a 5 MW

Received 19 February 2020, revised 5 September 2020, accepted 15 September 2020

Corresponding author Jin-Yeong Park: +82-42-866-3835, jinyeong96@kriso.re.kr

It is a recommended paper from the Proceedings of the 2019 Fall Conference of the Korea Marine Robot Technology (KMRTS), which is one of the divisions of the Korean Society of Ocean Engineers (KSOE).

© 2020, The Korean Society of Ocean Engineers

This is an open access article distributed under the terms of the creative commons attribution non-commercial license (<http://creativecommons.org/licenses/by-nc/4.0>) which permits unrestricted non-commercial use, distribution, and reproduction in any medium, provided the original work is properly cited.

test infrastructure in the sea near Chagwi Island of Jeju-do for the distribution and expansion of wave power generation and promotion of related domestic industries. The final goal of the infrastructure is to allow performance evaluation, installation and recovery technique verification, operating technique optimization, and system stability tests of wave power generators. Various performance tests related to wave power generation are expected to be performed after the completion of the infrastructure (Choi et al., 2019b). Among those wave power generators, the oscillating water column (OWC) wave power generator (or wave power test-bed) constructed in the sea is expected to provide test environments for a variety of maritime equipment in addition to wave power generation-related technologies, as facilities for supplying electricity and relaying communication can be additionally installed and space for maintenance and operation of mid and small equipment can be secured.

The Oceanic Platform of the Canary Islands (PLOCAN), which is representative of similar overseas facilities, is currently used based on the technical science services of multipurpose maritime equipment. It has ROVs and underwater gliders and has secured approximately 23 km² of sea as a test site. Using PLOCAN, tests are being performed on a variety of equipment (González et al., 2015). This includes application to ocean surveillance technology development by using an autonomous surface vehicle (ASV) equipped with a passive acoustic signature detector (ASD) in the Protecting European Seas and Borders through the Intelligent Use of Surveillance (PERSEUS), carried out with support from the European Union (Real-Arce et al., 2015). This study describes preliminary research on the investigation of the suitability of OWC as infrastructure in maritime equipment tests. The preliminary research is to procure terrain information for the underwater lower structure of a wave power test-bed and the surrounding seabed environment. To do so, multi-beam echo sounder (MBES) and single-beam scanning sonar (hereafter, the scanning sonar) data are to be acquired using a vessel. In operation, the MBES is mounted on the bottom of a vessel and the scanning sonar is launched and installed on the seabed. The former acquires three-dimensional point clouds, whereas the latter obtains two-dimensional images. The above two types of equipment are typical seabed mapping sensors. First, the seabed space information around the OWC is acquired to be taken into consideration when selecting target test equipment and establishing test plans. In addition, the case where maritime equipment performance tests are carried out using small vessels is postulated to derive a model based on the integrated computer-aided manufacturing (ICAM) definition (IDEF0) for function modeling, and refer to the model for the identification of the required conditions, criteria, resources, etc. Jangmok No. 1 belonging to the SSRI, KIOST was used in the tests. The vessel is equipped with the necessary equipment including a MBES for this experiment. The measurement data of the MBES were processed along with the location and attitude data of the vessel to extract and store three-dimensional points with respect to the earth-fixed coordinate system. The computers for the scanning sonar operation and its data storage needed to be prepared separately. The

tests were carried out for two days in April 2019.

The wave power test-bed and environment, including location characteristics and building specifications, are introduced in Chapter 2. Chapter 3 describes experiments using the MBES and scanning sonar and includes experiment goals to demonstrate the experimental results for each sensor and the results of establishing the experiment procedure using an IDEF0 function modeling method. Suitability analysis results and characteristics of the experiment environment of the OWC and derived, and applicable fields/businesses are described in Chapter 4.

2. Wave Power Test-Bed Site

2.1 Wave Power Test-Bed

The wave power test-bed is being constructed in the sea near Chagwi Island of Jeju-do. The surrounding sea has high wave energy density and light maritime traffic, and includes medium ports such as the Hallim port and Aewol port. The appropriateness of the site was verified through seabed exploration (Kim et al., 2017). The wave power test-bed site consists of total five berths, with Berth 1 being the OWC wave power generator. Fig. 1 shows the conceptual diagram. The offshore substation installed on the sea is the OWC. Fig. 2 shows the size using the upper structure of the OWC exposed above the sea surface (left) and three-dimensional modeling (right). The height of the OWC from the seabed is 27.5 m, and the tide-dependent height of

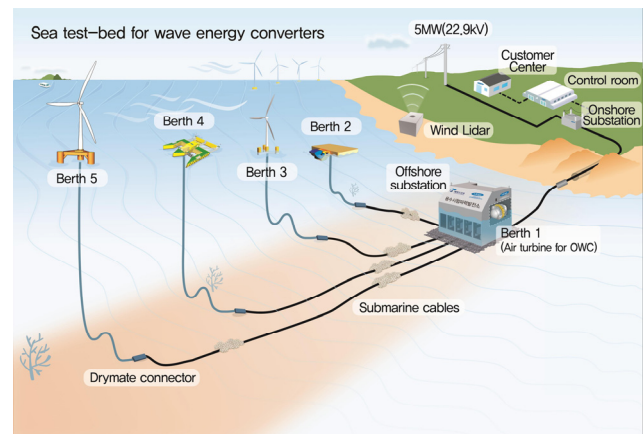


Fig. 1 Conceptual art of arrangement for open sea test site for wave energy converter

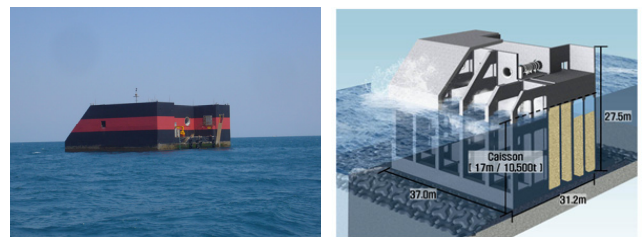


Fig. 2 Structure of the OWC (Oscillating Water Column) exposed above the sea surface (left). Perspective view of 3D modelling of the OWC structure showing its size (right)



Fig. 3 PLOCAN platform (PLOCAN, 2020)

the protruding portion above the sea surface is approximately 15 m. The length and width are 37.0 m and 31.2 m, respectively. The seabed terrain includes bedrock expected to have little feature change. The depth of water ranges from 10 m to 60 m. The turbidity is relatively lower than the West/South Sea. Power cables are laid here after construction. Fig. 3 shows the PLOCAN platform. PLOCAN is used as a real sea test-bed for ocean energy and maritime equipment similar to the OWC and is separated from the coast by 1.85 km. It is constructed in a region with a water depth of 30.5 m. The total area used is 5000 m², and the length and width are 33 m and 38 m, respectively. It has a helicopter deck, gantry crane, office space, drinking water purifier, and launch and recovery system (LARS). It includes a Seabotix ROV and a Slocum glider (PLOCAN, 2019).

2.2 Surrounding Environment

Nearby ports include Yongsu-ri, Hallim, and Aewol. The Yongsu-ri port is the closest, and the Aewol port is the farthest. Small ports exist between the three ports. A port limits the scale of the support vessel using it, which requires space for storage, management, repair, and must facilitate loading and unloading of sensors and equipment to be tested. The ports mentioned above do not meet these requirements. Weather and sea state are important elements of offshore experiments. Thus, time and space in preparation for these elements need to be secured.

The sea west of Jeju-do, on which wave power test facilities are built, along with the islands Dokdo, Ulleungdo, and Hongdo, is known as an area with high wave energy in South Korea (Ryu et al., 2011). Wave energy data for the power generation performance evaluation of a wave power generator is collated (Park et al., 2019), and numerical wave models are being developed. A database for wind direction and wind velocity information using wind light detection and ranging (LiDar) is also constructed.

3. MBES and Scanning Sonar Experiment

There are two main objectives of this experiment.

- Collect information on the seabed terrain around the OWC, and
- Collect fundamental information for establishing a performance test procedure around the OWC using a small vessel.



Fig. 4 Research vessel Jangmok No. 1

Once the information on the seabed terrain around the OWC is collected, changes caused by the construction of the OWC can be verified and are expected to be used as a reference in tracking seabed environment changes caused by the OWC or similar structures after a certain amount of time elapses. Moreover, a procedure for the case in which performance tests of maritime equipment are carried out around the OWC using a small vessel, is to be established through this experiment.

The support vessel used in this experiment is Jangmok No. 1 of the SSRI of KIOST. It is a small research vessel for coastal exploration and observation activities such as domestic coastal seabed geology, underwater resource exploration, and terrestrial magnetism investigation. Its full length is 24.22 m, international gross tonnage is 41 t, and sea speed is 13 kn (6.7 m/s). A maximum of 15 people (4 crew members and 11 researchers) can be onboard (KIOST, 2019a). Fig. 4 shows Jangmok No. 1. Typical sensors installed on it include conductivity temperature depth (CTD), sub-bottom profiler (SBP), acoustic Doppler current profiler (ADCP), EA400, and MBES.

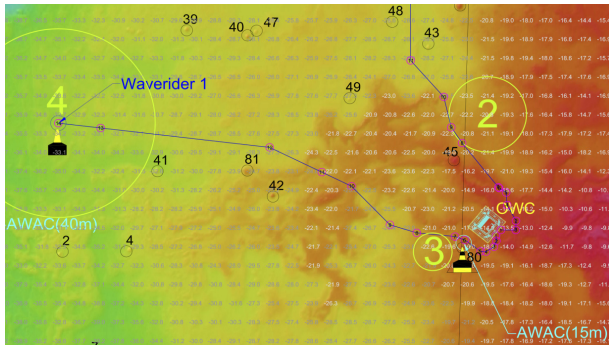
3.1 Multi-Beam Echo Sounder

The MBES installed on the bottom of Jangmok No. 1 is EM3002 and is provided by Kongsberg (Table 1). The data were acquired by turning the OWC around. A separate calibration process for the MBES prior to data acquisition was not undertaken due to limitations including budget and test schedule.

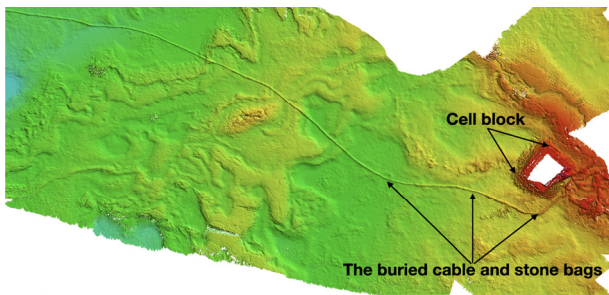
Fig. 5 shows the MBES results before OWC construction (a), and the MBES results acquired around the OWC along the submarine cables in this experiment (b). Although accurate comparisons of

Table 1 Specifications of EM3002 Kongsberg

Item	Description
Frequencies	293, 300, and 307 kHz
Number of sounding per ping:	
Single sonar head	Max. 254
Dual sonar head	Max. 508
Max. ping rate	40 Hz
Pulse length	150 μs
Depth resolution	1 cm



(a) Arrangement plan of the OWC and submarine cables



(b) Actual arrangement of the OWC and submarine cables

Fig. 5 A before-and-after comparison of the bathymetric images

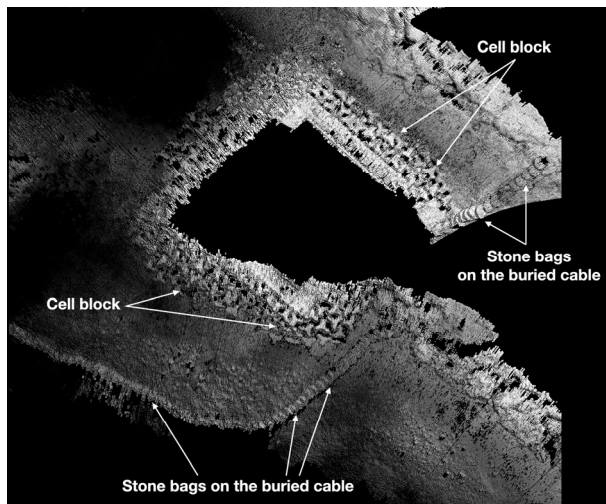


Fig. 6 Back-scattering data image

of the OWC can be verified. Fig. 6 is a back-scattering data image. Fibrous stone bags stacked on top of each other to protect the submarine cables and cell blocks around the lower structure of the OWC can be observed more clearly. Fig. 7 shows the cell blocks and stone bags photographed by an imaging camera.

3.2 Single-Beam Scanning Sonar

The scanning sonar used in this study is the 1171 high resolution scanning sonar model provided by Kongsberg Mesotech. Its detailed specifications are listed in Table 2. It is operable up to a maximum depth of 3000 m and uses a frequency of 675 kHz. It requires a tripod to independently acquire seabed images and can acquire circular

Table 2 Specifications of 1171 scanning sonar

Item	Description
Depth rating	3,000 m
Frequency	675 kHz
Range	0.5–100 m
Range resolution	≥ 19 mm
Scan speed	11 s / 360° @ 10 m & 1.8° step 36 s / 360° @ 100 m & 1.8° step
Scan width	360° continuous
Step size	≥ 0.225°
Pulse length	25–2,500 μs

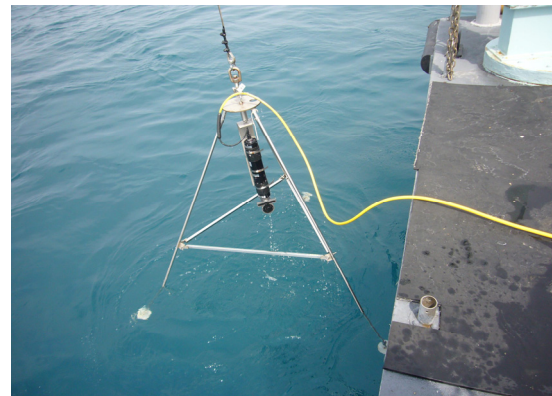
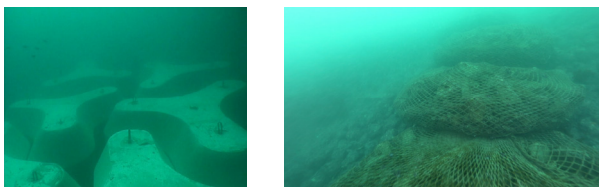


Fig. 8 Launch of 1171 scanning sonar from Jangmok No.1



(a) Cell blocks around submerged structure of the OWC (b) stone bags covering the underwater cable

Fig. 7 Cell blocks and stone bags taken by optical camera

coordinates are difficult to make because calibration before acquisition and postprocessing (such as tidal correction) after acquisition is not performed, submarine cable and cell blocks supporting the ground bed

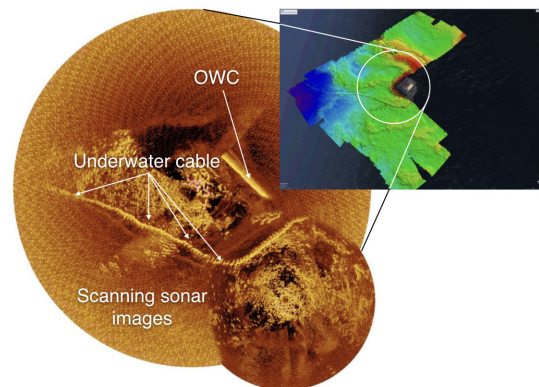


Fig. 9 Mosaicked images of 1171 scanning sonar

images of a scanning radius that is set in a scanning sonar operating program. The maximum scanning radius is 100 m. The scanning sonar can be operated with a minimum rotation angle of 0.225°. Fig. 8 depicts a scene in which the scanning sonar installed on a tripod is launched from the stern of Jangmok No. 1. Divers are normally required to stably install sensors on the seabed protected against the tidal current, but divers could not be recruited in this work due to the schedule and state of the sea. As a result, the vessel, sensor, and tripod were pushed by the tidal current. The tripod was pushed or fell from time to time during the measurement. Therefore, the sensor only briefly could be stable position while scanning.

Divers should be recruited for more precise observation in the future. Consequently, images at two points were acquired, and the mosaicked results are shown in Fig. 9. The images have a higher resolution than the MBES images and the stone bags for burying and protecting the submarine cables can be identified.

3.3 Maritime Equipment Performance Test Procedure Establishment

A test performed in an actual sea incurs high costs. The overall operation period and all items required for the operation are specified in a contract. If an operations company does not have a standardized procedure, the test is even more complex and difficult to perform. It is quite difficult for the company to come up with a standard (Rocha and De Tomi, 2015).

The IDEF0 modelling technique is a function modeling method that was developed as part of the ICAM project of the US Air Force in the 1970s, and can model any system in which people, hardware, and software are all connected. This method is used to systematically manage and utilize a target system to be analyzed or designed by defining functions, the information required of the system, and the order between the functions (the National Institute of Standards and Technology, 1993). Particularly, it has a feature of easily modeling a complex system as it supports a hierarchical model structure (Kim, 2005). Study cases that established complex work procedures

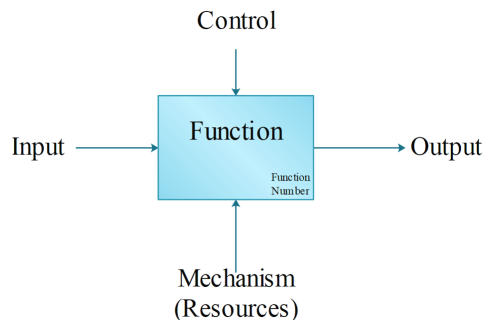


Fig. 10 IDEF0 box format

using equipment on the sea using the IDEF0 function modeling method include the case applied to the safety inspection of an offshore structure (Rocha and De Tomi, 2015), and the case applied to underwater unidentified object identification using a small ROV (Baek et al., 2019).

This section establishes the procedure based on the information obtained from the MBES and scanning sonar test site of Chapter 3 and is modelled by IDEF0. Fig. 10 shows the basic diagram of IDEF0. A function is expressed in a box format, and functions performed by people, machines, or computers are expressed as descriptions about what happens and under what conditions. Each function box is connected by input, control, output mechanism (ICOM), and a lower level can be decomposed into subfunctions in more detail.

Fig. 11 is assigned code A-0 as an activity of the highest level. The function of A-0 defines the provision of a multi-purpose technical scientific service as the function of the OWC, and its input/output, control, and mechanism are illustrated. Multi-purpose technical scientific service is a function for acquiring data required to evaluate the performance and precision of the sensor. Real-time surface environment data of an auto weather system (AWS) and data of the underwater environment (current direction, current velocity, sea level, etc.) installed on the OWC are input values. A final report with output values is generated by control. Control elements are defined as

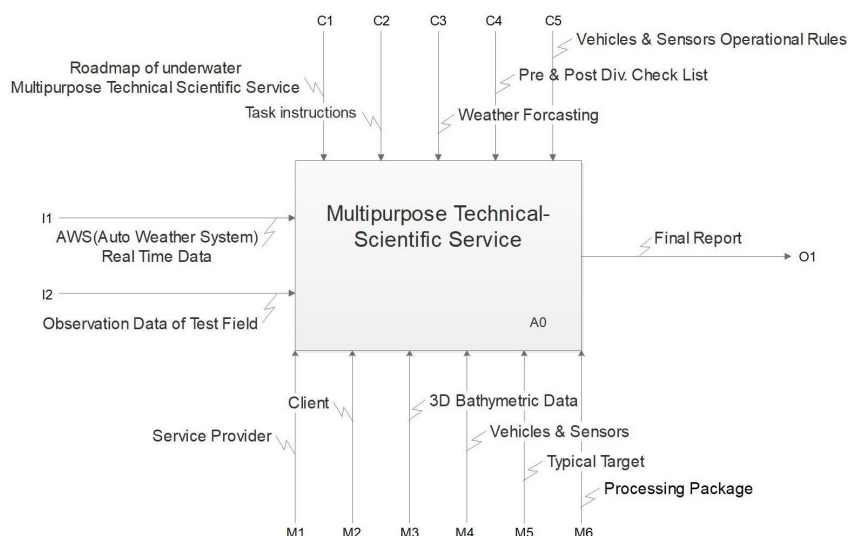


Fig. 11 A-0 diagram of multipurpose technical scientific service

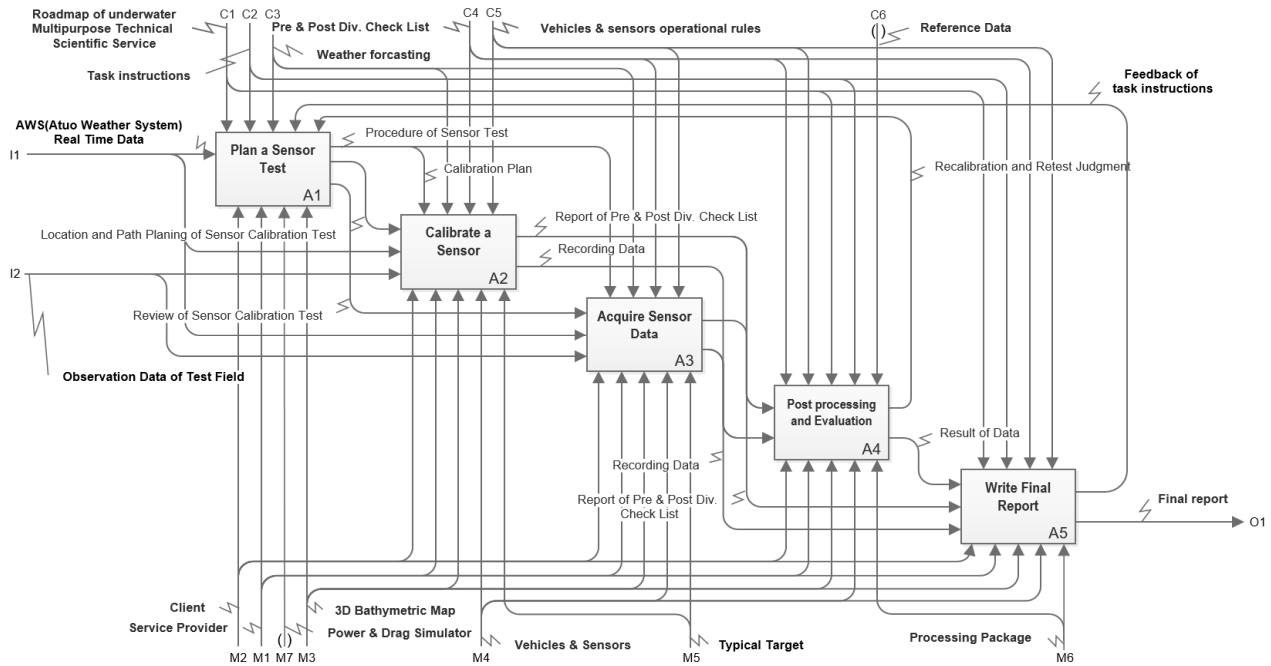


Fig. 12 A0 diagram subdivided from A-0 diagram

test-bed operation rules and roadmap, test request, weather forecast, pre- and post-diving check list for maritime equipment, and operation rules for equipment and sensors. Mechanism elements for acquiring data include wave power generation test-bed (service provider), customer, existing three-dimensional seabed terrain data, maritime equipment (vehicles and sensors) used in tests, fixed target structure, and processing software package. The next level down consists of five activities. A1 (sensor test plan), A2 (sensor calibration), A3 (sensor data acquisition), A4 (test data analysis and evaluation), and A5 (final report generation), as shown in Fig. 12. The activities are connected to each other by the ICOM flow and are expressed as a procedure.

In this section, an IDEF0 modeling method was selected to establish a standard procedure required to operate a variety of maritime equipment on an offshore wave power generation test-bed, and a draft of the procedure was established. As a result, it was found that data needed to be delivered to a user via a network in real time by installing underwater environment sensors and AWS in wave power plant facilities, and the shape and location information of artificial seabed structures and the topographic map of the seabed of neighboring sea prior to enforcement, need to be provided. It was also found that test-bed operation rules and roadmap were required. This study presents IDEF0 modeling results from the point of view of a person who acquires data. In future, research and development for integrated comprehensive real-sea experiment processes should be carried out from the point of view of a manager of the wave power test-bed.

4. Suitability Analysis of Test Environment of Maritime Equipment

Performance tests required for the development of autonomous underwater vehicles or remotely operated vehicles are often carried out

in a large water basins, lakes, or gulfs. When a deep-sea environment is required, a research vessel (R/V) such as Onnuri (KIOST, 2019b) or Isabu (KIOST, 2019c) are used to perform tests on far seas such as the East Sea and the Pacific Ocean. This section analyzes the characteristics of the wave power test-bed and existing cases and identify fields in which OWC facilities are expected to be used.

4.1 Differences from Existing Domestic Cases

A variety of maritime equipment and robots are being developed in South Korea. ASVs, AUVs, and ROVs are being developed, and related application technologies are being actively studied. Tests for performance verification in the development process of such platforms and technologies are necessary, and support vessels or facilities of various types are also required.

The KRISO has carried out performance tests on ISiMI 100 (AUV) (Jun et al., 2009), ISiMI 6000 (Lee et al., 2012), Hemire (ROV), and Crabster (ROV) at the SSRI in the aid of various research vessels. Up to two individuals worked to test the relatively small ISiMI 100 weighing approximately 20 kg in the air by using a small fishing boat (Fig. 13). The ISiMI 6000 (AUV) weighing 750 kg in the air and the Hemire (ROV) weighing 4 t were launched and recovered by using a crane installed at the wharf (Fig. 14). In such cases, the launch/



Fig. 13 ISiMI 100 AUV experiments using a small boat



Fig. 14 Launch and recovery of ISiMI 6000 AUV and Hemire ROV using a crane in a port

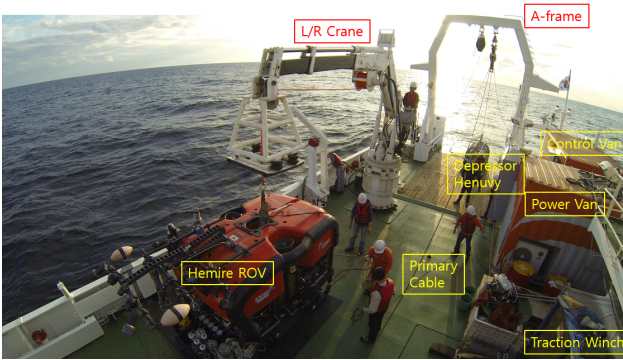


Fig. 15 Hemire ROV system on Onnuri R/V (Baek et al., 2012)

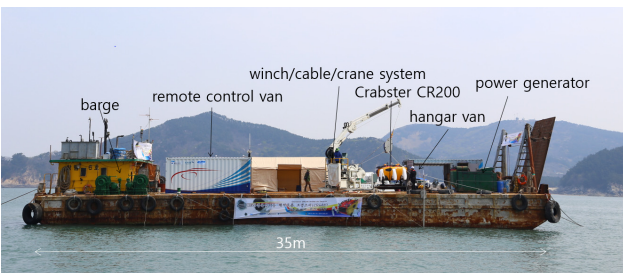


Fig. 16 Crabster ROV system on the barge (Jun et al., 2015a; Jun et al., 2015b)

recovery space is limited to the operating radius of the crane. In addition, an office space was constructed using a container for the research activities of test participants, and was used to analyze the data of the vehicles or change and modify the platform.

When tests on far seas such as the East Sea and the Pacific Ocean were required, research vessels such as Onnuri were used (Lee et al., 2016) (Fig. 15). When testing Crabster (walking ROV), a barge was used (Jun et al., 2017) (Fig. 16). The wave power test-bed is bound to be different from such research vessels and wharf environments.

4.2 Characteristics of Wave Power Test-bed

Qualitatively, the test-bed sea is between the environment of a lake or gulf, and the real-sea environment of the East Sea and the ocean. It takes approximately 40 minutes from the Hallim port and an hour and ten minutes from the Aewol port each way, travelling by a Jangmok No. 1-class vessel. Scheduled marine operation and the presence of other vessels must be checked before entering the test sea. Moreover, although marine traffic is light, it must be investigated in advance as it can change according to season and quantum of fish caught.



Fig. 17 Deck space of the OWC

Table 3 General conditions and preference levels for marine equipment test-sites

Item	Offshore		Onshore		
	OWC	R/V	Port	Seashore	
Operation	Op. 1	3	5	5	4
	Op. 2	5	5	5	2
	Op. 3	5	5	5	2
	Op. 4	3	4	5	3
	Op. 5	3	4	5	2
Support	Sp. 1	4	3	4	2
	Sp. 2	3	4	3	2
	Sp. 3	3	3	5	4
	Sp. 4	3	3	5	3

Item	Description
Op. 1	1. Operator support facility
	- 24hours operation (Kitchen & bads) - 12hours operation (Day work)
Op. 2	2. Power & communication
	- Electricity from ground - Wired & wireless communication
Op. 3	3. CCTV & surveillance
	- Monitoring for operation and sea state - Surveillance for warehouse and facility
Op. 4	4. Washing and maintenance
	- Fresh water - Space for maintenance
Op. 5	5. Launch and recovery system
	- Crane, A-Frame, J-Frame - Peripheral devices such like power generators
Sp. 1	6. Berth of support vessels - Barge, boat, etc
Sp. 2	7. Mobility of support vessels
Sp. 3	8. Accessibility
	- Sea state - Installation & disassemble
Sp. 4	9. Accessibility to land resources
	- Repair and replacement - Manufacturing such like milling or drilling

5: Best, 4: Good, 3: Average, 2: Bad, 1: Worst

The OWC can supply electricity and relay communication. If real-time kinematic (RTK) GPS is installed, it can be used as a location reference point. If a long-range (LoRa) low-power wide-area network is installed, it can supply a wireless communication network up to a range of approximately 10 km. If a network camera illuminates the surroundings, it is expected that the weather and sea state can be checked in real time from a remote location to make a more suitable test plan. A space that can be used as a deck is provided on the outside (Fig. 17), and a space for maintenance, repair, and storage of equipment as well as office work is provided on the inside. The water depth ranges from 10 m to 60 m. The laid cables can be used as a landmark. The wave power energy density is relatively high as the wave power test-bed is installed at this location.

It is comparable to Onnuri-class research vessels in supplying power, relaying communication, and monitoring sea state. However, research vessels are equipped with room and board facilities, whereas the wave power test-bed is not. Moreover, research vessels have various support devices for launch and recovery, whereas the wave power test-bed is still in preparation for construction. The advantages and disadvantages of offshore and land test-beds from an operational and support facility perspective are listed in Table 3.

Table 3 is divided into an operation area and a support area. The operation area is divided into five sub-items and the support area is divided into four sub-items. Locations to be compared include a research vessel (R/V), port, and seashore. Furthermore, the convenience of each item according to a comparative location is quantified. A score of 5 points means best, and a score of 1 means worst. The quantifying process is heuristically derived based on the experience of the authors, and the advantages and disadvantages of facilities may be changed depending on the target to be tested.

Op. 1 refers to operator support facilities, which denotes the ability to provide room and board in a 24 h operation or daytime work convenience in a 12 h operation. The R/V and port are preferred, and the OWC is average. This is because it is not yet equipped with facilities for room and board, kitchen, and bathroom. Op. 2 is items related to power and communication. If power can be supplied from land/ground, the system utilization can be improved in most cases. The communication network can also better acquire related information and analyze data with the aid of wired/wireless internet and long-term evolution (LTE) mobile data. Accordingly, the OWC can provide a very favorable environment. Op. 3 relates to closed-circuit television (CCTV) installation and security (CCTV & surveillance). A CCTV has security elements (e.g., intruder identification) and can provide a function for observing large research equipment from multiple angles while it is being driven. Numerous CCTVs can be installed on the OWC. Op. 4 relates to washing and maintenance space for test equipment. The OWC can provide a good environment in Op. 3 and Op. 4. Op. 5 is the launch and recovery system for equipment. The equipment can enter the sea directly from the OWC, but support facilities for launching and recovering heavy equipment still need to be procured. Sp. 1 relates to ease of berthing support vessels. The OWC

and port are better in Sp. 1. Sp. 2 relates to mobility of support vessels and recovery support when equipment is lost. The immediately movable research vessel is favored, and the OWC is not. Sp. 3 is accessibility to the test sea and includes the ease with which test participants enter and withdraw as sea states such as rain and wave height change. Sp. 4 is accessibility to land resources and relates to unexpected faults of equipment, manufacturers or repair companies, and how easily replacements can be purchased. The port is favored highly, and the OWC is average.

4.3 Applicable Fields/Businesses

The fields expected to make use of the facilities described in this paper were identified as follows.

(1) Wave energy-based mobile unmanned system test evaluation

This relates to performance tests and evaluation for mobile wave power generation systems, or marine mobile unmanned systems using wave energy. It can be used as a berth facility for launch and recovery of unmanned vehicles and can be used as an integrated control center for monitoring, remotely controlling, and tracking the location of an unmanned vehicle.

(2) Construction of a wave power test-bed using a wave glider and long-term surrounding environment monitoring system

This relates to construction of a continuous environment monitoring system using wave gliders that use wave energy to secure safety and predict the energy production of a wave power test-bed. The gliders can be used as a monitoring system for stable energy production prediction of the wave power test-bed, and the wave power test-bed can be used as an integrated control center of the wave gliders.

(3) Domestic maritime measurement sensor performance tests and evaluation

Various sensors are arranged on the wave power test-bed and can be used in preparation of a standard operation procedure and their performance verification. The power and communication provided by the wave power test-bed can be used to provide investigating entities with location correction and real-time environment information. It can be used in search performance evaluation activities such as navigation or underwater exploration missions using laid submarine cables as a landmark.

(4) Independent and group operation performance evaluation support system for marine unmanned vehicles

The wave power test-bed can operate as a control center of unmanned vehicles. If RTK GPS is installed in the future, it can operate as a location reference point and monitor each vehicle.

(5) Underwater communication network performance evaluation support system

Underwater communication technology is advancing beyond one-to-one communication to realize networks for three or more nodes. Performance test demands in the real sea are also expected to increase. The test-bed can be used as a single node, and a location reference point and can relay offshore and land communication.

5. Conclusions

In this study, preliminary research was carried out on the suitability of OWC surroundings (Berth No. 1 of the wave power test-bed) to test the performance of maritime equipment. The authors boarded Jangmok No. 1 and accessed the sea of the wave power test-bed from the Hallim port and Aewol port for this study. While operating typical seabed mapping sensors, the multi-beam echo sounder and single-beam scanning sonar, the conditions that would be required when used as a test-bed of maritime equipment in the future were investigated, and the terrain information for the underwater lower structure of the wave power test-bed and the surrounding seabed environment was procured. The procured terrain information is expected to be used as reference data when investigating terrain changes in the future. In addition, the procedure required to use the facilities described in this paper was modeled using IDEF0 techniques. The modeling results provide a reference procedure for carrying out various complex and novel experiments in future, and are used to minimize technology duplication and risk. Feedback from additional experiments can correct and modify the model to develop a thorough standard procedure. Past cases were also analyzed, and the characteristics of the test-bed were derived based on the analysis. Finally, five fields expected to make use of the facilities were identified.

Acknowledgments

This research was supported by a grant from National R&D Project “Establishment of sea test-bed for wave energy converters” funded by Ministry of Oceans and Fisheries, Korea (PMS4040) and was supported by a grant from Endowment Project of “Development of rated power control technology for OWC wave energy converter using flow control system” funded by KRISO (PRS0200).

References

- Baek, H., Jun, B., Choi, G., & Lee, P. (2012). A Case Study on the Operation Strategy of Hemire from the Analysis of Deep-Sea ROV Operations. Abstract book of The Korean Society for Marine Environment & Energy, 1723-1729.
- Baek, H., Jun, B.H., Yoon, S.M., & Noh, M. (2019). Study on Identification Procedure for Unidentified Underwater Targets Using Small ROV Based on IDEF Method. *Journal of Ocean Engineering and Technology*, 33(3), 289-299. <https://doi.org/10.26748/KSOE.2019.022>
- Baek, H., Kim, K.H., Jun, B.H., Lee, P.M., & Lim, Y.K. (2008). Estimation of the Hydrodynamic Coefficients for the Deep-sea UUV. *Journal of Ocean Engineering and Technology*, 22(4), 97-105.
- Choi, J., Park, J., Jung, J. & Choi, H.T. (2019a). Development of Underwater 3D Positioning System using Underwater Acoustic Modem. *Journal of Institute of Control, Robotics and Systems* 25(10), 916-922. <https://doi.org/10.5302/J.ICROS.2019.19.0155>
- Choi, J.S., Lee, J.K., Lim, C.H., Ko, T.K., Park, J.Y., Kim, K., ... & Cho, I.H., (2019b). Current State of Development of the Open Sea Test Site for Wave Energy Converters. Proceedings of The Joint Conference of the Korean Association of Ocean Science and Technology Societies 2019.
- González, J., Monagas, V., Remírez, X., Luque, A., Hernández J., & Llinás, O. (2015). PLOCAN. An Offshore Test Site for Ocean Energy Converters. Proceedings of OCEANS 2015 - Genova, Genova, 1-4, <https://doi.org/10.1109/OCEANS-Genova.2015.7271245>.
- Jeollabuk-do. (2019). Report of Feasibility Analysis Research of Establishment for Small Marine Unmanned System Demonstration Platform. Republic of Korea
- Jun, B.H., Jeong, Y.H., Shim, H., & Lee, P.M., (2015a). An Experiment on Searching, Identification and Recovery of Underwater Artefacts off the Western Coast of Korea Using Underwater Walking Robot Crabster CR200. Proceedings of the 2015 Spring conference of the Korean Society of Mechanical Engineers, 710-712.
- Jun, B.H., Lee, F.Y., Park, J.Y., Lee, P.M. & Kim, S.M. (2009). Analysis of Control Responses in the Field Test of ISiMI100 AUV, Proceedings of the 2009 Fall conference of the Korean Society of Ocean Engineers, 12-16.
- Jun, B.H., Lee, P.M., & Jung, Y.H. (2015b). Experience on Underwater Artefact Search using Underwater Walking Robot Crabster CR200. Proceedings of OCEANS 2015 MTS/IEEE Washington, Washington, DC, 1-5, <https://doi.org/10.23919/OCEANS.2015.7404618>.
- Jun, B.H., Yoo, S.Y., Lee, P.M., Park, J.Y., Shim, H., & Baek, H. (2017). The Sea Trial of Deep-sea Crabster CR6000 System. *IEMEK Journal of Embedded Systems and Applications*, 12(5), 331-341. <https://doi.org/10.14372/IEMEK.2017.12.5.331>
- Kim, C.W. (2005). A Study on the Information Modeling of Defense R&D Process Using IDEF Methodology. *The Journal of Society for e-Business Studies*, 10(1), 41-60.
- Kim, H., Kim, J., Cho, I.H., Paeng, D.G. & Choi, J.S. (2017). Survey of Seafloor at Chagwi-do of Jeju Island to Select 60-m-class Sea Test Bed of Wave Energy Converter. *Journal of Ocean Engineering and Technology*, 31(4), 308-314. <https://doi.org/10.26748/KSOE.2017.08.31.4.308>
- Korea Institute of Ocean Science & Technology (KIOST). (2019a). R/V Jangmok No. 1. Retrieved from https://www.kiost.ac.kr/lab/sub05_04.do
- Korea Institute of Ocean Science & Technology (KIOST). (2019b). R/V ONNURI. Retrieved from https://www.kiost.ac.kr/lab/sub05_02.do
- Korea Institute of Ocean Science & Technology (KIOST). (2019c). R/V ISABU. Retrieved from https://www.kiost.ac.kr/lab/sub05_01.do
- Lee, G.M., Park, J.Y., Lee, P.M., Jun, B.H., Kim, K.H., Lee, C.M., ... & Jeong, H.S. (2012). Design of 6000m Autonomous Underwater Vehicle ISiMI6000. Proceedings of The Joint Conference of the

- Korean Association of Ocean Science and Technology Societies 2012. 1719-1722.
- Lee, P.Y., Park, S.K., Kwon, S.T., Park, S., Jung, H., Park, M.S., & Lee, P.M. (2015). Dynamic Modeling of Autonomous Underwater Vehicle for Underwater Surveillance and Parameter Tuning with Experiments. *Journal of Ocean Engineering and Technology*, 29(6), 488-498. <https://doi.org/10.5574/KSOE.2015.29.6.488>
- Lee, P.M., Jun, B.H., Baek, H., Kim, B., Shim, H., Park, J.Y., ... & Kim, W.S., (2016). Explorations of Hydrothermal Vents in Southern Mariana Arc Submarine Volcanoes using ROV Hemire. *Journal of Ocean Engineering and Technology*, 30(5), 389-399. <https://doi.org/10.5574/KSOE.2016.30.5.389>
- Park, J.Y., Ko, T.K., Choi, J.S., Kim, K.H., Lee, J.K., Kim, G.W., ... & Baek, W.D. (2019). Establishment of Wave Energy Data for Performance Assessment of Wave Energy Converter. *Proceedings of the 2019 Fall Conference of the Korean Society for Marine Environment and Energy*, 79-84.
- Park, S.K., Lee, P.Y., Park, S.W., Jung, H.S., & Park, M.S. (2015). Design and Field Test of Heading and Depth Control for Autonomous Underwater Vehicle HW200. *Proceedings of Institute of Control, Robotics and System Annual Conference*. 365-366.
- Plataforma Oceánica de Canarias (PLOCAN). (2020). Oceanic Offshore Platform. Retrieved from <https://www.plocan.eu/en/offshore-platform>
- Real-Arce, D.A., Barrera, C., Hernández, J., & Llinás, O. (2015). Ocean Surface Vehicles for Maritime Security Applications (The PERSEUS Project). *Proceedings of OCEANS 2015 - Genova, Genoa*, 1-4. <https://doi.org/10.1109/OCEANS-Genova.2015.7271504>.
- Rocha, F., & De Tomi, G. (2015). Basic Mapping of the Inspection Process in Offshore Oil Production Facilities. *Proceedings of OCEANS 2015 MTS/IEEE, Washington*, 1-8. <https://doi.org/10.23919/OCEANS.2015.7404581>
- Ryu, H.J., Hong, K., Shin, S.H., Kim, S.H., & Kim, Y.D. (2011). Study on Analysis of Wave Energy Resources and Wave Energy Density Map of the Korean Sea Area. *Proceedings of Joint Meeting of the Korean Association of Ocean Science and Technology*, 1464-1468.
- The National Institute of Standards and Technology. (1993). *Draft Federal Information Processing Standards Publication 183*. U.S. Department of Commerce(Springfield), Virginia.

Author ORCIDs

Author name	ORCID
Park, Jin-Yeong	0000-0002-8255-6402
Baek, Hyuk	0000-0002-3371-4160
Shim, Hyungwon	0000-0002-7314-2881
Choi, Jong-Su	0000-0003-4904-8390

Study for Operation Method of Underwater Cable and Pipeline Burying ROV Trencher using Barge and Its Application in Real Construction

Min-Gyu Kim¹, Hyungjoo Kang¹, Mun-Jik Lee², Gun Rae Cho³, Ji-Hong Li⁴,
Tae-Sam Yoon⁵, Jaeheung Ju⁶ and Han-Wan Kwak⁷

¹Assistant Researcher, Korea Institute of Robot and Convergence (KIRO), Pohang, Korea

²Associate Researcher, Korea Institute of Robot and Convergence (KIRO), Pohang, Korea

³Senior Researcher, Korea Institute of Robot and Convergence (KIRO), Pohang, Korea

⁴Principal Researcher, Korea Institute of Robot and Convergence (KIRO), Pohang, Korea

⁵Technical Representative Director, Korea Offshore Company (KOC), Busan, Korea

⁶Assistant Manager, Korea Offshore Company (KOC), Busan, Korea

⁷Vice President, Korea Environmental Science & Technology Institute, Seoul, Korea

KEY WORDS: ROV (Remotely operated vehicle), Sea floor cable burying, PLIB (Post lay inspection and burial), Operation using, Construction works of water supply in Yokji-do

ABSTRACT: We developed a heavy-duty work class ROV trencher named URI-T (Underwater robot it's trencher) that can conduct burial and maintenance tasks for underwater cables and small diameter pipelines. It requires various supporting systems, including a dynamic positioning (DP) vessel, launch and recovery system (LARS), A-frame, and winch in order to perform burial tasks because of its dimensions (6.5 m × 5.0 m × 4.5 m, 20 t) and the tough working environment. However, operating a DP vessel has disadvantages as it is expensive to rent and operate and it is difficult to adjust the working schedule for some domestic coast construction cases. In this paper, we propose a method using a barge instead of a DP vessel to avoid the above disadvantages. Although burying the cable and pipeline using a barge has lower working efficiency than a DP vessel, it can save construction expenses and does not require a large crew. The proposed method was applied over two months at the construction of the water supply in Yokji-do, and the results were verified.

1. Introduction

In general, subsea cables and pipelines are buried for the purpose of supplying power and communication between land and islands (subsea cables), transporting fossil fuels (pipelines), and connecting waterworks (pipelines). Since these cables and pipelines are exposed to man-made hazards (tools such as anchors, trawl doors, etc.) and natural hazards (earthquakes, typhoons, etc.) (Jones and Hirai, 2001; Yoo and Shin, 2010), the burial is performed using various protection methods for economical feasibility and stability (Ahn and Kim, 2009). This research institute developed an underwater heavy-duty Remotely Operated Vehicle (ROV) trencher (Underwater Robot. It's Trencher, URI-T) to conduct the post-lay inspection and burial (PLIB) of pre-laid cables and pipelines beneath the seabed using a water jetting system. URI-T was one part of a project to develop underwater robots for the construction of marine structures and infrastructure for

performance verification from 2013 to 2019 (Jang, 2014) (Fig. 1). Subsequently, from 2019 to the present, the performance of URI-T, which was developed to promote the use of marine equipment research results, has been enhanced, and efforts are being made to secure



Fig. 1 ROV Trencher, URI-T

Received 30 June 2020, revised 9 September 2020, accepted 10 September 2020

Corresponding author Min-Gyu Kim: +82-54-279-0475, zxdwa0817@kiro.re.kr

© 2020, The Korean Society of Ocean Engineers

This is an open access article distributed under the terms of the creative commons attribution non-commercial license (<http://creativecommons.org/licenses/by-nc/4.0>) which permits unrestricted non-commercial use, distribution, and reproduction in any medium, provided the original work is properly cited.

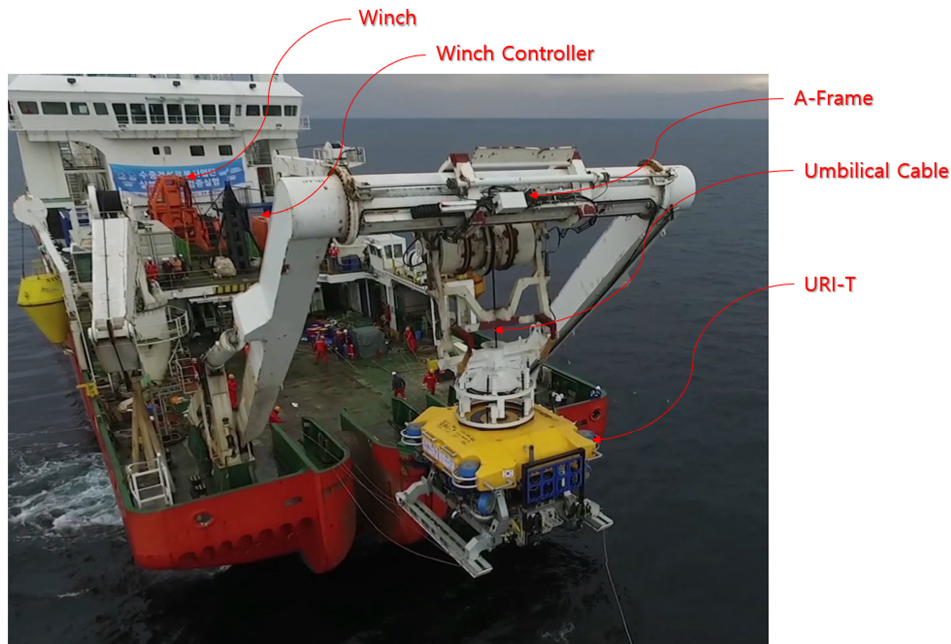


Fig. 2 A LARS with a winch and A-Frame

commercial results by introducing the ROV trenchers on-site. As described above, the URI-T is an ROV trencher that buries and maintains cables and pipelines using water jetting and various work tools at depths of up to 2,500 m; it is 6.6 m (L) \times 4.5 m (W) \times 3.5 m (H) and weighs approximately 21 tons (Kang et al., 2019; Cho, et al., 2019a).

At an actual burial work site, it is necessary to have a dynamic positioning (DP) vessel equipped with a launch and recovery system (LARS), including a winch and an A-Frame to launch and recover the ROV trencher and move the ship according to the movement of the ROV trencher. The A-Frame is a device used to stably move the ROV trencher from the deck to the surface of the water; it is used with a winch that winds and unwinds an umbilical cable used for the power supply and communication connection of the ROV trencher (Fig. 2). When the URI-T is operated using a DP vessel, the work efficiency can be maximized by enabling continuous operation for 24 hours, and the work stability can be improved by using a dedicated launch and recovery device. Nevertheless, a large amount of manpower is required for the operation of ships and ROV trenchers. Moreover, the rental and operation cost of ships is high, and it is difficult to coordinate rental schedules when using foreign ships. It is not easy to use both domestic and foreign DP vessels at some domestic sites that require burial tasks (e.g., for the construction work on the water supply in Yokji-do) because the work zone is small (within 10 km) and construction must be conducted with a fixed schedule and cost.

In this paper, we introduce the method of operating the ROV trencher using a barge. The method can be applied to several burial work sites in Korea where it is difficult to use DP vessels. Each function of the DP vessel and its accompanying LARS device are replaced by using an anchor winch, a crane, and the newly designed

cable handling system of the barge. Some of the existing operation scenarios are modified accordingly to the method. The proposed method was successfully applied to the Yokji-do waterworks construction that was conducted from November 2019 to January 2020. Using barges for the burial of subsea cables and pipelines has lower operational efficiency and operational stability than using DP vessels. However, since the rental cost of barges is comparatively low and manpower required for their operation is smaller, using barges can significantly reduce construction cost and facilitate schedule coordination in short work zones on the domestic coast. In Chapters 2 to 4, the overall system of the URI-T, its proposed method of operation, and its application to the Yokji-do waterworks construction are described, respectively. Conclusions and future plans are discussed in Chapter 5.

2. URI-T System Overview

The detailed performance and specifications of the URI-T are described in detail in Tables 1 and 2 below.

The URI-T is divided into a hydraulic system, a water jet system, an onboard remote control and power supply system, a hydraulic-based

Table 1 URI-T performance

Item	Verification
Working depth	Max. 2,500 m
Burying depth	Max. 3 m
Burying speed	Max. 2.36 km/h
Forward Speed	Max. 1.7 m/s
Payload	\leq 540 kg

Table 2 URI-T's specifications (Kang et al., 2019)

Item		Specification
Size		6.6 m (<i>L</i>) × 4.5 m (<i>W</i>) × 3.5 m (<i>H</i>)
Weight		Approximately 21 t
Hydraulic system	HPU (Hydraulic powered unit)	250 kW, RiSEA
	Thruster	10535 N, 835 r/min, RiSEA
Water jet system	Water-Pump	224 kw, 986 m ³ /h
	IMU (Inertial measurement unit)	HG1700AG37, Honeywell
Navigation	DVL (Doppler velocity log)	WHN600K3, Teledyne
	Depth	Series8000, Paroscientific
	Multibeam sonar	M900-250, Blueview
	Cable detection system	TSS350&440 ¹ , Teledyne

¹ TSS is a subsea pipe and cable tracking system and is divided into TSS350 and TSS440 according to the method of operation. TSS350 uses pulse induction technology to detect the magnetic field of the cable, and TSS440 detects the tone pulse. In the URI-T, TSS350 and TSS440 are dual-tracked to maximize the detection performance.

cable work tool, and a manipulator system. Details for each system follow.

(1) Hydraulic system: A 250 kW hydraulic powered unit (HPU) is used to control the position and location of the ROV trencher and to drive the burial and maintenance tools. The HPU supplies the flow to 4 valve packs (2 for driving a thruster and 2 for driving a work tool), and each valve pack controls the flow rate of 8 thrusters (4 horizontal and 4 vertical thrusters), 2 manifolds (with 5 and 7 axes), 2 work tools (cutters and grippers), and 6 hydraulic cylinders (2 TSS handlers and 4 motion bases).

(2) Water jet system: The water jet system is for spraying seawater on the seabed for a burial task. It sprays seawater by using 2 water pumps (1 port jetting arm and 1 starboard jetting arm) capable of supplying 986 m³ of water per hour and 2 jetting arms (1 port and 1 starboard) that spray water. In addition, a motion base is used to control the left/right and up/down position of the jetting arms; it can be adjusted from 0.2 m to 0.7 m in the left/right direction and by up to 3 m in up/down direction (Li et al., 2014).

(3) Onboard remote control and power supply system: The onboard remote control system is implemented in a specially manufactured container and consists of a monitor wall, 2 control console chairs, a touch screen, and a power and communication distribution panel. It monitors the state of the URI-T and the power supply system and controls the functions and state necessary for the given task. The power supply system is implemented with two specially manufactured containers; it stably supplies the internal driving power of the URI-T and HPU and the power for the 2 water pumps.

(4) Hydraulic-based cable work tools and manipulators: Work tools such as grippers, cutters, and manipulators are used for the maintenance of subsea cables and pipelines. The gripper and cutter are operated by the manipulator. The gripper can grip a cable with a diameter of 17 ~ 110 mm with a force of 25 tons, and the cutter can cut a cable with a diameter of up to 110 mm using pressure of up to 69 mPa (Cho et al., 2019b).

3. Operation of the ROV Trencher using a Barge

3.1 ROV Trencher Operation Scenario using a DP Vessel

For burial tasks completed with an ROV trencher, it is typical to use a DP vessel equipped with a LARS device including a winch and A-Frame for the launch, recovery, and stability of the ROV trencher, as mentioned above. The actual operation scenario can be divided into 4 stages as shown in Fig. 3. The details are as follows.

(1) ROV trencher launch: For a LARS device connected to the ROV trencher as shown in Fig. 2, the umbilical cable is connected to the ROV trencher through the an A-Frame, and the depth of the ROV trencher is controlled by adjusting the length of the umbilical cable with the corresponding winch controller. As shown in Fig. 3, the A-Frame is used for surface deployment from the DP ship deck. A winch is then used to position the ROV trencher on the seabed. After the ROV lands at a given depth, the position of the ROV trencher is monitored by the onboard remote control system using the Ultra-short baseline (USBL)¹⁾ and Quincy system²⁾.

(2) Position detection of pre-laid cables and pipelines using the cable and pipeline detection system (TSS350 and TSS440): After landing on the seabed, the ROV trencher deploys and moves the TSS handler and detects the location of cables and pipelines laid on the seabed. After the cables and pipelines have been located, the ROV trencher is placed over them. Meanwhile, the DP vessel follows the movement of the ROV trencher, keeping the umbilical cable as straight as possible. Otherwise, the ROV trencher could be inadvertently lifted by the umbilical cable and burial depth could not be guaranteed. Moreover, the umbilical cable could be damaged, causing damage or

1) USBL is an underwater positioning system using sound waves; the transmitter is mounted on top of the ROV trencher, and the receiver is installed and operated in the bottom of the ship.

2) Quincy is a program used to manage survey planning, data collection, data organization, volume calculation, and depth chart generation in marine navigation, positioning and surveying activities for ROV and AUV tracking and data collection purposes.

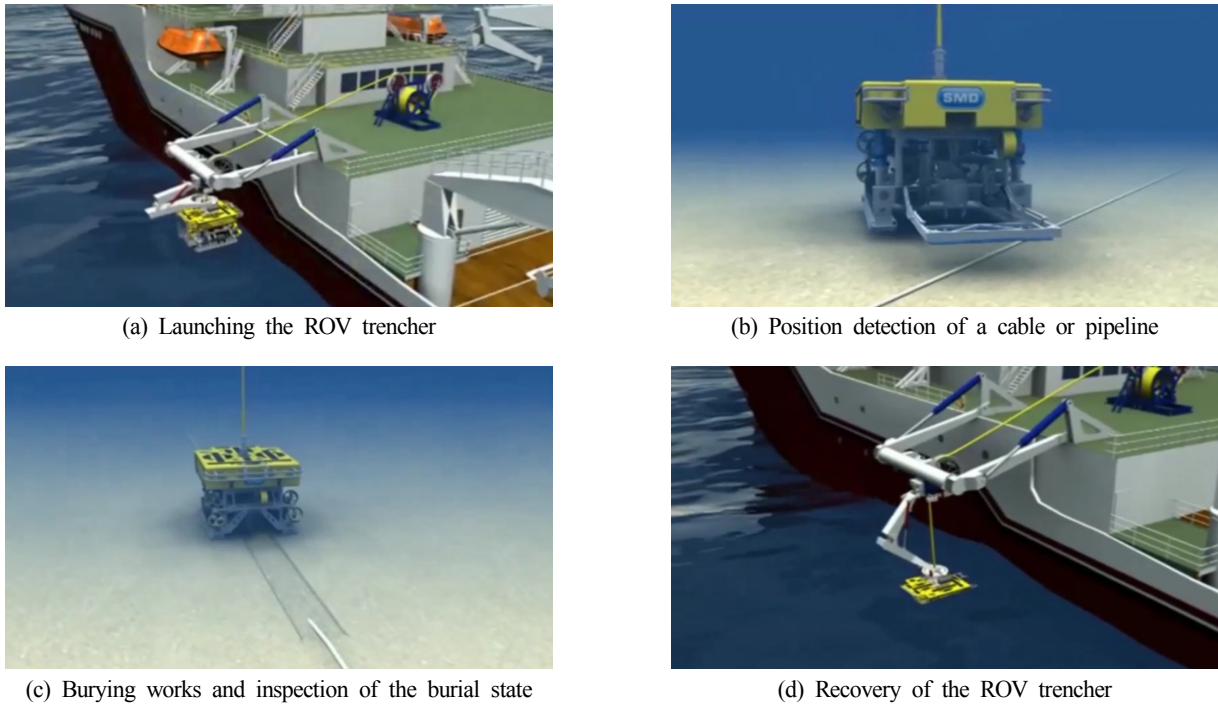


Fig. 3 Operating scenario of the ROV trencher using a DP vessel

in the worst case, loss of the ROV trencher.

(3) Cable and pipeline burial and post-lay survey: The ROV trencher located above the cables and pipelines tracks the location information of the TSS. It uses the waterjet system to perform the burial task and then uses the TSS350 and TSS440 to perform a post-lay survey after completion. Simultaneously, the DP vessel follows the movement line of the ROV trencher, keeping the umbilical cable as straight as possible.

(4) ROV trencher recovery: The ROV trencher is recovered by steps in the reverse order of the launch. After the winch pulls the ROV trencher to the end of the A-Frame, the A-Frame is folded onto the

deck of the ship. The length of the umbilical cable is then adjusted with a winch, recovering and tying it onto the deck. In the field, the work must be carried out according to the above scenario, otherwise the efficiency and accuracy of the work can be degraded, and the stability of the ROV trencher will not be guaranteed.

3.2 Improving the Operation of the ROV Trencher using a Barge

As mentioned above, for some burial work on the domestic coast, it is not only extremely difficult to find a DP ship in which an A-Frame or winch can be installed within the specified time limit, but the cost of construction may also be economically infeasible. A barge can



Fig. 4 Barge anchor system

therefore be a good alternative to a DP ship. When using a barge, the operational efficiency and stability are lower, but the cost of renting and operating the ship is also lower. A barge can be operated with a smaller workforce, which can provide a significant advantage at some burial sites along the domestic coast. In order to operate the ROV trencher using a barge, the following two problems must be solved: (1) When the ROV trencher moves on the seabed, as in the second and third steps of the scenario above, the barge must move with the ROV trencher (DP function). (2) A LARS device cannot be installed on a barge due to its size and weight, thus an operating system that can

replace it is required. The following method is proposed to solve these problems.

(1) It is possible to move a barge using a tugboat. This is, however, not suitable for use with an ROV trencher since the position of the barge is difficult to control and the speed is slow. We therefore propose using four or more anchors and anchor winches to fix the barge at sea, as shown in Fig. 4. The first and second anchors are used to fix the position of the barge, while the third and fourth anchors are installed at the initial working position using a tugboat. The first anchor is then retrieved and installed at the final working position

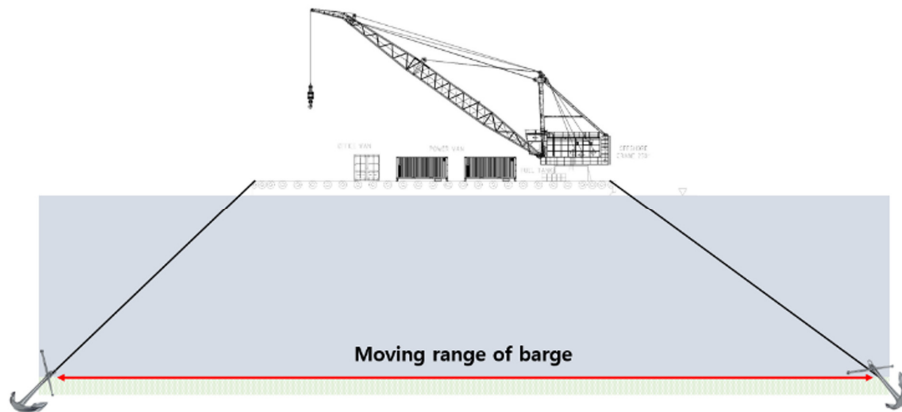
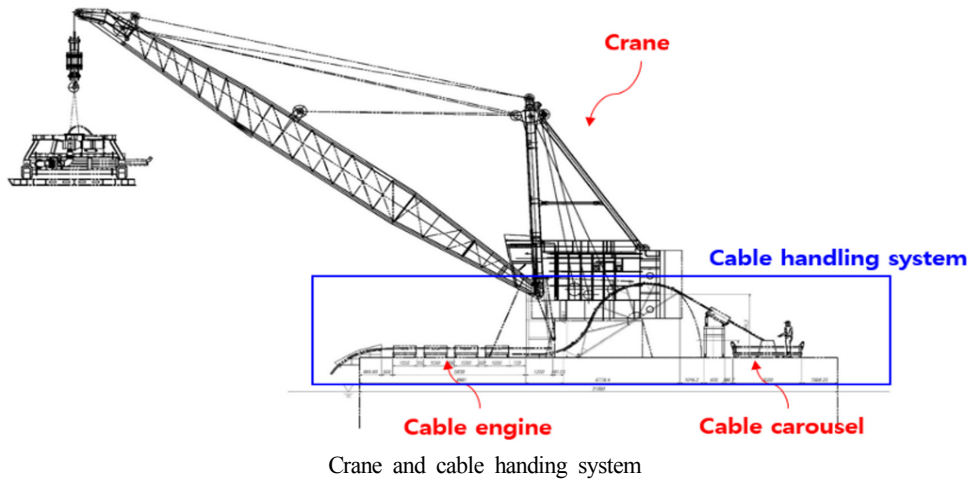
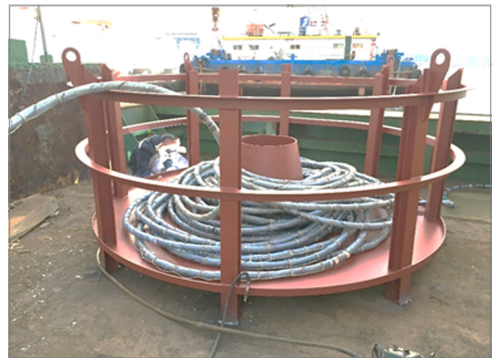


Fig. 5 Method of moving a barge using anchor winches



Cable engine



Cable carousel

Fig. 6 Crane and cable handling system

using a tugboat. After the second anchor has been retrieved, it is also installed at the final working position. In this way, when the first and second anchor winches and the third and fourth anchor winches are synchronously pulled in and let out, the barge can be moved according to the movement of the ROV trencher (Fig. 5). The performance of the barge movement depends on the length of the anchor lines of the barge and the power of the anchor winches. With a single anchoring operation, the maximum length of the burial task is limited by the length of the anchor line. For example, assuming an anchor line length of 500 m and a water depth of 50 m, the barge can move up to approximately 280 m with one anchor installation operation.

(2) To fulfill the function of the LARS device on a barge, we propose a method using a crane and a newly designed cable handling system, as shown in Fig. 6. The proposed cable handling system consists of a cable engine and a carousel. The cable engine has the function of unwinding and winding the umbilical cables, which are difficult to handle. It is composed of a number of cable tensioners arranged in a row. The carousel has a structure for storing the umbilical cables on the barge and can be easily removed when the umbilical cables are released. In addition, an automatic release device is installed on the crane hook on which the ROV trencher is hung to facilitate its launch and its recovery when deployed on the seabed. If a buoy is installed on the raveling device of the crane hook as shown in Fig. 7, it is raveled in the air. On the water, it floats due to the buoyancy of the buoy, releasing the raveling device and the connecting rope between the hook and the ROV trencher. A buoy is also installed on the connecting rope to prevent the

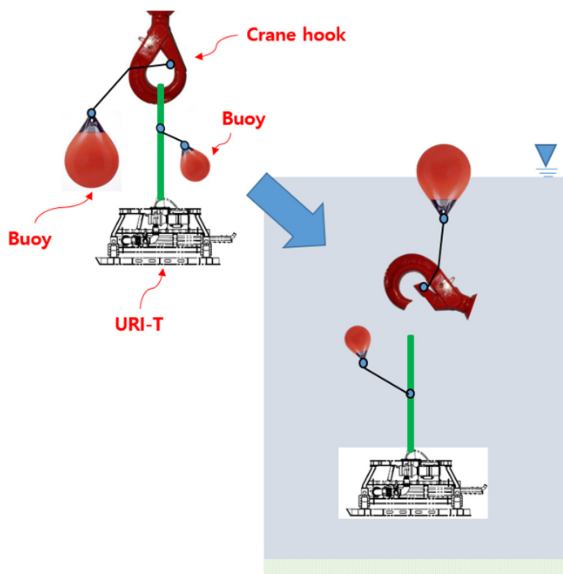


Fig. 7 Automatic raveling device

connecting rope from getting caught in the thruster during operation and to easily connect the connecting rope with the crane hook when recovering the ROV trencher.

Table 3 below compares the operational stages of an ROV when using a DP vessel to those when using a barge. Details for each stage of the barge operation are described in the following chapter.

3.3 Operational Scenario of an ROV Trencher using a Barge

The operational scenario of an ROV trencher using a barge follows the same general sequence as the general ROV trencher operation, but the details of each step differ, as shown in Fig. 8.

(1) **Launch of the ROV trencher:** A 20-mm wire is connected to the ROV trencher and the redundant barge winch to prevent loss in case of emergency. The umbilical cables are marked with colors at intervals of 5 ~ 10 m to allow for continuous monitoring of the looseness of the cable. A connecting rope and an automatic unraveling device are installed on the ROV trencher and the crane hook, respectively, and the ROV trencher is launched on the water surface using the crane. During this step, the length of the umbilical cable must be continuously adjusted using the cable handling system. The ROV trencher sinks by its own force as it is released from the crane by the automatic unraveling device, and it slowly comes to rest on the seabed using the propulsion system. After the ROV lands at a given depth, its position is monitored by the onboard remote control system using the USBL and Quincy systems.

(2) **Position detection of pre-laid cables and pipelines using the cable and pipeline detection system (TSS350 and TSS440):** While the ROV trencher tracks and lands over the pre-laid cables and pipelines, the anchor winch is used to keep the umbilical cable as straight as possible while the ROV trenches moves below the barge. The length of the umbilical cable is adjusted using the cable handling system.

(3) **Cable and pipeline burial and post-lay survey:** While the burial and post-lay survey task is in progress, an anchor winch must be used to follow the movement of the ROV trencher, and the length of the umbilical cable must be adjusted using the cable handling system.

(4) **ROV trencher recovery:** In the reverse order of the launch process, the propulsion system of the ROV trencher is used to elevate it to the water surface, and the umbilical cable is wound using the cable handling system. The connecting rope of the ROV trencher and the crane hook is connected by the deck management manager. At this time, the ROV trencher must maintain a constant depth and position. In particular, it must not float underneath the barge. Once connected to the crane hook, the ROV trencher can be retrieved onto the barge using the crane.

Table 3 Comparison of operating an ROV with a DP vessel and a barge

Stage	DP vessel	Barge
Launch & recovery of the ROV trencher	LARS with A-Frame and winch	Crane and cable handling system
Position detection of cables & pipelines	The dynamic positioning function is used to follow the ROV trencher.	Anchors and anchor winches are used to follow the ROV trencher in a limited area.
Burying works & inspection of the burial		

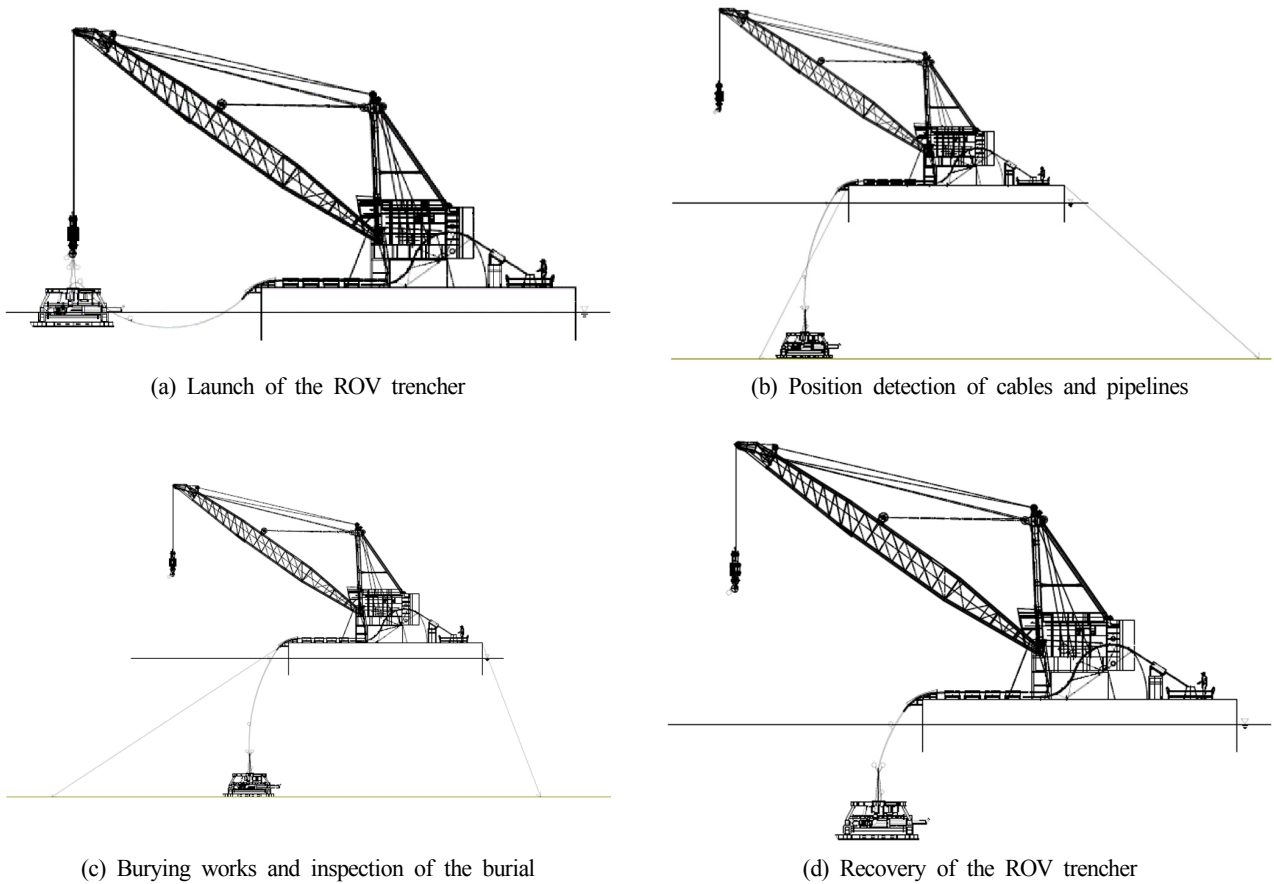


Fig. 8 Operating scenario for an ROV trencher using a barge

4. Application to Buried Construction Sites

4.1 Overview of the Construction on the Water Supply in Yokji-do

The ‘Construction works of water supply in Yokji-do’ is a project that was carried out to expand the water supply area of the water purification plant in Yokji-do and to secure the future water supply and supply capacity. The Korea Offshore Company (KOC), a participating

company in the ‘Site demonstration and commercialization of the developed heavy-duty ROV’ project, constructed the water supply pipe connections between the islands as part of this project. The water supply construction zones ‘Yokjido-Nodaedo’ and ‘Yokjido-Yeonhwado’ are 2.1 km and 5.4 km long, respectively, as shown in Fig. 9. Since the bottom of the seabed in the ‘Yokjido-Nodaedo’ zone is mainly dense sand and rock, the URI-T was only operated on part of this zone. The URI-T

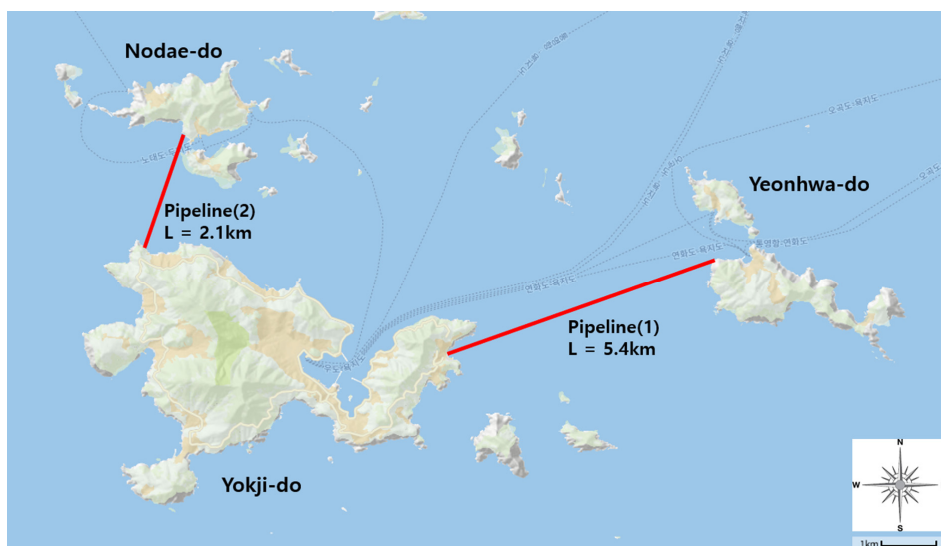


Fig. 9 Overview of the Yokji-do water supply construction work



Fig. 10 Water supply pipe

mainly performed the burial task in the ‘Yokjido-Yeonhwado’ zone, which has a soft and muddy seabed. This zone is about 2.5 m deep on average, and the burial task was conducted on 4.6 km of the total 5.4 km as the bedrock at the beginning and end of the zone were excluded. The burial depth was set to be at least 1.8 m from the top of the pipe to the seabed. The buried water supply pipe shown in Fig. 10 is about 300 mm thick, which includes two water supply pipes, a case to protect them, and a frame connecting the two cases.

4.2 Burial of the Yokji-do Water Supply Pipeline using a Barge

For the burial task in this zone, the 4000p barge Lamir and 72-ton tugboat Changyoung were used. The equipment was placed on the Lamir as shown in Fig. 11. A 160-ton class crane was installed for

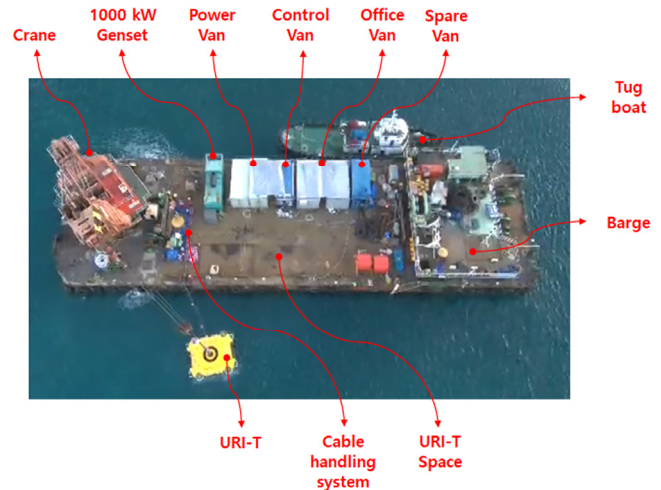


Fig. 11 Equipment arrangement plan on the barge

launch and recovery along with two 20-ton class anchor winches, two 30-ton class anchor winches, a 5-ton class auxiliary winch, and a 500-m long anchor. A 1000-kW genset generator was used to supply power to the URI-T. The office van space was used to observe the work conditions and for meetings, and the spare van was used to store work tools.

The water pipe burial work was conducted in consideration of site safety according to the scenario described above. Depending on the material and depth of the seabed, the burial was carried out 2~4 times, with an approximate daily burial length of 200 to 600 m. Since the work environment is near an actual fishing village, as shown in Fig.



Fishing net on the thruster



Rope on the thruster



Damaged jetting arm



Damaged URI-T frame

Fig. 12 Damage to the URI-T

12, there were incidents of fishing gear, such as ropes, buoys, and fishing nets, getting caught on the platform frame and thruster during the burial, resulting in damage to the frame. There was also damage to the jetting arm and safety rope winding the platform frame caused by operational errors. These errors were responded to immediately and

remedied at the site, and the burial was completed.

4.3 Results of the Yokji-do Waterworks Pipeline Burial

Results of the pipeline burial in the Yokjido-Yeonhwado zone are illustrated in Figs. 13 and 14. The burial task was performed over a

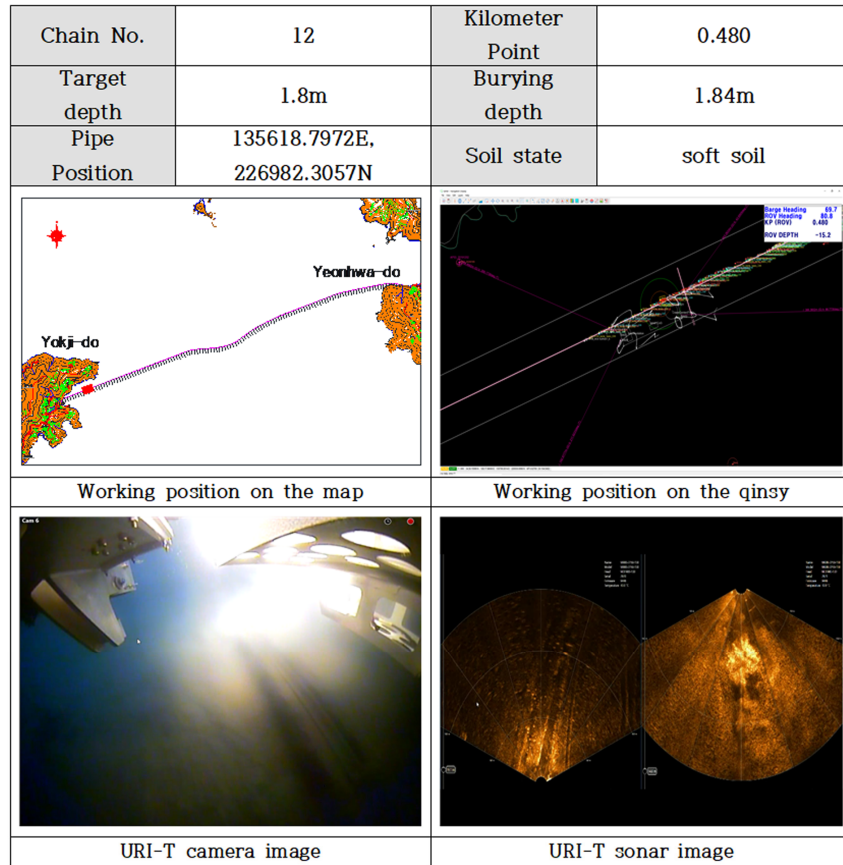


Fig. 13 Results of burying the pipeline

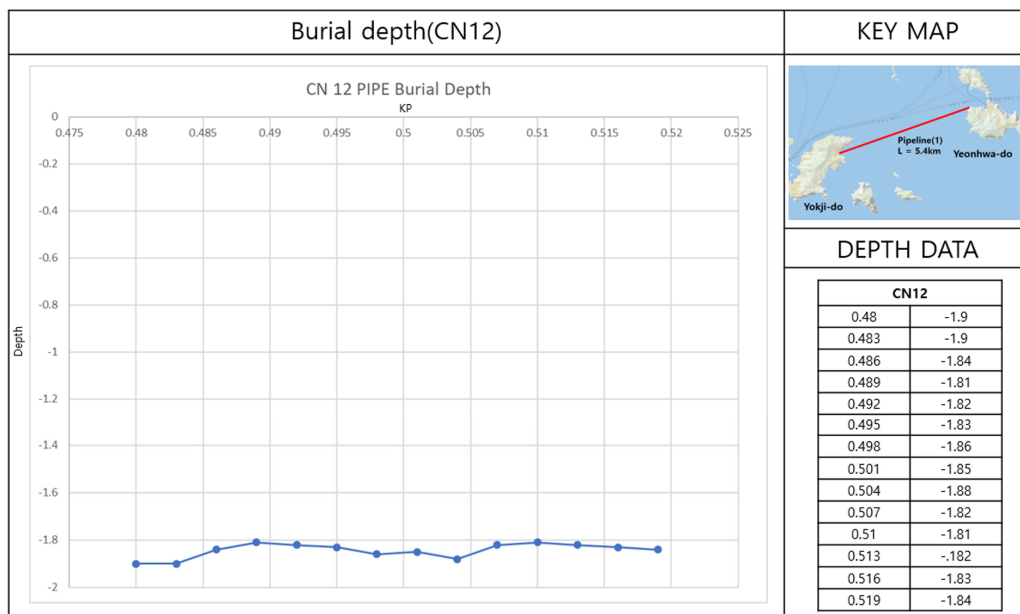


Fig. 14 Burial depth results

distance of about 400 m from a point 480 m away from Yokji-do. The average burial depth in this zone was 1.84 m, which met the target depth of 1.8 m. This indicates that the proposed ROV trencher operation method using a barge is applicable to actual work sites.

5. Conclusion and Future Plans

In this paper, we proposed an ROV trencher operation method using a barge as a method that can be applied for burial construction on the domestic coast, in particular to short construction zones with an urgent schedule and low construction cost, and the applicability of the proposed operation method was verified. One disadvantage of the proposed method is that the launch and recovery and burial operation stages are complicated when compared to the method using an existing DP vessel, resulting in lower operational efficiency and operational stability. However, the proposed method can reduce the manpower required for the operation of the ship and ROV trencher as well as the ship rental and operating costs and can facilitate adjusting the working hours and schedule. It thus provides significant benefits in terms of the construction cost and scheduling for construction such as the water supply in Yokji-do. Going forward, we are in the process of securing a gas pipeline burial project in Vietnam (planned in August 2020), and modification and supplementation (2020.02 ~ 2020.06) of the URI-T are underway accordingly. In addition, we are attempting to win bids for construction work on the domestic coast.

Acknowledgement

This paper relies on research conducted by the Ministry of Oceans and Fisheries funded by the Ministry of Oceans and Fisheries with the support of the Korea Institute of Maritime Science & Technology Promotion in 2020 (Underwater Construction Robot Project for Marine Development, PJT200539).

References

Ahn, S.H., & Kim, D.S. (2009). Submarine Cable Installation and Protection Methods According as Characteristics of Ocean Environment. *Journal of the Korean Society of Marine Environment and Safety*, 15(1), 25-32.

- Cho, G.R., Kang, H.J., Lee, M.J., & Li, J.H. (2019a). Heading Control of URI-T, an Underwater Cable Burying ROV: Theory and Sea Trial Verification. *Journal of Ocean Engineering and Technology*, 33(2), 178-188. <https://doi.org/10.26748/KSOE.2019.010>
- Cho, G.R., Ki, G.H., & Li, J.H. (2019b). Touch Screen Based Assistance Technique for Underwater Manipulation of Cable Burying ROV. *Journal of the Korean Society for Precision Engineering*. 36(4), 349-361. <https://doi.org/10.7736/KSPE.2019.36.4.349>
- Jang, I.-S. (2014). Reporting: Korea Institute Ocean Science & Technology Underwater Construction Robotics R&D Center. *Magazine of the Korean Society of Steel Construction*, 26(2), 84-85.
- Jones, M., & Hirai, M. (2001). A Novel ROV Developed for the Future Requirements of Cable Installation and Maintenance. *Proceedings of Sub Optic 2001*, Kyoto, Japan, T6.3.4.
- Kang, H.J., Lee, M.J., Cho, G.R., Ki, G.H., Kim, M.G., & Li, J.H. (2019). Development of a ROV Trencher URI-T and its Sea Trial. *Journal of Ocean Engineering and Technology*, 33(3). 300-311. <https://doi.org/10.26748/KSOE.2019.018>
- Li, J.H., Kim, J.T., Lee, M.J., Lee, H.J., Kang, H.J., Han, S.C., Lee, J.W., & Kwak, H.W. (2014). Conceptual Design of Optimal Thrust System for Efficient Cable Burying of ROV Trencher. In *2014 Oceans-St. John's, IEEE*. <https://doi.org/10.1109/OCEANS.2014.7003153>
- Yoo, J.D., & Shin, H.S. (2010). Analyses of the Submarine Cable Faults of EAC and Protection Ways. *The Journal of the Korea Institute of Electronic Communication Sciences*, 5(3), 227-232.

Author ORCIDs

Author name	ORCID
Kim, Min-Gyu	0000-0001-8517-6352
Kang, Hyungjoo	0000-0001-8838-3285
Lee, Mun-Jik	0000-0001-7806-3237
Cho, Gun Rae	0000-0002-8536-4844
Li, Ji-Hong	0000-0002-5162-2737
Yoon, Tae-Sam	0000-0002-7274-8355
Ju, Jaeheung	0000-0002-9549-7982
Kwak, Han-Wan	0000-0002-1705-8124

Underwater Acoustic Research Trends with Machine Learning: Ocean Parameter Inversion Applications

Haesang Yang¹, Keunhwa Lee², Youngmin Choo³ and Kookhyun Kim⁴

¹Research Professor, Department of Naval Architecture & Ocean Engineering, Seoul National University, Seoul, Korea

²Associate Professor, Department of Defense System Engineering, Sejong University, Seoul, Korea

³Assistant Professor, Department of Defense System Engineering, Sejong University, Seoul, Korea

⁴Associate Professor, School of Naval Architecture & Ocean Engineering, Tongmyong University, Busan, Korea

KEY WORDS: Underwater acoustics, Sonar system, Machine learning, Deep learning, Signal processing, Parameter inversion

ABSTRACT: Underwater acoustics, which is the study of the phenomena related to sound waves in water, has been applied mainly in research on the use of sound navigation and range (SONAR) systems for communication, target detection, investigation of marine resources and environments, and noise measurement and analysis. Underwater acoustics is mainly applied in the field of remote sensing, wherein information on a target object is acquired indirectly from acoustic data. Presently, machine learning, which has recently been applied successfully in a variety of research fields, is being utilized extensively in remote sensing to obtain and extract information. In the earlier parts of this work, we examined the research trends involving the machine learning techniques and theories that are mainly used in underwater acoustics, as well as their applications in active/passive SONAR systems (Yang et al., 2020a; Yang et al., 2020b; Yang et al., 2020c). As a follow-up, this paper reviews machine learning applications for the inversion of ocean parameters such as sound speed profiles and sediment geoacoustic parameters.

1. Introduction

Underwater acoustics is the study of the phenomena related to the generation, propagation, transmission, and reception of sound waves in underwater environments. It has been applied in underwater communication, target detection, marine resource and environment investigation using sound navigation and range (SONAR) systems, and the measurement and analysis of underwater sound source characteristics. The main representative field that utilizes underwater acoustics is remote sensing, wherein information on a target object is acquired indirectly from acoustic data. Machine learning, which has recently achieved substantial success in information acquisition and extraction, is actively utilized in remote sensing. In the previous parts of this work, the research trends in the machine learning techniques and theories that are mainly used in underwater acoustics and their applications in active and passive SONAR systems were reviewed (Yang et al., 2020a; Yang et al., 2020b; Yang et al., 2020c). In this paper (the final part of this work), its application to the field of ocean parameter inversion is described.

2. Application of Machine Learning in the Field of Ocean Parameter Inversion

A sound wave measured in the form of a signal on a hydrophone contains information of the medium along the propagation path. The process of indirectly extracting necessary information such as ocean parameters by processing acoustic signals is called inversion. In underwater acoustics, inversion can be largely divided into the localization of surface vehicles and underwater vehicles (Parvulescu and Clay, 1965; Clay, 1966; Clay, 1987; Clay and Li, 1988; Buckner, 1976; Baggeroer et al., 1993; Tolstoy, 1993); tomography inversion, wherein the inversion operation is performed on the physical properties of seawater, such as the temperature profile over a broad area of water (Shang, 1989; Tolstoy et al., 1991; Tolstoy, 1992); and geoacoustic inversion, which yields the composition, morphology, and geological properties of the marine sediment (Rajan et al., 1987; Lynch et al., 1991). The localization of underwater sound sources has been covered in the previous parts of this review work (Yang et al., 2020b; Yang et al., 2020c). The results and trends of tomography inversion and geoacoustic inversion are reviewed herein.

Received 2 March 2020, revised 11 April 2020, accepted 13 April 2020

Corresponding author Youngmin Choo: +82-2-6935-2532, ychoo@sejong.ac.kr

© 2020, The Korean Society of Ocean Engineers

This is an open access article distributed under the terms of the creative commons attribution non-commercial license (<http://creativecommons.org/licenses/by-nc/4.0>) which permits unrestricted non-commercial use, distribution, and reproduction in any medium, provided the original work is properly cited.

The ocean parameter inversion established in underwater acoustics is model based. Model-based inversion is a technique that compares the measured signal and simulated signal with a model and then adopts the model that yields the result most similar to the inversion solution. The matched field processing (MFP) technique is a representative technique. Here, the physical quantities of main interest in underwater acoustics are the sound speed profile and the environmental information related to the geological properties of marine sediment. These are essential factors for improving the prediction accuracy of the acoustic propagation model.

In the 1990s, the modeling of wave propagation in complex marine environments was realized, and model-based parameter inversion began to be studied extensively. To address the mismatch problem arising from sound source localization using an MFP, the sound source location and sound speed profile were inverted simultaneously (Collins and Kuperman, 1991). Subsequently, the inversion technique for the geoacoustic parameters of marine sediments was developed to address the mismatch problem (Collins et al., 1992; Lindsay and Chapman, 1993; Dosso et al., 1993; Gerstoft, 1994; Tolstoy et al., 1998). Until recently, the inversion technique has been steadily undergoing development in conjunction with the most advanced signal processing and optimization techniques. This article aims to review the research trends in ocean parameter inversion using machine learning techniques.

As mentioned previously, the ocean parameter inversion technique underwent development in conjunction with the emergence of a representative model-based inversion technique (MFP) and exhibited significantly good results. However, when utilizing the inversion method using MFP, the ambiguity of the inversion solution increases. Furthermore, the method is not robust against model mismatch when the wave propagation environment becomes complex, such as in the case of shallow waters. In addition, the problem becomes more challenging in restrictive situations where a high signal-to-noise ratio in the sensor array cannot be guaranteed. To address this, recently, studies with high-resolution results have been reported in conjunction with the development of a sparse signal representation in the spatial or temporal (frequency) domain, e.g., the compressive sensing (CS) technique. The fundamental theory underlying CS is that in a linear system, the raw signal can be recovered under appropriate conditions even when the raw signal has a dimension higher than that of the observed data (Candes and Wakin, 2008). The CS technique utilizing this principle has been applied to active and passive SONAR signal processing and ship radiation noise analysis. Further details are available in the special issue of the *Journal of the Acoustical Society of America* (Gerstoft et al., 2018).

As observed from these cases, as in the case of problems of inversion of underwater acoustics, the most advanced signal processing theory was first applied to improve the localization performance of underwater sources in combination with MFP. It was then applied to the inversion of ocean parameters such as marine sediment properties and sound speed profile (Yardim et al., 2014;

Bianco and Gerstoft, 2016; Choo and Seong, 2018). An example of a subsequent related study is sound speed profile inversion using dictionary learning which is an unsupervised machine learning technique. The existing MFP method is disadvantageous in that it is considerably complex and time-consuming in terms of computation. Moreover, it is challenging to apply the method with limited resources because it requires a number of sensors to acquire data. From this perspective, signal processing techniques using sparse signal representation, one of which is dictionary learning, have attracted attention in the field of underwater acoustic signal processing. Dictionary learning is a technique in which a dictionary is introduced from the measured data, sparse signal representation of meaningful information is extracted, and training is performed with the extracted information. In particular, when this is applied to ocean parameter inversion, to represent the sound speed profile as an optimum sparse signal, the dictionary of the shape function is developed to increase the resolution of the sound speed profile (Bianco and Gerstoft, 2017). The sound speed profile can be expressed as an expansion of the empirical orthogonal function for the sound speed variation. Bianco and Gerstoft (2017) developed a dictionary through a sparse signal representation that reduces the dimension of the empirical orthogonal function vectors. The training was performed using a clustering-based algorithm to obtain the recovered sound speed profile (Fig. 1).

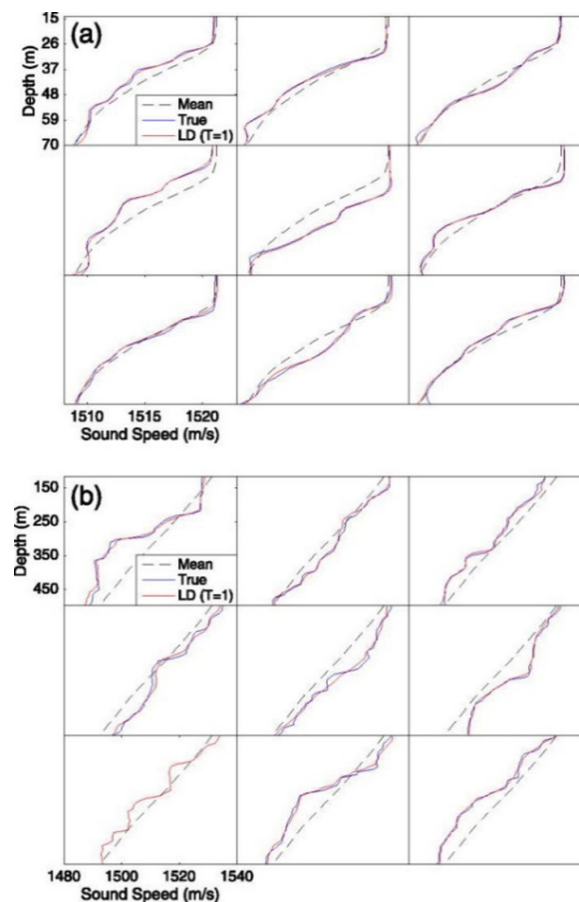


Fig. 1 Sound speed profile reconstruction using the dictionary learning (Bianco and Gerstoft, 2017).

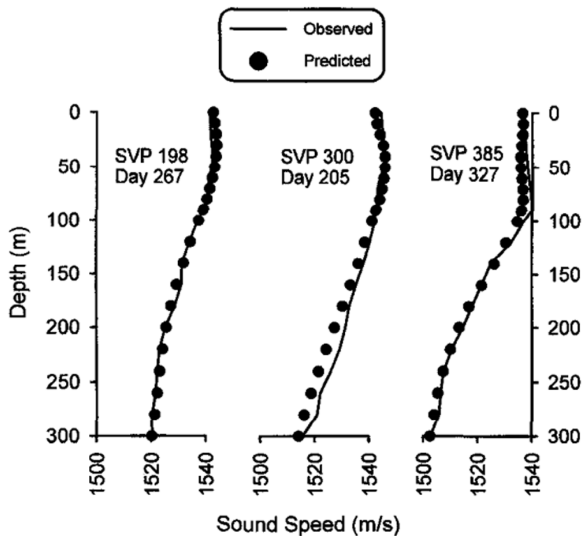


Fig. 2 Comparison of sound speed profiles between observations and predictions produced by using multi-layer perceptron (Park and Kennedy, 1996)

An early machine learning-based approach to sound speed profile inversion used a multi-layer perceptron-based technique composed of a much shallower network than the state-of-the-art deep neural network models (Park and Kennedy, 1996; Jain and Ali, 2006). Park and Kennedy (1996) estimated the sound speed profile using a combination of sound speed records and environmental information, and a multi-layer perceptron structure, given that the sound speed profile can be estimated as an expansion of the empirical orthogonal function for the sound speed variation (Fig. 2).

Here, the environmental information includes date, sea surface temperature obtained by the infrared sensor of a satellite, seafloor temperature measured by a temperature sensor embedded in the seafloor, and time of flight between two acoustic sensors buried in the seafloor calculated using the wave propagation model to consider the multiple paths of a sound wave in the corresponding environment. With regard to the sound speed records, the large amount of data from the World Ocean Atlas constructed by the National Oceanic and Atmospheric Administration was used. It was demonstrated that sound speed profile prediction is possible almost in real time through a simple multi-layer perceptron structure using only two layers of the hidden layer. However, the temperature and time information they used as input factors had limitations: the mean record had to be stable and the acoustic model used to calculate the multiple paths was applicable only in a range-independent environment. The research results of Jain and Ali (2006) were not considerably different from those of the above research. However, they estimated the sound speed profile using surface observations from a mooring that were measured on an hourly basis for one year as input parameters, utilizing a backpropagation algorithm and multi-layer perceptron structure with two hidden layers.

Early machine learning-based approaches to geoacoustic parameter inversion (such as that for sound velocity, density of marine sediments, layer thickness, and damping coefficients) were also based on the

expansion of the basis function. This is similar to the case mentioned above. Caiti and Jesus (1996) investigated the estimation of the seafloor's geoacoustic parameters from sound field measurements of the water layer. In particular, the Gaussian radial basis function was used to approximate the inverse function to speed up the computation. In addition, the results of inversion of sound velocity, damping coefficient, and density were demonstrated by applying the function to simulation data and marine experimental data measured using a horizontal towed line array. The results of their research exhibited very high efficiency in terms of inversion speed. However, there was a limitation: the method was applicable only when all the information on the depth, sound speed profile, and configuration of the source and receiver were provided.

Another approach to geoacoustic parameter inversion is to introduce neural networks into model-based inversion, which can be considered as an optimization problem. Benson et al. (2000) trained a neural network with the calculation data of the sound field of each sensor in a vertical line array using a wave propagation model in a shallow water environment. In particular, the spectral component of transmission loss was used as the input parameter of the neural network. In-situ experimental data were used to verify the neural network model. The distance and depth of the sound source and the sound speed and thickness of the marine sediment were estimated with high accuracy.

With regard to the exact physical quantity of marine sediments, traditionally, only sample information with sparse distribution has been obtained through core collection, which introduces the problem of uncertainty. From a probabilistic perspective, this uncertainty was quantitatively calculated by reflecting random characteristics using a multivariate probability density function or a joint ensemble moment. This can result in questions on the estimation results from places where data are unavailable. Research is underway to determine solutions using a machine learning-based approach. In particular, the geoacoustic inversion technique is gradually becoming sophisticated, e.g., using machine learning techniques for extraction of physical quantities such as porosity and hydraulic conductivity (Tartakovsky et al., 2008; Martin et al., 2015). Because existing porosity estimation methods using interpolation or regression did not sufficiently reflect seafloor topography or geological properties, Martin et al (2015) used the random forest (RF) technique, which utilizes multiple predictor variables, to predict the seafloor porosity (Fig. 3). They developed

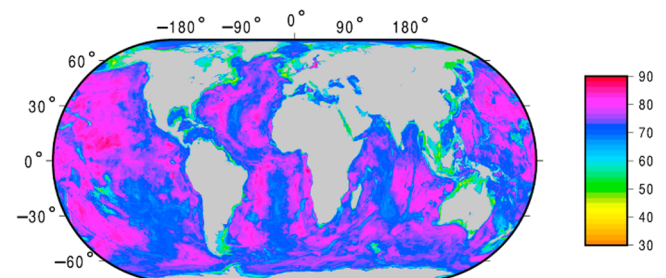


Fig. 3 Seafloor porosity prediction produced using machine learning (Martin et al., 2015)

predictor grids that added several variables related to porosity to vast geological property data obtained from deep sea/marine drilling and combined them with RF, a tool for regression tree analysis. The results were compared with the existing porosity estimation results in terms of root-mean-square error, Nash-Sutcliffe efficiency, Benchmark efficiency, etc. Their proposed method demonstrated the highest prediction performance compared to the existing methods.

Finally, we provide a brief summary of the application of the inversion technique on sediment geology. The geological form of sediments is essential information for dredging to secure a route, laying submarine cables, and dredging of rivers to regulate flow. In the case of underwater and marine sediments, classification techniques based on machine learning and statistical methods have been undergoing continuous development. Starting from the early classification of surficial sediments using neural network architecture and statistical classifiers (Michalopoulou et al., 1995), recent classification techniques based on supervised learning that perform classification on the type of surficial sediment and grain size based on multi-beam SONAR, backscattered acoustic data, and bathymetry have been reported to display considerably high performance (Stephens and Diesing, 2014; Diesing et al., 2014; Buscombe and Grams, 2018). In particular, Stephens and Diesing (2014) selected six types of machine learning approaches (k-nearest neighbor, support vector machine, classification tree, RF, neural network, and Naïve Bayes) as supervised learning-based classification techniques for seabed mapping. The secondary features such as roughness, curvature, Moran's I, and Sobel filter were newly extracted from the water depth data and backscattered acoustic data, and the results of prediction of the type of surficial sediment were compared. Diesing et al. (2014) compared the classification results of surficial sediments and grain

sizes (Fig. 4) that were predicted by manual interpretation, image analysis using a 2D Fourier filter, geostatistics techniques, and RF (Fig. 4). The comparison indicated that the results could be improved by the ensemble technique (combining multiple techniques to produce the desired output). Buscombe and Grams (2018) proposed a fully connected conditional random field that can consider the relative size and proximity of backscattered acoustic data for substrate characterization and compare the results with those obtained by the Gaussian mixture model to evaluate the performance.

3. Conclusion

In this review, we examined the trend of research conducted by applying machine learning (including deep learning) to underwater acoustics and SONAR applications. It is evident that machine learning techniques need to be improved further for application in the areas of underwater acoustics, acoustical oceanography, and technologies related to SONAR through follow-up studies. Furthermore, the implementation of machine learning is likely to provide flexibility in future research directions and increase the applicability of the approach.

However, in the case of data-based techniques represented by deep learning, the problem wherein securing data including class information is essential based on the inherent characteristics of deep learning still remains. More specifically, in underwater acoustics, it is challenging to obtain such data, and understanding of the environment is essential. Therefore, in addition to the development of physical intuition and theory, the use of verified wave propagation models or statistical and mathematical models requiring a relatively marginal amount of data should be developed in parallel to overcome the above challenges and limitations.

References

- Baggeroer, A.B., Kuperman, W.A., & Mikhalevsky, P.N. (1993). An Overview of Matched Field Methods in Ocean Acoustics. *IEEE Journal of Oceanic Engineering*, 18(4), 401-424. <https://doi.org/10.1109/48.262292>
- Benson, J., Chapman, N.R., & Antoniou, A. (2000). Geoacoustic Model Inversion Using Artificial Neural Networks. *Inverse Problems*, 16(6), 1627-1639. <https://doi.org/10.1088/0266-5611/16/6/302>
- Bianco, M., Gerstoft, P. (2016). Compressive Acoustic Sound Speed Profile Estimation. *The Journal of the Acoustical Society of America*, 139(3), EL90-EL94.
- Bianco, M., & Gerstoft, P. (2017). Dictionary Learning of Sound Speed Profiles. *The Journal of the Acoustical Society of America*, 141(3), 1749-1758.
- Bucker, H.P. (1976). Use of Calculated Sound Fields and Matched Field Detection to Locate Sound Sources in Shallow Water. *The Journal of the Acoustical Society of America*, 59(2), 368-373.
- Buscombe, D., & Grams, P.E. (2018). Probabilistic Substrate

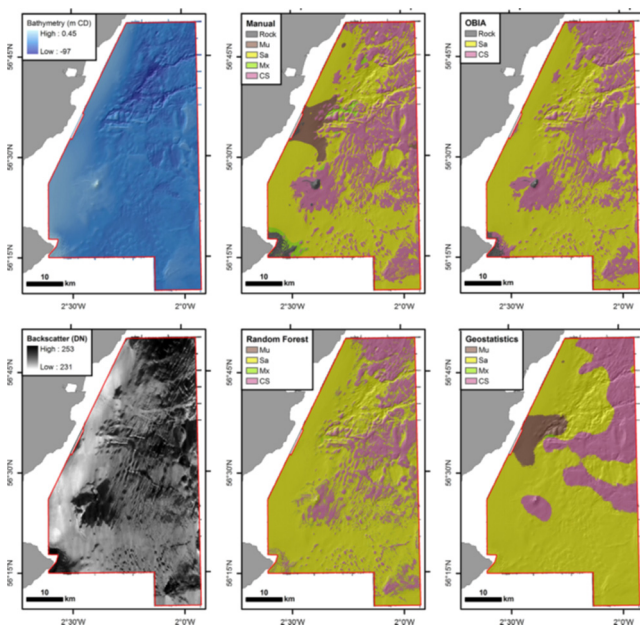


Fig. 4 Seabed substrate maps including bathymetry, backscatter strength, and machine learning and geostatistics results (Diesing et al., 2014)

- Classification with Multispectral Acoustic Backscatter: A Comparison of Discriminative and Generative Models. *Geoscience*, 8(11), 395. <https://doi.org/10.3390/geosciences8110395>
- Candes, E.J., & Wakin, M.B. (2008). An Introduction to Compressive Sampling. *IEEE Signal Processing Magazine*, 25(2), 21-30.
- Caiti, A., & Jesus, S.M. (1996). Acoustic Estimation of Seafloor Parameters: A Radial Basis Functions Approach. *The Journal of the Acoustical Society of America*, 100(3), 1473-1481.
- Choo, Y., & Seong, Y. (2018). Compressive Sound Speed Profile Inversion Using Eamforming Results. *Remote Sensing*, 10, 704.
- Clay, C.S. (1966). Use of Arrays for Acoustic Transmission in a Noisy Ocean. *Review of Geophysics*, 4(4), 475-507.
- Clay, C.S. (1987). Optimum Time Domain Signal Transmission and Source Location in a Waveguide. *The Journal of the Acoustical Society of America*, 81(3), 660-664.
- Clay, C. S., & Li, S. (1988). Time Domain Signal Transmission and Source Location in a Waveguide: Matched Filter and Deconvolution Experiments. *The Journal of the Acoustical Society of America*, 83(4), 1377-1417.
- Collins, M.D., & Kuperman, W.A. (1991). Focalization: Environmental Focusing and Source Localization. *The Journal of the Acoustical Society of America*, 90(3), 1410-1422.
- Collins, M.D., Kuperman, W.A., & Schmidt, H. (1992). Nonlinear Inversion for Ocean-bottom Properties. *The Journal of the Acoustical Society of America*, 92, 2770-2783.
- Diesing, M., Green, S.L., Stephens, D., Lark, R.M., Stewart, H.A., & Dove, D. (2014). Mapping Seabed Sediment: Comparison of Manual, Geostatistical, Object-based Image Analysis and Machine Learning Approaches. *Continental Shelf Research*, 84, 107-119. <https://doi.org/10.1016/j.csr.2014.05.004>.
- Dosso, S.E., Y Jeremy, M.L., Ozard, J.M., & Chapman, N.R. (1993). Estimation of Ocean Bottom Properties by Matched-field Inversion of Acoustic Field Data. *IEEE Journal of Oceanic Engineering*, 18, 232-239.
- Gerstoft, P. (1994). Inversion of Seismoacoustic Data Using Genetic Algorithms and a Posteriori Probability Distribution. *The Journal of the Acoustical Society of America*, 95, 770-782.
- Gerstoft, P., Mecklenbräuker, C.F., Seong, W., & Bianco, M. (2018). Introduction to Compressive Sensing in Acoustics. *The Journal of the Acoustical Society of America*, 143(6), 3731-3736. <https://doi.org/10.1121/1.5043089>
- Jain, S., & Ali, M.M. (2006). Estimation of Sound Speed Profiles Using Artificial Neural Network. *IEEE Geoscience and Remote Sensing Letters*, 3(4), 467-470. <https://doi.org/10.1109/LGRS.2006.876221>
- Lindsay, C.E., & Chapman, N.R. (1993). Matched Field Inversion for Geoacoustic Model Parameters Using Adaptive Simulated Annealing. *IEEE Journal of Oceanic Engineering*, 18(3), 224-231. <https://doi.org/10.1109/JOE.1993.236360>
- Lynch, J.F., Rajan, S.D., & Frisk, G.V. (1991). A Comparison of Broadband and Narrow-band Modal Inversions for Bottom Properties at a Site Near Corpus Christi, Texas. *The Journal of the Acoustical Society of America*, 89(2), 648-665. <https://doi.org/10.1121/1.400676>
- Martin, K.M., Wood, W.T., & Becker, J.J. (2015). A Global Prediction of Seafloor Sediment Porosity Using Machine Learning. *Geophysical Research Letters*, 42(24), 10640-10646. <https://doi.org/10.1002/2015GL065279>
- Michalopoulou, Z-H., Alexandrou, D., & de Moustier, C. (1995). Application of Neural and Statistical Classifiers to the Problem of Seafloor Characterization. *IEEE Journal of Oceanic Engineering*, 20(3), 190-197. <https://doi.org/10.1109/48.393074>
- Park, J.C., & Kennedy, R.M. (1996). Remote Sensing of Ocean Sound Speed Profiles by a Perceptron Neural Network. *IEEE Journal of Oceanic Engineering*, 21(2), 216-224. <https://doi.org/10.1109/48.486796>
- Parvulescu, A., & Clay, C.S. (1965). Reproducibility of Signal Transmission in the Ocean. *Radio Electronic Engineer*, 29(4), 223-228. <https://doi.org/10.1049/ree.1965.0047>
- Rajan, S.D., Lynch, J.F., & Frisk, G.V. (1987). Perturbative Inversion Methods for Obtaining Bottom Parameters in Shallow Water. *The Journal of the Acoustical Society of America*, 82(3), 998-1017. <https://doi.org/10.1121/1.395300>
- Shang, E.C. (1989). Ocean Acoustic Tomography Based on Adiabatic Mode Theory. *The Journal of the Acoustical Society of America*, 85(4), 1531-1537. <https://doi.org/10.1121/1.397355>
- Stephens, D., & Diesing, M. (2014). A Comparison of Supervised Classification Methods for the Prediction of Substrate Type Using Multibeam Acoustic and Legacy Grain-size Data. *Plos One*, 9(4), e93950.
- Tartakovsky, D.M., Guadagnini, A., & Wohlberg, B.E. (2008). Machine learning methods for inverse modeling. *Geostatistics for Environmental Applications*, 117-125, Springer Science Business Media.
- Tolstoy, A. (1992). Linearization of the Matched Field Processing Approach to Acoustic Tomography. *The Journal of the Acoustical Society of America*, 91(2), 781-787. <https://doi.org/10.1121/1.402538>
- Tolstoy, A. (1993). Matched Field Processing for Underwater Acoustics. Singapore: World Scientific.
- Tolstoy, A., Chapman, N.R., & Brooke, G. (1998). Workshop '97: Benchmarking for Geoacoustic Inversion in Shallow Water. *Journal of Computational Acoustics*, 6(1&2), 1-28. <https://doi.org/10.1142/S0218396X9800003X>
- Tolstoy, A., Diachok, O., & Frazer, L.N. (1991). Acoustic Tomography via Matched Field Processing. *The Journal of the Acoustical Society of America*, 89(3), 1119-1127. <https://doi.org/10.1121/1.400647>
- Yang, H., Lee, K., Choo, Y., Kim, K. (2020a). Underwater Acoustic Research Trends with Machine Learning: General Background. *Journal of Ocean Engineering and Technology*, 34(2), 147-154. <https://doi.org/10.26748/KSOE.2020.015>
- Yang, H., Lee, K., Choo, Y., & Kim, K. (2020b). Underwater Acoustic Research Trends with Machine Learning: Passive SONAR

Applications. *Journal of Ocean Engineering and Technology*, 34(3), 227-236. <https://doi.org/10.26748/KSOE.2020.017>

- Yang, H., Byun, S.-H., Lee, K., Choo, Y., & Kim, K. (2020c). Underwater Acoustic Research Trends with Machine Learning: Active SONAR Applications. *Journal of Ocean Engineering and Technology*. In Press. <https://doi.org/10.26748/KSOE.2020.018>
- Yardim, C., Gerstoft, P., Hodgkiss, W.S., & Traer, J. (2014). Compressive Geoacoustic Inversion Using Ambient Noise. *The Journal of the Acoustical Society of America*, 135(3), 1245-1255. <https://doi.org/10.1121/1.4864792>

Author ORCIDs

Author name	ORCID
Yang, Haesang	0000-0001-7101-5195
Lee, Keunhwa	0000-0003-4827-3983
Choo, Youngmin	0000-0002-9100-9494
Kim, Kookhyun	0000-0002-4214-4673

Instructions for Authors

General information

To submit a manuscript to the Journal of Ocean Engineering and Technology (JOET), it is advised to first carefully read the aims and the scope section of this journal, as it provides information on the editorial policy and the category of papers it accepts. Unlike many regular journals, JOET usually has no lag in acceptance of a manuscript and its publication. Authors that find a match with the aims and the scope of JOET are encouraged to submit as we publish works from all over the world. JOET adheres completely to guidelines and best practices published by professional organizations, including Principles of Transparency and Best Practice in Scholarly Publishing (joint statement by COPE, DOAJ, WAME, and OASPA (<http://doaj.org/bestpractice>) if otherwise not described below. As such, JOET would like to keep the principles and policies of those professional organizations during editing and the publication process.

Research and publication ethics

Details on publication ethics are found in <http://joet.org/authors/ethics.php>. For the policies on research and publication ethics not stated in the Instructions, Guidelines on Good Publication (<http://publicationethics.org/>) can be applied.

Requirement for membership

One of the authors who submits a paper or papers should be member of the Korean Society of Ocean Engineers (KSOE), except a case that editorial board provides special admission of submission.

Publication type

Article types include scholarly monographs (original research articles), technical articles (technical reports and data), and review articles. The paper should have not been submitted to other academic journal. When part or whole of a manuscript was already published to conference papers, research reports, and dissertations, then the corresponding author should note it clearly in the manuscript.

Copyright

After published to JOET, the copyright of manuscripts should belong to KSOE. A transfer of copyright (publishing agreement) form can be found in submission website (<http://www.joet.org>).

Manuscript submission

Manuscript should be submitted through the on-line submission website (<http://www.joet.org>). The date that corresponding author submits a paper through on-line website is the official date of submission. Other correspondences can be sent by an email to the Editor in Chief or secretariat. The manuscript must be accompanied by a signed statement that it has been neither published nor currently submitted for publication elsewhere. The manuscript should be written in English or Korean. Ensure that online submission are in a standard word processing format (Hangul or MS Word are accepted). Ensure that graphics are high-resolution. Be sure all necessary files have been uploaded/ attached.

Authors' checklist

Please refer to "Authors' Checklist" for details.

Article structure

Manuscript must be edited in the following order: (1) Title, (2) Authors' names and affiliations, (3) Keywords, (4) Abstract, (5) Nomenclature (optional), (6) Introduction, (7) Main body (analyses, tests, results, and discussions), (8) Conclusions, (9) Acknowledgements (optional), (10) References, (11) Appendices (optional).

Abstract

A concise and factual abstract is required. The abstract should state briefly the background, purpose and methods of the research, the principal results and conclusions. An abstract should be written in around 300 words. References are not cited in abstract whenever possible. Also, non-standard or uncommon abbreviations should be avoided, but if essential they must be defined at their first mention in the abstract itself.

Keywords

Immediately after the abstract, provide a maximum of 5 or 6 keywords.

Unit

Use the international system units(SI). If other units are mentioned, please give their equivalent in SI.

Equations

All mathematical equations should be clearly printed/typed using well accepted explanation. Superscripts and subscripts should be typed clearly above or below the base line. Equation numbers should be given in Arabic numerals enclosed in parentheses on the right-hand margin.

Tables

Tables should be numbered consecutively with Arabic numerals. Each table should be fully titled. All tables should be referred to in the texts.

Figures

Figures should be numbered consecutively with Arabic numerals. Each figure should be fully titled. All figures should be referred to in the texts. All the illustrations should be of high quality meeting with the publishing requirement with legible symbols and legends.

Conflict of interest

It should be disclosed here according to the statement in the Research and publication ethics regardless of existence of conflict of interest. If the authors have nothing to disclose, please state: "No potential conflict of interest relevant to this article was reported."

Funding

Funding to the research should be provided here. Providing a FundRef ID is recommended including the name of the funding agency, country and if available, the number of the grant provided by the funding agency. If the funding agency does not have a FundRef ID, please ask that agency to contact the FundRef registry (e-mail: fundref.registry@crossref.org). Additional detailed policy of FundRef description is available from <http://www.crossref.org/fundref/>. Example of a funding description is as follows:

The study is supported by the Inha University research fund (FundRef ID: 10.13039/501100002632), and the Korea Health Personnel Licensing Examination Institute research fund (FundRef ID: 10.13039/501100003647).

Acknowledgments

Any persons that contributed to the study or the manuscript, but not meeting the requirements of an authorship could be placed here. For mentioning any persons or any organizations in this section, there should be a written permission from them.

References in text

References in texts follow the APA style. Authors can also see how references appear in manuscript text through the 'Template'.

Reference list

Reference list follows the APA style. Authors can see how references should be given in reference section through the 'Template'.

Appendices

The appendix is an optional section that can contain details and data supplemental to the main text. If there is more than an appendix, they should be identified as A, B, C, etc. Formulae and equations in appendices should be given separate numbering: Eq. (A1), Eq. (A2), etc.; in a subsequent appendix, Eq. (B1) and so on. Similarly for tables and figures: Table A1; Fig. A1, etc.

ORCID (Open Researcher and Contributor ID)

All authors are recommended to provide an ORCID. To obtain an ORCID, authors should register in the ORCID web site: <http://orcid.org>. Registration is free to every researcher in the world. Example of ORCID description is as follows:

Joonmo Chung: <https://orcid.org/0000-0003-1407-9031>

Peer review and publication process

The peer review process can be broadly summarized into three groups: author process, review process, and publishing process for accepted submissions. General scheme is presented in Figure 1.

Check-in process for review

If the manuscript does not fit the aims and scope of the Journal or does not adhere to the Instructions to Authors, it may be rejected immediately after receipt and without a review. Before reviewing, all submitted manuscripts are inspected by Similarity Check powered by iThenticate (<https://www.crossref.org/services/similarity-check/>), a plagiarism-screening tool. If a too high degree of similarity score is found, the Editorial Board will do a more profound content screening.

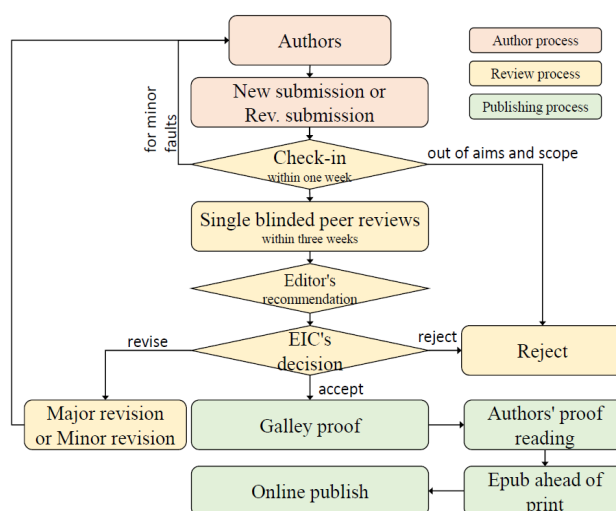


Figure 1 Flow chart of the peer review and publication process of JOET

The criterion for similarity rate for further screening is usually 15%; however, rather than the similarity rate, the Editorial Board focuses on cases where specific sentences or phrases are similar. The settings for Similarity Check screening are as follows: It excludes quotes, bibliography, small matches of 6 words, small sources of 1%, and the Methods section.

Number of reviewers

Reviewers will be selected from the list of reviewers. Manuscripts are then peer reviewed by at least 2 experts in the corresponding field, usually by 2.

Peer review process and the author response to the reviewer comments
JOET adopts single blind review, which means that the authors do not know the identity of the reviews. All papers, including those invited by the Editor, are subject to peer review.

The review period is 4 weeks. Usually the first decision is made within a week after completion of the review. The Editorial Board's decision after the review will be one of followings: Accept, Minor revision, Major revision, or Rejection. The Editorial Board may request the authors to revise the manuscript according to the reviewers' comments. If there are any requests for revision of the manuscript by the reviewers, the authors should do their best to revise the manuscript. If the reviewer's opinion is not acceptable or is believed to misinterpret the data, the author should reasonably indicate that. After revising the manuscript, the author should upload the revised files with a separate response sheet to each item of the reviewer's commentary. The author's revisions should be completed within 3 months after the request. If it is not received by the due date, the Editorial Board will notify the author. To extend the revision period beyond 3 months, the author should negotiate that with the Editorial Board. The manuscript review process can be provided for up two rounds. If the authors wish further review, the Editorial Board may consider it. The Editorial Board will make a final decision on the approval of the submitted manuscript for publication and can request any further corrections, revisions, and deletions of the article text if necessary. Statistical editing is also performed if the data requires professional statistical review by a statistician.

Processing after acceptance

If the manuscript is finally accepted, the galley proof will be sent to the corresponding author after professional manuscript editing and English proofreading. Proofreading should be performed for any misspellings or errors by the authors. After final proofreading, the manuscript may appear at the journal homepage as an article in press with a unique DOI number for rapid communication. All published articles will be replaced by the replacement XML file and a final PDF.

Feedback after publication

If the authors or readers find any errors, or contents that should be revised, it can be requested from the Editorial Board. The Editorial Board may consider erratum, corrigendum or a retraction. If there are any revisions to the article, there will be a CrossMark description to announce the final draft. If there is a reader's opinion on the published article with the form of Letter to the editor, it will be forwarded to the authors. The authors can reply to the reader's letter. Letter to the editor and the author's reply may be also published.

How the journal handle complaints and appeals

The policy of JOET is primarily aimed at protecting the authors, reviewers, editors, and the publisher of the journal. If not described below, the process of handling complaints and appeals follows the guidelines of the Committee of Publication Ethics available from: <https://publicationethics.org/appeals>

- Who complains or makes an appeal?

Submitters, authors, reviewers, and readers may register complaints and appeals in a variety of cases as follows: falsification, fabrication, plagiarism, duplicate publication, authorship dispute, conflict of interest, ethical treatment of animals, informed consent, bias or unfair/inappropriate competitive acts, copyright, stolen data, defamation, and legal problem. If any individuals or institutions want to inform the cases, they can send a letter via the contact page on our website: <https://www.joet.org/about/contact.php>. For the complaints

or appeals, concrete data with answers to all factual questions (who, when, where, what, how, why) should be provided.

- Who is responsible to resolve and handle complaints and appeals?

The Editorial Board or Editorial Office is responsible for them. A legal consultant or ethics editor may be able to help with the decision making.

- What may be the consequence of remedy?

It depends on the type or degree of misconduct. The consequence of resolution will follow the guidelines of the Committee of Publication Ethics (COPE).

Article processing charge

Payment due

Article processing charge (APC) covers the range of publishing services JOET provides. This includes provision of online tools for editors and authors, article production and hosting, and customer services. Upon editorial acceptance of an article for the regular review service and upon submission of an article for the fast review service, the corresponding author will be notified that payment is due.

APC

The APC up to 6 pages is ₩200,000 (or \$200) for the regular review service and ₩550,000 (or \$550) for the fast review service. For papers longer than 6 pages, an extra APC of \$30 per page is charged. No taxes are included in this charge.

Payment methods

Credit card payment can be made online using a secure payment form as soon as the manuscript has been editorially accepted. We will send a receipt by email once payment has been processed. Please note that payment by credit card carries a surcharge of 10% of the total APC.

Invoice payment is due within 7 days of the manuscript receiving editorial acceptance. Receipts are available on request.



Title of Article

Firstname Lastname¹, Firstname Lastname² and Firstname Lastname³

¹Professor, Department of OO, OO School, OO University, Busan, Korea

²Graduate Student, Department of OO, OO University, Seoul, Korea

³Senior Researcher, Department of OO, OO Engineering. Corp., Seoul, Korea

KEY WORDS: Lumped mass line model, Explicit method, Steel lazy wave riser (Immediately after the abstract, provide a maximum of 5 or 6 keywords.)

ABSTRACT: A concise and factual abstract is required. The abstract should state briefly the purpose of the research, the principal results and major conclusions. An abstract should be written in around 300 words and is often presented separately from the article, so it must be able to stand alone. For this reason, References should be avoided, but if essential, then cite the author(s) and year(s). Also, non-standard or uncommon abbreviations should be avoided, but if essential they must be defined at their first mention in the abstract itself.

Nomenclature

<i>I</i> TOC	Increment of total operating cost (\$/yr)
<i>L</i> HV	Lower heating value (kJ/kg)
<i>P</i> w	Power (kW)
<i>T</i>	Temperature (K)
<i>V</i>	Volume (m ³)
ρ	Density (kg/m ³)

1. Introduction

The introduction should briefly place the study in a broad context and highlight why it is important. It should define the purpose of the work and its significance. The current state of the research field should be reviewed carefully and key publications cited. Please highlight controversial and diverging hypotheses when necessary. Finally, briefly mention the main aim of the work and highlight the principal conclusions. As far as possible, please keep the introduction comprehensible to scientists outside your particular field of research.

2. General Information for Authors

2.1 Requirement for Membership

One of the authors who submits a paper or papers should be member of

The Korea Society of Ocean Engineers (KSOE), except a case that editorial board provides special admission of submission.

2.2 Publication type

Manuscript is made up of scholarly monographs, technical reports and data. The paper should have not been submitted to other academic journal. Conference papers, research reports, dissertations and review articles can be submitted to Journal Of Ocean Engineering and Technology (JOET). When part or whole of a paper was already published to conference papers, research reports, dissertations, and review articles, then corresponding author should note it clearly in the manuscript. After published to JOET, the copyright of manuscript belongs to KSOE.

(example) It is noted that this paper is revised edition based on proceedings of KAOST 2100 in Jeju.

2.3 Manuscript submission

Manuscript should be submitted through the on-line manuscript website (<http://www.joet.org>). The date that corresponding author submits a paper through on-line website is official date of submission. Other correspondences can be sent by an email to the Editor in Chief. The manuscript must be accompanied by a signed statement that it has been neither published nor currently submitted for publication elsewhere. The manuscript should be written in English or Korean and a

Received 00 February 2100, revised 00 October 2100, accepted 00 October 2100

Corresponding author Firstname Lastname: +82-51-759-0656, e-mail@e-mail.com

It is a recommended paper from the proceedings of 2019 spring symposium of the Korea Marine Robot Technology (KMRTS).

© 2100, The Korean Society of Ocean Engineers

This is an open access article distributed under the terms of the creative commons attribution non-commercial license (<http://creativecommons.org/licenses/by-nc/4.0>) which permits unrestricted non-commercial use, distribution, and reproduction in any medium, provided the original work is properly cited.

minimum standard of the proficiency in the English or Korean language should be met before submission to the editorial office.

Ensure that online submission or submission by e-mail text files are in a standard word processing format (Hangul or MS Word are preferred). Ensure that graphics are high-resolution. Be sure all necessary files have been uploaded/attached.

2.3.1 Author's checklist and Transfer of copyright

Author's checklist and Transfer of copyright can be found in submission homepage (<http://www.joet.org>).

2.4 Research and Publication Ethics

Authorship should be limited to those who have made a significant contribution to the conception, design, execution, or interpretation of the reported study. All those who have made significant contributions should be listed as co-authors. Where there are others who have participated in certain substantive aspects of the research project, they should be acknowledged or listed as contributors.

The corresponding author should ensure that all appropriate co-authors and no inappropriate co-authors are included on the paper, and that all co-authors have seen and approved the final version of the paper and have agreed to its submission for publication.

Details on publication ethics are found in the journal's website (<http://joet.org/authors/ethics.php>). For the policies on research and publication ethics not stated in the Instructions, Guidelines on Good Publication (<http://publicationethics.org/>) can be applied.

3. Manuscript

Manuscript must consist of as follow: (1) Title, (2) Author's information (include title), (3) Key word, (4) Abstract, (5) Nomenclature description, (6) Introduction, (7) Body (analysis, test, results and discussion), (8) Conclusion, (9) Acknowledgements, (10) Reference, (11) Appendix, etc.

3.1 Unit

Use the international system units(SI). If other units are mentioned, please give their equivalent in SI.

3.2 Equations

All mathematical equations should be clearly printed/typed using well accepted explanation. Superscripts and subscripts should be typed clearly above or below the base line. Equation numbers should be given in Arabic numerals enclosed in parentheses on the right-hand margin. They should be cited in the text as, for example, Eq. (1), or Eqs. (1)-(3).

$$G_{GEV}(x;\mu,\sigma,\xi) = \begin{cases} \exp[-(1+\xi(x-\mu)/\sigma)^{-1/\xi}] & \xi \neq 0 \\ \exp[-\exp(-(x-\mu)/\sigma)] & \xi = 0 \end{cases} \quad (1)$$

in which μ , σ , and ξ represent the location ("Shift" in figures), scale, and shape parameters, respectively.

3.3 Tables

Tables should be numbered consecutively with Arabic numerals. Each table should be typed on a separate sheet of paper and be fully titled. All tables should be referred to in the text.

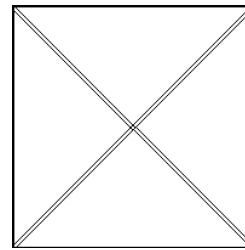
Table 1 Tables should be placed in the main text near to the first time they are cited

Item	Buoyancy riser
Segment length ¹ (m)	370
Outer diameter (m)	1.137
Inner diameter (m)	0.406
Dry weight (kg/m)	697
Bending rigidity (N·m ²)	1.66E8
Axial stiffness (N)	7.098E9
Inner flow density (kg·m ³)	881
Seabed stiffness (N/m ²)	6,000

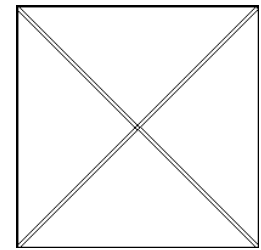
¹Tables may have a footer.

3.4 Figures

All the illustrations should be of high quality meeting with the publishing requirement with legible symbols and legends. In preparing the illustrations, authors should consider a size reduction during the printing process to have acceptable line clarity and character sizes. All figures should have captions. They should be referred to in the text as, for example, Fig. 1, or Figs. 1-3.



(a) Description of what is contained in the first panel



(b) Description of what is contained in the second panel

Fig. 1 Schemes follow the same formatting. If there are multiple panels, they should be listed as: (a) Description of what is contained in the first panel; (b) Description of what is contained in the second panel. Figures should be placed in the main text near to the first time they are cited

3.5 How to describe the references in main texts

All references should be listed at the end of the manuscripts, arranged in order of Alphabet. References in texts follow the American Psychological Association (APA) style. The exemplary form of listed references is as follows:

Single author: (Kim, 1998) or Kim (1998)

Two authors: (Kim and Lee, 2000) or Kim and Lee (2000)

Three or more authors: (Kim et al., 1997) or Kim et al. (1997)

Two or more papers: (Lee, 1995a; Lee, 1995b; Ryu et al., 1998)

Year unknown: (Kim, n.d.) or Kim (n.d.)

4. Results

This section may be divided by subheadings. It should provide a concise and precise description of the experimental results, their interpretation as well as the experimental conclusions that can be drawn. Tables and figures are recommended to present the results more rapidly and easily. Do not duplicate the content of a table or a figure with in the Results section. Briefly describe the core results related to the conclusion in the text when data are provided in tables or in figures. Supplementary results can be placed in the Appendix.

5. Discussion

Authors should discuss the results and how they can be interpreted in perspective of previous studies and of the working hypotheses. The findings and their implications should be discussed in the broadest context possible. Future research directions may also be highlighted

6. Conclusions

This section can be added to the manuscript.

Funding

Please add: “This research was funded by Name of Funder, grant number XXX” and “The OOO was funded by XXX”. Check carefully that the details given are accurate and use the standard spelling of funding agency names at <https://search.crossref.org/funding>

Acknowledgments

In this section you can acknowledge any support given which is not covered by the author contribution or funding sections. This may include administrative and technical support, or donations in kind (e.g., materials used for experiments). For mentioning any persons or any organizations in this section, there should be a written permission from them.

Conflict of interest

It should be disclosed here according to the statement in the Research and publication ethics regardless of existence of conflict of interest. If the authors have nothing to disclose, please state: “No potential conflict of interest relevant to this article was reported.”

References

- Journal name should not be abbreviated.
- A private report with limited access or download availability can not be a reference.
- Include the digital object identifier DOI or URL for all references

where available.

- Reference list follows the American Psychological Association (APA) style.

Referring to journal publications:

- Author, A.A., Author, B.B., & Author, C.C. (Year). Title of Article. Journal Title, vol(no), pp-pp. <https://doi.org/xx.xxxx/xxxxxx>
- Author, A.A., Author, B.B., Author, C.C. (accepted; in press). Title of Article. Title of Periodical. Retrieved from <http://xx.xxx/x.pdf>
- Lee, T.K., Kim, T.W., Rim, C.W., & Kim, S.C. (2013). A Study on Calculation of Local Ice Pressures for ARAON Based on Data Measured at Arctic Sea. Journal of Ocean Engineering and Technology, 27(5), 88-92. <https://doi.org/10.5574/KSOE.2013.27.5.088>
- Lee, T.K., Kim, T.W., Rim, C.W., & Kim, S.C. (accepted; in press). A Study on Calculation of Local Ice Pressures for ARAON Based on Data Measured at Arctic Sea. Journal of Ocean Engineering and Technology, Retrieved from <http://xxx.xxx/xxx.pdf>

Referring to conference proceedings:

- Author, A.A., Author, B.B., & Author, C.C. (Year). Title of Article. Proceeding Title, City, Country, pp-pp. <https://doi.org/xx.xxxx>
- Aoki, S., Liu, H., & Sawaragi, T. (1994). Wave Transformation and Wave Forces on Submerged Vertical Membrane. Proceedings of International Symposium Waves - Physical and Numerical Modeling, Vancouver, Canada, 1287-1296.
- Tsukamoto, C.L., Lee, W., Yuh, J., Choi, S.K., & Lorentz, J. (1997). Comparison Study on Advanced Thruster Control of Underwater Robots. Proceedings of International Conference on Robotics and Automation, 1845-1850. <https://doi.org/110.1109/ROBOT.1997.619056>

Referring to books:

- Author, A.A. (Year). Title of Book (xx ed.). Location: Publisher.
- Strunk, W., & White, E.B. (2000). The Elements of Style (4th ed.). New York, USA: Longman.
- Schlichting, H. (1968). Boundary Layer Theory (6th ed.). New York, USA: McGraw-Hill.

Referring to theses or dissertations:

- Author, A.A. (Year). Title of Doctoral Dissertation or Master's thesis (Doctoral Dissertation or Master's thesis). Name of Institution, City, Country.
- Giovanni, I. (1998). Modelling and Identification of Underwater Robotic Systems (Ph.D. Thesis). University of Genova, Genova, Italy.

Referring to technical reports, rules, or guidelines:

- Author, A.A. (Year). Title of report (Reprot No. xxx), Location: Publisher.
- Likhomanov, V. (2010). Full-Scale Ice Trials of the Korean Research Icebreaker ARAON. Daejeon, Korea: Arctic and Antarctic Research Institute (AARI).
- ABS. (2011). Guide for Ice Loads Monitoring Systems. Houston, USA: American Bureau of Shipping.
- Lloyd's Register. (2011). FDA ICE Fatigue Induced by Ice Loading,

ShipRight Design and construction - Fatigue Design Assessment. London, United Kingdom: Lloyd's Register.

Larson, M., & Kraus, N.C. (1989). SBEACH: Numerical Model for Simulating Storm-Induced Beach Change - Report 1 Empirical Foundation and Model Development (Technical Report CERC-89-9). Coastal Engineering research center Vicksburg Ms.

Referring to patents:

Rightholder, A.A. (Year). Title of Patent. Patent number, Patent office with country.

Dawoo Shipbuilding & Marine Engineering (DSME). (2013). Distance Length Standardization Method for Preventing Interference at the time of Uploading Cell Guide of Container Ship. Unexamined Patent Publication 1020130044635, Korean Intellectual Property Office.

Referring to websites:

Rightholder, A.A. (Year). Title of webpage. Retrieved Month Year from <http://xxxx>

International Association of Classification Societies (IACS). (2010a). Common Structural Rules for Bulk Carriers. Retrieved July 2010 from <http://www.iacs-data.org.uk>

US Congressional Hearing. (2009). Strategic Importance of the Arctic in Us Policy. Retrieved June 2019 from <https://fas.org/irp/arctic.pdf>

Dawoo Shipbuilding & Marine Engineering (DSME). (2013). Distance Length Standardization Method for Preventing Interference at the time of Uploading Cell Guide of Container Ship. Retrieved June 2019 from <https://patentimages.storage./pdfs/792.pdf>

Referring to software:

Rightholder, A.A. (Year). Title of Software. Downloaded Month Year from <http://xxxx>

Referring to some exceptional cases:

- when authors are missing, institution can replace authors

National Oceanic and Atmospheric Administration (NOAA). (2015). Deep-ocean Assessment and Reporting of Tsunamis (DART). Retrieved December 2019 from <https://nctr.pmel.noaa.gov/Dart/>

- when dates or years are missing, it is replaced with "n.d."

National Oceanic and Atmospheric Administration (NOAA). (n.d).

Deep-ocean Assessment and Reporting of Tsunamis (DART).

- when more than seven authors, first 6 authors ... last author.

Yeu, T., Choi, H.T., Lee, Y., Chae, J., Lee, Y., Kim, S.S., ... Lee, T.H. (2019). Development of Robot Platform for Autonomous Underwater Intervention. Journal of Ocean Engineering and Technology, 33(2), 168-177. <https://doi.org/10.26748/KSOE.2019.021>

Appendix

The appendix is an optional section that can contain details and data supplemental to the main text. For example, explanations of experimental details that would disrupt the flow of the main text, but nonetheless remain crucial to understanding and reproducing the research shown; figures of replicates for experiments of which representative data is shown in the main text can be added here if brief, or as Supplementary data. Mathematical proofs of results not central to the paper can be added as an appendix.

All appendix sections must be cited in the main text. In the appendixes, Figures, Tables, etc. should be labeled starting with 'A', e.g., Fig. A1, Fig. A2, etc.

Examples:

<https://doi.org/10.26748/KSOE.2019.022>

<https://doi.org/10.26748/KSOE.2018.4.32.2.095>

Author ORCIDs

All authors are recommended to provide an ORCID. To obtain an ORCID, authors should register in the ORCID web site: <http://orcid.org>. Registration is free to every researcher in the world. Example of ORCID description is as follows:

Author name	ORCID
So, Hee	0000-0000-000-00X
Park, Hye-Il	0000-0000-000-00X
Yoo, All	0000-0000-000-00X
Jung, Jewelry	0000-0000-000-00X

Authors' Checklist

The following list will be useful during the final checking of a manuscript prior to sending it to the journal for review. Please submit this checklist to the KSOE when you submit your article.

< Checklist for manuscript preparation >

- I checked my manuscript has been 'spell-checked' and 'grammar-checked'.
- One author has been designated as the corresponding author with contact details such as
 - E-mail address
 - Phone numbers
- I checked abstract 1) stated briefly the purpose of the research, the principal results and major conclusions, 2) was written in around 300 words, and 3) did not contain references (but if essential, then cite the author(s) and year(s)).
- I provided 5 or 6 keywords.
- I checked color figures were clearly marked as being intended for color reproduction on the Web and in print, or to be reproduced in color on the Web and in black-and-white in print.
- I checked all table and figure numbered consecutively in accordance with their appearance in the text.
- I checked abbreviations were defined at their first mention there and used with consistency throughout the article.
- I checked all references mentioned in the Reference list were cited in the text, and vice versa according to the APA style.
- I checked I used the international system units (SI) or SI-equivalent engineering units.

< Authorship checklist >

JOET considers individuals who meet all of the following criteria to be authors:

- Made a significant intellectual contribution to the theoretical development, system or experimental design, prototype development, and/or the analysis and interpretation of data associated with the work contained in the article.
- Contributed to drafting the article or reviewing and/or revising it for intellectual content.
- Approved the final version of the article as accepted for publication, including references.

< Checklist for publication ethics >

- I checked the work described has not been published previously (except in the form of an abstract or as a part of a published lecture or academic thesis).
- I checked when the work described has been published previously in other proceedings without copyright, it has clearly noted in the text.
- I checked permission has been obtained for use of copyrighted material from other sources including the Web.
- I have processed Plagiarism Prevention Check through reliable web sites such as www.kci.go.kr, <http://www.ithenticate.com/>, or <https://www.copykiller.org/> for my submission.
- I agree that final decision for my final manuscript can be changed according to results of Plagiarism Prevention Check by JOET administrator.
- I checked one author at least is member of the Korean Society of Ocean Engineers.
- I agreed all policies related to 'Research and Publication Ethics'
- I agreed to transfer copyright to the publisher as part of a journal publishing agreement and this article will not be published elsewhere including electronically in the same form, in English or in any other language, without the written consent of the copyright-holder.
- I made a payment for reviewing of the manuscript, and I will make a payment for publication on acceptance of the article.
- I have read and agree to the terms of Authors' Checklist.

Title of article :

Date of submission : DD/MM/YYYY

Corresponding author :

signature

Email address :

※ E-mail this with your signature to ksoehj@ksoe.or.kr

Publishing Agreement

ARTICLE DETAILS

Title of article :
Corresponding author :
E-mail address :
DOI : <https://doi.org/10.26748/KSOE.2XXX.XXX>

YOUR STATUS

I am one author signing on behalf of all co-authors of the manuscript.

ASSIGNMENT OF COPYRIGHT

I hereby assign to the Korean Society of Ocean Engineers, the copyright in the manuscript identified above and any tables, illustrations or other material submitted for publication as part of the manuscript (the "Article"). This assignment of rights means that I have granted to Korean Society of Ocean Engineers the exclusive right to publish and reproduce the Article, or any part of the Article, in print, electronic and all other media (whether now known or later developed), in any form, in all languages, throughout the world, for the full term of copyright, and the right to license others to do the same, effective when the Article is accepted for publication. This includes the right to enforce the rights granted hereunder against third parties.

SCHOLARLY COMMUNICATION RIGHTS

I understand that no rights in patents, trademarks or other intellectual property rights are transferred to the Journal owner. As the author of the Article, I understand that I shall have: (i) the same rights to reuse the Article as those allowed to third party users of the Article under the CC-BY-NC License, as well as (ii) the right to use the Article in a subsequent compilation of my works or to extend the Article to book length form, to include the Article in a thesis or

dissertation, or otherwise to use or re-use portions or excerpts in other works, for both commercial and non-commercial purposes. Except for such uses, I understand that the assignment of copyright to the Journal owner gives the Journal owner the exclusive right to make or sub-license commercial use.

USER RIGHTS

The publisher will apply the Creative Commons Attribution-Noncommercial Works 4.0 International License (CC-BY-NC) to the Article where it publishes the Article in the journal on its online platforms on an Open Access basis.

The CC-BY-NC license allows users to copy and distribute the Article, provided this is not done for commercial purposes and further does not permit distribution of the Article if it is changed or edited in any way, and provided the user gives appropriate credit (with a link to the formal publication through the relevant DOI), provides a link to the license, and that the licensor is not represented as endorsing the use made of the work. The full details of the license are available at <http://creativecommons.org/licenses/by-nc/4.0/legalcode>.

REVERSION OF RIGHTS

Articles may sometimes be accepted for publication but later rejected in the publication process, even in some cases after public posting in "Articles in Press" form, in which case all rights will revert to the author.

I have read and agree to the terms of the Journal Publishing Agreement.

Corresponding author:

name

signature

※ E-mail this with your signature to ksoehj@ksoe.or.kr (Papers will not be published unless this form is signed and returned)

Research and Publication Ethics

Journal of Ocean Engineering and Technology (JOET) adheres to the guidelines published by professional organizations, including Committee on Publication Ethics (COPE; <https://publicationethics.org/>)

1. Authorship

JOET considers individuals who meet all of the following criteria to be authors:

- 1) Made a significant intellectual contribution to the theoretical development, system or experimental design, prototype development, and/or the analysis and interpretation of data associated with the work contained in the article.
- 2) Contributed to drafting the article or reviewing and/or revising it for intellectual content.
- 3) Approved the final version of the article as accepted for publication, including references.

Contributors who do not meet all of the above criteria may be included in the Acknowledgment section of the article. Omitting an author who contributed to your article or including a person who did not fulfill all of the above requirements is considered a breach of publishing ethics.

Correction of authorship after publication: JOET does not correct authorship after publication unless a mistake has been made by the editorial staff.

2. Originality and Duplicate Publication

All submitted manuscripts should be original and should not be in consideration by other scientific journals for publication. Any part of the accepted manuscript should not be duplicated in any other scientific journal without permission of the Editorial Board, although the figures and tables can be used freely if the original source is verified according to the Creative Commons Attribution License (CC BY-NC). It is mandatory for all authors to resolve any copyright issues when citing a figure or table from other journal that is not open access.

3. Conflict-of-Interest Statement

Conflict of interest exists when an author or the author's institution, reviewer, or editor has financial or personal relationships that inappropriately influence or bias his or her actions. Such relationships are also known as dual commitments, competing interests, or competing loyalties. These relationships vary from being negligible to having a great potential for influencing judgment. Not all relationships represent true conflict of interest. On the other hand, the potential for conflict of interest can exist regardless of whether an individual believes that the relationship affects his or her scientific judgment. Financial relationships such as employment, consultancies, stock ownership, honoraria, and paid expert testimony are the most easily identifiable conflicts of interest and the most likely to undermine the credibility of the journal, the authors, or of the science itself. Conflicts can occur for other reasons as well, such as personal relationships, academic competition, and intellectual passion. If there are any conflicts of interest, authors should disclose them in the manuscript. The conflicts of interest may occur during the research process as well; however, it is important to provide disclosure. If there is a disclosure, editors, reviewers, and reader can approach the manuscript after understanding the situation and the background of the completed research.

4. Management Procedures for the Research and Publication Misconduct

When JOET faces suspected cases of research and publication misconduct such as a redundant (duplicate) publication, plagiarism, fabricated data, changes in authorship, undisclosed conflicts of interest, an ethical problem discovered with the submitted manuscript, a reviewer who has appropriated an author's idea or data, complaints against editors, and other issues, the resolving process will follow the flowchart provided by the Committee on Publication Ethics (<http://publicationethics.org/resources/flowcharts>). The Editorial Board of JOET will discuss the suspected cases and reach a decision. JOET will not hesitate to publish

errata, corrigenda, clarifications, retractions, and apologies when needed.

5. Editorial Responsibilities

The Editorial Board will continuously work to monitor and safeguard publication ethics: guidelines for retracting articles; maintenance of the integrity of the academic record; preclusion of business needs from compromising intellectual and ethical standards; publishing corrections, clarifications, retractions, and apologies when needed; and excluding plagiarism and fraudulent data. The editors maintain the following responsibilities: responsibility and authority to reject and accept articles; avoiding any conflict of interest with respect to articles they reject or accept; promoting publication of corrections or retractions when errors are found; and preservation of the anonymity of reviewers.

6. Hazards and human or animal subjects

If the work involves chemicals, procedures or equipment that have any unusual hazards inherent in their use, the author must clearly identify these in the manuscript. If the work involves the use of animal or human subjects, the author should ensure that the manuscript contains a statement that all procedures were performed in compliance with relevant laws and institutional guidelines and that the appropriate institutional committee(s) has approved them. Authors should include a statement in the manuscript that informed consent was obtained for experimentation with human subjects. The privacy rights of human subjects must always be observed.

Ensure correct use of the terms sex (when reporting biological factors) and gender (identity, psychosocial or cultural factors), and, unless inappropriate, report the sex and/or gender of study participants, the sex of animals or cells, and describe the methods used to determine sex and gender. If the study was done involving an exclusive population, for example in only one sex, authors should justify why, except in obvious cases. Authors should define how they determined race or ethnicity and justify their relevance.

7. Secondary publication

It is possible to republish manuscripts if the manuscripts satisfy the conditions of secondary publication. These are:

- The authors have received approval from the Editorial Board of both journals (the editor concerned with the secondary publication must have access to the primary version).
- The priority for the primary publication is respected by a publication interval negotiated by editors of both journals and the authors.
- The paper for secondary publication is intended for a different group of readers
- The secondary version faithfully reflects the data and interpretations of the primary version.
- The secondary version informs readers, peers, and documenting agencies that the paper has been published in whole or in part elsewhere, for example, with a note that might read, "This article is based on a study first reported in the [journal title, with full reference]"
- The title of the secondary publication should indicate that it is a secondary publication (complete or abridged republication or translation) of a primary publication.

8. Complaints and Appeals

The process of handling complaints and appeals follows the guidelines of the COPE available from: <https://publicationethics.org/appeals>

9. Post-publication discussions and corrections

The post-publication discussion is available through letter to editor. If any readers have a concern on any articles published, they can submit letter to editor on the articles. If there found any errors or mistakes in the article, it can be corrected through errata, corrigenda, or retraction.



The Korean Society of Ocean Engineers